Helium Ion Microscopy: A new tool to analyze and modify nanoscale objects

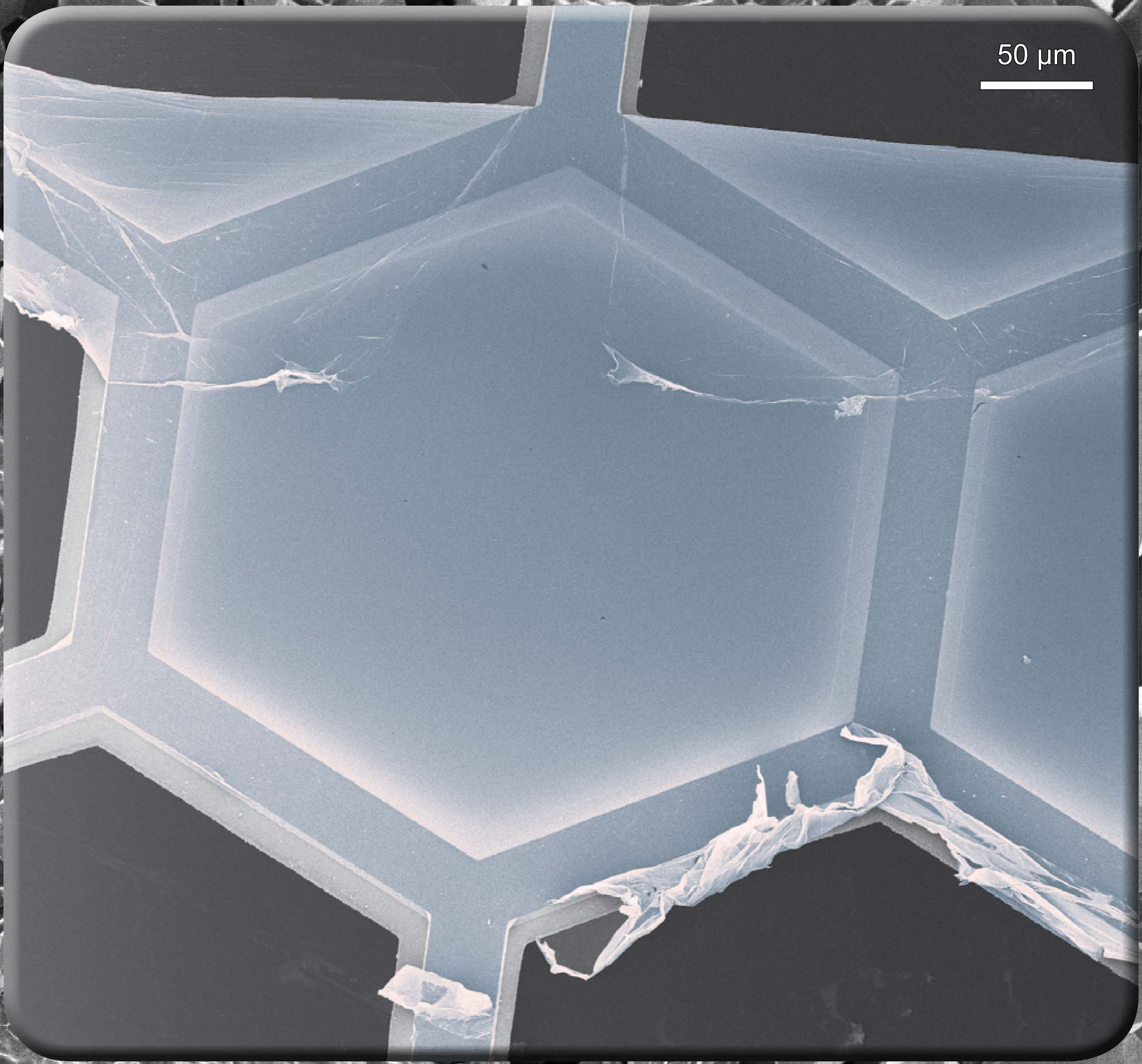

Henning Vieker - Bielefeld University - 2014

Universität Bielefeld

Fakultät für Physik

Helium Ion Microscopy: A new tool to analyze and modify nanoscale objects

Dissertation submitted in partial fulfillment
of the requirements for the degree of
Doktor der Naturwissenschaften
submitted by Dipl. Phys.

Henning Vieker

from Espelkamp, Germany

November 2014

Declaration:

I hereby declare that the work in this thesis is my original work. None but the indicated resources were used.

Parts of this work are already published in various scientific journals (see List of publications).

Committee:

1. Prof. Dr. Armin Gölzhäuser
2. Prof. Dr. Katharina Kohse-Höinghaus

Cover

Front: Freestanding carbon nanomembrane on copper grid. See chapter 3.1.

Background: Defective filament used in an electron floodgun. Extended re-crystallization of the hot tungsten filament together with carbon contaminations in the high vacuum environment caused massive changes on the wire.

Backside cover

Top left: Soot from a C3-flame sampled at 8 mm height. See chapter 3.2.

Top right: Gold nanowire in SE (left) - and RBI (right) – mode. See chapter 3.4.

Lower left: helium ion milled bow-tie structure in 30 nm gold on glass. See chapter 4.2.

Lower right: CVD-grown iron-cobalt oxide film. See chapter 3.3.

Gedruckt auf alterungsbeständigem Papier nach ISO 9706

List of Publications

Publications integrated in this thesis

(1) Zhang, X.; **Vieker, H**.; Beyer, A.; Gölzhäuser, A. Fabrication of Carbon Nanomembranes by Helium Ion Beam Lithography. *Beilstein Journal of Nanotechnology* **2014**, *5*, 188–194.

(2) Thiele, C.; **Vieker, H**.; Beyer, A.; Flavel, B. S.; Hennrich, F.; Torres, D. M.; Eaton, T. R.; Mayor, M.; Kappes, M. M.; Gölzhäuser, A.; *et al.* Fabrication of Carbon Nanotube Nanogap Electrodes by Helium Ion Sputtering for Molecular Contacts. *Applied Physics Letters* **2014**, *104*, 103102.

(3) Schenk, M.*; Lieb, S.*; **Vieker, H**.*; Beyer, A.; Gölzhäuser, A.; Wang, H.; Kohse-Höinghaus, K. Morphology of Nascent Soot in Ethylene Flames. *Proceedings of the Combustion Institute* **2014**, DOI: 10.1016/j.proci.2014.05.009. *: These authors contributed equally to this work.

(4) Kouotou, P. M.; **Vieker, H**.; Tian, Z.-Y.; Ngamou, P. T.; Kasmi, A. E.; Beyer, A.; Gölzhäuser, A.; Kohse-Höinghaus, K. Structure-Activity Relation of Spinel-Type Co-Fe Oxides for Low-Temperature CO Oxidation. *Catal. Sci. Technol.* **2014**, *4*, 3359–3367.

(5) Angelova, P.; **Vieker, H**.; Weber, N.-E.; Matei, D.; Reimer, O.; Meier, I.; Kurasch, S.; Biskupek, J.; Lorbach, D.; Wunderlich, K.; *et al.* A Universal Scheme to Convert Aromatic Molecular Monolayers into Functional Carbon Nanomembranes. *ACS Nano* **2013**, *7*, 6489–6497.

(6) Gries, K.; **Vieker, H**.; Gölzhäuser, A.; Agarwal, S.; Greiner, A. Preparation of Continuous Gold Nanowires by Electrospinning of High-Concentration Aqueous Dispersions of Gold Nanoparticles. *Small* **2012**, *8*, 1436–1441.

Publications thematically addressed in this thesis

(1) Tian, Z.-Y.; **Vieker, H**.; Kouotou, P. M.; Beyer, A. In-Situ Characterization of Cu-Co Oxides for Catalytic Application. *Faraday Discussions* **2014**, *Manuscript accepted*.

(2) Tian, Z.-Y.; Kouotou, P. M.; El Kasmi, A.; Tchoua Ngamou, P. H.; Kohse-Höinghaus, K.; **Vieker, H**.; Beyer, A.; Gölzhäuser, A. Low-Temperature Deep Oxidation of Olefins and DME over Cobalt Ferrite. *Proceedings of the Combustion Institute* **2014**, DOI: 10.1016/j.proci.2014.06.111.

(3) Schenk, M.; Hansen, N.; **Vieker, H**.; Beyer, A.; Gölzhäuser, A.; Kohse-Höinghaus, K. PAH Formation and Soot Morphology in Flames of C4 Fuels. *Proceedings of the Combustion Institute* **2014**, DOI: 10.1016/j.proci.2014.06.139.

(4) Mitschang, F.; Langner, M.; **Vieker, H**.; Beyer, A.; Greiner, A. Preparation of Conductive Gold Nanowires in Confined Environment of Gold-Filled Polymer Nanotubes. *Macromolecular Rapid Communications* **2014**, *Manuscript accepted*.

(5) Kollmann, H.; Piao, X.; Esmann, M.; Becker, S. F.; Hou, D.; Huynh, C.; Kautschor, L.-O.; Bösker, G.; **Vieker, H**.; Beyer, A.; *et al.* Toward Plasmonics with Nanometer Precision: Nonlinear Optics of Helium-Ion Milled Gold Nanoantennas. *Nano Lett.* **2014**, *14*, 4778–4784.

(6) Ai, M.; Shishatskiy, S.; Wind, J.; Zhang, X.; Nottbohm, C. T.; Mellech, N.; Winter, A.; **Vieker, H**.; Qiu, J.; Dietz, K.-J.; *et al.* Carbon Nanomembranes (CNMs) Supported by Polymer: Mechanics and Gas Permeation. *Adv. Mater.* **2014**, *26*, 3421–3426.

(7) Tian, Z.-Y.; Herrenbrück, H. J.; Kouotou, P. M.; **Vieker, H**.; Beyer, A.; Gölzhäuser, A.; Kohse-Höinghaus, K. Facile Synthesis of Catalytically Active Copper Oxide from Pulsed-Spray Evaporation CVD. *Surface and Coatings Technology* **2013**, *230*, 33–38.

(8) Schenk, M.; Lieb, S.; **Vieker, H**.; Beyer, A.; Gölzhäuser, A.; Wang, H.; Kohse-Höinghaus, K. Imaging Nanocarbon Materials: Soot Particles in Flames Are Not Structurally Homogeneous. *ChemPhysChem* **2013**, *14*, 3248–3254.

(9) Ritter, R.; Wilhelm, R. A.; Stöger-Pollach, M.; Heller, R.; Mücklich, A.; Werner, U.; **Vieker, H**.; Beyer, A.; Facsko, S.; Gölzhäuser, A.; *et al.* Fabrication of Nanopores in 1 nm Thick Carbon Nanomembranes with Slow Highly Charged Ions. *Applied Physics Letters* **2013**, *102*, 063112–063112 – 5.

(10) Kouotou, P. M.; Tian, Z.-Y.; **Vieker, H**.; Beyer, A.; Gölzhäuser, A.; Kohse-Höinghaus, K. Selective Synthesis of A-Fe2O3 Thin Films and Effect of the Deposition Temperature and Lattice Oxygen on the Catalytic Combustion of Propene. *J. Mater. Chem. A* **2013**, *1*, 10495–10504.

(11) Kouotou, P. M.; Tian, Z.-Y.; **Vieker, H**.; Kohse-Höinghaus, K. Pulsed-Spray Evaporation CVD Synthesis of Hematite Thin Films for Catalytic Conversion of CO. *Surface and Coatings Technology* **2013**, *230*, 59–65.

(12) Walter, A.; Muzik, H.; **Vieker, H**.; Turchanin, A.; Beyer, A.; Gölzhäuser, A.; Lacher, M.; Steltenkamp, S.; Schmitz, S.; Holik, P.; *et al.* Practical Aspects of Boersch Phase Contrast Electron Microscopy of Biological Specimens. *Ultramicroscopy* **2012**, *116*, 62–72.

Other publications

(1) Wu, Z.-S.; Parvez, K.; Winter, A.; **Vieker, H**.; Liu, X.; Han, S.; Turchanin, A.; Feng, X.; Müllen, K. Layer-by-Layer Assembled Heteroatom-Doped Graphene Films with Ultrahigh Volumetric Capacitance and Rate Capability for Micro-Supercapacitors. *Adv. Mater.* **2014**, *26*, 4552–4558.

(2) Takei, H.; Bessho, N.; Ishii, A.; Okamoto, T.; Beyer, A.; **Vieker, H**.; Gölzhäuser, A. Enhanced Infrared LSPR Sensitivity of Cap-Shaped Gold Nanoparticles Coupled to a Metallic Film. *Langmuir* **2014**, *30*, 2297–2305.

(3) Schrader, I.; Wittig, L.; Richter, K.; **Vieker, H**.; Beyer, A.; Gölzhäuser, A.; Hartwig, A.; Swiderek, P. Formation and Structure of Copper(II) Oxalate Layers on Carboxy-Terminated Self-Assembled Monolayers. *Langmuir* **2014**, *30*, 11945–11954.

(4) Goldman, J. L.; Cason, M. W.; Wetzel, D. J.; **Vieker, H**.; Beyer, A.; Gölzhäuser, A.; Gewirth, A. A.; Nuzzo, R. G. Directed Transport as a Route to Improved Performance in Micropore-Modified Encapsulated Multilayer Silicon Electrodes. *J. Electrochem. Soc.* **2013**, *160*, A1746–A1752.

(5) Fenske, M. T.; Meyer-Zaika, W.; Korth, H.-G.; **Vieker, H**.; Turchanin, A.; Schmuck, C. Cooperative Self-Assembly of Discoid Dimers: Hierarchical Formation of Nanostructures with a pH Switch. *J. Am. Chem. Soc.* **2013**, *135*, 8342–8349.

(6) Knust, S.; Spiering, A.; **Vieker, H**.; Beyer, A.; Gölzhäuser, A.; Tönsing, K.; Sischka, A.; Anselmetti, D. Video-Based and Interference-Free Axial Force Detection and Analysis for Optical Tweezers. *Review of Scientific Instruments* **2012**, *83*, 103704–103704 – 6.

(7) **Vieker, H**.; Beyer, A.; Blank, H.; Weber, D. H.; Gerthsen, D.; Gölzhäuser, A. Low Energy Electron Point Source Microscopy of Two-Dimensional Carbon Nanostructures. *Zeitschrift für Physikalische Chemie* **2011**, *225*, 1433–1445.

Contents

1 Introduction

Since the first invention of optical microscopes, science made constant progress in developing techniques to image smaller and smaller objects. For optical microscopy, the fundamental resolution limit was described by Ernst Abbe in 1873.[1] Nowadays, various charged particle methods are used for high resolution imaging. Especially the scanning electron microscope (SEM)[2] is widely distributed due to its ease of use and intuitively understandable images. It uses a finely focused beam of electrons that are scanned pixel by pixel over a surface. Electrons emitted from the surface are detected and an image is built.

Obviously, the size of the probing beam is an important resolution limit for all scanning microscopes using charged particles. The smallest possible spot diameter depends on several factors, but the wavelength of the incident radiation is crucial. This causes fundamental limitations of electron-based microscopy that the long-lasting development of SEM is now facing. A promising development possibility is changing the primary particle. Ions of the same energy have a much smaller wavelength, and using helium ions in the same way provides one solution for the “next generation microscopy”. The wavelength for He^+ is ~100 times smaller than for electrons, so this is no limiting factor anymore. This allows spot sizes smaller than 0.35 nm and a much smaller semi-angle, so the depth of field is ~ 10 times higher than in SEM in comparable circumstances.[3]

So far, these are the advantages originating directly from the optical system. But for the final image the beam-sample interaction is also highly important. Ion beams promise a more localized interaction than electrons and thus a higher resolution and better surface sensitivity.[4] In addition, it is possible to neutralize charge accumulation on insulating samples with the built-in electron floodgun.

The technological challenge of actually building such a microscope was the source of a helium ion beam. It is based on the effect of field emission. From the apex of a small tip (the “gas field ion source”, GFIS) only the emission originating from one single atom is directed on the sample. Some years ago, it was possible to obtain a stable and reliable source, so in 2007 Zeiss commercialized the first helium ion microscope (HIM) and is still the only manufacturer. Right now, the third generation (Orion Nanofab) is available with the possibility to irradiate samples with helium, neon, gallium and electrons in one chamber. In this work the previous model “Orion Plus” is used, which exclusively employs helium and has a better resolution specification (0.35 instead of 0.5 nm spot size for helium). As we are using the technology build by Zeiss, it is not our focus to enhance the technology of the microscope itself.

1.1 Overview of this work

The goal of this work is to explore and analyze the capabilities of helium ion microscopy for today’s scientific applications. In the course of this work, a huge variety of samples were investigated. To show the unique possibilities in practice, a number of scientifically challenging sample systems were chosen to be presented in this thesis. The outline is as following:

The next chapter describes the fundamentals and technology of the helium ion microscope. Its focus is the beam-sample interaction and the imaging process, providing all necessary information for a correct interpretation of micrographs.

Chapter 3 presents several aspects of imaging with this microscope. Ultrathin carbon nanomembranes (CNMs) are a fascinating new material produced from self-assembled monolayers. Due to the high surface sensitivity, HIM is perfectly suited to image this kind of material. In addition, it is insulating and not very stable in conventional electron based microscopy. High resolution images are used to thoroughly study the porosity on the nm-scale of these membranes.

For another sample system, i.e. soot, the high resolution of the microscope is used for a better understanding and improvement of combustion processes. Soot is a matter consisting of carbon-based nanoparticles generated in flames. The knowledge about soot growth at very early stages was enhanced with this work, where HIM settled a new lower size boundary for imaging such particles.

Staying close to combustion, catalytically active films were analyzed. Transition metal oxide (TMO) films were produced by pulsed spray evaporation chemical vapor deposition (PSE-CVD). With its high depth of focus at full resolution the HIM is well suited to investigate the morphology of these functional films. To obtain additional information about the chemistry, X-ray photoelectron spectroscopy (XPS) was used on both combustion-related sample systems.

Limited spectroscopic information is also available within the HIM: Rutherford backscattered ions (RBI) could be detected and analyzed. However, the second detector mode is used here only to measure the backscatter rate, as the spectrometer is not available in Bielefeld. However, it is providing the HIM with a second imaging channel to distinguish elements from each other. The combination of RBI and voltage contrast enables interesting application in the analysis of nanowires.

In addition to imaging, it is possible to use the helium beam to modify samples. In chapter 4 examples are shown where the HIM provides new possibilities. Cutting of nanometer wide gaps in carbon nanotubes (CNTs) and producing extremely well defined gold nanostructures for plasmonic applications is presented. Finally, helium ion lithography is used to directly pattern (crosslink) a carbon nanomembrane. A dose dependent crosslinking process is visualized for the first time.

2 Methods and Devices

2.1 Helium Ion Microscopy

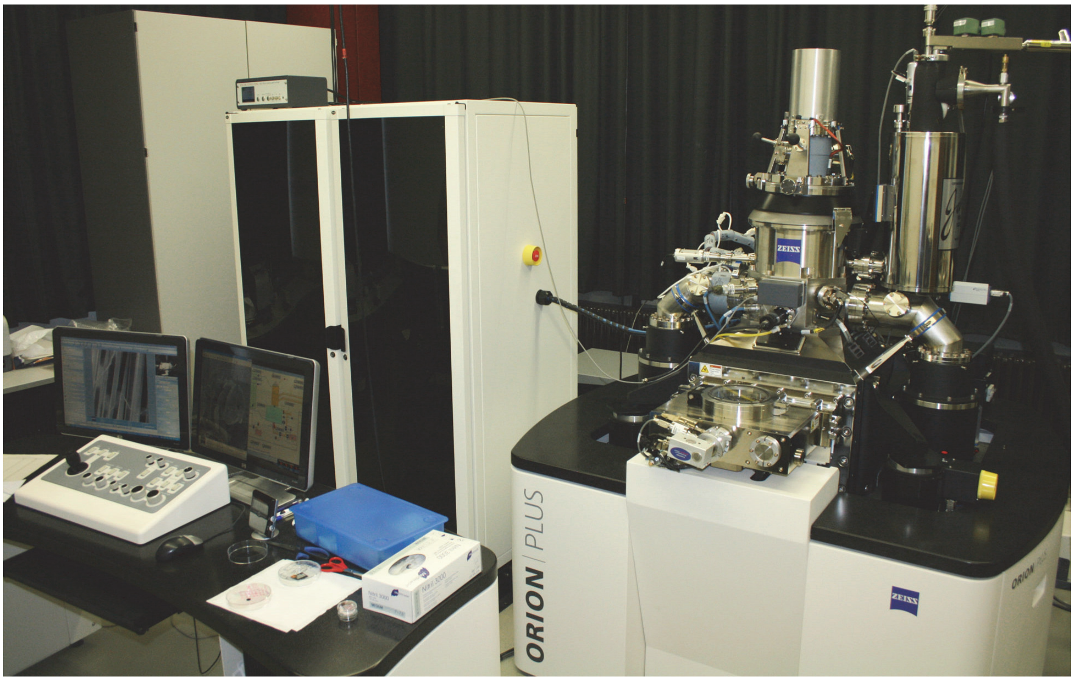

Figure 1: Photography of the HIM used in this work with the microscope body on the right side, the electronics rack in the background and the user interface on the left.

Helium Ion Microscopy (HIM) is a recently developed imaging technique that shares similarities with scanning electron microscopy (SEM).[5] In HIM, a finely focused beam of helium ions with a diameter of less than 0.35 nm is scanned over the sample,[3] and the secondary electrons (SE) generated by the He^+ impact are detected. In SE imaging, the topology of the sample produces contrast as more electrons are ejected when the He^+ beam hits the sample at glancing incidence. Compared to SEM, the energy of the SEs is lower, resulting in a higher surface sensitivity. Edge resolutions of 0.24 nm (asbestos fiber[6]) and 0.29 nm (HOPG[7]) are reported. Since the first article on helium ion microscopy by Ward, Notte and Economou in 2006,[8] the number of publications using this technique grows quickly. A couple of monographs are already available,[3,9–14] all with a different focus.

There is also an article about “The history and development of the helium ion microscope” written by the developers from the ALIS corporation and Carl Zeiss.[15] Zeiss bought ALIS in 2006 and commercialized the helium ion microscope under the brand “Orion”.

Figure 1 is a photography of the microscope used in this work, a Carl Zeiss Orion Plus (serial number 5016). It is operating in Bielefeld since the middle of 2010. It is still equipped with its first ion source.

2.1.1 Beam formation in the HIM

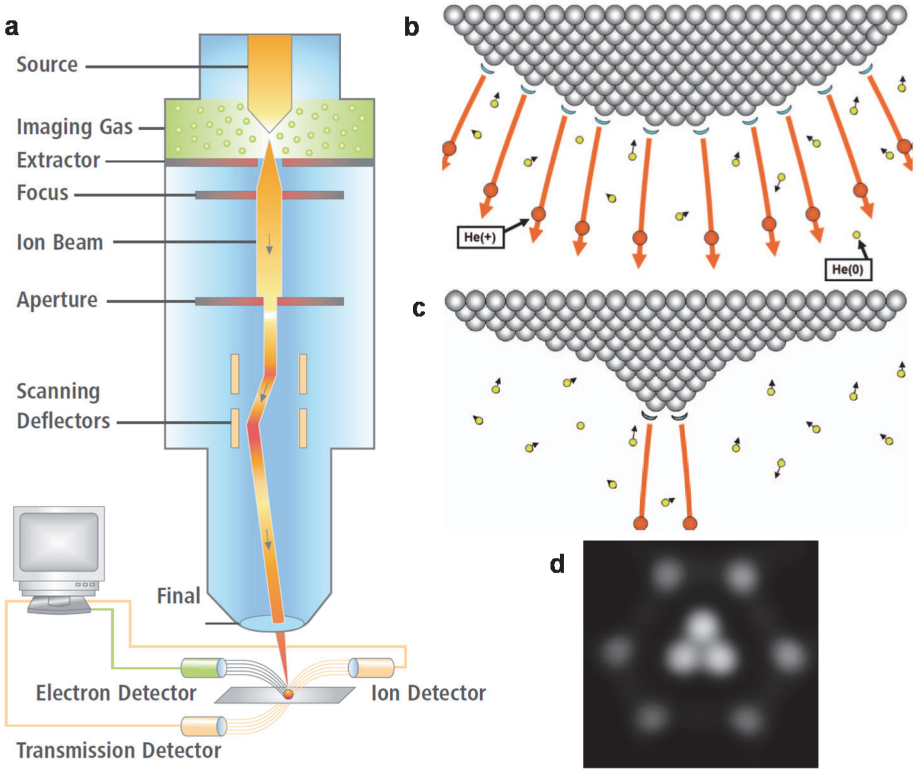

Figure 2: (a): Schematic of the Orion HIM imaging system (from [5]) (b): Ion source after a “source build”, (c): source in a proper arrangement for measurements. Helium ions are ionized predominantly at the top of a pyramid forming the “ionization disks”. (Reprinted with permission[8]) This configuration could produce an emission pattern as in (d), which is an actual SFIM emission image of a working source.

Presented here will be only a brief introduction to the technology itself, as this development was done by the Zeiss Corporation. A comprehensive overview of the technology with details on the source and the design of the column is given by Hill, Notte and Scipioni.[3]

The fundamental part of the microscope is a small metallic needle, the “Gas Field Ion Source” (GFIS). It is based on the effect of field ionization, where strong electric fields ionize a gas atom by pulling away one of its electrons. With this, Erwin Müller designed the Field Ion Microscope (FIM), the first method able to directly image the atomic structure of metals.[16,17] The material under investigation itself is sharpened to a fine tip with a radius below 100 nm and put on a positive potential. This tip is then ionizing gas atoms around it, preferentially at positions with the strongest electric field – “ionization disks” are formed close to protruding atoms (see Figure 2b). The ionized, positive gas atom is then accelerated away from the tip by the electric field and imaged on a screen. This tool is also useful to investigate atomic movements on metals.[18]

In HIM, this tip is not investigated itself, it is used as source of helium ions. To use this as a beam source in a microscope, it was necessary to develop a stable, high brightness source with low energy spread and a small virtual source size. This was achieved by forming a trimer of single atoms on top of a pyramid, where most of the ionization is taking place (see Figure 2c). The ion beam originating from only one atom is selected by an aperture, then focused by the ion optics (Figure 2a) and scanned over the sample.

The ion optics provides the HIM not only with an extremely small spot size, it also shifts the optimum semi-angle (see Figure 3b) for imaging to ~10 times smaller values compared to SEM. This is possible as the diffraction contribution to the beam size is so much smaller (see Figure 3). The depth of field (distance where a sample is in focus) is then in most cases higher than the field of view. Hill and coworkers calculated this with realistic assumptions and got a value of 0.75 µm for images in highest resolution.[3]

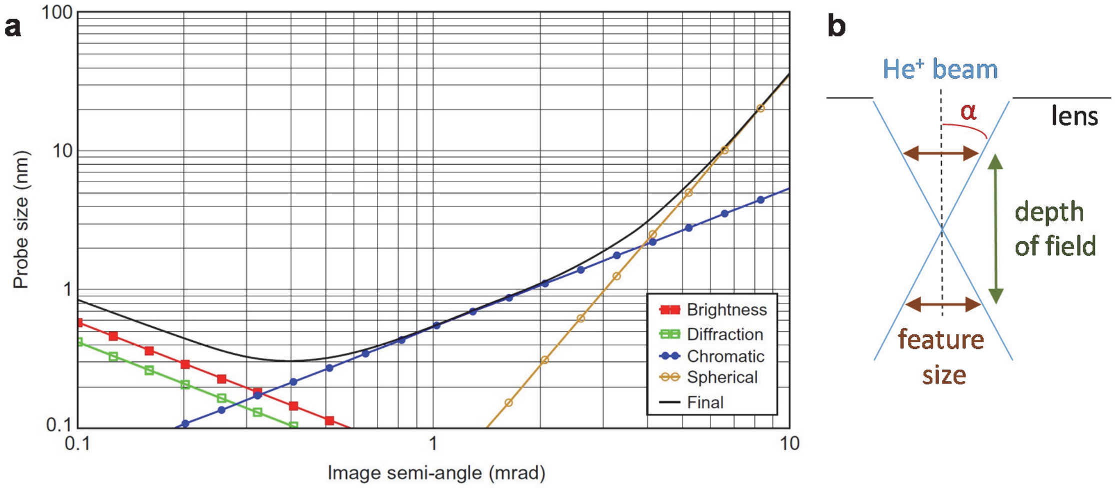

Figure 3 (a): Plot of probe size versus semi-angle, calculated for the Orion Plus column. It shows the four contributions of brightness, diffraction, chromatic- and spherical aberration, and the final probe size. Conditions are 35 kV acceleration voltage, 0.25 pA beam current, and 4 mm working distance. Probe size is defined as diameter with 50% of the ions inside. Reprinted with permission[3]. (b): Definition of semi-angle α and depth of field.

2.1.2 Beam-sample interaction

Both electrons and ions travel and penetrate through solids, where they scatter within the target material. Initially directed forward, they form an interaction volume with increasing number of scattering events. The shape and size of this interaction volume plays, despite the initial beam diameter, an important role in the final resolution and contrast. Helium is a lot heavier than an electron, thus giving it a momentum sufficiently higher.

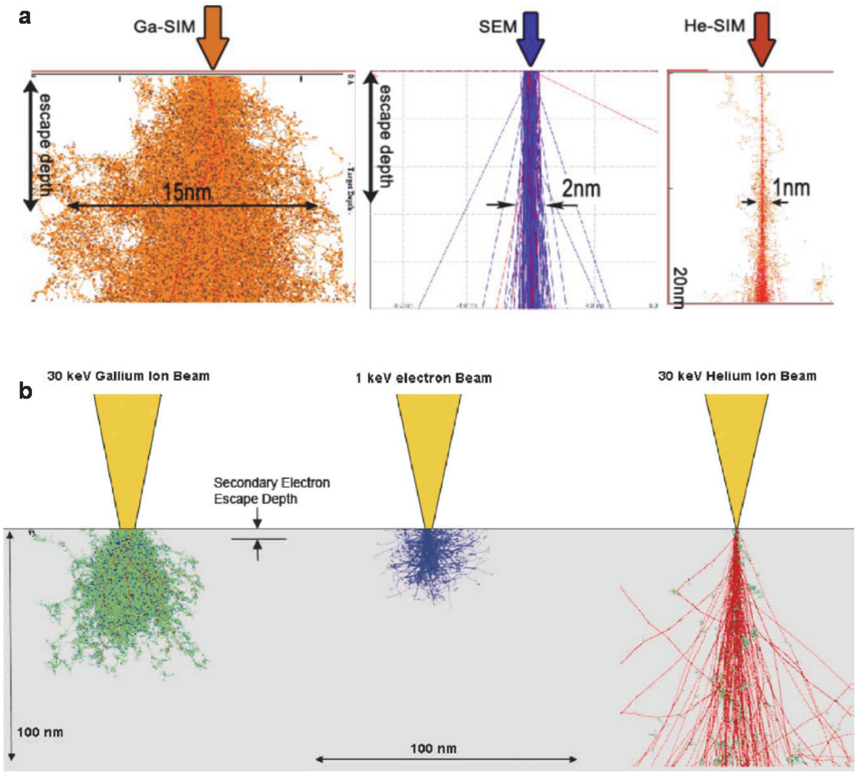

Figure 4: Simulation of beam-sample interaction of gallium, helium and electron trajectories hitting a silicon surface. These are the two typical examples of simulations about beam-sample interaction: either using the same energy for SEM and HIM (a, 30kV) or using conditions of similar contrast, i.e. low-voltage SEM (b). Both show, that the helium beam stays more collimated, especially in the range of the escape depth of secondary electrons. Reprinted with permission (a)[4]; (b)[19]

Figure 4 compares simulations of typically used charged particles, Ga-ions, He-ions and electrons, penetrating a solid. Generally, the full interaction volume of helium is bigger than that of electrons, as the ions travel very deep in the material. Gallium beams on the other hand interact strongly with a sample. As a consequence, the interaction volume broadens immediately below the point of impact but stays close to the surface. All these interactions produce a number of measurable signals. For imaging, the interaction volume for generating secondary electrons (SE) is most important. From Figure 4 it is visible, that the He+ beam stays pretty collimated in the relevant depth of less than 10 nm. Scattering of the target nuclei (Silicon) with the helium beam is inefficient due to the low ion mass. So the SEs collected in a measurement are from a cylinder with minimal diameter.

In the many available simulations of SEM to HIM comparison, there are generally two versions: comparing the same energy of the primary particle, or comparing a similar contrast (or surface sensitivity)[12] when using the microscopes in practice. Figure 4a compares 30 keV beams. The electron beam diameter under these conditions stays within ~ 2nm. This is only a bit more than for helium, but if one looks at the interaction outside this 20x20 nm² box, a quite big amount of these electrons are scattered back to the surface. They excite additional secondary electrons (often called SE2), which provide no information about the sample at the penetration point – so they decrease contrast and the effective spatial resolution. The simulations for low-voltage SEM (1keV) in Figure 4b shows a more evident advantage of using helium. The electrons strongly scatter near the surface, reducing the available resolution in practice.

The simulation in Figure 5 investigates the details close to the surface. It shows the mean radius of a beam penetrating a solid, starting with a radius of 0 (Figure 5a). This average diameter of interaction volume broadens up with penetration depth. Combined with the SE escape probability (Figure 5b), it shows that by far most SEs are generated within a radius smaller than the expected He beam size.

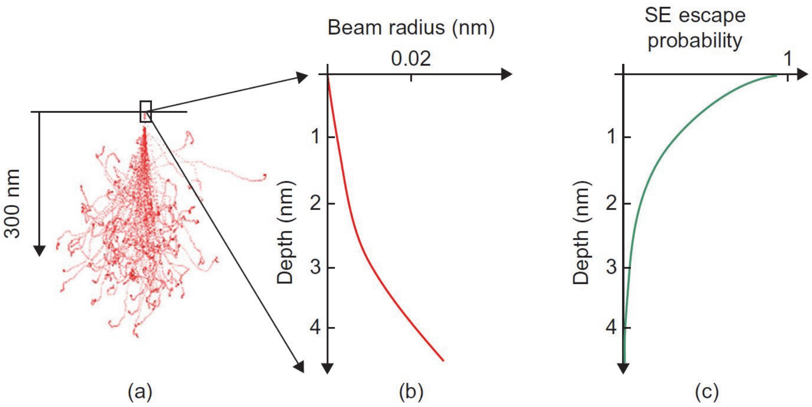

Figure 5: simulation of beam-sample interaction, escape depth probability and beam spread in samples. Reprinted with permission[3]

This very small SE escape depth is caused by the low energy of the SEs generated by He ions, in particular the SE energy is much smaller than in an SEM.[20] G. Hlawacek demonstrated this effect with comparison measurements of HIM and SEM on carbon-coated gold nano-rods. This carbon coating was almost invisible in SEM, where in HIM it dominated the image.[21]

Backscatter events of helium to the surface are rare, so the number of SE2s is small. Again in comparison to SEM, the fraction of SE1s in the secondary electron signal is in most cases considerably larger. Looking at the absolute SE-yields it is also substantially higher (2-8 e^- per incident He^+), and increasing with the primary beam energy.

Ramachandra and Joy made big efforts on simulating SE-yields for different materials and developed the software package “IONiSE”.[22]

Sample damage is a concern for all charged particle microscopes. Using ions, any sample is additionally altered, where incident ions get implanted, and dislocate, amorphizate and knock out sample atoms, clusters and molecules (sputtering). With the strong interaction of the heavy gallium ions (Figure 4), sputtering occurs so frequently that materials modification is the main application of Ga^+ ion beams as well as chemical analysis (secondary ion mass spectrometry, SIMS). The interaction of He^+ ions with solids is much weaker, but limits the available resolution. The operator has to find a compromise between noise level and an ion dose at which a certain feature of the sample is removed.

Castaldo and coworkers developed a method to investigate and quantify this for the case of Tin nanospheres and found a minimum detectable particle size between 1 and 5 nm.[23] They stated that the “fundamental limit to the resolution in scanning microscopy is not given by the spot size, but by the dynamics of the interaction of the beam with the sample and the consequent modification of the sample’s geometry, even for beams of light ions”, which is also called a useful lateral resolution.[23]

It is also possible to use this as beneficial effect, as the very low sputter yield combined with the small beam size allows the direct fabrication of prior impossible (small) patterns.

2.1.3 **Contrast in secondary electron imaging**

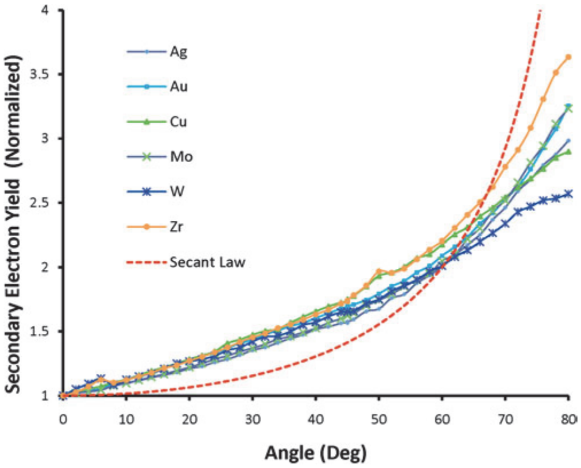

Figure 6: Secondary Electron (SE) Yield for different elements and sample angle, measured with an Everhart-Thornley (ET) detector in a HIM. Reprinted with permission[12].

Imaging with secondary electrons is by far the most used method in HIM. The primary contrast effect is the so-called “topographic contrast”. For SEM and HIM it is based on the dependence of the secondary electron yield to the angle of the surface plane. Theory predicts an increase following the “secant law” as plotted in Figure 6. However, actual measurements show a more linear behavior with helium.

Apart from topography, there are more complex effects regarding the final contrast. On thin films, nanomaterials or edges, a relevant fraction of the primary helium may leave the sample again. In such cases, SEs are emitted at the exit point and at any other material in the further path of the beam.[12] These other objects may be well behind the intended imaging plane (mm to cm), in case the path of SEs to the detector is not sufficiently shielded.

2.1.4 Imaging insulators: voltage contrast and charge compensation

For all charged particle microscopes, the accumulation of charge on the sample is an issue. In the HIM, areas with such a potential buildup are getting darker as more electrons are deflected by the local electric field and thus are not able to reach the detector. Different to SEM, the initial He^+ beam is marginally affected due to higher momentum of the He-ions. In mixed or “slightly charging” samples it is therefore possible to obtain good images by carefully adjusting beam current and contrast settings. With this “voltage contrast” it is also possible to identify insulating or insulated structures on samples – while scanning quickly they will simply get dark.

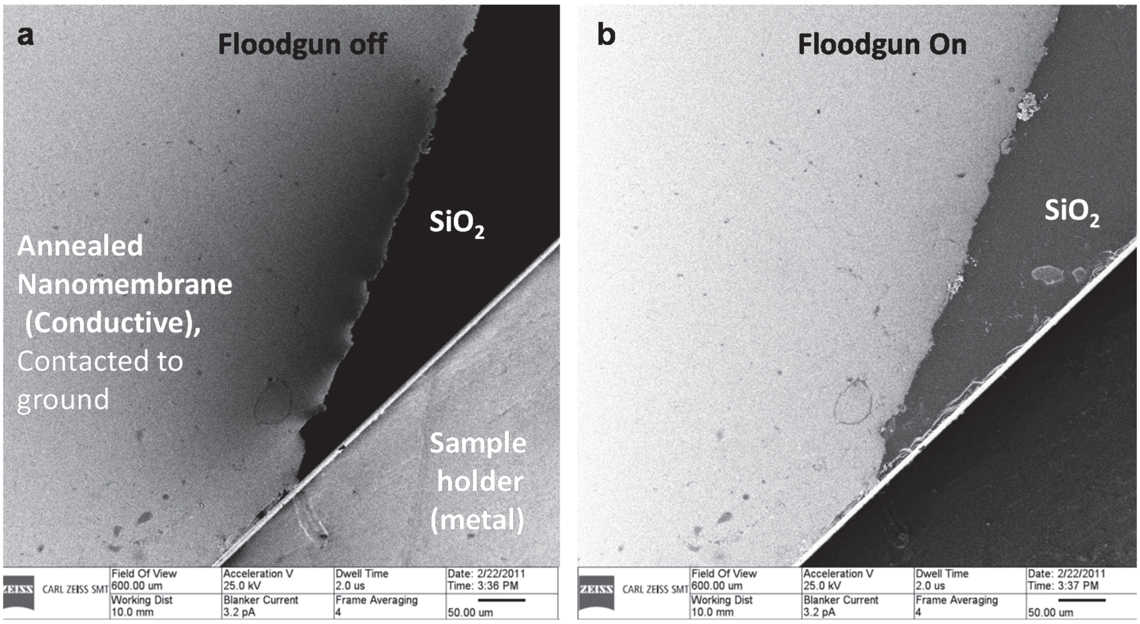

Figure 7: Example of using the electron floodgun: A conductive carbon nanomembrane is placed on a 300 nm SiO_2 silicon wafer piece.

On layered structures like SiO_2 on silicon wafer (see e.g. Figure 15) the surface potential will only reach a certain level allowing a lesser but still sufficient number of SEs to escape. In practice, highest resolution images are possible. This effect was explained by simulations made by Ohya et al.[24,25]

It is also possible to directly compensate charge accumulations with an electron floodgun. In an ion microscope, charging is always positive (In HIM, He^+ comes in, e^- are ejected). Therefore it is possible to neutralize surfaces with additional electrons to obtain stable image conditions without any conductive coatings.

In the HIM, an electron gun (~500-800 eV) with a spot diameter of some mm is centered on the sample under investigation (see Figure 8). The scanning He^+ beam for imaging is alternated with the electron beam for charge neutralization. A flood pulse is triggered after every scanning line or frame. Direct comparisons to state-of-the-art SEMs were reported by Boden et al. with butterfly wings[26] and recently by Joens et al. in an extended study on biological samples.[27] Both show exciting new possibilities of HIM in measuring uncoated organic material in highest resolution.

In summer 2013, the floodgun of the Bielefeld Orion HIM was re-calibrated by Zeiss, and new operating conditions were employed. The currently used electron pulse time (flood time) is about 100x smaller than previously used, accelerating the imaging times significantly. In addition, the quality of the images on insulators was improved.

In practice, images obtained with charge compensation generally show a lower contrast. In Figure 7b another floodgun artifact at the left border is visible: a bright strip in vertical direction is generally observed. It is often possible to reduce this effect by careful adjustments of the floodgun settings.

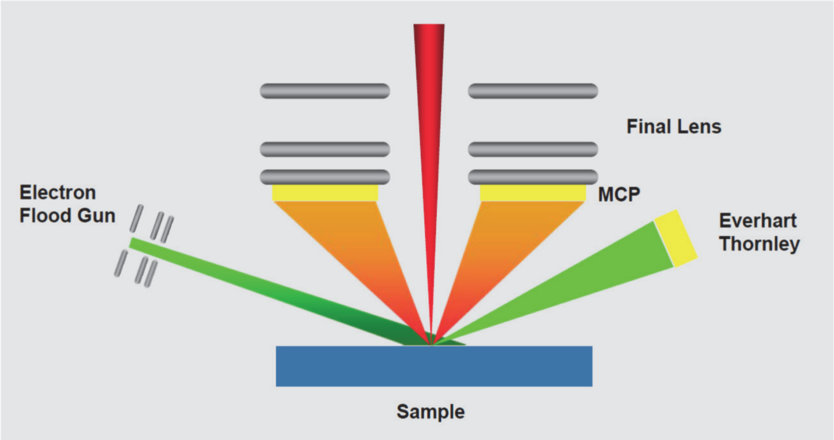

Figure 8: Sketch of the measurement chamber with the incident He^+ beam, the Everhart-Thornley (ET) electron detector, the micro channel plate (MCP) ion detector, and the electron floodgun. (Image from Zeiss material, [28])

2.1.5 **Backscattered ion imaging**

As second imaging mode, the number of Rutherford backscattered ions (RBI) is measured by an additional detector. Therefore, an annular micro channel plate (MCP) detector (Figure 8) is inserted in the primary beam path measuring highly energetic helium atoms scattered back from the sample. This geometry maximizes the measured angle (fraction of the backscattered ions), but decreases the performance for SE imaging.

Other than SE images, the backscattered signal is insensitive to surface morphology, but provides a strong elemental contrast. The contrast of these images originates from the bulk of the sample, where the information depth is depending on material and chosen beam energy. Figure 9 depicts experimentally measured backscatter rates for various elements. Despite the first assumption of a monotonically growing yield there is a dependence on the structure of the periodic table.[29] Kostinski and Yao made extensive simulations of this effect and found a correlation to the stopping power of the sample material.[30]

Backscattered ions are insensitive to charging of samples due to their high energy. Therefore, it is possible to directly measure insulators.

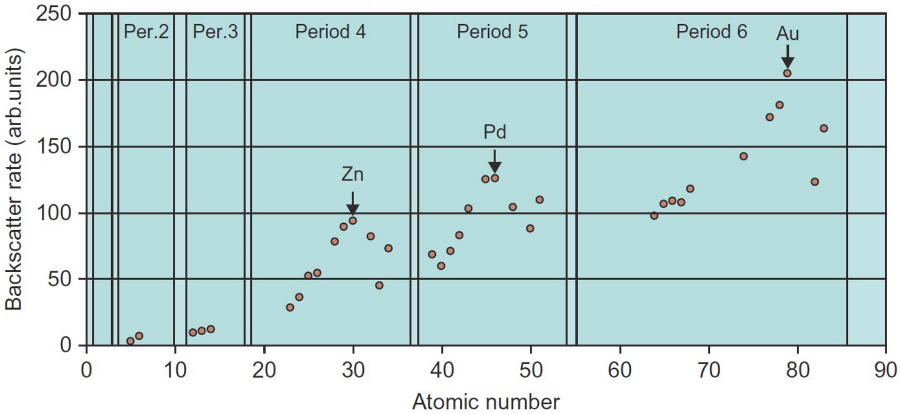

Figure 9: Measured Backscatter – Yield versus atomic number. Reprinted with permission[31]

Another way to analyze backscattered ions is RBI-Spectroscopy (RBS). In this add-on (not available in Bielefeld), the RBI energy is measured by a silicon drift detector to provide quantitative element identification and information. RBS is generally a widespread used technique for thin film analysis, but the available ion energies in HIM are not favorable (usually ~MeV energies are used).[32]

2.1.6 Image acquisition settings and practical issues of using the HIM

The measured signal of a single pixel depends on the sum of all electrons reaching the detector at the time (!) the beam is pointed at this pixel. The final signal value of a pixel is nevertheless not directly connected to a defined number of electrons. A number of settings can be optimized by the HIM operator to obtain a good visibility of the features under investigation. Firstly, the settings for “contrast” and “brightness”, that in fact change the hardware settings in the Everhart-Thornley (ET) electron detector for gain and zero-level (black point), respectively, can be adjusted. Subsequently, the signal is integrated and digitalized in the HIM electronics. Then, the setting for “image intensity” provides a translation of the signal to the 8 bit brightness information of the final image providing the operator with an additional possibility for contrast optimization.

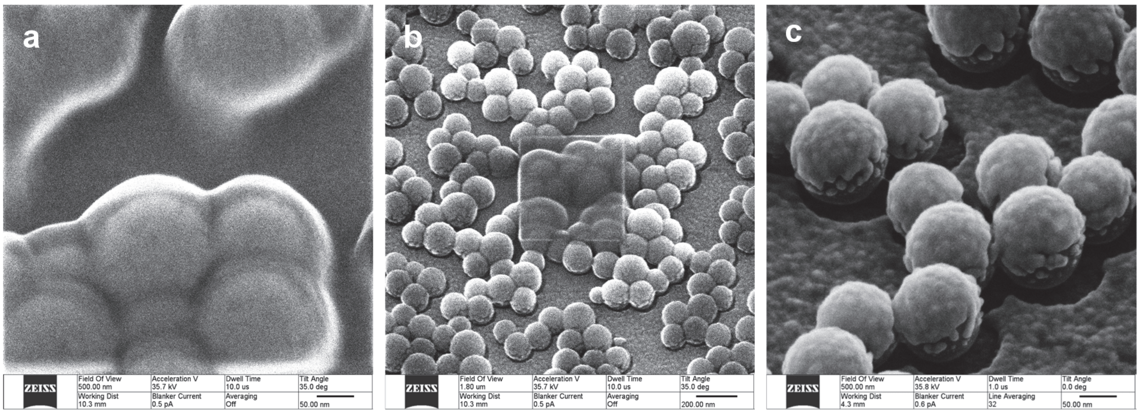

Figure 10 (a,b): Contamination diminishes available resolution. (c): the same sample after plasma cleaning. The samples are Si spheres coated with 18 nm sputtered gold (information about the sample and a series of HIM images are provided in literature.[33])

Another crucial aspect is the helium-induced deposition of hydrocarbons on the sample. Figure 10 is an example of a contaminated sample, where in (a) the surface structure is totally hidden under a thick contaminant layer, deposited while scanning this high magnification image. Figure 10b is a zoom-out of the same position after the acquisition of Figure 10a. Such contaminants could originate from different sources. In practice, contaminants directly on the sample under investigation is most severe. This is supported by the fact that at the time Figure 10 was acquired, there were 5 similar samples on the sample holder inside the microscope chamber. They were imaged without contamination problems.

To solve problems occurring with contaminations, different strategies are available and proved to be useful. At first, working in a clean environment to not let any hydrocarbons accumulate on the samples or any vacuums part is the most preferred solution. Another alternative is a plasma cleaner inside the HIM load-lock.[34] Figure 10c is an image of the above discussed sample after such a treatment. This is obviously not possible if the sample is organic or other sensitive material. In this case, mild heating (~80°C) for some hours proved to be helpful. In general, one has to make sure that features under investigation are not destroyed or altered by the cleaning process.

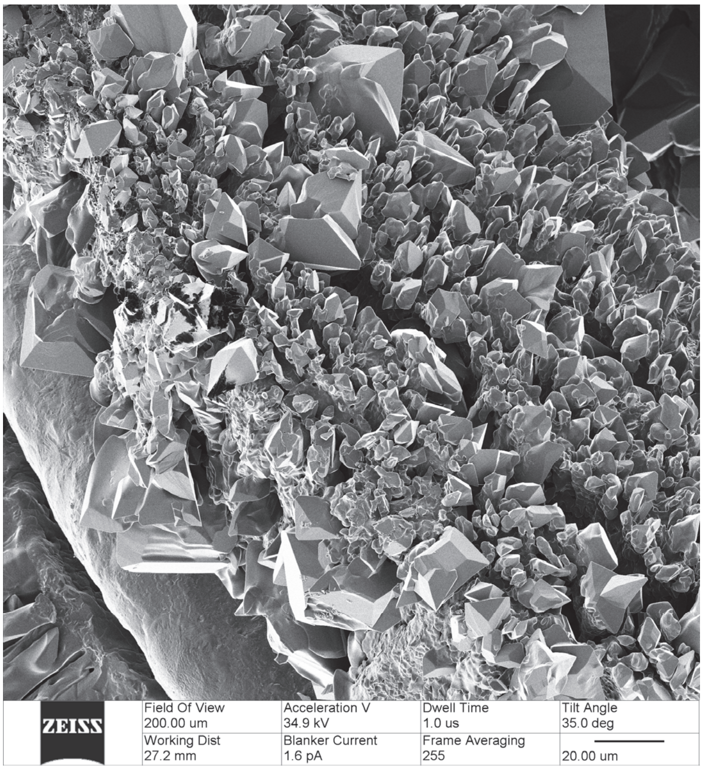

Figure 11: Defective filament used in an electron floodgun. Extended re-crystallization of the hot tungsten filament together with carbon contaminations in the high vacuum environment caused massive changes on the wire.

The Orion HIM allows different acquisition settings to obtain micrographs. A collection of important information is collected in the bar below the image itself (See Figure 11). In this work, they are not cropped, when they provide useful information to the reader. Important settings of the imaging process, where not all of them are in the information bar:

- Image size: the number of scanned pixels. It can be varied between 256x256, 512x512, 1024x1024 and 2048x2048 px. The standard setting is 1024x1024 px.
- Field Of View (FOV): The full size of the area imaged. More important to the imaging process is pixel spacing, the distance of two scanned pixels on the sample. (Could be calculated by dividing the FOV through the number of pixels)
- Working Distance (WD): A calculated value describing the distance between the column and the plane where the helium beam is in focus. As this is usually set to the sample in investigation it describes the distance to the sample.

- Tilt Angle: This describes the angle of the beam to the sample stage normal. It is possible to tilt the sample stage from 0° to 45°.
- Acceleration Voltage: The energy of the helium ions hitting the sample surface
- Blanker Current: The beam is “blanked” (directed in a faraday cup in the column) automatically if no image acquisition is running. The value is the current of the helium beam at the time where the beam was “blanked” the last time before saving the image.
- Dwell time: The time the beam “stays” at one pixel, while scanning over a sample.
- Frame or Line Averaging (x = 2 - 256 times): Describes the integration strategy used to obtain the image. In Frame Averaging mode, the full image is scanned and averaged with repeated scans. In Line Averaging mode, a line scan is averaged x times followed by the next line.
- Irradiation dose: This depends on the discussed values of blanker current, dwell time, averaging mode and FOV and has to be calculated manually. It is a compromise set by the operator between sample damage, noise level, and available time.

2.2 X-Ray Photoelectron Spectroscopy (XPS)

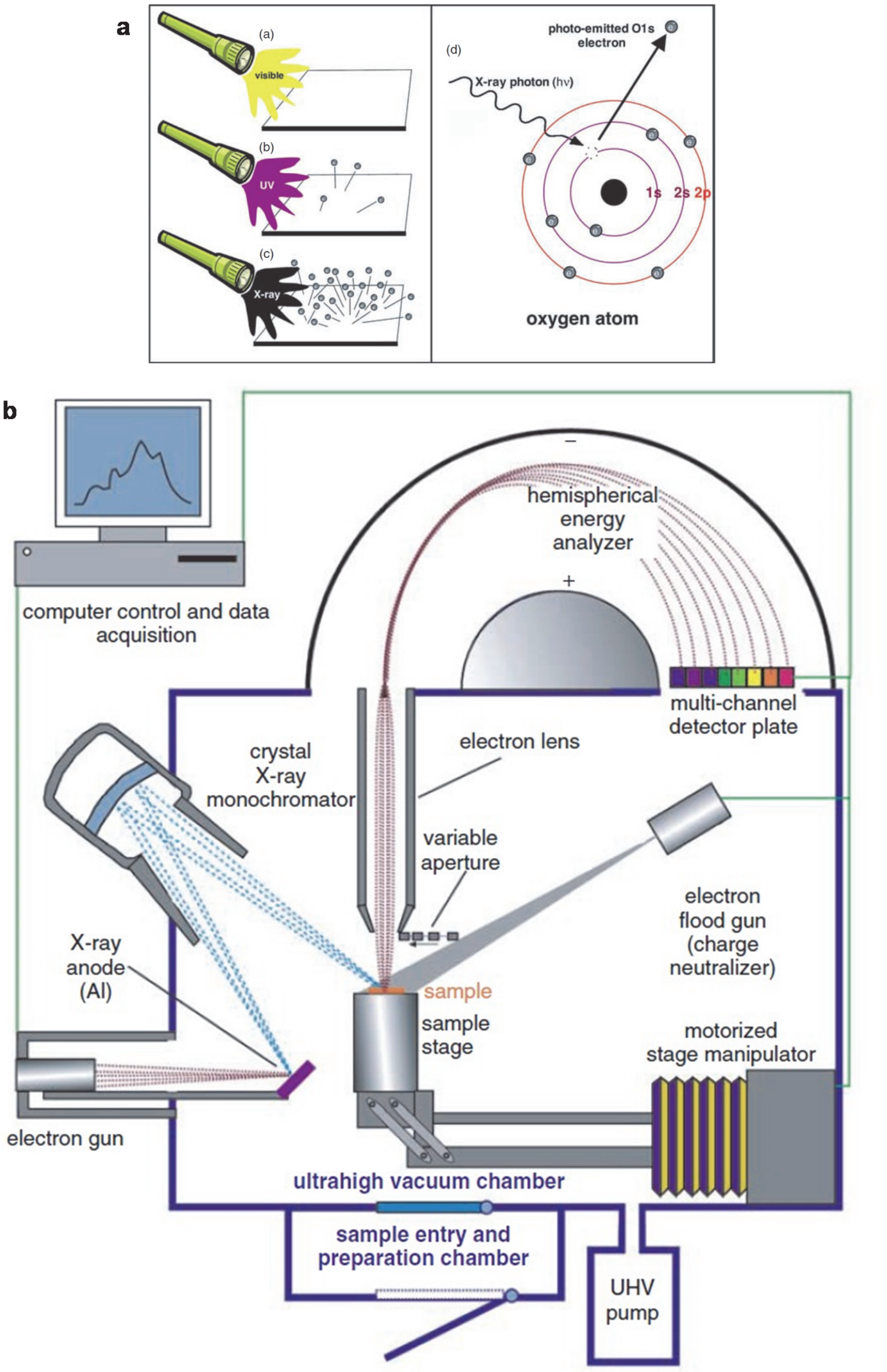

Figure 12 (a): Basic principle of the photo effect and the emission of core electrons by X-rays. (b): Scheme of currently used XPS tools equipped with a monochromatic X-ray source. Reprinted with permission.[35]

XPS or ESCA (Electron Spectroscopy for Chemical Analysis) is a spectroscopic method to determine elemental composition and oxidation state of surfaces.[36] Although this thesis concentrates on HIM, XPS was used as additional surface characterization technique. It provided valuable information on the composition of soot and CVD films shown in chapter 3.2 and 3.3.

If a surface is irradiated by photons above a certain energy, electrons are ejected from it due to the photoelectric effect (Figure 12a). In XPS, the energy of the photons is sufficient to eject core level electrons. Only in close proximity (some nm) to the surface, such electrons are able to actually leave the solid. It is therefore a very surface sensitive technique (some nm). Energy and number of these emitted electrons are measured. In the spectrum, the intensity of the emitted electrons is plotted against their energy. With the knowledge of the incident photons energy, the energy loss in the emission process is calculated, which is depending on to the binding energy (BE) of core level electrons.

Thus, the position of the peaks is characteristic for each element. In addition, the binding energy shifts slightly if an atom is bound to different chemical species. With this chemical shift, the oxidation state of elements is detected. This is rather simple for electrons from 1s orbitals like C1s and O1s, where the peak position is mainly shifting.

However, for all transition metals the identification and analysis is more complex. The binding energy of different species is often interfering with each other and complex satellite structures appear. An example is given in Figure 13, where the Co2p doublet peaks from cobalt in metallic and two oxidic states are shown. Nevertheless, it is possible to identify different compositions using references. Especially the work of Biesinger and coworkers was very useful in this thesis.[37–39]

Due to the wide use of XPS, there is countless literature data available covering almost all possible aspects.[35,36,40,41] For daily use, there are numerous reference databases and spectra to identify all measured effects.[42,43]

In this work, an ultra-high vacuum (UHV) Multiprobe XPS by Omicron Nanotechnology was used. A monochromatic Al Kα X-ray source (1486.7 eV) and a hemi-spherical electron energy analyzer (Sphera) in constant analyzer energy mode were employed. The base pressure of the chamber is 2×10^{-10} mbar. CasaXPS (Version 2.3.16 PR 1.6) was used to analyze the spectra, and a Shirley background subtraction procedure was employed. The elemental composition was calculated using the peak areas with the according Scofield[44] cross-sections.

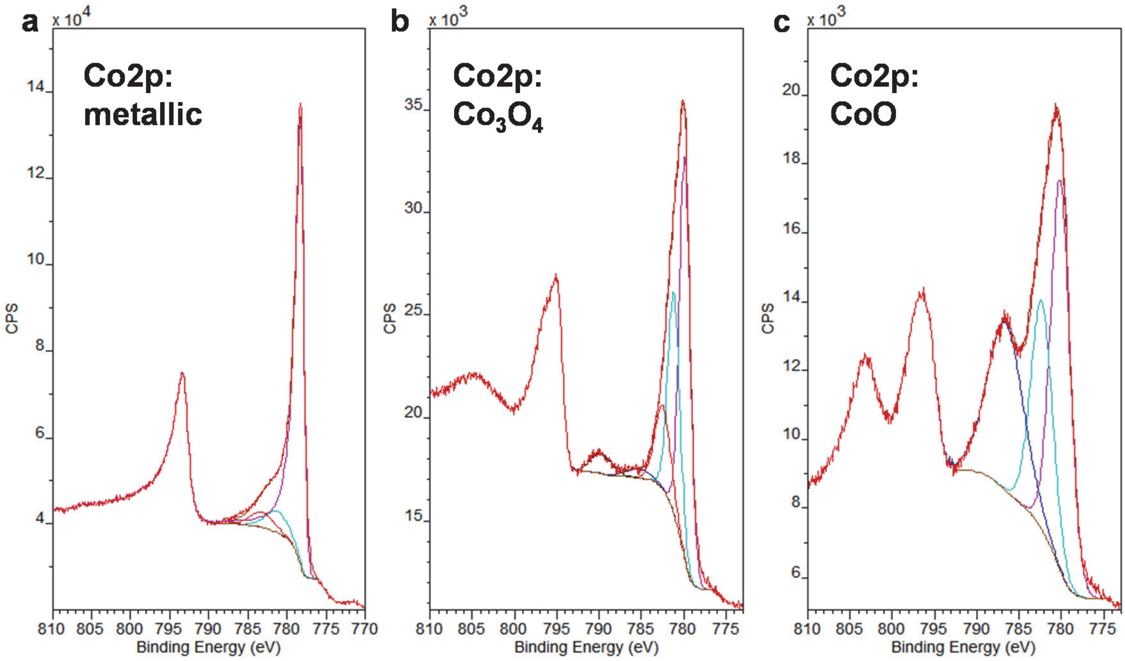

Figure 13: XP-spectra of the cobalt 2p region of a cobalt metal (a), Co_3O_4 (b), and a CoO (c) sample.

3 Imaging with the Helium Ion Microscope (HIM)

3.1 Imaging of carbon nanomembranes (CNMs)

3.1.1 Introduction

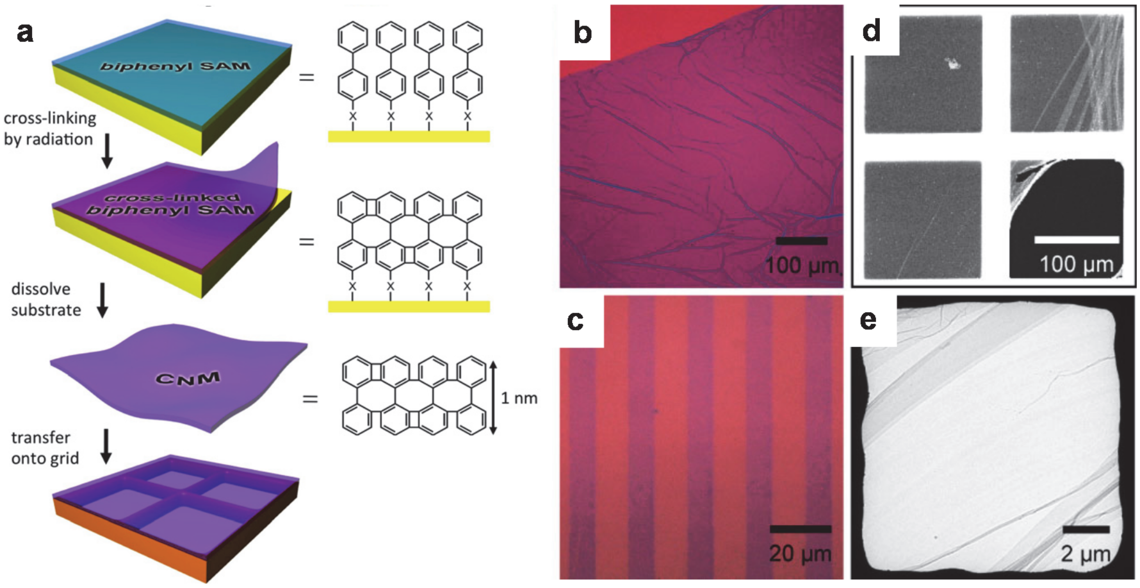

Figure 14: (a) Fabrication scheme and microscopy images of CNMs made from aromatic self-assembled monolayers (biphenyl-thiol in this case). (b,c): Optical microscopy images of CNM on silicon wafer with 300 nm SiO_2. The CNM is visible due to an interference contrast effect.[45] (a) shows a large membrane with some folds from the transfer process. (b) A line pattern image fabricated by e-beam lithography. (d) SEM micrograph of four 130µm x 130µm holes in a TEM grid with CNM on top. (e): TEM image of a conductive CNM transferred onto a TEM grid. The CNM was pyrolysed at 1100 K, transforming it to a nanocrystalline and conductive film.[46] Both electron microscopy images (d,e) show some folds and wrinkles in the membrane. Reprinted with permission[46,47]

Carbon nanomembranes (CNMs) are extremely thin and homogeneous two-dimensional objects consisting of a monolayer of cross-linked molecules. They are made by exposing a self-assembled monolayer (SAM) of aromatic molecules with electron[48] or soft X-ray irradiation[49]. In Figure 14a the SAM is exemplified with the by far most investigated system, a biphenylthiol (BPT) on gold. The CNM is subsequently released from its substrate by dissolving the latter.[50] Thickness, chemical composition, and density of the original SAM determine the properties and composition of the resulting CNM. Freely suspended CNMs are made by transferring the cross-linked SAM from its substrate to a porous structure, such as a metal grid (see Figure 14 a,d,e). The freely suspended CNM is about as thick as the original SAM and can span large areas of more than 500x500 μm^2.

The mechanical elasticity and the electrical conductivity of a CNM can be tailored via pyrolysis in ultra-high vacuum (UHV)[46,51] or under inert atmosphere.[52] CNMs have a potential for a variety of technical applications, like filters,[53] sensors,[46] resists,[48] nano-sieves,[54] or “lab-on-a-chip“ devices.[55]

In 2012, Turchanin and Gölzhäuser published a review with all relevant aspects of the research on carbon nanomembranes made from self-assembled monolayers.[56] In addition, the PhD thesis of Christoph Nottbohm is a good source for all aspects of CNMs (or carbon nanosheets).[57]

The samples investigated in this study were fabricated by members in the group of Prof. Gölzhäuser, “Physics of Supramolecular Systems and Surfaces” at Bielefeld University. A main goal of this group is the production and investigation of CNMs, and therefore a fast and reliable imaging method is essential. Optical microscopy is suitable on SiO_2/Si wafer pieces as depicted in Figure 14b,c, but on other surfaces, the CNM is not or only barely visible. Freestanding membranes are imaged by transmission electron microscopy (Figure 14e), with obvious limitations due to the transmission method. Scanning electron microscopy (SEM) shows a very low contrast on these membranes (Figure 14d), and tends to be destructive for freestanding membranes. Previous reports (Zharnikov et al.) demonstrate that low-voltage SEM (500eV) could overcome some of these limitations.[58,59]

There is scarce literature data HIM imaging of such ultrathin membranes. The thickness of graphene is comparable, but a fundamental difference is its good conductivity. Due to the high interest in the material it is used by various groups, where the main focus is the modification and production of small structures and, finally, circuits (see, e.g. [60–63]). Nanocrystalline graphene was extensively investigated in the course of this thesis. The images are documented in the PhD thesis of Nils-Eike Weber.[64] Small flakes of hexagonal boron nitride (h-BN), a material that shares a lot of similarities to graphene, were imaged in a comparative study by Guo and coworkers.[65] They show that HIM is more sensitive and consistent than FE-SEM for characterizing the number of layers and morphology of 2D materials. Hlawacek et al. investigated thin organic layers and proved the extremely high surface sensitivity of HIM for such materials.[21,66]

The CNMs imaged in this thesis were produced by: Polina Angelova, André Beyer, Xianghui Zhang, Nils Weber, Isabella Meier, Min Ai, Oliver Reimer, Hanno Meyer zu

Theenhausen, Robin Klett, Nils Mellech, Matthias Büenfeldt, Andreas Winter, Albert Schnieders, Daniel Emmrich, Vahe Chinaryan, and Christoph Neumann.

3.1.2 Imaging of CNMs by helium ion microscopy

For imaging with the HIM, the important aspects of a CNM is that it is an ultrathin (~1nm) and insulating material. Due to the thickness, the high surface sensitivity of the HIM is beneficial to obtain good images with high contrast. It is also important to note, that the helium beam will penetrate the CNM easily, striking anything below a freestanding membrane. Charging of the membrane is also challenging, but can be controlled by either using low beam currents or using the electron floodgun for compensation.

3.1.3 Imaging CNMs on solid supports

For a number of applications, CNMs are transferred on solid supports. For all of these applications, a fast and reliable production control is mandatory. On all substrates imaged so far, HIM images of CNMs provide high contrast and good visibility of features of the membrane.

Figure 15 shows examples on six widespread substrates with transferred CNMs in a very low magnification (overview, about 2 mm FOV) and higher magnification to show typical features of the membranes. Please note that a perfect (defect-free) sample will not provide meaningful images, as contrast originates from defects, folds or the edge of the membrane.

In Figure 15a, the edge of a CNM is imaged on oxidized silicon, together with a big scratch for further navigation in other techniques. Defects and folds like in image (d) are frequently observed at edges of transferred CNMs, together with contaminations, also very well visible in an example on mica (b). Imaging at higher magnification of this sample (e) shows only a small scratch without CNM in the middle, and some double-layers in the upper part of the image.

A CNM double-layer is transferred on a silicon nitride chip in Figure 15c. Defects, folds and contaminations (Figure 15f) can be assessed in high detail. The same is visible for a CNM on silicon carbide (g,j). CNMs on polymers are used in gas permeation measurements, where the defective area is an important factor to calculate the final influence of the CNM. The images on PDMS (h,k) are part of an experimental series on gas permeation published recently.[53] The teflon used as substrate in Figure 15i,l is rough itself and has a pore in the middle.

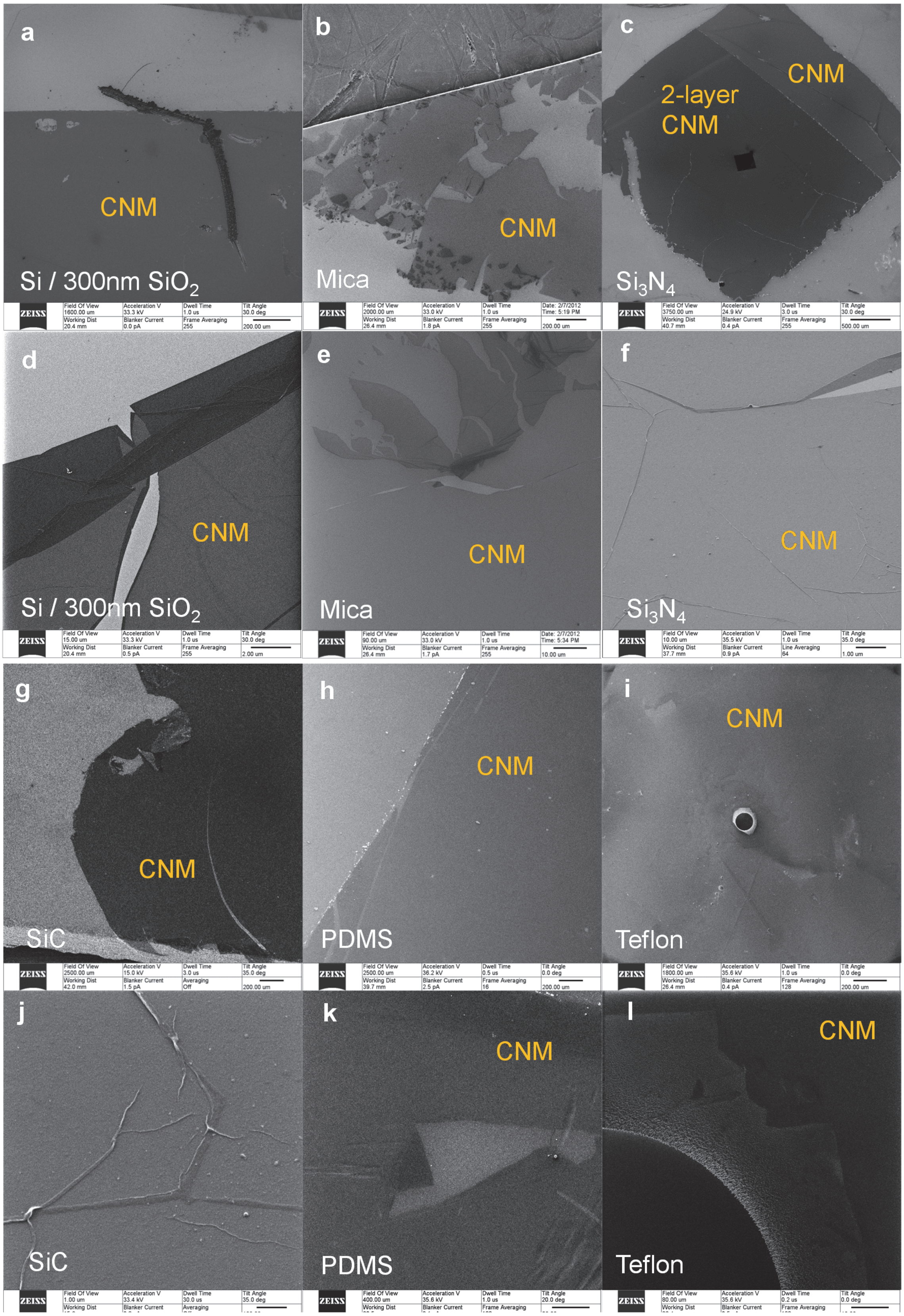

Figure 15: CNMs on various solid substrates. See text for details.

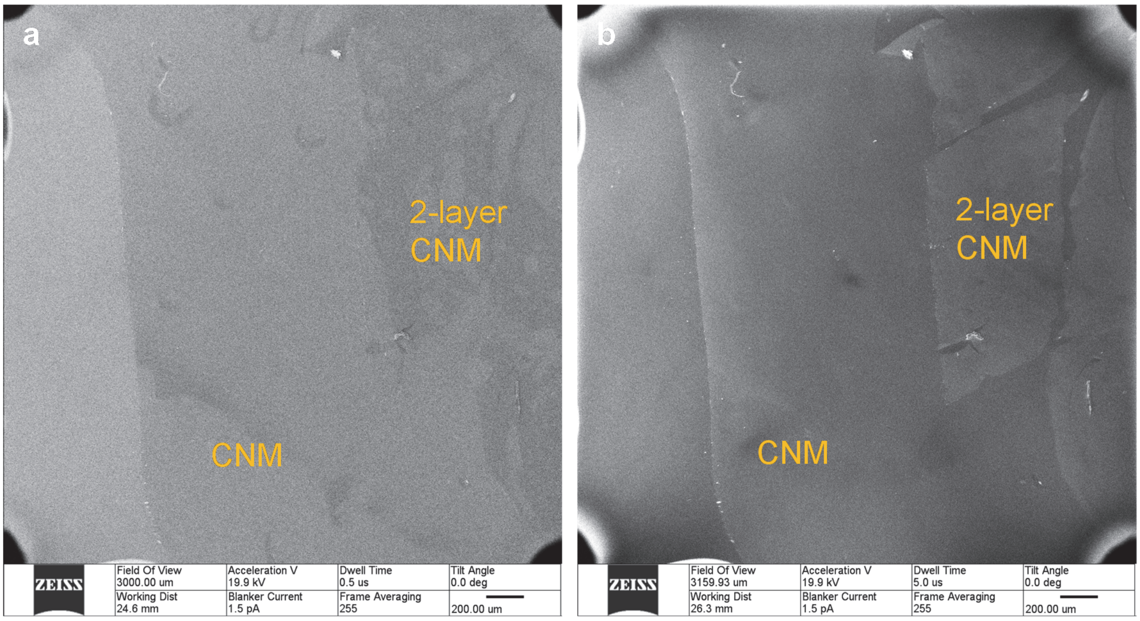

Figure 16: Two layers of CNM on PDMS – contrast changes with floodgun settings. The circular objects in the corners are artifacts from the column.

In most cases the CNM lowers the final SE-intensity compared to the bare substrates. However, Figure 16 depicts an example of a double-layer CNM on PDMS where different floodgun settings change the contrast.

In general, it is difficult to use the image intensity as an analytical feature. The value depends on a lot of settings like timing (dwell, floodtime) and dose density / ion dose per area (magnification, beam current, charge compensation, etc). In summary, the contrast is a dynamic feature to be optimized by the HIM operator.

3.1.4 **CNMs on porous supports (TEM grids)**

The final test whether a membrane production was successful is the transfer on porous support to prove that it is freestanding and stable. As discussed earlier, the final intensity in a pixel is a measure of all electrons reaching the detector at the time the beam is positioned at a certain point. This is important to consider as the beam easily penetrates the CNM, hitting parts of the sample stage or the grid below where again SEs are ejected. This must be considered when interpreting the images.

Figure 17 shows a rather extreme example for such effects. The images in (a) and (b) show the same sample, where in (a) secondary electrons from the transmitted helium ions are hitting the stage well below the TEM grid and are free to reach the SE detector. In case (b) the path for the secondary electrons is blocked. To guide the eye, arrows in the figure depict the same position in the sample.

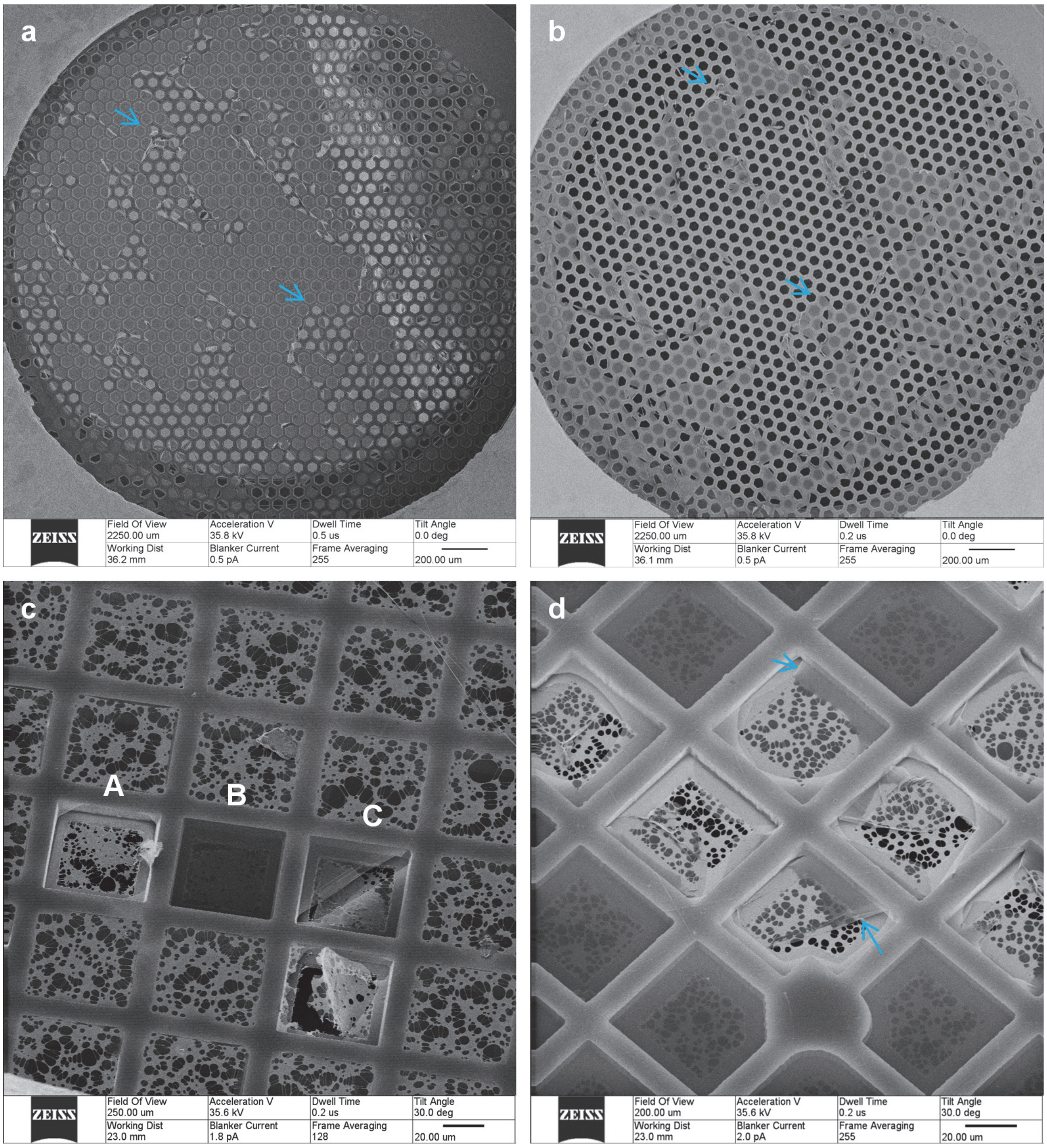

Figure 17: In images with suspended CNMs on TEM grids, the background is important. Images (a,b) show the same sample mounted differently. The arrows show similar positions to guide the eye. (c,d): CNMs on a TEM grid with holey carbon film.

More complex examples are in Figure 17c,d. Here, a holey carbon film on a copper grid is used as substrate. The carbon film should be on top of the copper grid, as in most of the squares in Figure 17c. The grid is almost fully covered. In the top right corner a small wrinkle of the CNM is visible. In the areas marked with A,B & C some contrast features are well visible. At A, the CNM is not intact, thus the holes in the holey carbon film appear darker. The holey carbon film and the copper grid itself are brighter than in surrounding areas. At B, the CNM is freestanding some µm above the holey carbon foil. A large fraction of the SE's from beneath the CNM are blocked, thus providing a dark appearance. At C, the CNM is again freestanding above the holey carbon film, but with a large crack. SE's from beneath are able to escape through this crack providing a brighter appearance of the features the closer they are to the crack. Figure 17d is another example. In the middle, CNMs span from the copper grid to the holey carbon film, which is some µm lower. As long as they are not directly supported they have a darker appearance (see arrows).

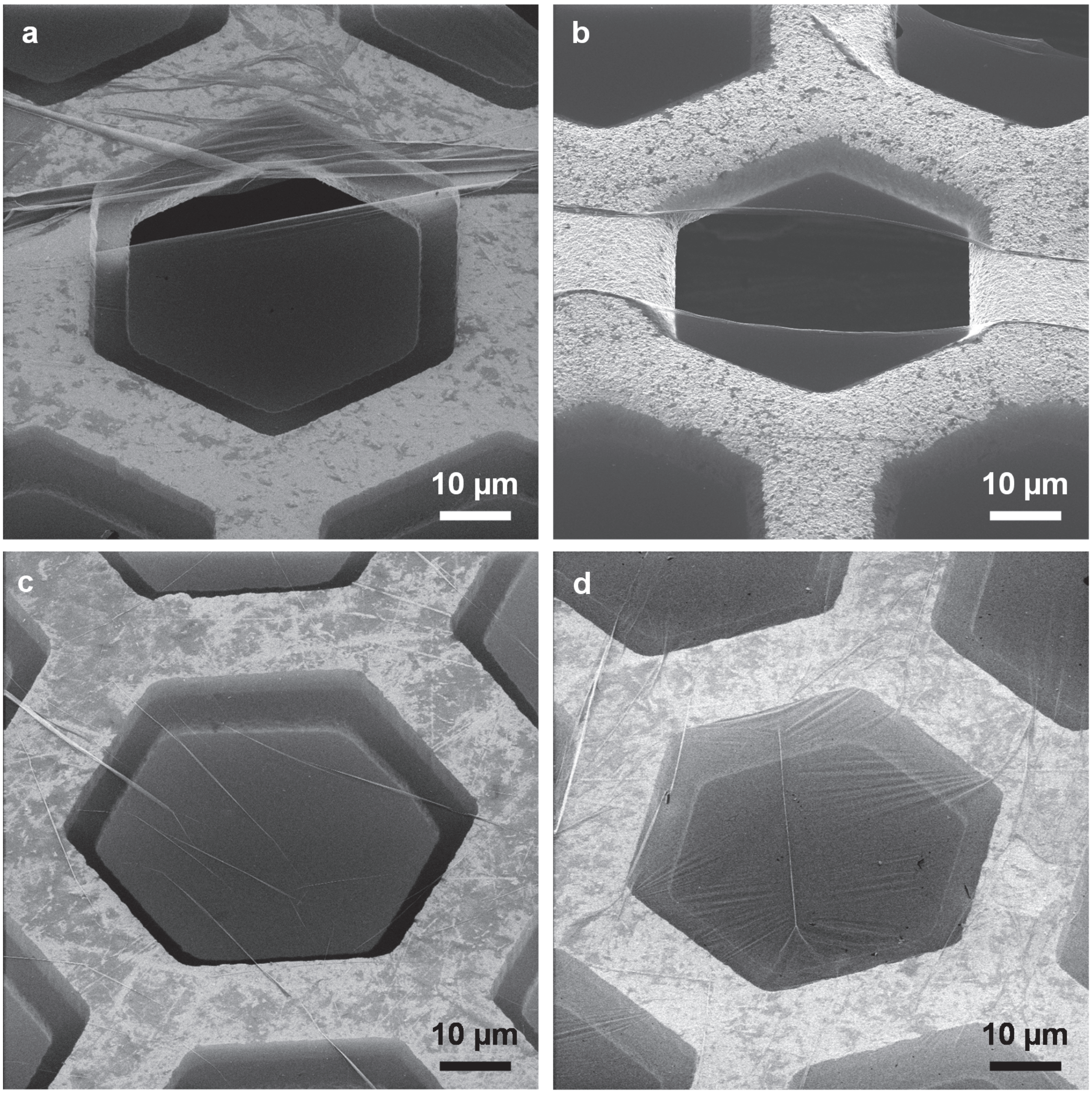

Figure 18: CNMs transferred on copper grids with ~80µm hexagonal openings. (b): image obtained by André Beyer.

Figure 18 represents different features of a CNM itself that are visible in HIM. In (a) larger folds on the upper side of the image, and one rupture in the center are visible. (b) is an interesting example of the membrane rolling up at a rupture, showing the high flexibility of CNMs. Small folds are a feature that is frequently observed (c). Wrinkling (or waves) of the freestanding membrane is a not often observed feature, where (d) is a nice example of such structures in an image.

There are even larger freestanding CNMs, Figure 19 shows the largest intact CNMs produced so far. Please note that structures on the CNM, originating from the background (sample stage), are visible as discussed earlier.

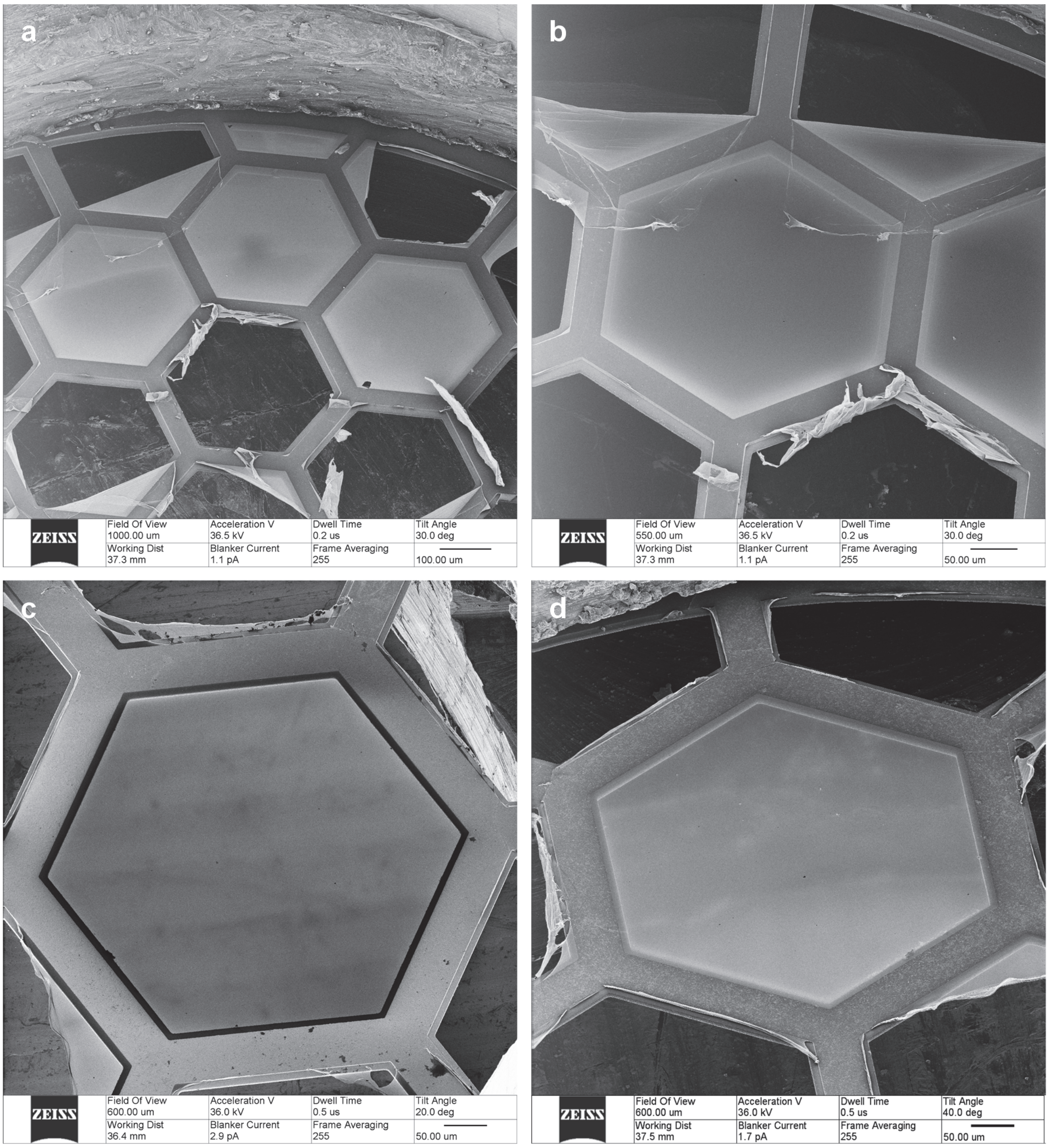

Figure 19: CNMs transferred on copper grids with ~500µm hexagonal openings.

CNMs with different thicknesses are imaged in this study. Despite the high surface sensitivity, an increasing thickness should provide a higher SE-yield on freestanding samples. This is slightly visible in Figure 20b, where the CNM was folded back in the transfer process. In the overview image (a) this double-layer from the top left corner to the right middle of the image is visible. The square marks the position of the magnified image in (b) where the start of the second layer is marked with arrows.

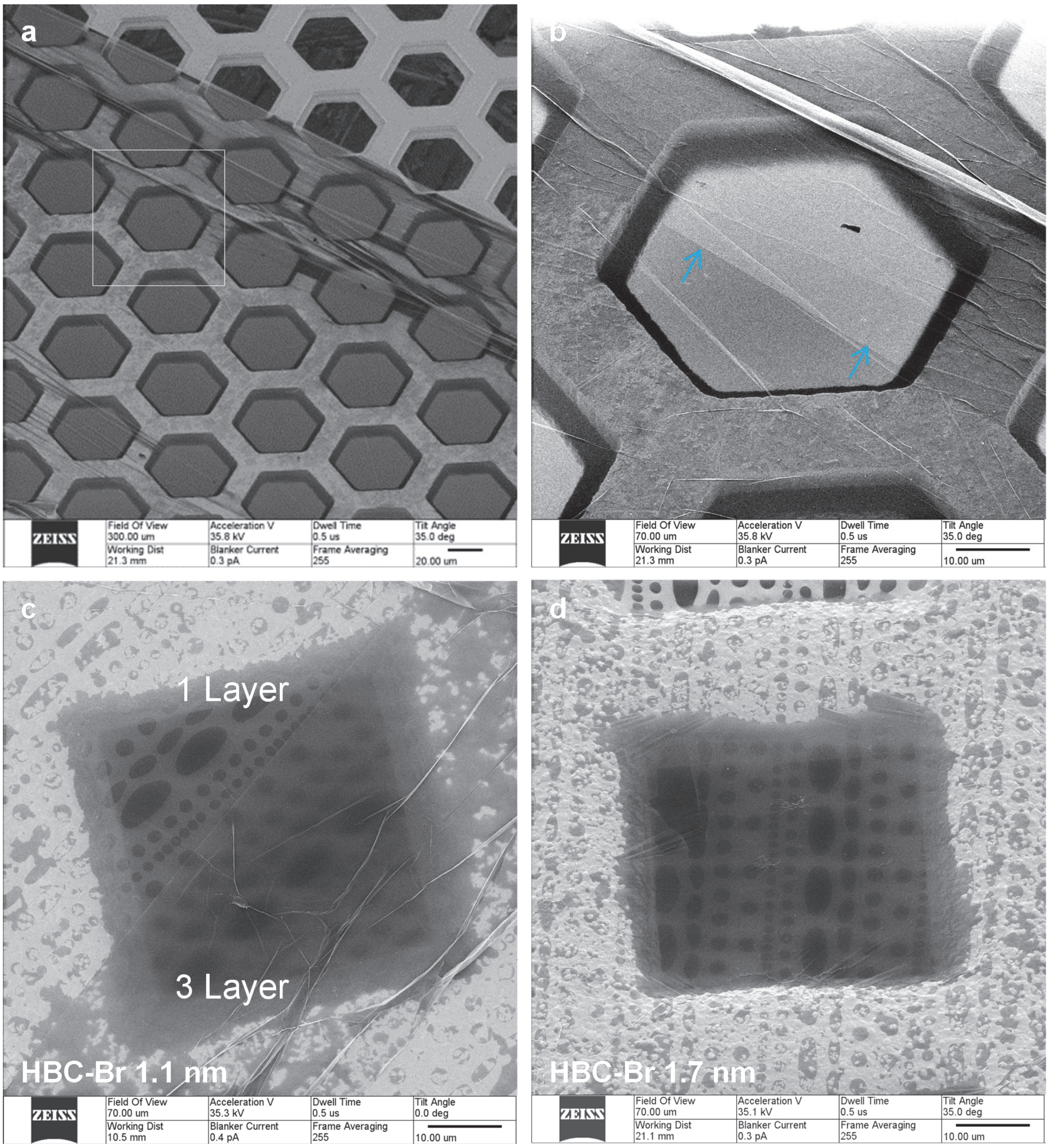

Figure 20: CNMs transferred on copper (a,b) and quantifoil multi-A (c,d) TEM grids. (b) is a magnified image of the square in (a). (c,d): different SAM structures lead to different thickness of the CNMs, in this case with 1.1 and 1.7 nm thickness (In this case HBC-Br, see chapter 3.1.9).

In Figure 20c,d the CNM is suspended on a copper grid with a holey carbon layer some µm below it (similar to Figure 17c,d). The CNM in (c) is folded, so the lower right part is in fact a CNM with ~3.3 nm thickness, where in the upper left part there is only one layer (~1.1 nm). (d) shows a CNM with 1.7 nm thickness. The structures of the holey carbon grid are getting more blurry with increasing thickness due to an increase in scattering of the incident helium beam. An increase in brightness with increasing thickness is not visible here. This effect is superimposed by the interaction with the underlying carbon grid.

In general, it is possible to show a thickness difference in cases with well comparable environment. Unfortunately, this effect is not quantitative so a direct thickness measurement is not possible.

3.1.5 **High resolution imaging of CNMs**

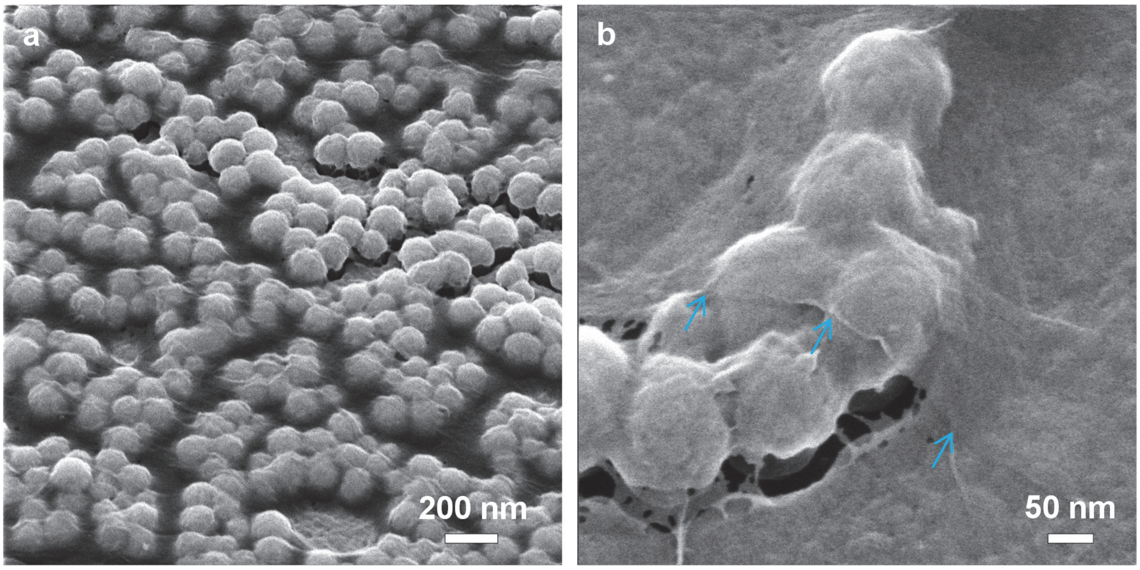

Figure 21: High resolution images of CNM transferred on a gold-coated silicon janus nanoparticle surface. (a): the structures are fully covered, only a small rupture in the middle right region is visible (brighter nanoparticles). (b): CNM begins at the arrows.

It is also very well possible to image CNMs in high resolution (field of view smaller than 1 µm). Position, morphology and defects are imaged in high detail. Figure 21 is a CNM on top of a surface enhanced Raman spectroscopy (SERS) substrate. It consists of silicon nanospheres sputter-coated with gold. The spheres are gold coated only on top providing so-called “janus nanoparticles”. The substrate was prepared by Prof. Takei. It was studied in detail, also with HIM, in a recent publication.[33]

As the CNM is transferred on the substrate, it is important to investigate the success of the transfer process and the final morphology of the membrane. What is visible with the CNM on top is that the membrane stays intact after transfer. Due to its high flexibility it follows the particle shape very well. Figure 21b the edge of a CNM (see arrows) on a group of single nanoparticles is shown.

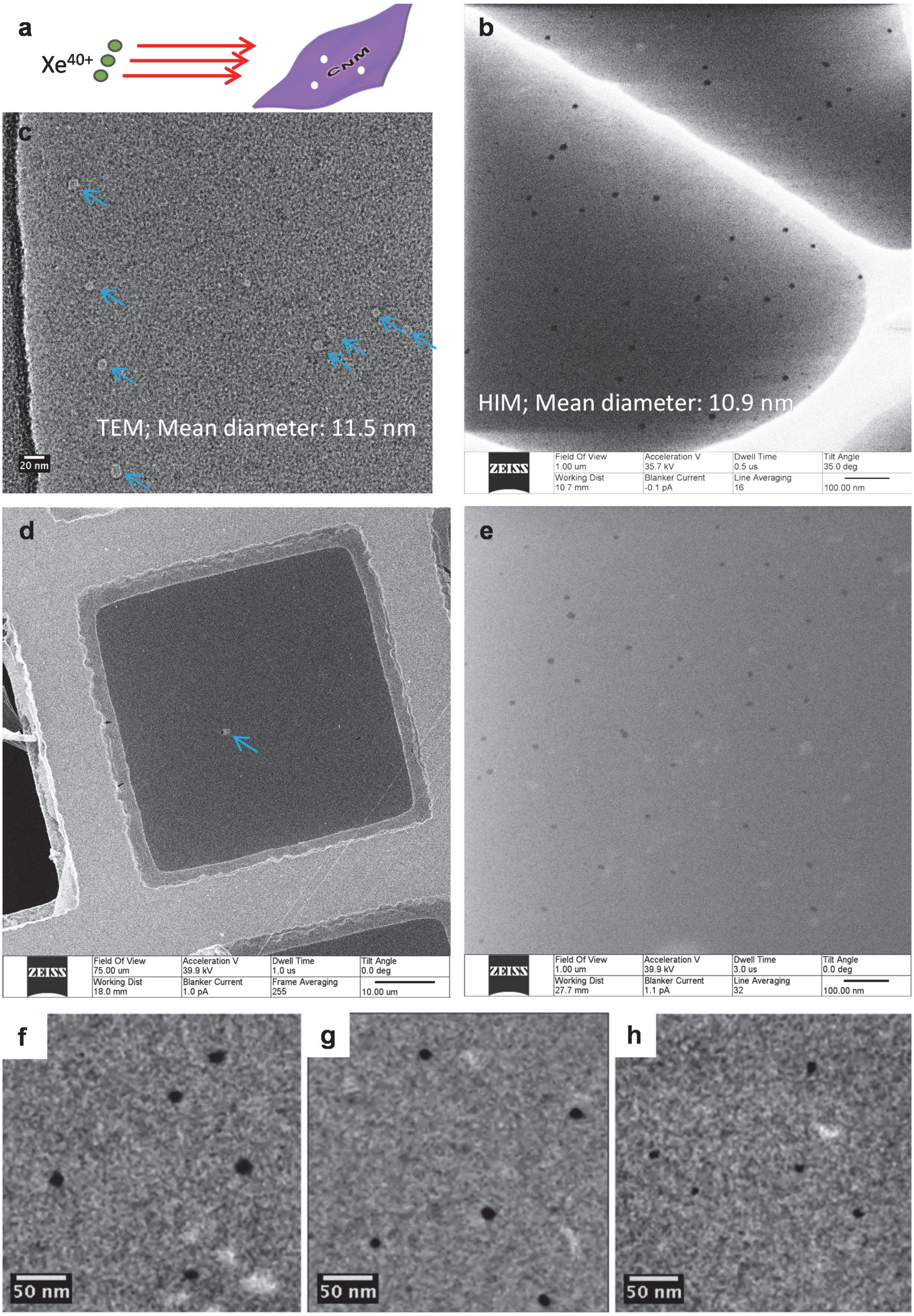

Figure 22: Micrographs of CNMs irradiated with highly charged ions (HCI). (b,c) show a CNM on a holey carbon film with pore diameters of some µm. The sample was imaged by HIM (b) and TEM (c) showing similar pore diameters. Pores appear dark in HIM and bright in TEM. (d-h): CNM on copper grid with ~50 µm openings, the electron floodgun was used for these HIM images. (d): Overview of one field. High resolution images are taken in the middle of such a grid opening. The arrow points at the approximate position of image (e). 3 CNM-covered grids like in (d) were stacked and irradiated with HCIs. The ions penetrated the samples in the order (f)-(g)-(h).

3.1.6 Imaging of porous CNMs made by highly charged ions (HCI)

Porous membranes are of high interest for all aspects of filtering liquids or gases. For this purpose, a suitable analysis method is necessary. As model example, samples of CNMs irradiated with slow highly charged ions (HCI) are investigated.[47] This study was performed in cooperation with Robert Ritter[67], Richard Wilhelm and coworkers from TU Vienna and HZDR Dresden.

On the irradiation with HCIs, every ion is producing one hole in the CNM with a relative narrow size distribution. Figure 22a-c depicts the same sample which was irradiated with Xe 40+ ions and later investigated by TEM and HIM. In direct comparison, HIM provides higher contrast of the pores, thus making it easier to be analyzed. The size analysis from a number of images resulted in similar results of both methods. Thus, it can be concluded that HIM is a suitable method for such an analysis on CNMs.

In a follow-up study, the irradiation of a stack of 3 CNMs is carried out to learn about the development of pore sizes and calculate energy loss in every layer. Here it is desirable to use grids with large holes to be able to align them properly. On such large freestanding CNMs (Figure 22d), an analysis with TEM is impossible because the membrane ruptures instantaneously due to forces caused by charge buildup. This is also the case in HIM, but with the floodgun in operation such membranes could be imaged. However, imaging time is high and the achieved contrast is low.

An example of a first layer is shown in Figure 22e. The images in (f,g,h) are contrast optimized and show the pore size development through the stack of CNMs.

3.1.7 **Imaging of porous CNMs made from different SAMs**

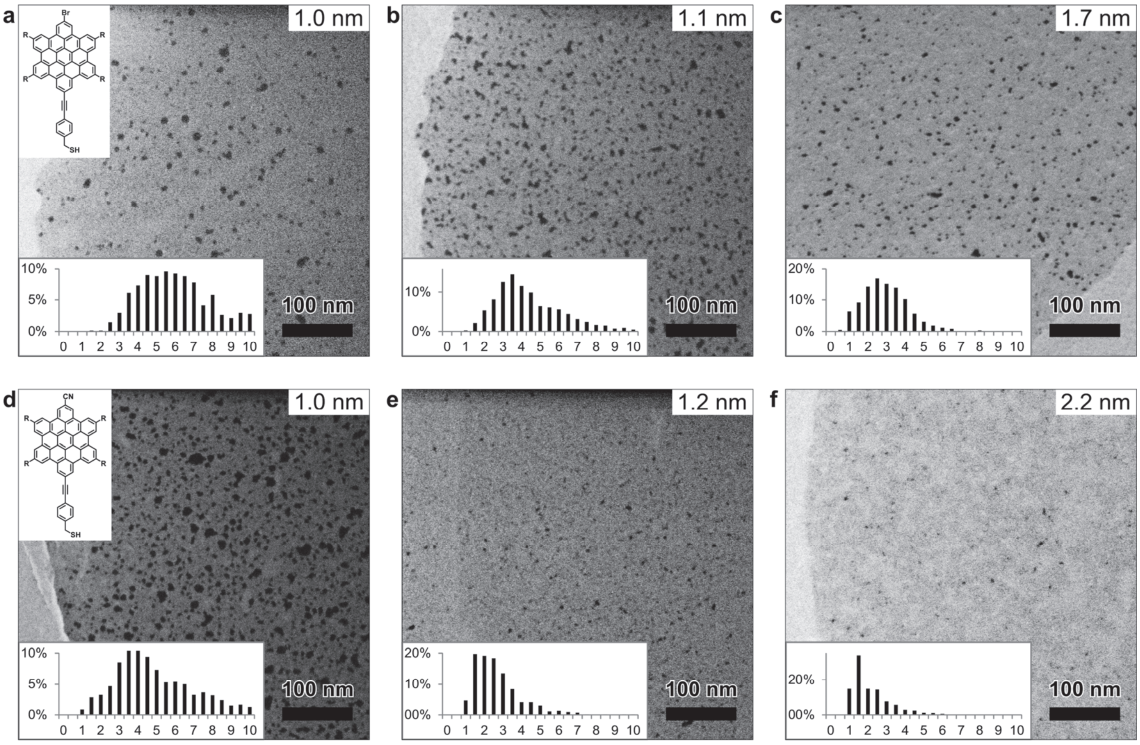

Figure 23: HIM images of free-standing, porous CNMs of different thickness. (a-c): prepared from HBC-Br. (d-f): prepared from HBC-CN (3c); see inset in a,d for structural formula. The thickness of the membranes is given at the top right corner of each image. The histograms in the insets show the distribution of the pore diameter with a step of 0.5 nm. The membranes are placed onto Quantifoil TEM grids type Multi A. Image from published supporting information.[68]

Since the thickness of CNMs is determined by the precursor molecules, the substrate and preparation conditions, it can be controlled by varying these parameters. In an elaborate study, a number of different molecules were studied for their ability to form CNMs (see Chapter 3.1.9 for full details). Two molecules were identified where the thickness varies with the preparation condition of the SAM. They are extended disc-type polycyclic aromatic hydrocarbons, hexa-peri-benzocoronene (HBC) derivatives, with either Bromide (HBC-Br) or cyano (HBC-CN) tail groups (see structural formula in Figure 23a,d; or chapter 3.1.9).

For the analysis, important aspects of the imaging process are: charging, deposition of contaminations and sputtering. The CNMs here are transferred on Quantifoil TEM grids with openings of some µm, so it is always possible to measure areas of CNM very close to this supporting film. There, charging is limited and imaging is well possible without any charge compensation. Contamination and sputter effects are somehow working against each other. On dirty samples holes are directly closed by scanning. This visually does not cause any problem because this effect can be easily observed by the operator. Too high scanning doses on regular samples increase pore sizes. In this study, optimized scanning strategies are used, that do not notably increase the pore diameters. It is important to note that all positions are only scanned once.

From both molecules, CNMs with thicknesses of about 1, 1.2 and 2 nm were prepared and analyzed for porosity. With increasing CNM thickness, smaller size of the pores with a narrower distribution were observed. The histograms present averaged data from many images; between 550 and 1300 pores were counted for every graph.

In Figure 24 the mean pore diameter and the pore density from these samples are plotted against the thickness of the CNM. Both CNMs show a consistent decrease in mean pore size from ~6 nm to 2-3 nm with increasing thickness.

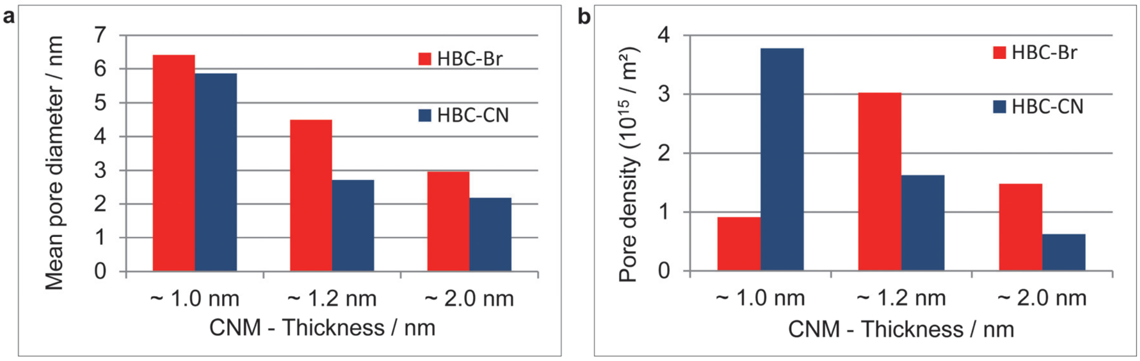

Figure 24: Quantification of porosity of CNMs, prepared from HBC molecules (3b-c). (a): Mean pore diameter versus thickness of the parent self-assembled monolayers.(b): pore density (number of pores per area) versus thickness of the parent self-assembled monolayers. Image from published supporting information.[68]

3.1.8 Summary: Imaging of CNMs

In this chapter it is shown that the helium ion microscope is very useful in imaging of CNMs. The high surface sensitivity allows high contrast images on the macroscale and thus a fast and reliable product control. Freestanding CNMs are imaged and provide all necessary information on the morphology of membranes. In highest resolution it is even possible to analyze defects or wanted porosity of membranes down to the nm – range. In conclusion, it is possible to follow the production by one microscopy method.

3.1.9 Publication: A Universal Scheme to Convert Aromatic Molecular Monolayers into Functional Carbon Nanomembranes (ACS Nano 2013)

This Chapter is reprinted with permission from ACS Publications. The original article appeared as:

> Angelova, P.; Vieker, H.; Weber, N.-E.; Matei, D.; Reimer, O.; Meier, I.; Kurasch, S.; Biskupek, J.; Lorbach, D.; Wunderlich, K.; *et al.* A Universal Scheme to Convert Aromatic Molecular Monolayers into Functional Carbon Nanomembranes. *ACS Nano* **2013**, *7*, 6489–6497.

Contribution:

Helium Ion Microscopy was performed by the author.

A Universal Scheme to Convert Aromatic Molecular Monolayers into Functional Carbon Nanomembranes

Polina Angelova,† Henning Vieker,† Nils-Eike Weber,† Dan Matei,† Oliver Reimer,† Isabella Meier,† Simon Kurasch,‡ Johannes Biskupek,‡ Dominik Lorbach,§ Katrin Wunderlich,§ Long Chen,§ Andreas Terfort,⊥ Markus Klapper,§ Klaus Müllen,§ Ute Kaiser,‡ Armin Gölzhäuser,†,* and Andrey Turchanin†

†Faculty of Physics, University of Bielefeld, 33615 Bielefeld, Germany, ‡Central Facility of Electron Microscopy, University of Ulm, 89081 Ulm, Germany, §Max Planck Institute for Polymer Research, 55128 Mainz, Germany, and ⊥Institute of Inorganic and Analytical Chemistry, University of Frankfurt, 60438 Frankfurt, Germany

ABSTRACT Free-standing nanomembranes with molecular or atomic thickness are currently explored for separation technologies, electronics, and sensing. Their engineering with well-defined structural and functional properties is a challenge for materials research. Here we present a broadly applicable scheme to create mechanically stable carbon nanomembranes (CNMs) with a thickness of ~0.5 to ~3 nm. Monolayers of polyaromatic molecules (oligophenyls, hexaphenylbenzene, and polycyclic aromatic hydrocarbons) were assembled and exposed to electrons that cross-link them into CNMs; subsequent pyrolysis converts the CNMs into graphene sheets. In this transformation the thickness, porosity, and surface functionality of the nanomembranes are determined by the monolayers, and structural and functional features are passed on from the molecules through their monolayers to the CNMs and finally on to the graphene. Our procedure is scalable to large areas and allows the engineering of ultrathin nanomembranes by controlling the composition and structure of precursor molecules and their monolayers.

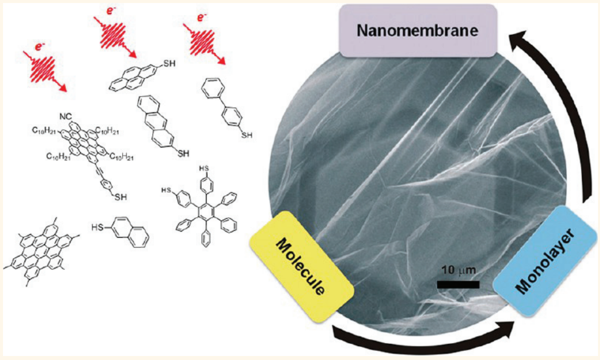

KEYWORDS: two-dimensional materials · carbon nanomembranes · graphene · molecular self-assembly · helium ion microscopy

The creation of functional two-dimensional (2D) materials is a fast-growing field within nanoscience. Nanomembranes,[1] i.e. free-standing films with a thickness of a few nanometers, have been predicted to possess a superior performance in the separation of materials where they should allow a faster passage of the selected—gas or liquid—molecules than any conventional filter.[2] Nanomembranes were integrated in stretchable electronics[3] and have been applied as mechanical resonators in nanoelectro–mechanical systems;[4] further, hybrids of nanomembranes with fluid lipid bilayers were built as biomimetic interfaces for molecular recognition and sensing.[5]

Diverse strategies have been developed to build nanomembranes. Since the 1990s the so-called layer-by-layer (LbL) technique is employed to fabricate membranes for corrosion protection, sensing, and drug delivery.[6,7] In the LbL process, an electrically charged surface is sequentially dipped into positively and negatively charged polyelectrolytes, leading to the formation of polymeric membranes of well-defined molecular composition with thicknesses from ~15 nm to several 100 nm. Much thinner membranes can be made by exfoliating single sheets out of a layered material.[8] Graphene, consisting of a few (~1– 5) layers of carbon atoms, was initially made by exfoliation[9] and is nowadays produced by a variety of techniques,[10] allowing researchers to gain new insights into the physics and chemistry in two dimensions. However, the surface of graphene is homogeneous and chemically inert, which makes an efficient functionalization with other molecules difficult. On the contrary, covalent organic frameworks[11,12] (COFs) and related two-dimensional systems[13–16] are nanomembranes with heterogeneous, chemically reactive surfaces. The first step in

* Address correspondence to ag@uni-bielefeld.de.

Received for review May 26, 2013 and accepted June 26, 2013.

10.1021/nn402652f

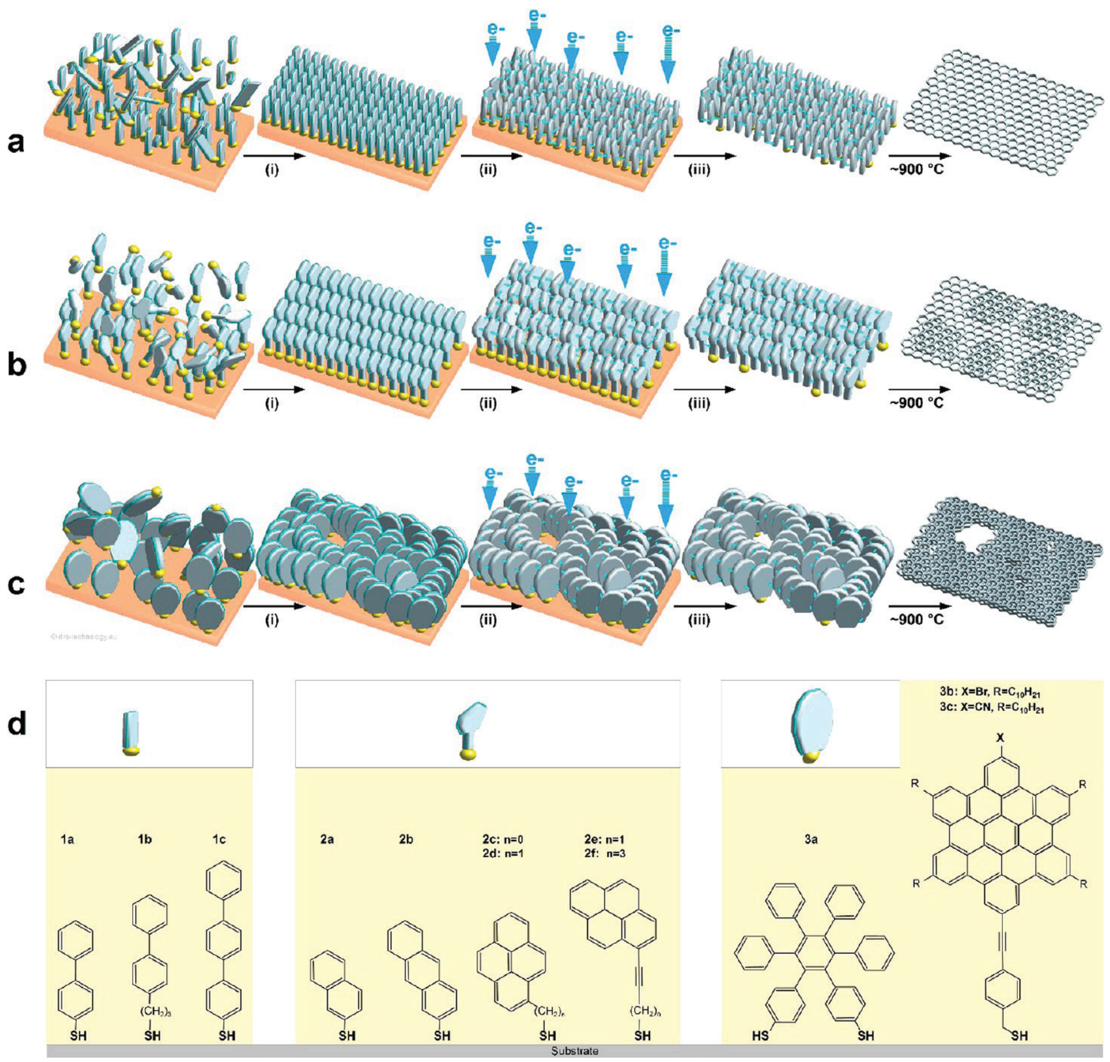

Figure 1. Schematic for the formation of carbon nanomembranes (CNMs) and graphene from molecular precursors. (a–c) Schematic illustration of the fabrication route for CNMs and graphene: Self-assembled monolayers are prepared on a substrate (i), then cross-linked by electron irradiation to form CNMs of monomolecular thickness (ii). The CNMs are released from the underlying substrate (iii), and further annealing at 900 °C transforms them into graphene. (a) Fabrication of thin CNMs and graphene (from "linear" precursor molecules 1a–1c in d). (b) Fabrication of thicker CNMs and few layer graphene sheets (from "condensed" precursors 2a–2f in d). (c) Fabrication of CNMs and graphene sheets with nanopores (from "bulky" precursors 3a–c in d). (d) Chemical structures of the different precursor molecules used in this study.

their creation is the synthesis of organic molecules of well-defined size and shape with functionalities at defined positions. When brought into proximity, adjacent molecules form multiple covalent bonds and assemble, such as Wang tiles, in a 2D lattice. COF nanomembranes look very aesthetic; however, their fabrication is time-consuming and requires high skill in organic synthesis.

In this article, we present a modular and broadly applicable construction scheme to efficiently fabricate ultrathin carbon nanomembranes (CNMs) that unite the thinness of graphene with the chemical functionality of a COF and the ease of fabrication of LbL films. It was found earlier[17] that self-assembled monolayers (SAMs) of 1,1′-biphenyl-4-thiol (BPT) are laterally cross-linked by low-energy electrons and can be removed from the surface forming 1 nm thick CNMs. When these CNMs are pyrolized at ∼1000 K, they transform into graphene.[18,19] Motivated by these findings, we applied similar protocols to a variety of other polyaromatic molecules. Our scheme (Figure 1a–c) utilizes a sequence of (i) molecular monolayer assembly on a solid surface, (ii) radiation induced two-dimensional cross-linking, and (iii) a lift-off of the network of cross-linked molecules. The product is a free-standing CNM, whose thickness, homogeneity, presence of pores, and surface chemistry are determined by the nature of the initial molecular monolayer. We investigated three types of thiol-based precursors: nonfused oligophenyl derivatives (Figure 1d: **1a**–**1c**) which possess linear molecular backbones providing an improved structural ordering of the formed SAMs; condensed polycyclic precursors like naphthalene (NPTH), anthracene (ANTH) and pyrene (MP) mercapto derivatives (Figure 1d: **2a**−**2f**) which are more rigid and should result in a higher stability and an increased carbon density of the monolayers; "bulky" molecules, like the noncondensed hexaphenylbenzene derivative with a propeller-like structure (Figure 1d: **3a**) and extended disc-type polycyclic aromatic hydrocarbons such as hexa-*peri*-benzocoronene (HBC) derivatives (Figure 1d: **3b**,**c**).[20,21] The former are specially functionalized with long alkyl chains and a surface active group which is attached to the π-conjugated backbone through a flexible methylene linker. This molecular design enables a control over the thickness and packing density of the SAMs by varying the conditions of preparation. Figure 1a−c shows schematics of our process applied to different types of monolayers. In Figure 1a oligophenyls with a linear molecular backbone form well-ordered monolayers that cross-link into homogeneous CNMs. After pyrolysis, the CNMs transform into graphene, whose thickness depends on the density of carbon atoms in the monolayers. In Figure 1b, small condensed polycyclic precursors also form monolayers that cross-link into CNMs. After pyrolysis, the CNMs transform into graphene, whose thickness is higher than in **1a**, even if the carbon density is the same as in **1a**. Figure 1c shows bulky aromatic hydrocarbons that assemble in a less-ordered monolayer and cross-link into CNMs with pores. After annealing, these nanomembranes transform into thicker graphene sheets with pores. Hence, the produced graphene takes on structural features from the preceding CNM, which itself has taken on features from the preceding monolayer, i.e. from molecules and surface. Structural and functional properties are thus passed on from the molecules through their monolayers to the nanomembranes. Our procedure is scalable up to square meters and can produce CNMs and graphene of defined thickness, chemical composition and pore density. We investigated how the molecular size, composition, and structure of the monolayers affect the resulting nanomembranes by employing X-ray photoelectron spectroscopy (XPS), scanning tunneling microscopy (STM), low-energy electron diffraction (LEED), helium ion microscopy (HIM), and aberration-corrected high-resolution transmission electron microscopy (HRTEM).

RESULTS AND DISCUSSION

First, we characterized the structure of SAMs on gold from aromatic thiols shown in Figure 1d; Au(111)/mica substrates were immersed into the solutions of the precursor molecules (see Supporting Information (SI) for details of the preparation). SAMs form due to the making of strong bonds between the sulfur and the gold atoms that is accompanied by van der Waals interactions between the carbon atoms.[22] To obtain SAMs with a desired molecular packing, we can adjust parameters like immersion time, temperature, concentration, and polarity of the solvents (see SI). XPS data of aromatic SAMs, representing diverse types of precursors, are shown in Figure 2 (left). For each SAM, its chemical composition and the thickness can be derived from the binding energy and intensity of the C1s, S2p and Au4f photoelectron signals. The sulfur signal consists of a doublet with a $S2p_{3/2}$ binding energy (BE) of 162.0 eV, which unambiguously demonstrates the formation of sulfur−gold bonds.[23] Only for the HBC derivatives (**3b**,**c**), the presence of a second sulfur species with the BE of the $S2p_{3/2}$ signal at 163.6 eV is observed. This signal originates from physisorbed HBC and/or of disulfides,[24] which may be stabilized by $\pi-\pi$ interactions between the large aromatic cores, indicating a lower degree of order in these SAMs. Aromatic and aliphatic carbons contribute to the C1s signal at BEs of ~284.2 eV and ~285.0 eV, respectively.[23] Stoichiometry and thickness as obtained from XPS correspond to the composition of the precursor molecules, and indicate the formation of SAMs with an "upright" molecular orientation. By varying the precursors, the thickness of the aromatic monolayers can be adjusted from ~6 Å for NPTH (Figure 1: **2a**) to ~24 Å for HBC−CN (Figure 1: **3c**), which directly correlates with their molecular lengths (see Figure 1a and Table 1). In addition, the temperature and solvent dependent intermolecular interactions of the HBC derivatives[25] allow one to tune the final SAM thickness by varying the preparation conditions (see Table 1). A detailed analysis of the XPS data is presented in Table S1 (see SI).

To determine structure and surface density of the SAMs, they were studied by STM and LEED. Figure 3 shows three molecular precursors containing different numbers of carbon atoms per molecule − anthracene (C14), 3-(biphenyl-4-yl)propane (C15) and terphenyl (C18) thiols. We found that precursor molecules **1b**, **1c**, **2a**, **2b**, **2c**, and **2e** (see Figure 1d) form ordered SAMs with the densely packed[26] ($\sqrt{3} \times \sqrt{3}$) unit cell of the adsorption places and with the ($2\sqrt{3} \times \sqrt{3}$) superstructure of the molecular backbones. These structures are clearly deduced from LEED as well as STM data (see Figure 3) and correspond to a surface area of 21.6 Å^2 per molecule. Note that for these SAMs the surface density of carbon atoms in the monolayer can be precisely tuned by the carbon content of the respective molecular precursors. Short biphenylthiols (**1a**) exhibit a (2×2) arrangement of the adsorption places, which corresponds to a less densely packed monolayer of 28.7 Å^2 per molecule.[27] We did not observe the formation of LEED patterns and well-ordered SAMs by STM for precursor molecules **2d** and **2f** and **3a**−**c**. As XPS indicates a formation of sulfur−gold bonds for all precursors, we conclude that monolayers of the "bulky" and polycyclic molecules **2d**, **2f**, **3a**−**c** are less ordered and probably less densely packed than the monolayers

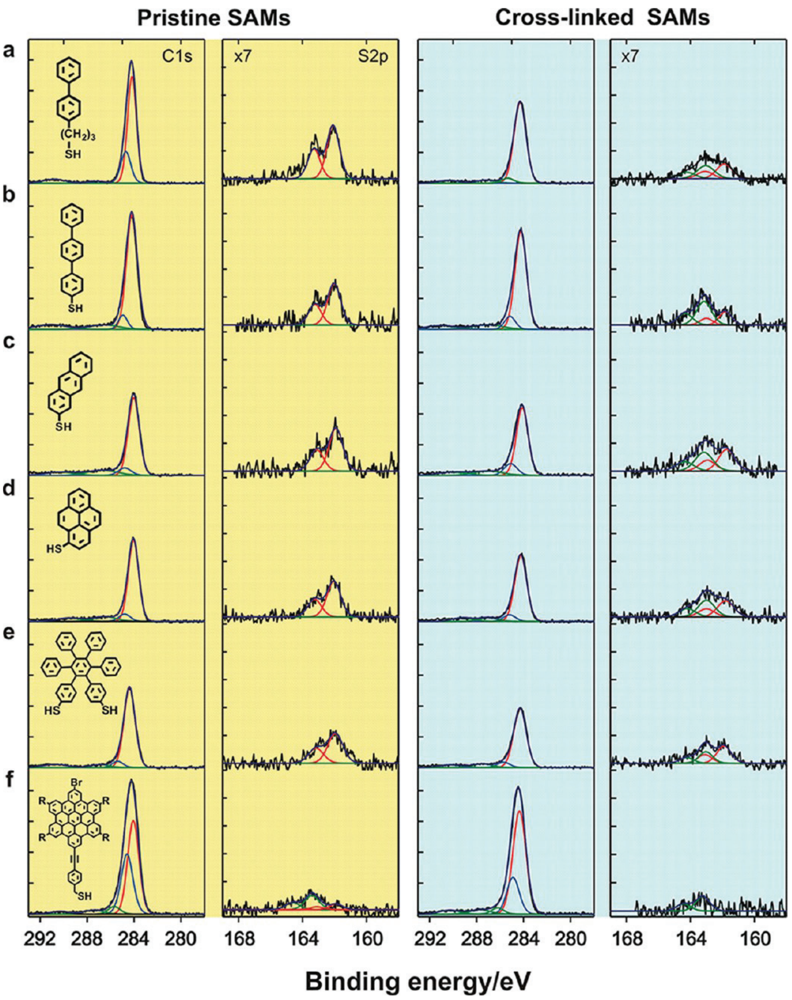

Figure 2. XPS data of pristine SAMs and CNMs. XP spectra of C1s and S2p signals of the pristine (in yellow) and electron-irradiated (50 eV, 60 mC/cm^2) monolayers (in blue) of (a) BP3, **1b**. (b) TPT, **1c**. (c) ANTH, **2b**. (d) 1MP, **2c**. (e) HPB, **3a**. (f) HBC-Br, **3b**.

TABLE 1. Effective thickness of pristine SAMs and CNMs; carbon reduction upon electron irradiation (100 eV, 60 mC/cm^2)

Sample	Thickness SAM [Å]	Thickness CNM [Å]	Reduction of C [%]
1a (BPT)	10	9	5
1b (BP3)	12	10	16
1c (TPT)	13	12	4
2a (NPHT)	6	6	9
2b (ATRH)	9	9	2
2c (1MP)	9	8	10
2d (MP1)	9	8	4
2g (MP3)	11	10	8
2f (MP5)	10	8	11
3a (HPB)	8	8	13
3b^1 (HBC-Br)	10	10	4
3b^2 (HBC-Br)	12	11	5
3b^3 (HBC-Br)	19	17	2
3c^1 (HBC-CN)	12	10	6
3c^2 (HBC-CN)	14	12	5
3c^3 (HBC-CN)	24	22	3

[*] Different conditions were applied for preparation of SAMs from **3b**$^{1-3}$ and **3c**$^{1-3}$. For details see SI.

of oligophenyls (**1a**−**c**) and the small fused-ring systems (**2a**−**c**, **2e**).

The next step of our process is the radiation-induced conversion of the aromatic monolayers into 2D carbon nanomembranes. Therefore, we irradiated the SAMs with low-energy electrons (50 or 100 eV, see SI), using typical doses of ~60 mC/cm^2, corresponding to ~3500 electrons per 1 nm^2, which leads to a loss of order, as observed in LEED and STM. It is known from previous studies of thiol SAMs[28,29] on gold, that low-energy electron irradiation results in the cleavage of C−H bonds. In aliphatic SAMs, this C−H cleavage is accompanied by conformational changes and C−C cleavage that lead to molecular decomposition and desorption. Conversely, after C−H cleavage in aromatic SAMs, the delocalization of π-electrons over the σ-framework of the aromatic ring, retains its integrity through the irradiation process and we observe a predominant cross-linking between adjacent molecules into a mechanically stable 2D network. As suggested by UV photoelectron spectroscopy and quantum chemical

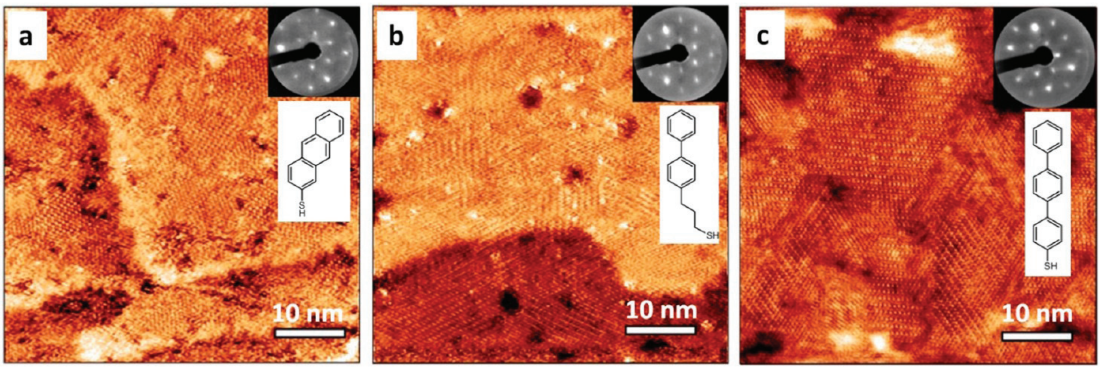

Figure 3. Structure of pristine SAMs. STM micrographs and LEED patterns (insets) of SAMs from molecular precursor: (a) ANTH, 2b; LEED pattern at 116 eV. (b) BP3, 1b; LEED pattern at 127 eV. (c) TPT, 1c; LEED pattern at 129 eV. For molecular structures see Figure 1d.

calculations of BPT SAMs on gold (see Figure 1: **1a**), the formation of single- and double-links (C–C bonds) between phenyl rings of the molecules prevails the cross-linking.[29] Unabling the specificity this picture is also supported by UV–vis spectroscopy of the formed CNMs.[30] Figure 2 shows XPS data before and after electron irradiation in the left and right parts, respectively. As seen from the intensities of the C1s and Au4f (not shown), for purely aromatic SAMs (Figure 2b–d) the irradiation reduces carbon content and monolayer thickness by ~5–10%; in SAMs with aliphatic chains up to ~20% (Figure 2a). However, this small loss of material is not relevant for the effectiveness of the cross-linking. We find that the irradiation and the subsequent molecular reorganization also affects the sulfur–gold bonds, as indicated by the appearance of a signal with the S$p_{3/2}$ binding energy of 163.5 eV, which we assign to thioethers or disulfides forming after the cleavage of S–Au bonds.

After the electron irradiation of the aromatic monolayers, we transferred the obtained CNMs from their gold substrates onto perforated supports (e.g., TEM grids)[18] and imaged them with a helium ion microscope[31] (HIM). This novel charged particle microscopy combines high resolution (~4 Å) with high surface sensitivity and the possibility to image nonconducting ultrathin specimens.[32] Figure 4 shows HIM micrographs of free-standing CNMs from different types of aromatic molecular precursors (see Figure 1d: **1**–**3**). Simply the fact that one can take these images demonstrates that the SAMs of all these molecules have been cross-linked into mechanically stable CNMs. In Figure 4a–c free-standing CNMs from precursors **1c**, **2c**, and **2d** are shown. These HIM micrographs were acquired at different magnifications, demonstrating the successful fabrication of CNMs of various lateral sizes. The field of view in Figure 4a is 40 × 40 μm^2, which allows to observe some folds in the free-standing 1.2 nm thick CNM. In the lower left corner of Figure 4b, the boundary between the free-standing or supported CNM and substrate can clearly be seen. Figure 4c shows the field of view of 300 × 300 μm^2 with a large and homogeneous CNM of a thickness of 0.8 nm. Macroscopic defects in these nanomembranes are practically negligible on the length scale of these images.

Since the thickness of CNMs is determined by the precursor molecules and their packing density in SAMs, it can be controlled by tailoring these parameters. Figure 4 displays examples of CNMs where the thinnest nanomembrane is from precursor **2a** with a thickness of only 0.6 nm and the thickest one is from precursor **3c** with an about four times higher thickness (2.2 nm). The opportunity to flexibly control the thickness of CNMs opens broad avenues for the engineering of nanomembranes. Along this path, we investigated different CNMs by HIM and found a clear relation between properties of the precursor molecule, its SAMs and the appearance of the ensuing CNM. If the molecule forms a densely packed SAM (**1a**–**c**, **2a**–**c**, **2e** in Figure 1d), the following CNM is continuous and free of holes. Figure 4g shows a high magnification HIM image of a homogeneous CNM made from terphenylthiol (**1c**). Conversely, CNMs made from HBC (**3b**–**c** in Figure 1d) or HPB (**3a** in Figure 1d) precursors, two molecules that possess larger sizes and form less well-ordered SAMs, exhibit pores, cf. the HIM images in Figure 4h and Figure 4i. The dark spots in these images are pores that have a very small diameter and a narrow size distribution, as shown in the respective histograms (see insets). In case of the HBC precursor the mean size of the nanopores is ~6 nm with the surface density of 9.1 × 10^{14} pores/m^2; the more compact HPB precursor shows a size of ~2.4 nm with a surface density of 1.3 × 10^{15} pores/m^2. The formation of nanopores in these CNMs is thus attributed to the large van der Waals radii of HBC and HPB structures and in the case of HBCs to the propensity of the disk like molecules for intermolecular stacking which competes with the molecule–substrate interactions and lowers the order in the respective SAMs. We also observe that the average pore diameter decreases from 6.4 to 3.0 nm

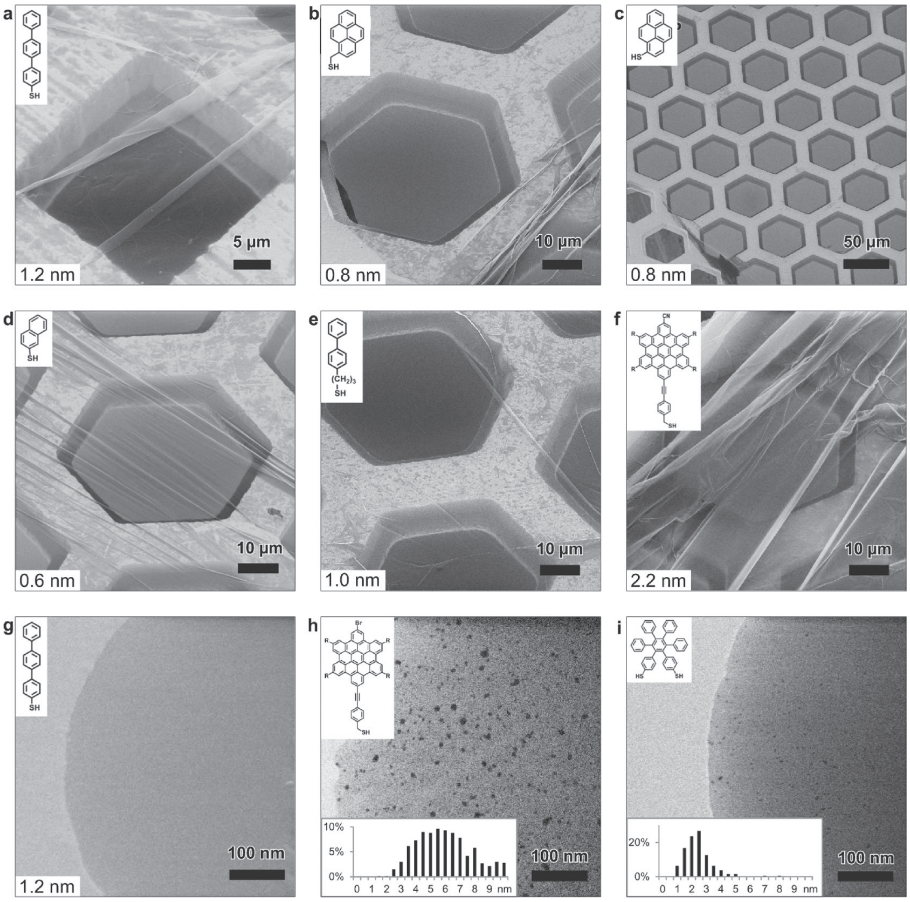

Figure 4. Helium ion microscope (HIM) micrographs of free-standing CNMs. After cross-linking the nanomembranes were transferred onto TEM grids and images were taken at different magnifications (see scale bar). CNMs were prepared from: (a) TPT, 1c; (b) MP1, 2d; (c) 1MP, 2c; (d) NPTH, 2a; (e) BP3, 2b; (f) HBC−CN, 3c; (g) TPT, 1c; (h) HBC-Br, 3b; (i) HPB, 3a; the upper left insets show the precursor molecules. The CNM in a is suspended over a gold TEM grid, CNMs in (b−f) over copper grids, CNMs in (g−i) over Cu grids with thin carbon film. The numbers in the lower left corners in (a−g) indicate the CNM thicknesses, as determined from XPS before the transfer. HIM images (h and i) show CNMs with nanopores, the lower insets show the respective distributions (in %) of pore diameters (in nm).

when the SAM thickness increases from 1 to 2 nm (see SI for details).

Finally, we studied the conversion of CNMs from various molecular precursors into graphene[19] by annealing them at 900 °C in ultrahigh vacuum ($\sim 10^{-9}$ mbar) (see SI for details). Sulfur atoms, initially present in the CNM (see Figure 1d), desorb during this treatment.[29] Note that a high thermal stability of CNMs is essential for the conversion into graphene, as non-electron-irradiated aromatic thiol SAMs desorb from the substrate at temperatures[33] (~120 °C) that are much lower than necessary for their pyrolysis. The atomic structure of the CNMs after annealing was imaged by aberration-corrected (AC) high-resolution transmission electron microscopy (HRTEM) at 80 kV accelerating voltage. The atomically resolved AC-HRTEM micrographs of annealed CNMs from various precursor molecules are presented in Figure 5; in these images carbon atoms appear dark. Figure 5a shows one of the thinnest CNMs (0.8 nm, **3a** in Figure 1d) after annealing. Most of the sheet area consists of single-layer graphene (~50%, light-blue color coded) with the clearly recognizable hexagonal arrangement of carbon atoms; randomly oriented graphene nanocrystallites are connected with each other *via* the typical heptagon−pentagon[34] grain boundaries (see inset to Figure 5a). A small fraction of the sheet (~20%, light green color coded) consists of graphene double-layers, which reveals the respective moiré pattern.[35] Gray and light-red areas correspond to the disordered carbon and holes, respectively; pentagons (green) and heptagons (blue) are marked. The thickness of the formed graphene sheets depends on the structure of the precursor molecules and their abilities to form SAMs and to be cross-linked into CNMs. As seen in Figure 5b−g, graphene sheets from various precursors have the same nanocrystalline morphology as in Figure 5a; however, their thickness varies by a factor of ~3, depending on the precursor. This visual impression was confirmed by measuring the film thickness by quantitative electron energy loss spectroscopy (EELS) at the carbon K adsorption edge[36] (see SI, Table S2). The structural transformation of CNMs into

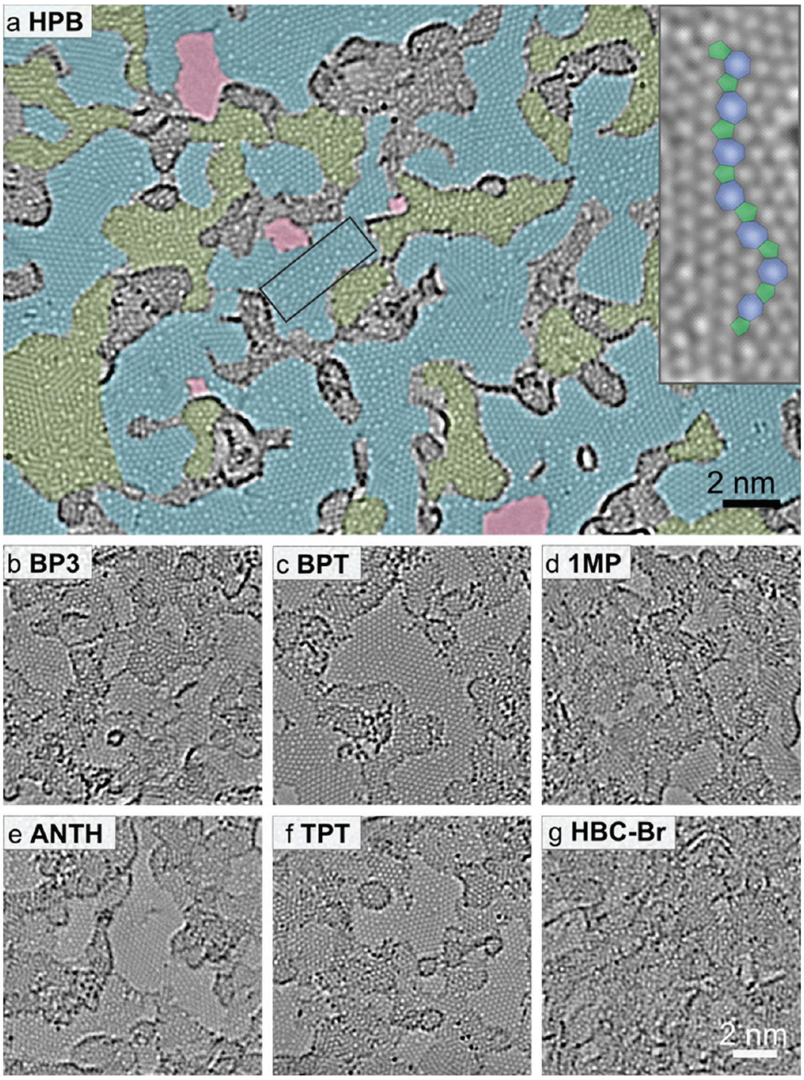

Figure 5. Atomic structure of CNMs of various thicknesses after conversion into graphene. Aberration-corrected high-resolution transmission electron microscope (AC-HRTEM) images at 80 kV of graphene samples, prepared from (a) HPB, 3a. (b) biphenylthiol, BP3, 1b. (c) BPT, 1a. (d) 1MP, 2c. (e) ANTH, 2b. (f) TPT, 1c. (g) HBC-Br, 3b. Regions of different layer thicknesses are color coded: single layers - light blue; double layers - light green; holes - light red. The insert in (a) shows a magnified grain boundary where arrangements of carbon atoms into pentagons (green) and heptagons (blue) are marked. For structures of the molecular precursors see Figure 1d.

graphene has a drastic impact on the electrical properties. Being initially dielectric, with a band gap of ~4 eV for CNMs from biphenylthiols[29] (**1a** in Figure 1d), annealing at 900 °C results in the conversion into conductive graphene with a sheet resistivity of ~100–500 kΩ/sq. The resistivity correlates with the thickness of the graphene sheets, with lower resistivity for the thicker sheets.

The above results clearly demonstrate that our procedure is a modular and broadly applicable construction scheme to fabricate nanomembranes that adopt properties from their preceding molecular monolayers. As the process utilizes electron-beam exposures, the size of the irradiated area can be varied. With a flooded (defocused) exposure, large area (up to m^2) CNM and graphene sheets can be fabricated. With a focused electron beam lithography exposure, micro- and nanometer sized sheets can be written.[37] In this study only thiols on gold were investigated; however, the fabrication of nanomembrane and graphene sheets can be expanded to a variety of other metal surfaces using sulfur-, nitrogen-, or phosphorus-containing surface active compounds as well as onto insulator and semiconductor substrates using hydroxy-[38] or silane-derivatives.[17] This flexibility allows a direct growth of CNM or graphene on technologically relevant substrates.

In order to become nanomembranes, the SAMs first need a stable scaffold that is rigid enough to sustain the electron irradiation and that can form intermolecular cross-links. Second, they have to possess a sufficient density of carbon atoms. These conditions are fulfilled by SAMs with a fair amount of aromatic groups. While SAMs from all molecules in Figure 1d can be converted into nanomembranes, monoaryl or short molecules such as pyridine-4-thiol and anthracene-9-thiol cannot. The shortest precursor that led to CNMs and graphene sheets was naphthalene-2-thiol (Figure 1d: **2a**) consisting of two fused benzene rings. Remarkably enough, the thickness of the formed sheets correlates with the density of carbon in the SAMs and with the packing of the constituting molecules. By selecting appropriate precursor molecules, large areas of single-layer graphene can thus be produced. Polycyclic aromatic hydrocarbons (Figure 1d: **2a**−**f**) led to thicker CNM and graphene sheets than oligophenyls with the same surface density of carbon atoms (Figure 1d: **1a**−**d**). Pristine SAMs of high structural quality result in the homogeneous CNM and homogeneous graphene sheets (see Figure 4g), whereas SAMs of low structural quality result in sheets with nanopores (Figure 4h, Figure 4i). The size of the resulting nanopores is quite small and varies from ∼1 to 10 nm (see SI), as it mainly depends on the precursor molecules and their packing density in the SAMs; one may tailor the CNMs for applications in ultrafiltration.[39] Some CNMs can form Janus nanomembranes[40] with two distinct faces possessing amino- and thiol-groups, respectively, allowing selective chemical functionalization on both faces. A chemical functionalization of CNMs, together with opportunities to mix precursor molecules, opens many doors to engineer novel 2D hybrid materials.

CONCLUSIONS

We have presented a universal and scalable route to ultrathin free-standing carbon nanomembranes and graphene using aromatic molecules as precursors. The properties of the resulting sheets can be flexibly adjusted including their thickness, conductivity, chemical functionalization, and appearance of nanopores. We expect that, due to its simplicity and universality, the approach will have a strong impact on (1) the rapidly growing field of free-standing 2D materials and facilitate their incorporation and application in NEMS devices and (2) the separation of molecules as metal-free catalysts or when properly functionalized as bio- or chemically sensing coatings.

EXPERIMENTAL METHODS

Samples Preparation. Molecular precursors used in this study are commercially available (**1a** and **2a**) or were specially synthesized (**1b**−**c**, **2b**−**f**, **3a**−**c**). SAMs were prepared by immersion of 300 nm thermally evaporated Au on mica substrates into the respective solvents (see SI for details). Cross-linking was achieved either in an ultrahigh vacuum (UHV) ($<10^{-9}$ mbar) chamber or in a high vacuum (HV) ($<5 \times 10^{-7}$ mbar) chamber employing 50 and 100 eV electrons, respectively, and a dose of ∼60 mC/cm^2. All XPS, LEED, and STM measurements were conducted on samples cross-linked *in situ* in the UHV chamber of XPS. For HIM and TEM measurements both samples cross-linked in the UHV chamber and in the HV chamber were employed. Transfer of CNMs and graphene onto TEM grid was conducted by spin-coating on their surface 500-nm-thick layers of poly(methyl methacrylate) (PMMA), etching the original gold substrates, transferring the CNM/PMMA or graphene/PMMA sandwiches onto TEM grids, and dissolving PMMA in acetone using a critical point dryer.[18] Annealing of the samples mounted in molybdenum sample holders was conducted for 30 min at 900 °C in an UHV chamber (5×10^{-9} mbar) using heating/cooling rates of 400 °C/h.

Characterization. The as-prepared SAMs and CNMs were analyzed by XPS, STM, and LEED in a multichamber UHV-system (Omicron). STM images were obtained using electrochemically etched tungsten tips, with tunneling currents of 30−50 pA and bias voltages of 300 mV. LEED patterns were recorded using a BDL600IR-MCP instrument (OCI Vacuum Microengineering) with a multichannel plate (MCP) detector with the electron beam currents below 1 nA. XPS was performed using a monochromatic X-ray source (Al Kα) and a Sphera electron analyzer (Omicron) with a resolution of 0.9 eV. HIM was conducted with a Carl Zeiss Orion Plus. The He$^+$ ion beam was operated at 33−37 kV acceleration voltage at currents of 0.2−0.4 pA. A working distance of 8−22 mm was employed, and secondary electrons were collected by an Everhart-Thornley detector. AC-HRTEM characterization was conducted with an aberration-corrected FEI Titan microscope operated at a beam energy of 80 kV to minimize knock-on damage and equipped with a postcolumn Gatan energy filter for local EELS analysis. Electrical measurements were done by a standard four-point setup using Suess probes and a Keithley source-measure unit.

Full Methods are available in the Supporting Information.

Conflict of Interest: The authors declare no competing financial interest.

Acknowledgment. This work was supported by the German Bundesministerium für Bildung und Forschung (BMBF, Grants 03X0108A and 03X0108B) and by the Deutsche Forschungsgemeinschaft (DFG) through priority program SPP1459 "Graphene" (Grants TU149/2-1 and KA1295/15-1). A.Tu. further thanks the DFG for a Heisenberg Fellowship (TU149/3-1). S.K., J.B. and U.K. thank the state Baden-Württemberg for financial support within SALVE (KA 1295/17-2).

Supporting Information Available: Description of materials, full description of methods, interpretation of XPS spectra, summary of EELS data, evaluation of porosity of HBC-based nanomembranes, and supporting references. This material is available free of charge via the Internet at http://pubs.acs.org.

REFERENCES AND NOTES

1. Rogers, J. A.; Lagally, M. G.; Nuzzo, R. G. Synthesis, Assembly and Applications of Semiconductor Nanomembranes. *Nature* **2011**, *477*, 45–53.
2. Wang, E. N.; Karnik, R. Water Desalination: Graphene Cleans up Water. *Nat. Nanotechnol.* **2012**, *7*, 552–554.
3. Li, X. S.; Cai, W. W.; An, J. H.; Kim, S.; Nah, J.; Yang, D. X.; Piner, R.; Velamakanni, A.; Jung, I.; Tutuc, E.; et al. Large-Area Synthesis of High-Quality and Uniform Graphene Films on Copper Foils. *Science* **2009**, *324*, 1312–1314.
4. Zande, A. M. v. d.; Barton, R. A.; Alden, J. S.; Ruiz-Vargas, C. S.; Whitney, W. S.; Pham, P. H. Q.; Park, J.; Parpia, J. M.; Craighead, H. G.; McEuen, P. L. Large-Scale Arrays of Single-Layer Graphene Resonators. *Nano Lett.* **2010**, *10*, 4869–4873.
5. Ang, P. K.; Jaiswal, M.; Lim, C. H. Y. X.; Wang, Y.; Sankaran, J.; Li, A.; Lim, C. T.; Wohland, T.; Barbaros, Ö.; Loh, K. P. A Bioelectronic Platform Using a Graphene−Lipid Bilayer Interface. *ACS Nano* **2010**, *4*, 7387–7394.
6. Lvov, Y.; Decher, G.; Möhwald, H. Assembly, Structural Characterization, and Thermal Behavior of Layer-by-Layer

Deposited Ultrathin Films of Poly(vinylsulfate) and Poly(allylamine). *Langmuir* **1993**, *9*, 481–486.

7. Decher, G. Fuzzy Nanoassemblies: Toward Layered Polymeric Multicomposites. *Science* **1997**, *277*, 1232–1237.
8. Novoselov, K. S.; Jiang, D.; Schedin, F.; Booth, T. J.; Khotkevich, V. V.; Morozov, S. V.; Geim, A. K. Two-Dimensional Atomic Crystals. *Proc. Natl. Acad. Sci. U.S.A.* **2005**, *102*, 10451–10453.
9. Geim, A. K.; Novoselov, K. S. The Rise of Graphene. *Nat. Mater.* **2007**, *6*, 183–191.
10. Novoselov, K. S.; Fal'ko, V. I.; Colombo, L.; Gellert, P. R.; Schwab, M. G.; Kim, K. A Roadmap for Graphene. *Nature* **2012**, *490*, 192–200.
11. Cote, A. P.; Benin, A. I.; Ockwig, N. W.; O'Keeffe, M.; Matzger, A. J.; Yaghi, O. M. Porous, Crystalline, Covalent Organic Frameworks. *Science* **2005**, *310*, 1166–1170.
12. Colson, J. W.; Woll, A. R.; Mukherjee, A.; Levendorf, M. P.; Spitler, E. L.; Shields, V. B.; Spencer, M. G.; Park, J.; Dichtel, W. R. Oriented 2D Covalent Organic Framework Thin Films on Single-Layer Graphene. *Science* **2011**, *332*, 228–231.
13. Grill, L.; Dyer, M.; Lafferentz, L.; Persson, M.; Peters, M. V.; Hecht, S. Nano-Architectures by Covalent Assembly of Molecular Building Blocks. *Nat. Nanotechnol.* **2007**, *2*, 687–691.
14. Kissel, P.; Erni, R.; Schweizer, W. B.; Rossell, M. D.; King, B. T.; Bauer, T.; Gotzinger, S.; Schluter, A. D.; Sakamoto, J. A Two-Dimensional Polymer Prepared by Organic Synthesis. *Nat. Chem.* **2012**, *4*, 287–291.
15. Schultz, M. J.; Zhang, X. Y.; Unarunotai, S.; Khang, D. Y.; Cao, Q.; Wang, C. J.; Lei, C. H.; MacLaren, S.; Soares, J.; Petrov, I.; et al. Synthesis of Linked Carbon Monolayers: Films, Balloons, Tubes, and Pleated Sheets. *Proc. Natl. Acad. Sci. U.S.A.* **2008**, *105*, 7353–7358.
16. Bauer, T.; Zheng, Z. K.; Renn, A.; Enning, R.; Stemmer, A.; Sakamoto, J.; Schlüter, A. D. Synthesis of Free-Standing, Monolayered Organometallic Sheets at the Air/Water Interface. *Angew. Chem., Int. Ed.* **2011**, *50*, 7879–7884.
17. Eck, W.; Küller, A.; Grunze, M.; Völkel, B.; Gölzhäuser, A. Freestanding Nanosheets from Crosslinked Biphenyl Self-Assembled Monolayers. *Adv. Mater.* **2005**, *17*, 2583–2587.
18. Turchanin, A.; Beyer, A.; Nottbohm, C. T.; Zhang, X.; Stosch, R.; Sologubenko, A. S.; Mayer, J.; Hinze, P.; Weimann, T.; Gölzhäuser, A. One Nanometer Thin Carbon Nanosheets with Tunable Conductivity and Stiffness. *Adv. Mater.* **2009**, *21*, 1233–1237.
19. Turchanin, A.; Weber, D.; Büenfeld, M.; Kisielowski, C.; Fistul, M. V.; Efetov, K. B.; Weimann, T.; Stosch, R.; Mayer, J.; Gölzhäuser, A. Conversion of Self-Assembled Monolayers into Nanocrystalline Graphene: Structure and Electric Transport. *ACS Nano* **2011**, *5*, 3896–3904.
20. Feng, X.; Pisula, W.; Zhi, L.; Takase, M.; Müllen, K. Controlling the Columnar Orientation of C3-Symmetric "Superbenzenes" through Alternating Polar/Apolar Substitutents. *Angew. Chem., Int. Ed.* **2008**, *47*, 1703–1706.
21. Wagner, C.; Kasemann, D.; Golnik, C.; Forker, R.; Esslinger, M.; Müllen, K.; Fritz, T. Repulsion between Molecules on a Metal: Monolayers and Submonolayers of Hexa-peri-hexabenzocoronene on Au(111). *Phys. Rev. B* **2010**, *81*, 035423.
22. Love, J. C.; Estroff, L. A.; Kriebel, J. K.; Nuzzo, R. G.; Whitesides, G. M. Self-Assembled Monolayers of Thiolates on Metals as a Form of Nanotechnology. *Chem. Rev.* **2005**, *105*, 1103–1169.
23. Zharnikov, M.; Grunze, M. Spectroscopic Characterization of Thiol-Derived Self-Assembling Monolayers. *J. Phys.: Condens. Matter* **2001**, *13*, 11333–11365.
24. Castner, D. G.; Hinds, K.; Grainger, D. W. X-ray Photoelectron Spectroscopy Sulfur 2p Study of Organic Thiol and Disulfide Binding Interactions with Gold Surfaces. *Langmuir* **1996**, *12*, 5083–5086.
25. Kastler, M.; Pisula, W.; Wasserfallen, D.; Pakula, T.; Müllen, K. Influence of Alkyl Substituents on the Solution- and Surface-Organization of Hexa-Peri-Hexabenzocoronenes. *J. Am. Chem. Soc.* **2005**, *127*, 4286–4296.
26. Vericat, C.; Vela, M. E.; Benitez, G.; Carro, P.; Salvarezza, R. C. Self-Assembled Monolayers of Thiols and Dithiols on Gold: New Challenges for a Well-Known System. *Chem. Soc. Rev.* **2010**, *39*, 1805–1834.
27. Matei, D. G.; Muzik, H.; Gölzhäuser, A.; Turchanin, A. Structural Investigation of 1,1′-Biphenyl-4-thiol Self-Assembled Monolayers on Au(111) by Scanning Tunneling Microscopy and Low-Energy Electron Diffraction. *Langmuir* **2012**, *28*, 13905–13911.
28. Zharnikov, M.; Frey, S.; Heister, K.; Grunze, M. Modification of Alkanethiolate Monolayers by Low Energy Electron Irradiation: Dependence on the Substrate Material and on the Length and Isotopic Composition of the Alkyl Chains. *Langmuir* **2000**, *16*, 2697–2705.
29. Turchanin, A.; Käfer, D.; El-Desawy, M.; Wöll, C.; Witte, G.; Gölzhäuser, A. Molecular Mechanisms of Electron-Induced Cross-Linking in Aromatic SAMs. *Langmuir* **2009**, *25*, 7342–7352.
30. Nottbohm, C. T.; Turchanin, A.; Beyer, A.; Stosch, R.; Gölzhäuser, A. Mechanically Stacked 1-nm-thick Carbon Nanosheets: Ultrathin Layered Materials with Tunable Optical, Chemical, and Electrical Properties. *Small* **2011**, *7*, 874–883.
31. Ward, B. W.; Notte, J. A.; Economou, N. P. Helium Ion Microscope: A New Tool for Nanoscale Microscopy and Metrology. *J. Vac. Sci. Technol., B* **2006**, *24*, 2871–2874.
32. Bell, D. C. Contrast Mechanisms and Image Formation in Helium Ion Microscopy. *Microsc. Microanal.* **2009**, *15*, 147–153.
33. Turchanin, A.; El-Desawy, M.; Gölzhäuser, A. High Thermal Stability of Cross-Linked Aromatic Self-Assembled Monolayers: Nanopatterning *via* Selective Thermal Desorption. *Appl. Phys. Lett.* **2007**, *90*, 053102.
34. Kim, K.; Lee, Z.; Regan, W.; Kisielowski, C.; Crommie, M. F.; Zettl, A. Grain Boundary Mapping in Polycrystalline Graphene. *ACS Nano* **2011**, *5*, 2142–2146.
35. Warner, J. H.; Rummeli, M. H.; Gemming, T.; Buchner, B.; Briggs, G. A. D. Direct Imaging of Rotational Stacking Faults in Few Layer Graphene. *Nano Lett.* **2009**, *9*, 102–106.
36. Egerton, R. F.; Malac, M. Improved Background-Fitting Algorithms for Ionization Edges in Electron Energy-Loss Spectra. *Ultramicroscopy* **2002**, *92*, 47–56.
37. Nottbohm, C. T.; Turchanin, A.; Beyer, A.; Golzhauser, A. Direct e-Beam Writing of 1 nm Thin Carbon Nanoribbons. *J. Vac. Sci. Technol., B* **2009**, *27*, 3059–3062.
38. Küller, A.; Eck, W.; Stadler, V.; Geyer, W.; Gölzhäuser, A. Nanostructuring of Silicon by Electron-Beam Lithography of Self-Assembled Hydroxybiphenyl Monolayers. *Appl. Phys. Lett.* **2003**, *82*, 3776–3778.
39. Striemer, C. C.; Gaborski, T. R.; McGrath, J. L.; Fauchet, P. M. Charge- and Size-Based Separation of Macromolecules Using Ultrathin Silicon Membranes. *Nature* **2007**, *445*, 749–753.
40. Zheng, Z.; Nottbohm, C. T.; Turchanin, A.; Muzik, H.; Beyer, A.; Heilemann, M.; Sauer, M.; Gölzhäuser, A. Janus Nanomembranes: A Generic Platform for Chemistry in Two Dimensions. *Angew. Chem., Int. Ed.* **2010**, *49*, 8493–8497.

3.2 Organic nanoparticles: nascent soot analysis

In this study, nascent soot particles are probed by using helium-ion microscopy (HIM) for the first time. It is a joint project with the physical chemistry I department in Bielefeld (Prof. Katharina Kohse-Höinghaus), the group of Prof. Hai Wang (University of Southern California / now Stanford University), and Nils Hansen (Sandia National Laboratories). The physics department in Bielefeld provided skills in HIM and XPS. The samples were prepared by Marina Schenk from the PCI in Bielefeld. The study started with one model ethylene flame,[69] where later the flame conditions[70], see Chapter 3.2.7, and the model fuels[71] were varied.

3.2.1 Introduction

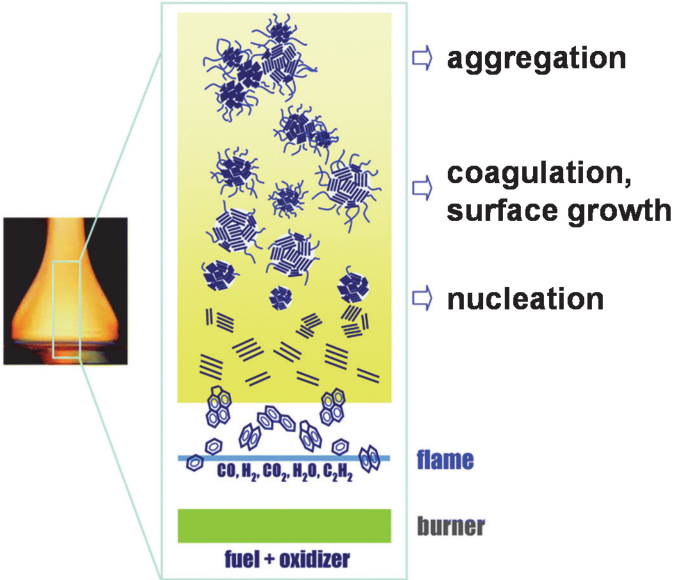

Figure 25: Schematic illustration of soot growth in a flat flame. Stacks of lines represent stacked aromatic structures, and the wiggly lines represents aliphatic components. (Illustration reprinted with permission[72], text on the right side is added to understand the chosen soot sampling heights for HIM and XPS with different stages of soot formation).

Soot is a particulate matter resulting from incomplete combustion processes of hydrocarbons. It is a known human carcinogen,[73] and has considerable negative effect on global climate change.[74] Thus, the understanding of the fundamental growth processes is of high scientific interest. Mature soot is known to consist of aggregates of nearly spherical particles, 20 - 50 nm in diameter, composed of large polycyclic aromatic hydrocarbons (PAHs).[75] The formation of soot in flames starts from the reaction of such PAHs into small particles. Young nascent soot is mostly aromatic in nature. Mass and size of the particles are growing quickly in flames. Experimentally, this nascent soot is difficult to characterize. However, it is this soot that undergoes the most rapid growth in a flame, and is eventually responsible for the emission of particulates into the atmosphere from fossil-fuel combustion. A better understanding of these early growth stages is necessary to identify and fill in the gaps of current kinetic descriptions of soot formation. A detailed review about the current knowledge of soot growth processes was published by Hai Wang in 2011.[72]

A standard method to analyze soot is Transmission Electron Microscopy (TEM), in which the beam penetrates the particle and an underlying support film. This support can reduce the image contrast substantially. In fact, the smallest soot particles detectable trough TEM are usually around 10 nm in diameter.[76,77] Note that an improvement in the signal-to-noise ratio by simply increasing the beam dose is limited by sample damage. The limited image contrast in TEM may be improved in future by new developments like dynamic TEM[78] or by depositing the soot on thinner substrates, e.g. the carbon nanomembranes discussed in a previous Chapter of this work. After the detection of a particle, TEM is then able to reveal the inner structure down to atomic resolution, whereas HIM provides detailed information about the outer shape.

In HIM, SEM, and AFM, imaging is possible on almost all sufficiently flat, bulk surfaces. In comparison, low-voltage SEM provides similar contrast as HIM, but the achievable resolution is substantially lower. AFM can detect particles smaller than 10 nm, but the probe tip is usually larger than the particle size; therefore, the particle image must be geometrically reconstructed with assumptions that are often difficult to verify. Also, fine features on a particle surface cannot be revealed easily in AFM, again owing to the finite tip size. An additional advantage of HIM is the substantially faster imaging process, which allows the investigation of a sufficiently large number of particles for statistical analysis.

3.2.2 **Soot sampling**

Soot sampling was carried out as shown in Figure 26. A premixed, burner-stabilized stagnation-flow flame was used for the production of nascent soot. Samples were probed by thermophoretic sampling, where a cold, flat surface is quickly swiped through the flame. The substrate was affixed on a sample holder mounted on a stepper motor. The exposure time to the flame is typically ~16 ms. We used standard p-doped silicon wafers without further cleaning as substrate for the HIM measurements. To ensure clean substrates, reference samples were measured for each batch. Samples were collected at specific distances from the burner surface, which coincided with the three separate stages of soot formation: nucleation, early mass growth, and aggregation (see Figure 25).

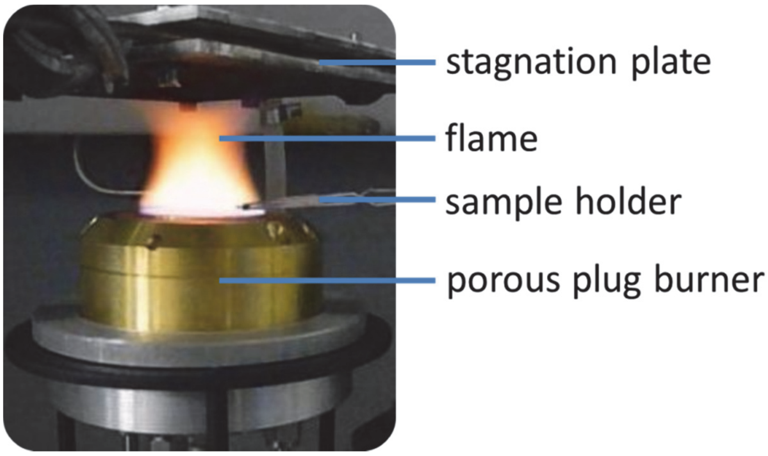

Figure 26: Sampling procedure. Stagnation flow ethylene flame, stabilized on porous plug burner. For the sampling of soot particles, the sample holder is quickly moved through the flame automatically. Reprinted from Supporting Information of [69]*.*

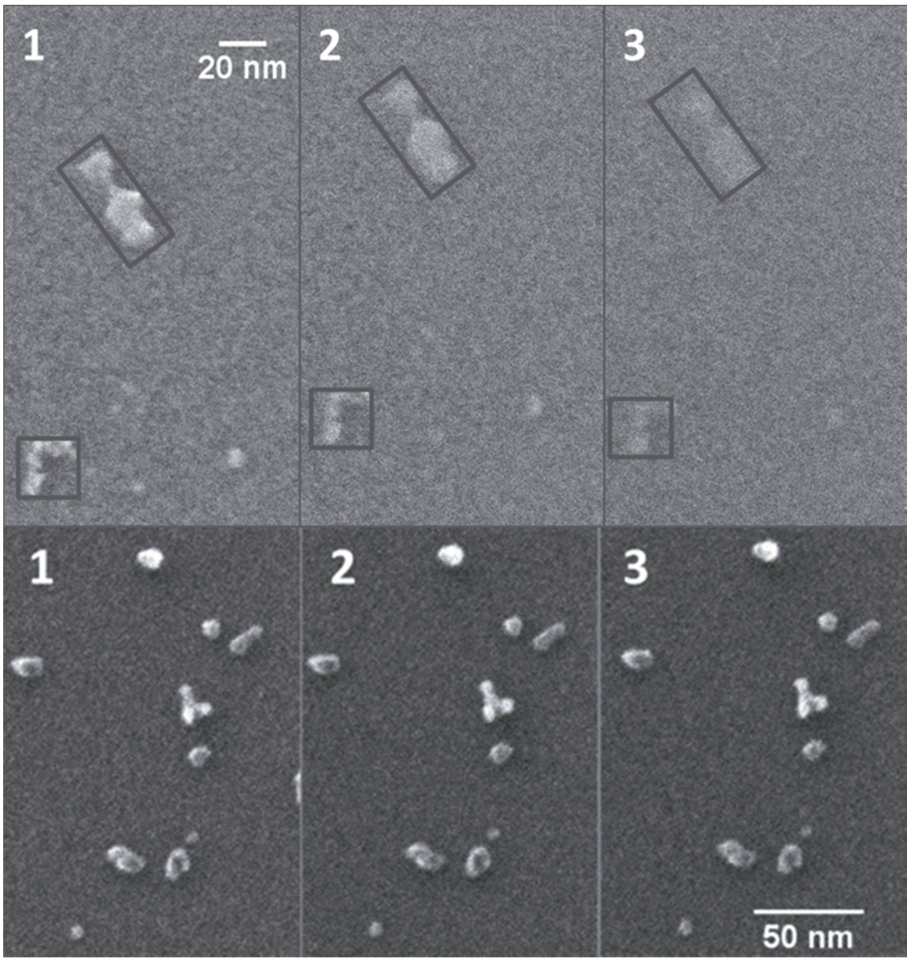

Figure 27: Beam damage evaluation: Series of consecutive HIM images of soot collected from an ethylene C3 flame. Top panels: sample collected at 1.0 cm from the burner surface with an ion dose density of 2182 ions/nm^2*. Bottom panels: sample collected at 0.8 cm from the burner surface and probed by exposing it to an ion dose density of 262 ions/nm*^{2}*. Reprinted with permission.*[69]

3.2.3 Imaging of soot

For HIM imaging of sensitive samples such as nascent soot, the level of damage caused by the probing beam is a crucial parameter. Herein, we discuss the procedures for identifying reliable HIM operating parameters to achieve optimal results. Figure 27 shows consecutive HIM images of two soot samples. The top panels represent images collected with a very high ion dose density of 2182 ions/nm^2 per image. The bottom panel shows consecutive images collected with a lower ion dose density of 262 ions/nm^2.

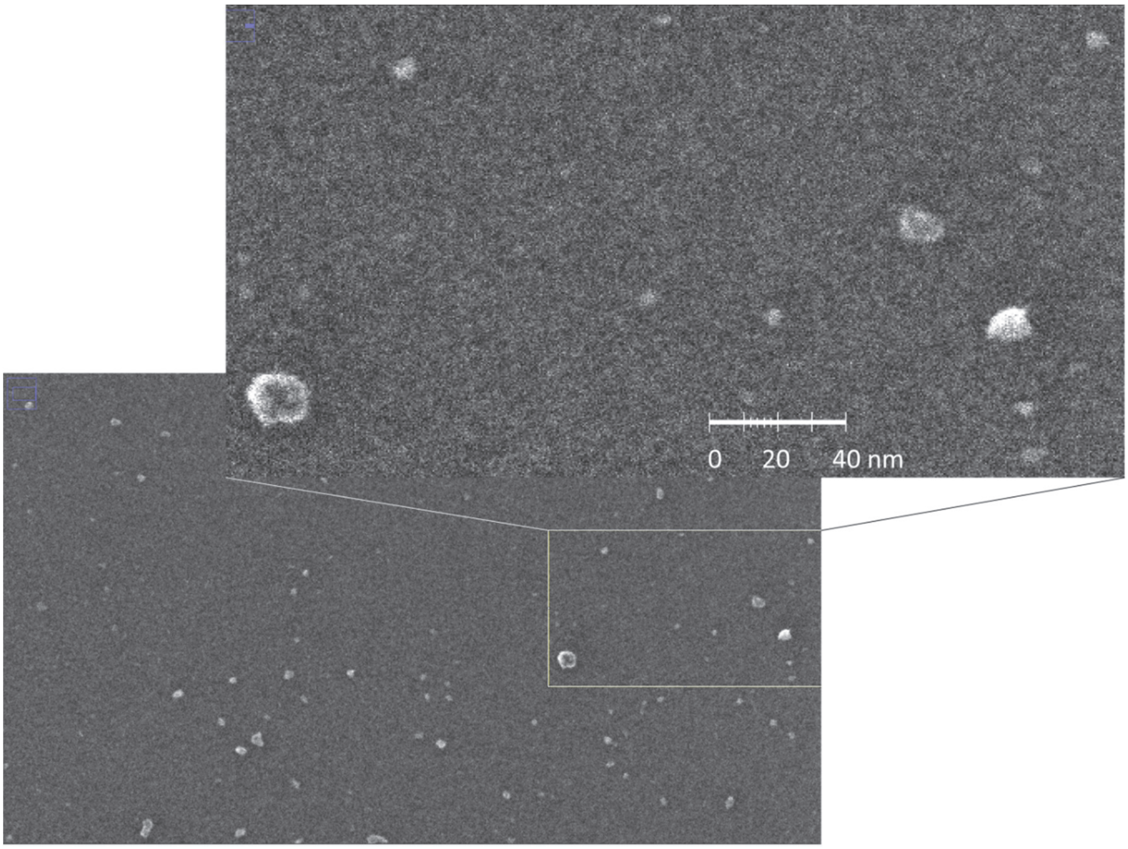

Figure 28: HIM image of soot particles collected at 0.5 cm distance from the burner, showing the capability of the technique for imaging nascent particles of 2-3 nm in size. Reprinted from Supporting Information of [69].

Exposing the samples to the ion beam causes no discernible degradation of the particles. Changes in the contrast were only observed at the higher dosage, but no change in particle size or shape occurred. The observed changes are attributed to condensation of evaporated organics onto the sample. Please note that for the highest doses also substrate swelling is occurring. All these sample modifications occur at higher ion doses than used for the evaluated images. All other images shown are taken from sample positions, which have not been scanned before.

As shown in Figure 28, HIM is able to identify nascent soot particles as small as 2 nm. For larger particles (>5 nm), HIM detects particles with high contrast, allowing for the accurate characterization of both size and morphology.

3.2.4 **Analysis of soot from ethylene flames**

Figure 29 shows typical HIM images of nascent soot, which were collected at the three different heights in the flame. The particle size is growing with the distance from the burner, as the soot has a longer residence time in the flame.

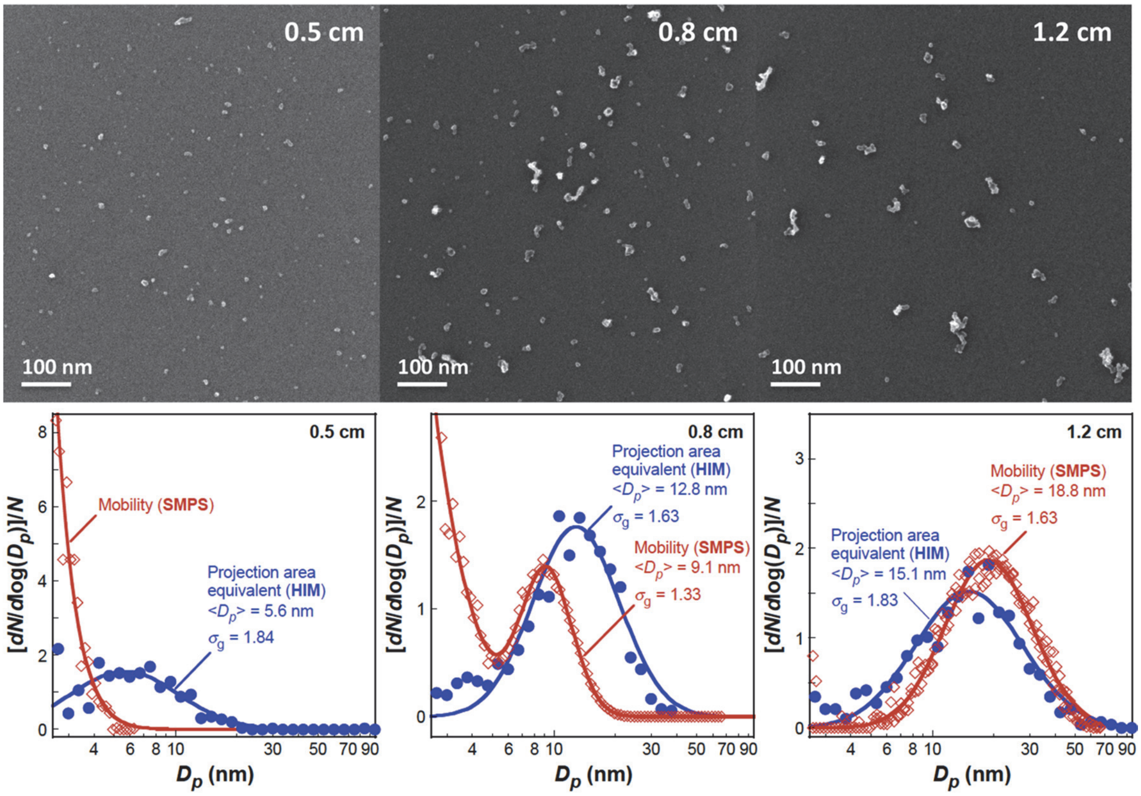

Figure 29: HIM images of nascent soot from an ethylene C3 flame. Particle size and morphology change as a function of the distance from the burner surface. Reprinted with permission.[69]

From these images, primary particle size distributions can be determined from the projected areas of the particles. Distribution functions of the particle size are plotted in Figure 29. They are superimposed by mobility diameter (scanning mobility particle size, SMPS) distributions of the same flame conditions, which were determined in the gas phase in a previous study by Hai Wang and coworkers.[79] The measured physical value is different in both techniques, as SMPS measures the surface area whereas HIM measures the 2D projection (the outline) of a particle. In a following publication, this study was extended to a variety of ethylene flame conditions, see chapter 3.2.7.

To extend the structural knowledge on soot sampled from these flame conditions, XPS was performed with a thicker soot layer (corresponding to a higher number of sweeps in the flame). Carbon and oxygen was found, with O/C ratios of 0.79, 0.44 and 0.31 at 0.5, 0.8 and 1.2 cm respectively. The C1s and O1s spectra are compared in Figure 30, where the C1s signal is fitted with synthetic components for carbon (C-C), hydroxyl (C-O), carbonyl (C=O) and carboxyl (O-C=O) oxidized species. Consistently, more oxidized species are visible at higher measured oxygen content. Only one species for aromatic and aliphatic carbon was used, as these species have only a small difference in binding energy. Vander Wal and coworkers[80] analyzed sp^2/sp^3 ratios from the C1s signal of several different soot samples. Unfortunately, slight changes in the fitting parameters had drastic effects on the resulting sp^2/sp^3 ratio, an effect also other researchers documented.[81] The high oxygen content in the samples is generally not expected from literature.[82] Caused by the sampling method, the soot is inevitably exposed to oxygen from air where the oxidation of the soot could take place. This would indicate a high reactivity of the early soot samples.

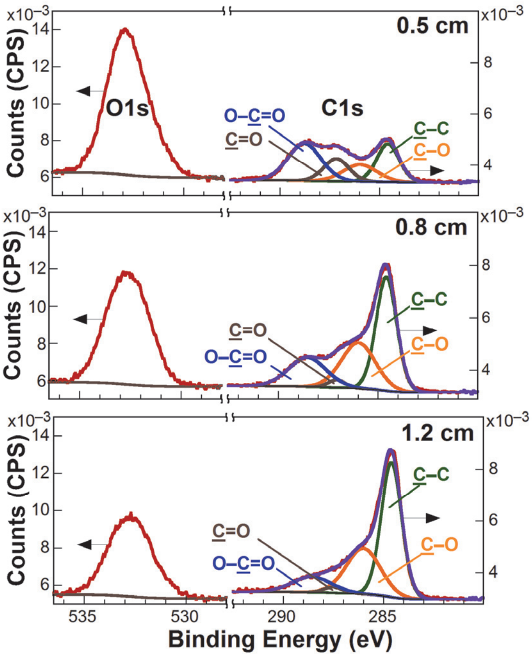

Figure 30: The carbon and oxygen XPS spectra of soot sampled from Flame C3 at distances of 0.5, 0.8 and 1.2 cm from the burner surface. Reprinted with permission.[69]

An additional unique strength of HIM is its ability to probe size and morphology of particles at the same time and at sizes that have previously been impossible. Figure 31 shows morphological variations of soot sampled in different heights. Particles sampled at 0.5 cm from the burner surface are spheroidals with a characteristic size of less than 10 nm. At 0.8 cm from the burner surface, a notable number of aggregated particles are observed, although the number of apparent spheroids exceeds that of aggregates, and the apparent primary particle diameter is around 10 nm. Images obtained at 1.2 cm from the burner show that the primary particles have grown to around 20 nm, and the number of aggregates greatly exceeds the number of primary particles.

In chapter 3.2.7 the morphology of soot from the ethylene flames is discussed and analyzed in terms of sphericity, circularity, and fractal dimension. The parameters do not vary much over the collected samples, but a comparison to representative real particle shapes indicates that the nascent soot particles have no simple or general shape.

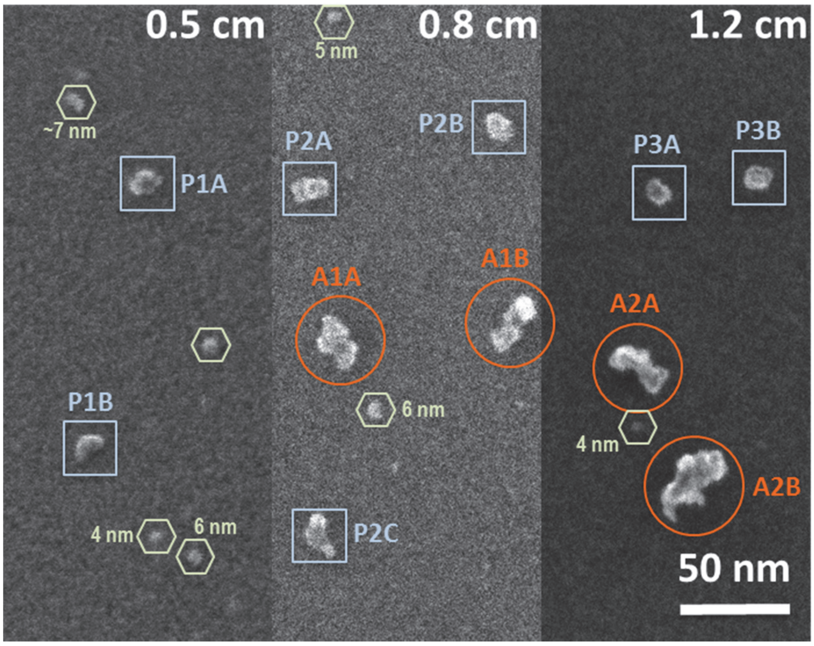

Figure 31: Morphological variations of nascent soot collected from the ethylene C3 flame at heights of 0.5, 0.8 and 1.2 cm and imaged by HIM, showing representative primary and aggregate structures. Particles shown in the hexagons are in the apparent size range of 4-8 nm; those in the squares are 14-18 nm. Particles shown in the circles are apparent aggregates. Reprinted with permission.[69]

3.2.5 **Imaging of soot from different C_4 fuels**

To analyze the influence of the fuel chemistry on the soot morphology the following C_4 fuels were analyzed: n-butane, i-butane, i-butene, and i-butanol.

HIM micrographs of soot from n-butane, i-butane, i-butene are very similar, thus, Figure 32 compares HIM micrographs of only n-butane and i-butanol. In both flames, relatively small particles with sizes smaller than 10 nm are deteced. However, the structure of the aggregates differs notably. The soot from i-butanol is at the lower height of 0.8 cm close to the detection limit, whereas the n-butane flame is already producing branched structures. Soot from i-butanol is almost spherical whereas n-butane soot is agglomerating to bigger structures.

This difference might indicate an influence of the fuel structure on the morphology of nascent soot particles. This could be caused by the different C/O ratios or the chemical structure of the fuel itself.

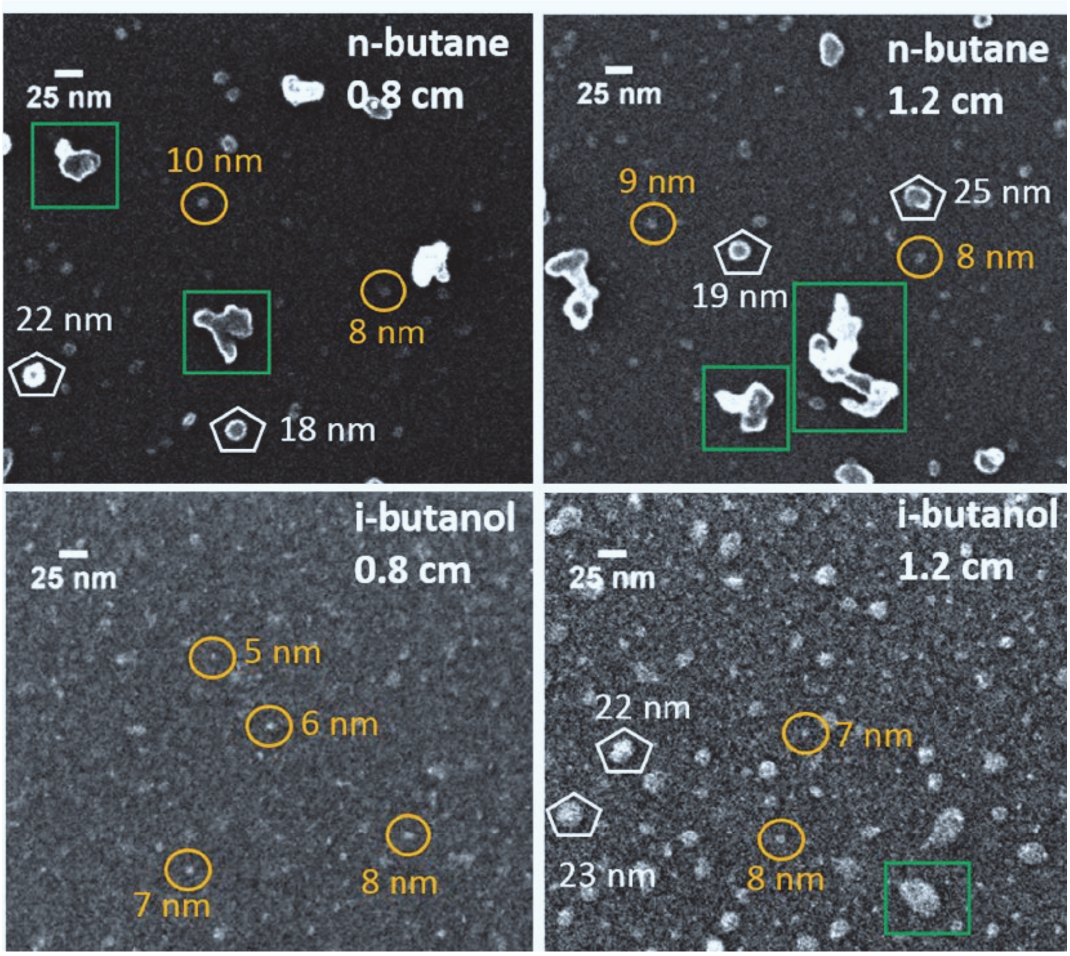

Figure 32: HIM micrographs for soot probed from atmospheric-pressure flames of n-butane (upper row) and i-butanol (bottom). For near-spherical particles (circles and pentagons), the diameter is given. Reprinted with permission.[71]

3.2.6 **Summary: imaging of nascent soot**

For imaging of soot, the HIM yields images with exceptional contrast even for smallest nanoparticles. This allows the unambiguous recognition of smaller nascent soot particles than those observed in previous electron microscopy studies. The results indicate that HIM is ideal for rapid and reliable probing of the morphology of nascent soot. Particles as small as 2 nm are detectable, with surface details of soot visible down to approximately 5 nm. The results also show that nascent soot is structurally inhomogeneous, and even the smallest particles can have shapes that deviate notably from a perfect sphere.

3.2.7 Publication: Morphology of nascent soot in ethylene flames (PROCI 2014)

This Chapter is reprinted with permission from Elsevier. The original article appeared as:

> Schenk, M.*, Lieb, S.*, Vieker, H.*, Beyer, A., Gölzhäuser, A., Wang, H., Kohse-Höinghaus, K., 2014. Morphology of nascent soot in ethylene flames. Proceedings of the Combustion Institute. doi:10.1016/j.proci.2014.05.009.
>
> *: These authors contributed equally to this work.

Contribution:

Helium Ion Microscopy and X-Ray Photoelectron Spectroscopy was performed by the author.

Available online at www.sciencedirect.com
ScienceDirect
Proceedings of the Combustion Institute xxx (2014) xxx–xxx
ELSEVIER
Proceedings of the Combustion Institute
www.elsevier.com/locate/proci

Morphology of nascent soot in ethylene flames

Marina Schenk [a,1], Sydnie Lieb [b,1], Henning Vieker [c,1], André Beyer [c], Armin Gölzhäuser [c], Hai Wang [d,*], Katharina Kohse-Höinghaus [a,*]

[a] *Department of Chemistry, Bielefeld University, Universitätsstraße 25, D-33615 Bielefeld, Germany*
[b] *Department of Aerospace and Mechanical Engineering, University of Southern California, Los Angeles, CA 90089, USA*
[c] *Department of Physics, Bielefeld University, Universitätsstraße 25, D-33615 Bielefeld, Germany*
[d] *Department of Mechanical Engineering, Stanford University, Stanford, CA 94305-3032, USA*

Abstract

Because of their significant impact on climate, environment and health, reducing the emission of soot from combustion processes remains a problem that requires detailed understanding of its formation as well as of the principles that govern how the result in terms of size, morphology, and chemical reactivity of soot particles depends upon the formation process. Especially very small, below ten nanometer-sized, particles in the early stages of the soot nucleation process are interesting targets for more detailed inspection, to reveal useful insight and to guide further model development. In this study, Helium-ion microscopy (HIM) is applied as an imaging technique new to combustion studies to analyze the morphology of soot particles >2 nm and to determine their geometrical characteristics. For this analysis, a series of premixed ethylene flames are investigated. Mobility size measurements from an earlier investigation have been compared with the particle sizes determined by HIM. Observed particle shapes and geometrical statistics suggest that in all flames under investigation, nascent soot possesses no well-defined morphologies. Additionally, investigations have been made using X-ray photoelectron spectroscopy (XPS) to obtain more information on the chemical characteristics of these particles.

Keywords: Soot particles; Morphology; Imaging; Geometric properties; Chemical composition

1. Introduction

As by-product of fuel combustion, flame-generated carbon nanoparticles, soot, can negatively impact global climate, air quality, and human health [1–3]. Recent studies have shown that endothelial cells treated with flame-generated carbon nanoparticles exhibit increased tendency of cell death [4]. The toxicity of flame soot appears to increase with oxidation in the ambient air [5]. Uncertainties about the properties and amounts of combustion soot continue to impact our understanding of its climate effects [6]. Clearly, detailed knowledge about the properties and reactivities of soot is useful to develop formation-predictive

---

* Corresponding authors. Fax: +1 650 497 1748 (H. Wang), +49 521 106 6027 (K. Kohse-Höinghaus).
E-mail addresses: haiwang@stanford.edu (H. Wang), kkh@uni-bielefeld.de (K. Kohse-Höinghaus).

[1] These authors contributed equally to this work.

http://dx.doi.org/10.1016/j.proci.2014.05.009
1540-7489/© 2014 The Combustion Institute. Published by Elsevier Inc. All rights reserved.

Please cite this article in press as: M. Schenk et al., *Proc. Combust. Inst.* (2014), http://dx.doi.org/10.1016/j.proci.2014.05.009

models and to understand the effects of soot emission.

Information about morphology and chemical composition of nascent soot is critical to a description of the surface area and the kinetics of surface reactions [7,8]. Earlier studies show mature soot to consist of aggregates of primary particles 20–40 nm in diameter [9], though more recent studies show primary particles as small as 10 nm probably because of improved microscopy resolution. Primary particles are nearly spherical and composed of polycyclic aromatic hydrocarbons (PAHs) arranged in a turbostratic manner [10–12]. These particles form from coalescence or reaction with PAHs, mass growth by surface reactions and size growth by coagulation [13]. In the later stage of particle growth, primary particles coagulate into aggregates [9,14]. It was thought that the coalescent growth of primary particles is the result of viscous forces among coalescing particles upon contact (see e.g. [15]). Carbonization solidifies them in a later stage; and the coagulation of solidified particles produces fractal aggregates [16]. Through Monte Carlo simulations, Frenklach and co-workers [17–19] advanced an alternative explanation for the morphological evolution of soot in flames. They proposed that aggregation starts as soon as particles nucleate out of the gas phase. The apparent sphericity of the primary particles may be explained by collision and aggregation with freshly nucleated, smaller "collector" particles. Indeed the size distribution of nascent soot is generally bimodal (e.g., [20,21]); the collector particles derive from the small-size mode in the bimodal distribution. The surface reaction smooths the particle surface. Hence, particle morphology is intimately related to the nucleation rate and surface deposition of the collector particles. Such theoretical results have been considered in models of soot formation (e.g. Ref. [22]), yet experimental verification remains unavailable.

Recently, Helium-ion microscopy (HIM) was used to probe the morphological and size evolution of nascent soot. Compared to electron microscopy, HIM allows for better contrast and surface sensitivity, and soot particles as small as 2 nm could be recognized [23]. The results show that soot collected in a burner-stabilized ethylene flame exhibits quite irregular shapes and structures even for those just a few nanometers in size, suggesting that some degree of aggregation starts as soon as soot nucleates, as predicted by simulation earlier [18]. Moreover, no distinctive transition was observed showing the primary-aggregate transition. In fact, particle geometric properties, including sphericity and fractal dimension, exhibit no distinctive, sudden change with particle size.

Here, we seek to provide additional evidence to understand the previous observations for a wide range of flames. Specifically, HIM analysis was extended to soot formed in a set of canonical ethylene flames studied previously, in which the flame temperature was adjusted systematically [24]. Additionally, an eventual relation between morphological variations of nascent soot and its composition is explored through a preliminary X-ray photoelectron spectroscopy (XPS) analysis. The question is motivated by recent findings that young [7,8] and mature soot [25] exhibits structural and compositional complexities which are not clearly understood. For example, soot microstructure varies with flame chemistry [11,26,27]. Raman spectroscopy shows that ~2 nm particles from premixed ethylene flames just above the critical sooting limit contain amorphous carbon with very little ordering of graphitic planes [28]. Increasing evidence shows that both young and mature soot can contain considerable sp^3 carbon and oxygenates (see e.g. [29–33]), and the sp^3 carbon appears to be matrix-bound [33]. Clearly, these structural and compositional variations, along with morphological changes, must impact soot surface chemistry in a way that currently is not well understood.

2. Experimental

Soot particles were probed from four burner-stabilized ethylene flames (burner diameter 5 cm) with the same composition but different cold gas velocities, as shown in Table 1. These flames were previously characterized in terms of Particle Size Distribution Function (PSDF) by Scanning Mobility Particle Sizing (SMPS) [24].

Soot particles were sampled thermophoretically by motor-controlled rapid insertion of a substrate into the flame zone [24,34]. The samples were collected at three heights for each flame. Substrate choice was made according to the respective analysis technique (see Supplemental material). The freshly deposited particles were examined by HIM (Carl Zeiss Orion Plus), where a fine beam of helium ions was scanned over a surface, and the emitted secondary electrons were detected [35,36]. Complementary to HIM, Atomic Force Microscopy (AFM) was used for a small number of samples. AFM (Vecco Multimode V) was operated in tapping mode to examine the interaction of the particle with the substrate.

Geometric analysis of approximately 50 particles from the HIM results was performed using ImageJ [37] with the Fraclac plugin to calculate the particle perimeter, area, diameter of a circle which fully encloses the particle, and the fractal dimension as determined by a box-counting method. The analysis requires a defined particle outline (see Supplemental material). In many cases the resolution of the image was not sharp enough to provide this outline. Instead the particles were carefully traced and the traced outline

Please cite this article in press as: M. Schenk et al., *Proc. Combust. Inst.* (2014), http://dx.doi.org/10.1016/j.proci.2014.05.009

Table 1
Summary of flames studied (C_2H_4: 16.3%, O_2: 23.7%, Ar: 60%). See [24] for details.

Flame No.	Cold gas velocity v_0 (cm/s)[a]	Maximum flame temperature T_f (K)
C1	13	1898 ± 50
C2	10	1805 ± 50
C3	8	1736 ± 50
C5	5.5	1660 ± 50

[a] 298 K and 1 atm.

Table 2
Geometric parameters of representative particles shown in Fig. 7.

Label	Sphericity	Circularity
P1	0.58	24.1
P2	0.61	25.9
P3	0.67	16.4
P4	0.59	22.8
P5	0.70	17.5
P6	0.52	37.2
P7	0.74	14.8

was used for the analysis. Some error may be introduced into the value of the geometric parameters by this procedure. The error was estimated to be at most 10% on the geometric parameters.

Additionally, XPS was used to obtain information on the surface composition of the soot. This surface-sensitive analytical technique uses a monochromatic X-ray beam to eject electrons from the top 1–10 nm of the sample surface. XPS was carried out in a multi-technique UHV instrument (Multiprobe, Omicron Nanotechnology) using monochromatic Al Kα radiation (for details, see Supplemental material).

3. Results and discussion

Representative images of soot particles are presented in Fig. 1. These samples were collected from Flame C2 at 0.55, 0.95, and 1.2 cm above the burner surface, which correspond roughly to the three stages of soot formation: nucleation, mass growth through surface reactions, and size growth due to aggregation. Despite the grainy background, the smallest discernible particles are ~2–3 nm in size. The four flames differ in the maximum flame temperature (see Table 1). From Flame C1 to C5, the linear velocity and thus the flame temperature decreases. At 1 cm from the burner surface, the volume fraction of soot peaks in Flame C3 [24]. Compared to Flame C3, the size and mass growth is limited by the kinetic rate in lower temperature flames, while the particle growth is limited by shorter convective time and kinetic reversibility in higher temperature flames [24].

The particle size distribution may be determined from HIM images as discussed in [23]. Figure 2 compares the HIM diameter distributions with the mobility diameter distributions taken earlier [24]. Note that the definitions of the two diameters are different. In the large Knudsen number limit where mobility measures the surface area of a particle freely suspended in a gas, the diameter was calculated by assuming spherical particle shape. For HIM size distribution, the diameter is a measure of the size of a circle of area equal to that of 2-D projection of a substrate-deposited particle, which can be of irregular shape and/or undergo shape distortion due to sample–substrate interaction [23].

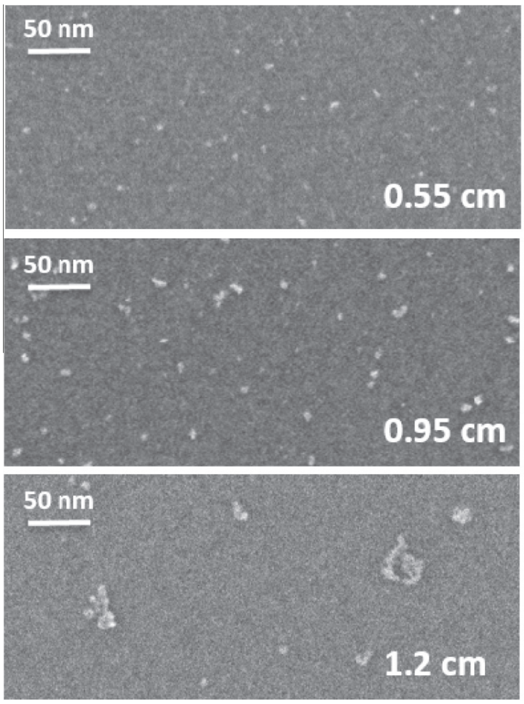

Fig. 1. Typical HIM images of soot particles probed from Flame C2 (additional images of Flames C1, C2 and C5 are presented in the Supplemental material and those of Flame C3 in the Supporting information of [23]).

To illustrate one possible interaction, Fig. 3 shows an AFM image of a soot particle (3–4 nm) compared to a TiO_2 particle of comparable size. TiO_2 is considerably more rigid than nascent soot, and is not expected to interact with the substrate upon impaction as much as soot. Because of finite probe-tip size (19 nm radius), the apparent AFM shape of a spherical particle is a spherical top [38]. The AFM height profile of the TiO_2 particle is closely characterized by an idealized spherical model (solid and dashed lines in the bottom panel of Fig. 3). For the soot particle, the modeled curve traces closely with the center of the height profile, but the rim around the center cannot be modeled and is indicative of the spread of a soft particle upon impact with the substrate – an effect that has been observed previously [23,24,38]. For this

Please cite this article in press as: M. Schenk et al., *Proc. Combust. Inst.* (2014), http://dx.doi.org/10.1016/j.proci.2014.05.009

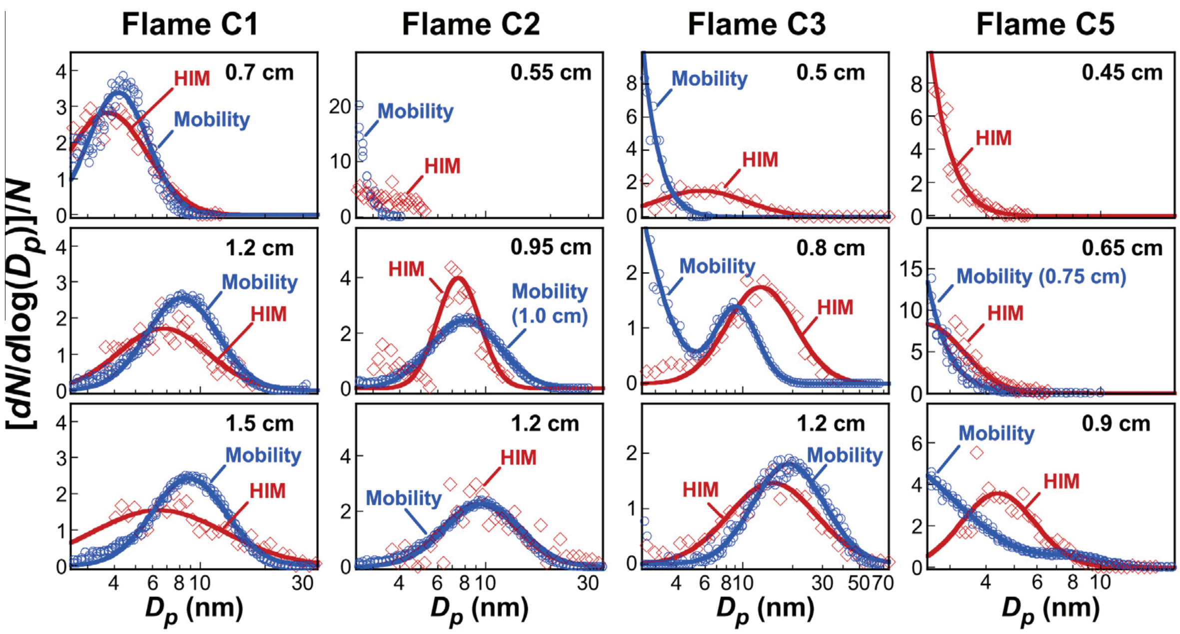

Fig. 2. Comparison of particle size distributions measured by a scanning mobility sizer and Helium-ion microscopy of between 280 and 1351 particles.

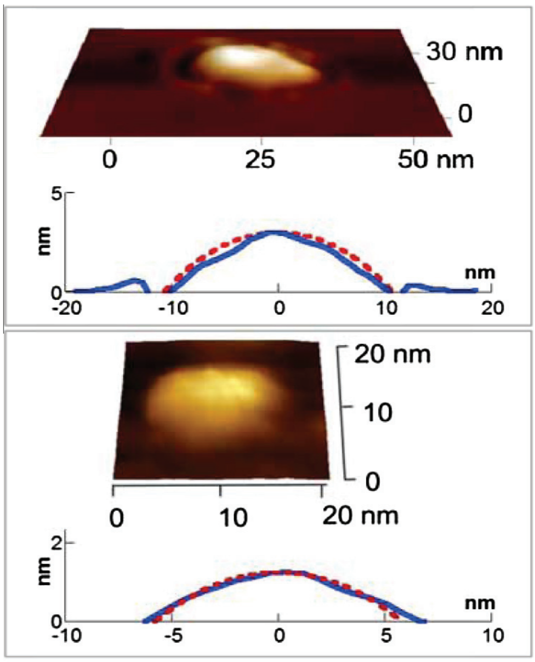

Fig. 3. AFM image and height profile (solid line: experiment; dashed line: modeled) of a representative soot particle sampled from Flame C3 at 0.7 cm distance from the burner surface (top panel) and a TiO_2 particle (bottom panel, [38]).

reason, the interpretation of HIM images requires caution especially for particles of just a few nanometers in diameter. Likewise, the mobility size measurement can be impacted by the assumption about particle sphericity and the effect of a rough, nonhomogeneous surface on charge equilibrium.

Despite the aforementioned problem, the HIM and mobility size distributions compare favorably, especially when the median particle diameter is around 10–20 nm. For smaller particles, HIM measures consistently larger particle size than mobility; for Flame C5, which has the lowest temperature, HIM is unable to reproduce the small-particle branch of the PSDF suggested by the mobility measurement. Probable causes include sample spread on the substrate and/or a lower thermophoretic velocity [39] and thus sampling efficiency for small particles.

Interestingly, the HIM micrographs show irregular shapes for particles in almost the entire size range (see Fig. 4). The shape irregularity is prevalent even for 10 nm or smaller particles and for all flames probed at nearly all positions. The morphological characteristics contrast to the notion of spherical primary particles. In fact, most particles, many of which feature sizes smaller than 10 nm, are aggregates, an observation that supports the theory discussed earlier [17–19]. Previous TEM studies showed that young soot particles ~20 nm in size are loosely coalesced doublets, triplets and multiplets [40], but the poor contrast provided little information about smaller particles. The current result also raises questions about the interpretation of the mobility diameter, since the aggregate structure can lead to an increase in the particle surface area – this issue deserves further study.

The morphology of the soot particles in Fig. 4 may be analyzed by several geometrical parameters. The circularity C is the ratio of the perimeter squared (P_p^2) to the 2D projected area (A_p) [41]:

Please cite this article in press as: M. Schenk et al., *Proc. Combust. Inst.* (2014), http://dx.doi.org/10.1016/j.proci.2014.05.009

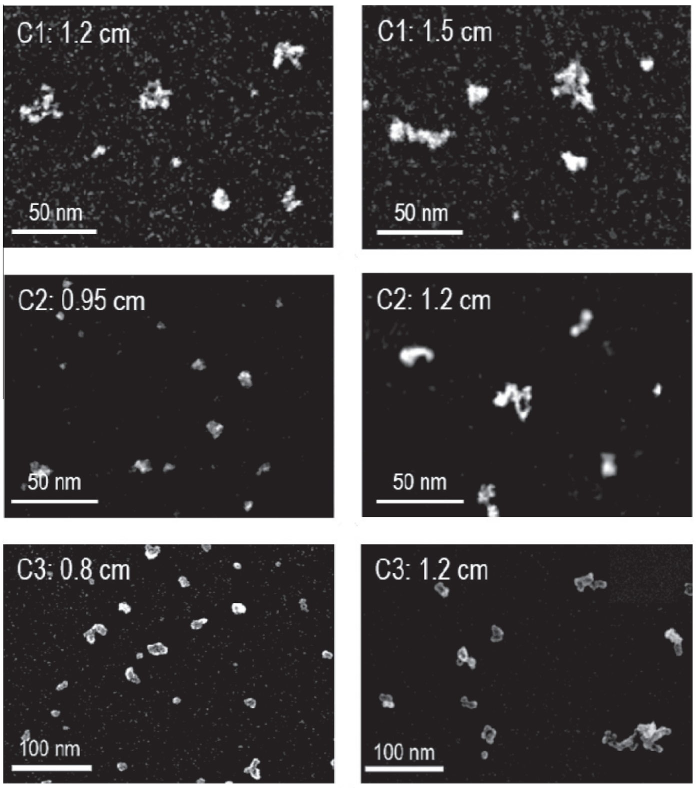

Fig. 4. Representative morphology of soot particles probed from Flames C1, C2 and C3.

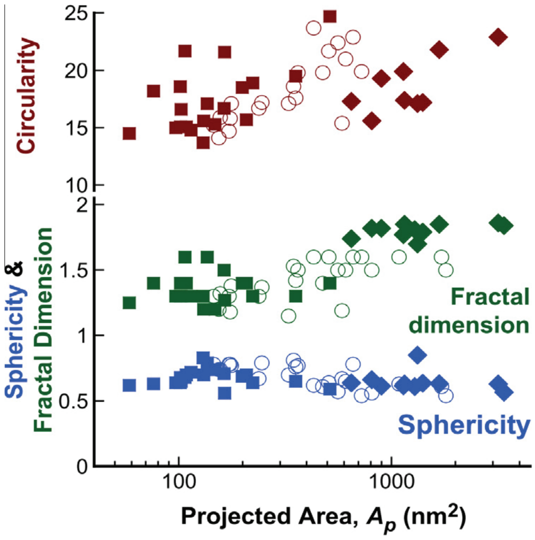

Fig. 5. Sphericity, circularity, and fractal dimension of particles probed from Flames C1 (diamonds, current work), C2 (squares, current work) and C3 (circles, published in [23]).

$C = P_p^2/A_p$. It measures the geometric compactness. A circular structure has the smallest C value, while a rectangular structure with a large aspect ratio gives a large C value. The sphericity Φ compares the ratio of the circle-area equivalent diameter (D_A) to the diameter of a circle that encloses the particle (D_C) [41]: $\Phi = D_A/D_C$. A perfect circle would have $\Phi = 1$ while a line has $\Phi = 0$. The fractal dimension, D_f, is calculated with the box-counting technique [23,42].

Figure 5 shows the variation of these parameters as a function of 2D projected area of the particles. The sphericity varies from 0.5 to 0.75 and shows no dependency on particle size. The circularity shows a minor dependency on the particle size, but this dependency is weaker than the spread of the circularity. For the particles meas-ured, the C values range from ~15 to 25. The fractal dimension ranges from 1.2 to 1.8, with a mild dependency on the particle size. It should be noted that there are two methods to describe the overall fractal dimension for a set of particles: individual and collective. In the current study we measured the fractal dimension of individual particles as in Köylü et al. [43]. The upper range of the D_f value is in agreement with their TEM ana-lysis of 12–26 nm particles from a counterflow methane flame. The D_f value of 2.15 ± 0.1 of Maricq and Xu [44] by combined mobility-aerodynamic analysis of particles from a burner-stabilized ethylene flame is larger than our values. The discrepancy is expected considering that mobility experiments measure mass fractal, whereas HIM and TEM measure the perimeter fractals [45] or the ruggedness of the particle edge. Particularly interesting is the lack of sudden transition in the D_f value of individual particles over the

Please cite this article in press as: M. Schenk et al., *Proc. Combust. Inst.* (2014), http://dx.doi.org/10.1016/j.proci.2014.05.009

entire range of particle size probed, indicating that there is no distinctive transition from spherical primary particles to aggregates.

For a better understanding of the geometric parameters, Fig. 6 presents the correlation between circularity and sphericity of soot particles meas-ured along with several representative shapes. The data appears to be bound between those of a linear array of 1 to 3 circles and ellipses of width-to-height ratio ranging from 1/1 (a circle) to 4/1. Combined with the mild dependency of the circularity on particle size, it may be concluded that the smaller particles have a greater tendency to assume the oval shape while larger particles tend to assume shapes that are irregular. The observed similarity in sphericity and circularity values across the particles and flames is not an indication that the particles have any well-defined shape. Rather, the geometry is uniformly irregular and neither spherical nor chain-like, as illustrated in Fig. 7.

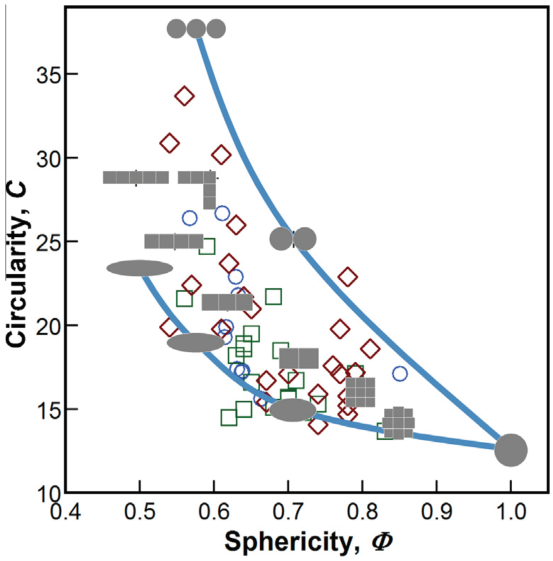

Fig. 6. Circularity versus sphericity for nascent soot and several model geometries.

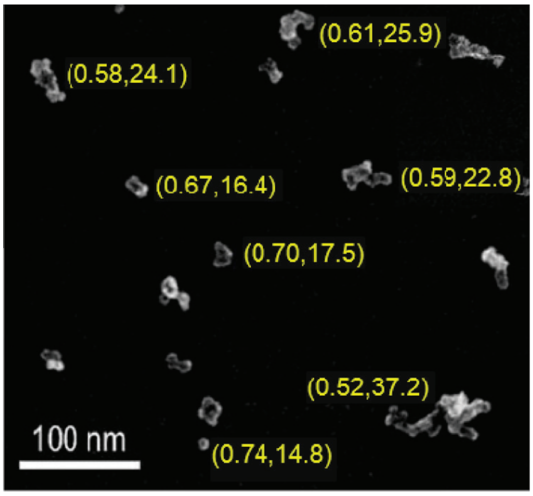

Fig. 7. Representative image of particles from Flame C3 at a distance of 1.2 cm above the burner surface with corresponding geometric parameters shown in Table 2.

The XPS spectra in Fig. 8 compare the evolution of the C1s and O1s peaks of soot samples collected in Flame C3. The results show a decrease in the O/C ratio (0.79, 0.44 and 0.31 at 0.5, 0.8 and 1.2 cm respectively) and a consistent C1s peak with a lower oxygen-related contribution to the total signal for samples at larger distances from the burner surface. Fitting of the C1s peak was done with only one species for aromatic and aliphatic carbon, as these species have only a small difference in binding energy. Vander Wal and coworkers [32] analyzed sp^2/sp^3 ratios from the C1s signal of several different soot samples. We found that slight changes in the fitting parameters can have drastic effects on the resulting sp^2/sp^3 ratio. Similar observations are reported elsewhere [46]. Compared to microFTIR results [30], where the soot samples were collected from the same flame, but using a probe and nitrogen dilution instead of thermophoretic sampling, the XPS results discussed here suggest a higher O/C ratio. As the soot samples were exposed to ambient air after thermophoretic collection, this may hint at a high reactivity of the particles extracted from the flame and thus a higher susceptibility to oxidation for the smaller particles collected closer to the particle nucleation zone.

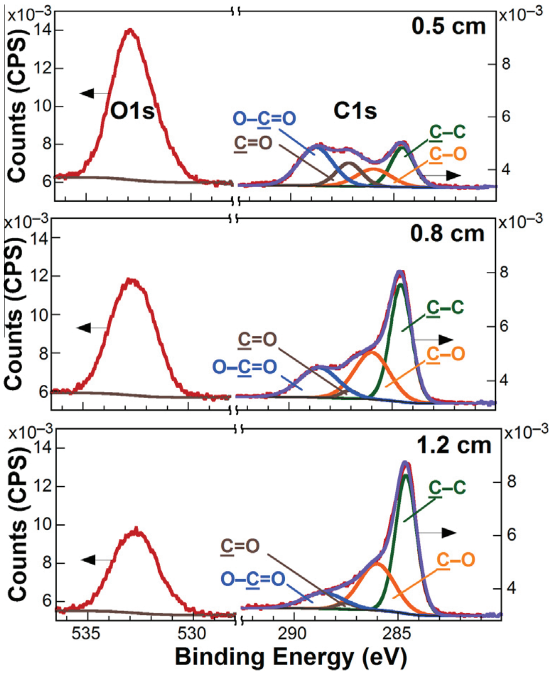

Fig. 8. The carbon and oxygen XPS spectra of soot samples from Flame C3 at 0.5, 0.8 and 1.2 cm from the burner surface. The C1s peak is fitted with synthetic components for carbon (C—C), hydroxyl (C—O), carbonyl (C═O) and carboxyl (O—C═O).

Please cite this article in press as: M. Schenk et al., *Proc. Combust. Inst.* (2014), http://dx.doi.org/10.1016/j.proci.2014.05.009

4. Summary and conclusion

Helium-ion microscopy was used to probe nascent soot particles. Because of its relatively soft interaction with the sample and high sensitivity, resolution, and contrast, this technique is reliable to analyze carbon structures of <10 nm dimension. Using HIM, morphological variations of thermophoretically-collected nascent soot samples were examined for a number of well-characterized, premixed ethylene flames at the same stoichiometry but different flame temperatures. Size distributions obtained from HIM are found in favorable agreement with previous mobility measurements. The images taken for soot collected from different heights (i.e. growth times) were analyzed with respect to their geometrical parameters, specifically circularity, sphericity, and fractal dimension. While variations of these parameters over the collected samples are not large, comparison with representative real particle shapes and illustrative simple geometrical shapes indicates that nascent particles in these flames have no well-defined shape. This is consistent with a conceptual assumption that particles are not spherical at their origin, but that lesser-defined structures arise at all phases of the nucleation and early growth process. There is some consistency between the evidence that soot particles as probed with AFM are softer than equivalent-sized TiO_2 particles, and that the reactivity of the surface of small soot particles with oxygen appears to be larger at earlier growth stages as observed with XPS.

Acknowledgments

Work at Stanford and USC was supported by the Combustion Energy Frontier Research Center (CEFRC), an Energy Frontier Research Center funded by the U.S. Department of Energy, Office of Science, Office of Basic Energy Sciences under Award Number DE-SC000119.

Appendix A. Supplementary data

Supplementary data associated with this article can be found, in the online version, at http://dx.doi.org/10.1016/j.proci.2014.05.009.

References

[1] T.C. Bond, S.J. Doherty, D.W. Fahey, et al., *J. Geophys. Res. Atmos.* 118 (2013) 5380–5552.
[2] B. Frank, M.E. Schuster, R. Schlögl, D.S. Su, *Angew. Chem. Int. Ed.* 52 (2013) 2673–2677.
[3] J.S. Lighty, J.M. Veranth, A.F. Sarofim, *J. Air Waste Manag. Assoc.* 50 (2000) 1565–1618.
[4] P. Pedata, N. Bergamasco, A. D'Anna, et al., *Toxicol. Lett.* 219 (2013) 307–314.
[5] A.L. Holder, B.J. Carter, R. Goth-Goldstein, D. Lucas, C.P. Koshland, *Atmos. Pollut. Res.* 3 (2012) 25–31.
[6] M.O. Andreae, V. Ramanathan, *Science* 340 (2013) 280–281.
[7] A. D'Anna, *Proc. Combust. Inst.* 32 (2009) 593–613.
[8] H. Wang, *Proc. Combust. Inst.* 33 (2011) 41–67.
[9] B.S. Haynes, H.Gg. Wagner, *Prog. Energy Combust. Sci.* 7 (1981) 229–273.
[10] J.B. Donnet, *Carbon* 20 (1982) 267–282.
[11] R.L. Vander Wal, A.J. Tomasek, *Combust. Flame* 134 (2003) 1–9.
[12] R.L. Vander Wal, *Combust. Flame* 112 (1998) 607–616.
[13] M. Frenklach, *Phys. Chem. Chem. Phys.* 4 (2002) 2028–2037.
[14] H.F. Calcote, *Combust. Flame* 42 (1981) 215–242.
[15] G. Prado, J. Jagoda, K. Neoh, J. Lahaye, *Proc. Combust. Inst.* 18 (1981) 1127–1136.
[16] R.A. Dobbins, *Combust. Flame* 130 (2002) 204–214.
[17] P. Mitchell, M. Frenklach, *Proc. Combust. Inst.* 27 (1998) 1507–1514.
[18] M. Balthasar, M. Frenklach, *Proc. Combust. Inst.* 30 (2005) 1467–1475.
[19] P. Mitchell, M. Frenklach, *Phys. Rev. E* 67 (2003) 61407.
[20] B. Zhao, Z. Yang, M.V. Johnston, et al., *Combust. Flame* 133 (2003) 173–188.
[21] L.A. Sgro, A. De Filippo, G. Lanzuolo, A. D'Alessio, *Proc. Combust. Inst.* 31 (2007) 631–638.
[22] R.I.A. Patterson, M. Kraft, *Combust. Flame* 151 (2007) 160–172.
[23] M. Schenk, S. Lieb, H. Vieker, et al., ChemPhysChem 14 (2013) 3248–3254.
[24] A.D. Abid, N. Heinz, E.D. Tolmachoff, D.J. Phares, C.S. Campbell, H. Wang, *Combust. Flame* 154 (2008) 775–788.
[25] R.L. Vander Wal, V.M. Bryg, M.D. Hays, *Aerosol Sci.* 41 (2010) 108–117.
[26] R.L. Vander Wal, A. Strzelec, T.J. Toops, C.S. Daw, C.L. Genzale, *Fuel* 113 (2013) 522–526.
[27] C. Han, Y. Liu, J. Ma, H. He, *J. Chem. Phys.* 137 (2012) 084507.
[28] P. Minutolo, G. Rusciano, L.A. Sgro, G. Pesce, A. Sasso, A. D'Anna, *Proc. Combust. Inst.* 33 (2011) 649–657.
[29] B. Öktem, M.P. Tolocka, B. Zhao, H. Wang, M.V. Johnston, *Combust. Flame* 142 (2005) 364–373.
[30] J.P. Cain, P.L. Gassman, H. Wang, A. Laskin, *Phys. Chem. Chem. Phys.* 12 (2010) 5206–5218.
[31] J.P. Cain, J. Camacho, D.J. Phares, H. Wang, A. Laskin, *Proc. Combust. Inst.* 33 (2011) 533–540.
[32] C.K. Gaddam, R.L. Vander Wal, *Combust. Flame* 160 (2013) 2517–2528.
[33] R.L. Vander Wal, V.M. Bryg, C.-H. Huang, *Combust. Flame* 161 (2014) 602–611.
[34] R.A. Dobbins, C.M. Megaridis, *Langmuir* 3 (1987) 254–259.
[35] B.W. Ward, J.A. Notte, N.P. Economou, *J. Vac. Sci. Technol. B* 24 (2006) 2871–2874.
[36] D.C. Bell, *Microsc. Microanal.* 15 (2009) 147–153.
[37] C.A. Schneider, W.S. Rasband, K.W. Eliceiri, *Nat. Methods* 9 (2012) 671–675.
[38] S. Lieb, H. Wang, Carbon, submitted for publication.

Please cite this article in press as: M. Schenk et al., *Proc. Combust. Inst.* (2014), http://dx.doi.org/10.1016/j.proci.2014.05.009

[39] Z. Li, H. Wang, *Phys. Rev. E* 70 (2004) 021205.
[40] M.M. Maricq, in: H. Bockhorn, A. D'Anna, A.F. Sarofim, H. Wang (Eds.), *Combustion Generated Fine Carbonaceous Particles*, KIT Scientific Publishing, 2009, pp. 347–369.
[41] S.J. Blott, K. Pye, *Sedimentology* 55 (2008) 31–63.
[42] T.G. Smith Jr., G.D. Lange, W.B. Marks, *J. Neurosci. Methods* 69 (1996) 123–136.
[43] U. Köylü, Y. Xing, D.E. Rosner, *Langmuir* 11 (1995) 4848–4854.
[44] M. Maricq, N. Xu, *J. Aerosol Sci.* 35 (2004) 1251–1274.
[45] C.M. Sorensen, *Aerosol Sci. Technol.* 45 (2011) 765–779.
[46] S. Kaciulis, *Surf. Interface Anal.* 44 (2012) 1155–1161.

3.3 Characterizing CVD-grown films of transition metals

This part of the thesis reports about an additional cooperative work with the physical chemistry I (PCI) in Bielefeld (Prof. Katharina Kohse-Höinghaus). Samples were prepared by Patrick Mountapmbeme Koutou, Achraf El-Kasmi, Patrick Hervé Tchoua Ngamou and Zhen-Yu Tian.

For these highly corrugated films, it is necessary to obtain images in high resolution and depth of field. The properties of the HIM are therefore especially helpful. In addition, XPS was used to analyze the surface chemistry. Special focus of this study were transition metals and their oxides, especially iron,[83,84] cobalt,[85] copper,[86] and mixtures thereof.[87–89]

3.3.1 Introduction

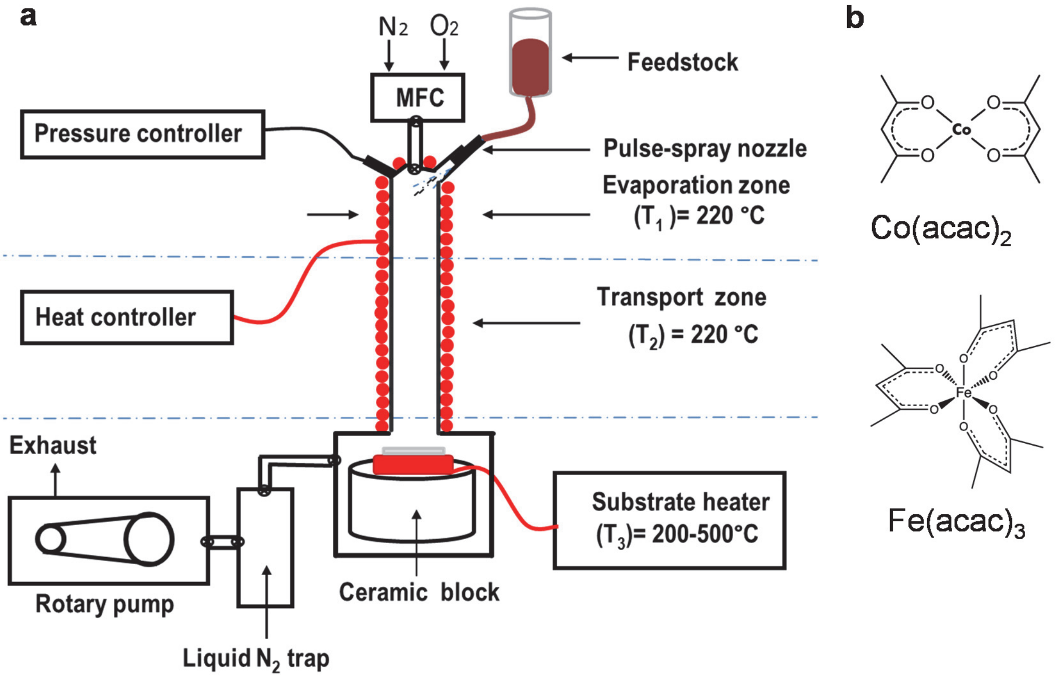

Figure 33 (a): Schematic of the PSE-CVD reactor used to manufacture the functional films. (b): Structure of the typical acetylacetonate (acac) precursors used.

The general scientific goal is the production and investigation of functional catalytic surfaces for a better and cleaner combustion. Burning organic material is not only producing soot as discussed in the previous chapter, but also volatile organic compounds (VOCs) are emitted. These are linked to a variety of environmental damages and negative effects on human health.[90] Many currently used catalysts are made from noble metals, so they are generally expensive. An alternative would be the use of transition metal oxides (TMOs), as they are quite inexpensive and show promising usability as catalyst.[91]

Chemical vapor deposition (CVD) is a deposition technique to produce thin films. The substrate is exposed to a precursor in the vapor phase. The film is then formed by decomposition or chemical reaction of this precursor on or near the vicinity of the heated substrate surface. This method can provide pure materials with atomic or nanometer scale level. In addition, it allows much control on the film structure and the growth in all sample directions (also on shadowed areas).

In this study, pulse spray evaporation chemical vapor deposition (PSE-CVD) is used. In PSE-CVD, the precursor is dissolved in a solvent, and this mixture is directly injected in the process chamber (evaporation zone, see Figure 33). Only small amounts (~µL) are sprayed with every pulse, so the solution immediately evaporates. A gas flow is then transporting this vapor to the heated substrate. PSE-CVD has advantages to conventional techniques due to its simple (thus inexpensive) setup, the high flexibility, a good growth rate control, and the high number of parameters to tune the properties of the final surface.[92,93]

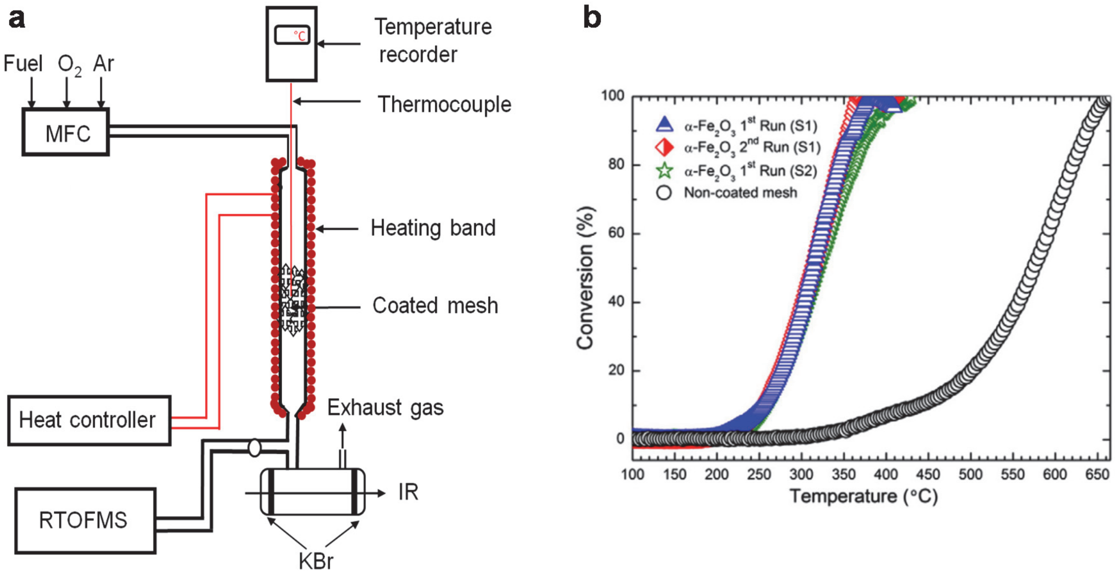

Figure 34: Testing of the catalytic functionality. (a): Schematic representation of the flow-reactor used for catalytic tests. (b): A typical test curve where the mesh temperature is plotted against the conversion rate. This example is α-Fe_2O_3 grown at 300°C substrate temperature. Reprinted with permission.[84]

As this study was application-related, the most important test was the catalytic functionality of the prepared film. This was done in a flow reactor as depicted in Figure 34. The oxidation of several model pollutants like carbon monoxide (CO), propene (C_3H_6) and others were studied and compared to known catalysts. In detail, a catalyst-coated steel mesh was placed inside a flow chamber and the exhaust pollutant concentration was measured. Good catalysts reduce the necessary temperature and are long-term stable. A typical “light-off curve” of such a measurement on α-Fe_2O_3 grown at 300°C is presented in Figure 34b.

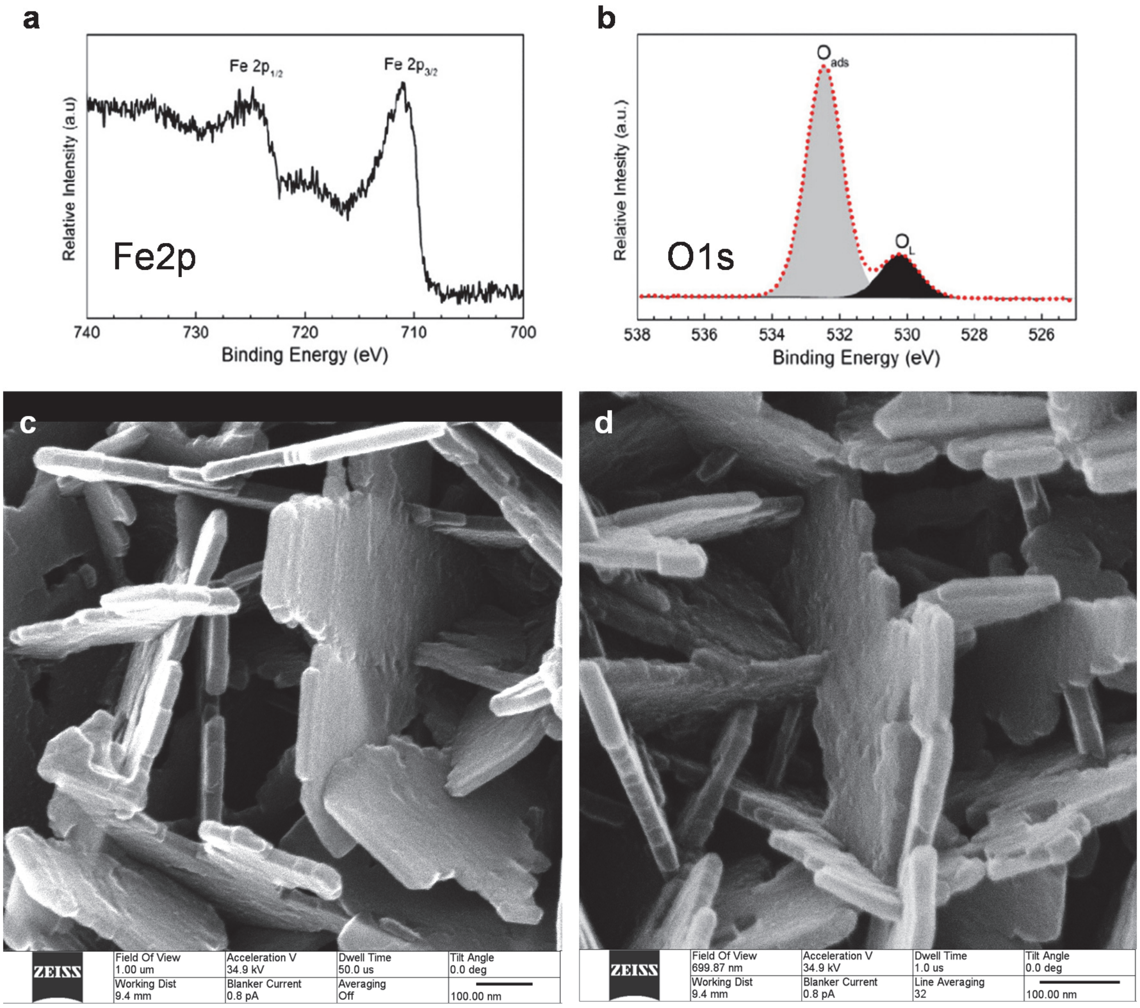

Figure 35: XPS and HIM of α-Fe2O3 grown at 300°C substrate temperature. (a,b,d): Parts reprinted with permission [84]

As this layer showed good results in the CO conversion, it was comprehensively characterized by X-ray diffraction (XRD), emission Fourier transform infrared (FTIR), Raman spectroscopy, Scanning electron microscopy (SEM), Energy-dispersive X-ray spectroscopy (EDX), and Ultraviolet–Visible (UV–Vis) spectroscopy (see[84]). To obtain a good knowledge of the catalyst surfaces, Helium ion microscopy (HIM) and X-ray photoelectron spectroscopy (XPS) were performed as part of this thesis. The methods of this thorough investigation of the materials properties were applied to all investigated films, one example is shown in the full publication in chapter 3.3.4.

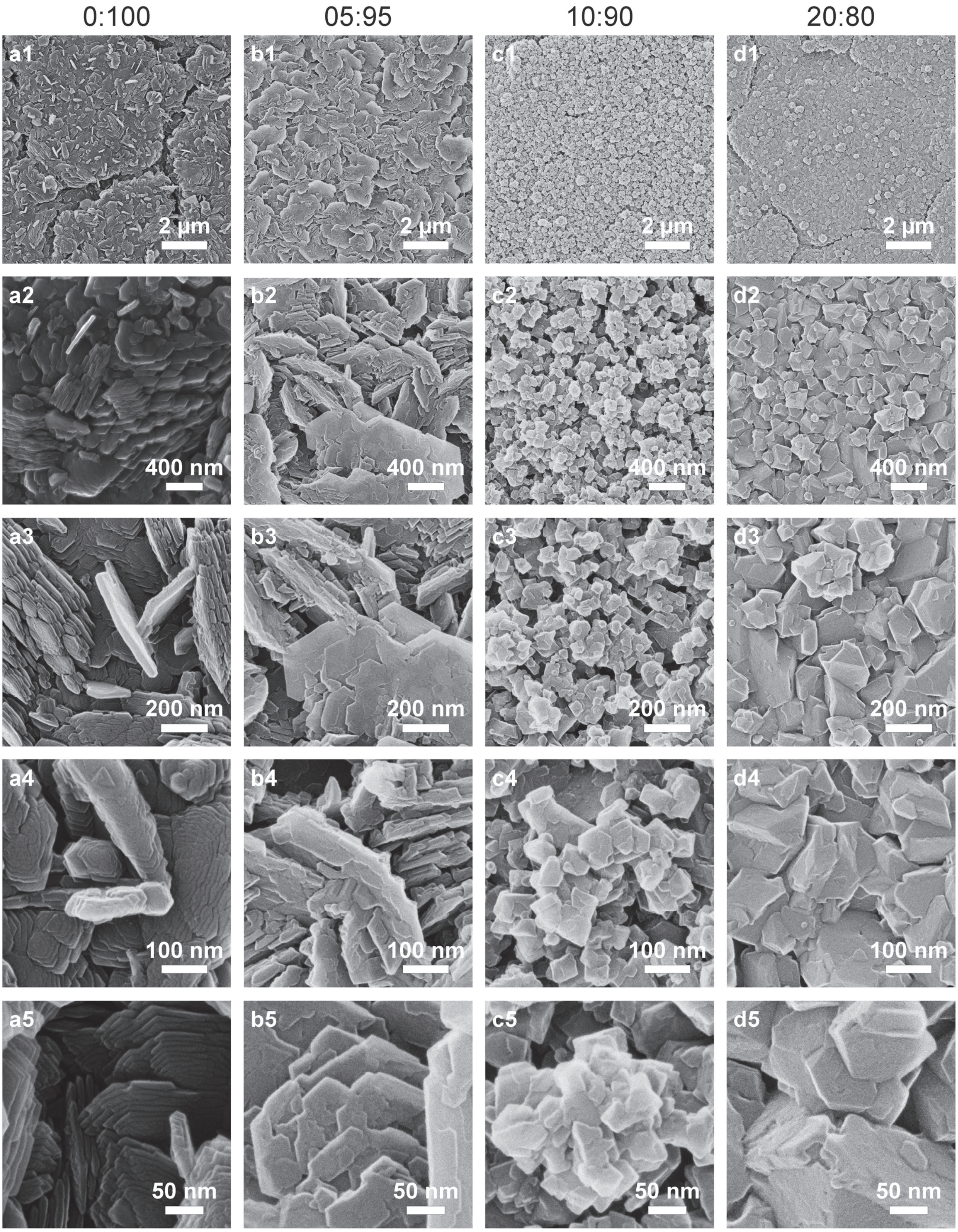

Figure 36: PSE-CVD grown films of iron and cobalt mixed oxides, Part 1. The precursor mixing ratio (Co(acac)$_2$:Fe(acac)$_3$) is given on top of the figure. The Field of View of the images increases from 10 µm (first row) to 2 µm, 1 µm, 500 nm until 300 nm (last row). (Continued in next figure)

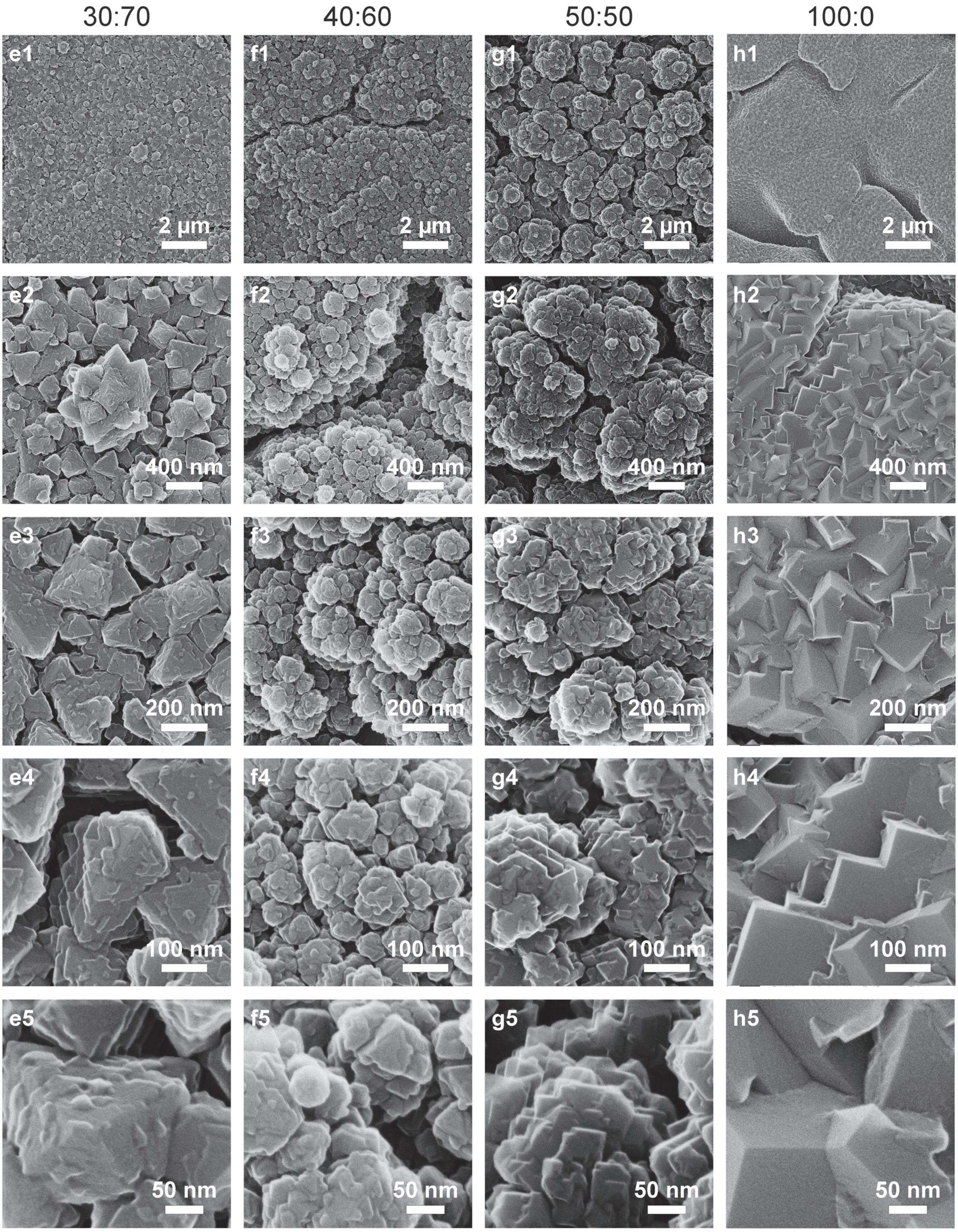

Figure 37: PSE-CVD grown films of iron and cobalt mixed oxides, Part 2. All films are grown at 400°C substrate temperature (some of the micrographs are already published.[83,87,88])

XPS revealed composition and oxidation state of the catalyst surface. The Iron Fe2p doublet spectrum in Figure 35a was identified to be consistent with the Fe^{3+} state.[94,95,37] For the oxygen spectrum in Figure 35b, two distinct species are visible: lattice oxygen (O_L) and adsorbed oxygen (O_{ads}). The HIM micrographs (Figure 35c,d) clearly reveal that the film is composed of a large quantity of plate-like geometric structures. It is also observed that the sample exhibits mainly nano-plate structures with random orientations. In literature, such a morphology is linked to better mechanical strength and a lower pressure drop, which allows for higher reactant gas velocities than fine powder catalysts. The observed morphology may thus be related with the catalytic performance of the deposited α-Fe_2O_3.[96] These images are good examples for the extraordinary depth of focus in the HIM, having all features in focus despite height differences of some micrometers.

3.3.2 **Binary mixtures of TMOs**

To further enhance the properties of the iron oxide films, other transition metals were mixed to the CVD process. Figure 36 and Figure 37 show significant differences in film morphology as the composition changes. The precursor was varied from 100% $Fe(acac)_3$ to 100% $Co(acac)_2$ providing mixed cobalt-iron oxide films. For this figure, only images grown at 400°C substrate temperature were selected.

The pure cobalt oxide (Figure 36h) grows in a closed layer of cubic crystals growing into each other at numerous orientations. On the other hand, pure iron oxide (Figure 36a) presents a uniform densely packed microstructure in octahedral shape. It is well structured and its well-shaped, pallet-shaped crystals are superimposed on each other with precise orientation. Increasing the amount of cobalt in the precursor to 5% (Figure 36b) leads to comparable, but somehow “disturbed” structures. At 10% Co, the morphology is totally different. Small grain sizes with a particular open, porous structure dominate the sample. Already at 30% Co, there is a better defined crystal structure with a pyramidal shape embedded in a matrix consisting of small cubic grains. The step to 50:50 precursor mixing ratio gives films composed of large grains which exhibit a cauliflower structure. These films show apparent open porosity, where the amount of rectangular angles like in the pure cobalt film is increasing.

The films with 10%, 30% and 50% cobalt precursor fraction were studied with the full set of analytical techniques and functional test. The results are in the publication (chapter 3.3.4).

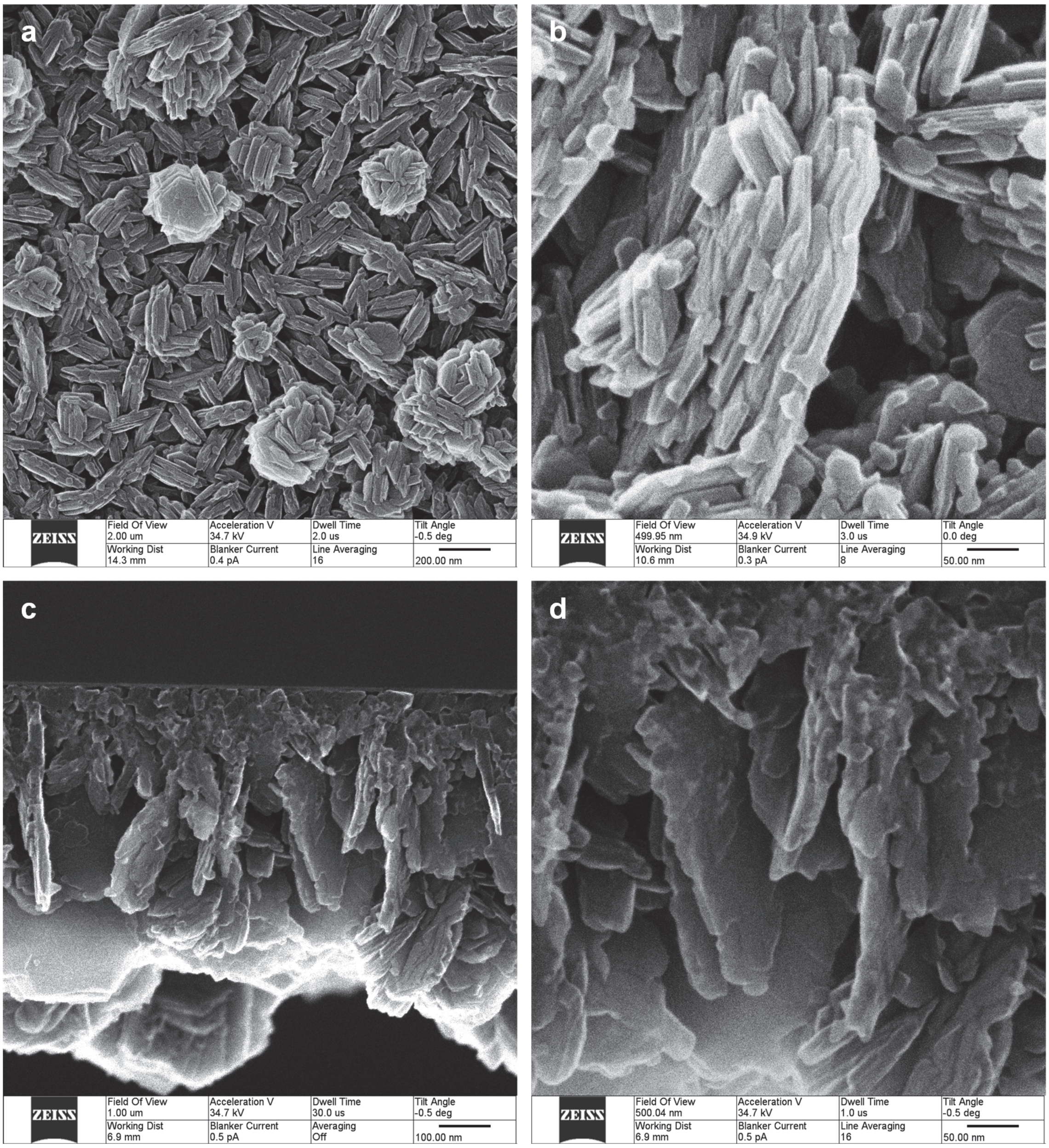

Figure 38: HIM micrographs of Iron-Copper oxide films on a Silicon wafer. (a,b): image of the top surface. (c,d): The silicon wafer was freshly cleaved and the sample was mounted at 90° in the HIM chamber. On top of the images is the Si wafer, with the Fe-Cu film growing down. The precursor ratio was 50:50 ($Fe(acac)_3$:$Cu(acac)_2$) at a substrate temperature of 400°C.

In most cases, the surface morphology was imaged. This allows the view on the top side, which is the catalytically active area. To obtain more information about the whole growth process, some samples were also grown on silicon wafers. These wafers are broken apart and the edges were imaged. This view allows more information on the growth process and a deep view inside the layer. Figure 38 is an iron-copper oxide, where again pallet shaped crystals are growing from the Si substrate to the top of the layer.

3.3.3 Summary: imaging PSE-CVD grown films

In these study, influences of changes in deposition temperature and composition are investigated. These changes affect all aspects of the films. Therefore a simple connection of catalytic activity to surface structure was not possible. However, in the light of all analytical tools it was possible to gain answers on growth process and details of the catalytic activity itself.

Due to the high resolution of the HIM it was possible to image very fine surface details. At the same time, the whole sample is in focus due to the high depth of focus. These two aspects of the helium ion microscope were especially useful for the analysis of CVD grown films.

3.3.4 Publication: Structure–activity relation of spinel-type Co–Fe oxides for low-temperature CO oxidation (Catal. Sci. Technol. 2014)

This Chapter is reprinted with permission from RSC. The original article appeared as:

> Kouotou, P. M.; Vieker, H.; Tian, Z.-Y.; Ngamou, P. T.; Kasmi, A. E.; Beyer, A.; Gölzhäuser, A.; Kohse-Höinghaus, K. Structure-Activity Relation of Spinel-Type Co-Fe Oxides for Low-Temperature CO Oxidation. *Catal. Sci. Technol.* **2014**, *4*, 3359–3367.

Contribution:

Helium Ion Microscopy and X-Ray Photoelectron Spectroscopy was performed by the author.

Catalysis Science & Technology

PAPER

Cite this: *Catal. Sci. Technol.*, 2014, 4, 3359

Structure–activity relation of spinel-type Co–Fe oxides for low-temperature CO oxidation†

P. Mountapmbeme Kouotou,*[a] H. Vieker,[b] Z. Y. Tian,‡*[a] P. H. Tchoua Ngamou,[a] A. El Kasmi,[a] A. Beyer,[b] A. Gölzhäuser[b] and K. Kohse-Höinghaus[a]

Received 11th April 2014, Accepted 14th June 2014

DOI: 10.1039/c4cy00463a

www.rsc.org/catalysis

A series of cobalt ferrite thin films was prepared *via* pulsed spray evaporation chemical vapour deposition (PSE-CVD). The samples were comprehensively characterised in terms of structure, surface, morphology, and optical and redox properties. Both X-ray diffraction (XRD) and Raman analysis show that all samples exhibited an inverse spinel structure. X-ray photoelectron spectroscopy (XPS) results indicate that the films were mainly composed of Co, Fe and O species, and an increase in the Co : Fe ratio with Fe substitution by Co was observed. Helium ion microscopy (HIM) images show the film morphology to be dependent on the Co : Fe ratio. The investigation of the optical property using ultraviolet-visible spectroscopy reveals that the increase in the Co content results in an increase in the band gap energy. *In situ* emission FTIR spectroscopy was used to evaluate the redox properties of the samples, and a shift of the redox temperature to higher values was observed upon increase in the Co content. The effect of Fe substitution by Co in the mixed oxide systems on their catalytic performance for CO oxidation was investigated. Co–Fe oxides exhibit substantially better catalytic performance than the single α-Fe_2O_3. The catalytic performance of the Co–Fe oxides towards CO oxidation was discussed with respect to the participation of surface and lattice oxygen in the oxidation process. According to XPS and temperature-programmed reduction/oxidation (TPR/TPO) results, a suprafacial mechanism where CO molecules react with surface-adsorbed oxygen functions to form CO_2 was proposed as the dominant mechanism.

Introduction

Catalytic oxidation has been recognized as one of the most efficient techniques for CO abatement.[1] Catalytic low-temperature combustion of CO is continuously being developed as an important research topic in environmental emission control.[2–4] The advantages of this process include extensive applications in numerous fields such as automotive exhaust emission control[5] and CO sensors[6] as well as traceable CO removal in enclosed atmospheres.[7,8]

Currently, metal (*e.g.*, Au) nanoparticles dispersed on solid supports and transition metal oxides (TMOs) have been found to be active catalysts for CO oxidation.[9–11] Although noble metals present high catalytic performance towards CO oxidation, they are generally costly and easily deactivated due to the trend of particle agglomeration which causes the decrease of the surface area.[2] TMOs are relatively cheap and can be easily synthesized, possess high thermal stability[12] and may show comparable activity with precious metals. Therefore, special attention has been focused on TMOs with different structures.[3,13] Among the investigated TMOs, much interest has been devoted to iron oxides because of their abundant availability and attractive properties such as high thermodynamic stability,[14,15] low cost, and environmentally friendly nature.[16] Several studies have shown the effectiveness of iron oxides and their composites towards the oxidation of CO.[17–20] However, compared to some catalytically active TMOs such as Co_3O_4 for CO oxidation,[21–23] good performance of iron oxide is mainly observed at relatively high temperature.

Cobalt ferrite oxide (Co–Fe–O) with a spinel structure could thus be a potentially interesting material with combined properties. Because of the versatility of mixed-oxide spinels, which offer tuneable composition, structural stability and a possibility for bifunctional redox or acid/base behaviour,[24] such combination could improve the physicochemical properties and catalytic performance. Different

---

[a] *Department of Chemistry, Bielefeld University, Universitätsstraße 25, D-33615 Bielefeld, Germany. E-mail: tianzhenyu@iet.cn, patrick.mountap@uni-bielefeld.de; Fax: +86 10 82483184; Tel: +86 10 82483184*

[b] *Department of Physics, Bielefeld University, Universitätsstraße 25, D-33615 Bielefeld, Germany*

† Electronic supplementary information (ESI) available: Table S1: estimated composition at the surface of the Co–Fe–O thin films; Fig. S1: iron oxide and cobalt oxide reference; S2: original spectra of Co2p and Fe2p; S3: additional HIM micrographs. See DOI: 10.1039/c4cy00463a

‡ Present address: Institute of Engineering Thermophysics, Chinese Academy of Sciences, Beijing 100190, China.

cations with more than one oxidation state can be accommodated and distributed between the available octahedral and tetrahedral sites[25] to endow such interesting and tuneable properties. For instance, $CoFe_2O_4$ adopts an inverse spinel arrangement and is thermodynamically stable at around 900 °C.[24,26–28] The contrasting site occupation between iron and cobalt in the cobalt ferrite composite is expected to create a significant modification of its properties and activity.

Cobalt ferrite spinels have been intensively investigated as catalysts for various reactions.[24,29,30] A single cobalt ferrite with a composition of $Co_{2.1}Fe_{0.9}O_4$ (identical with one of the materials discussed in this article) has also recently been used as a catalyst for DME, propene and *n*-butene oxidation.[31] Because it showed interesting catalytic behaviour against these compounds, it was used in this work to study the influence of the composition in a more systematic fashion. We have thus taken Fe_2O_3 as the starting material to improve its properties by Co addition. In fact, the activity of Co_3O_4 in the low-temperature conversion of CO has been systematically investigated and its high activity was reported to be due to the Co^{2+}–Co^{3+} ion pairs.[32,33] In most cases, CO oxidation over Co_3O_4 follows a redox mechanism where Co^{3+} is reduced to Co^{2+} after CO adsorption.[32] To improve the catalytic activity of α-Fe_2O_3, the aim here was to tailor the Co : Fe ratio and to deposit oxide composites in which both Co^{2+} and Co^{3+} are present with Fe^{3+} in the same phase.

The synthesis of Co–Fe–O thin films with varied composition for low-temperature CO oxidation was performed by pulsed spray evaporation chemical vapour deposition (PSE-CVD) and their properties were systematically characterised. PSE-CVD is a synthesis approach which offers distinct advantages over conventional CVD and is considered as a promising method of preparing pure films because of its relatively low cost, simplicity and high throughput.[34] The PSE precursor delivery system is advantageous as it allows using less stable precursors with good control of the process and thus permits improving the reproducibility of the film properties.[34] It is well adapted to the deposition of metal oxides with tailored composition[35,36] to systematically study their properties. The obtained samples were characterised in terms of structure, composition, morphology, and optical and redox properties using X-ray diffraction (XRD), Raman and X-ray photoelectron spectroscopy (XPS), helium ion microscopy (HIM), ultraviolet visible spectroscopy (UV-vis) and *in situ* emission FTIR. It should be mentioned that part of this information is also provided in ref. 31 for the composition $Co_{2.1}Fe_{0.9}O_4$. Upon variation of the cobalt content, the effect of the cobalt insertion in the iron oxide matrix on the redox properties and the catalytic performance was investigated here and an attempt was made to correlate the observed effects with the characterized properties of the deposited thin films.

Experimental

The preparation and characterization procedures are based on those presented in ref. 31. However, some details are necessary to understand the correlations between the physicochemical characteristics and catalyst behaviour addressed here, and a more in-depth analysis is given in the present paper.

Catalyst preparation

The Co–Fe–O thin films were prepared using a cold-wall stagnation-point flow CVD reactor associated with a PSE system for the delivery of liquid precursor feedstock.[20,31] The PSE delivery was achieved with a valve opening time of 2.5 ms and a frequency of 4 Hz. Firstly, cobalt acetylacetonate ($Co(acac)_3$) and iron acetylacetonate ($Fe(acac)_3$) were weighed in the adequate Co/Fe molar ratios, dissolved in tetrahydrofuran (THF) and kept at respective concentrations of 5 mM. The single phase of $Co_xFe_{3-x}O_4$ of the respective stoichiometric relations was obtained by adjusting the volume molar ratio of the two metallic elements (Co% vol : Fe% vol = 10 : 90, 30 : 70 and 50 : 50). The value of x was calculated from the Co/Fe ratio obtained by XPS. The liquid delivery allows overcoming the inherent contrast between the sticking probabilities of different precursors in the dual-source strategy for the growth of multi-component films. The evaporation of the injected feedstock took place at 220 °C. The resulting vapour was transported to the deposition chamber with N_2/O_2 flow rates of 0.16/1.0 standard litres per minute (SLM). Stainless steel and bare glass were used as substrates, heated with a flat resistive heater. After optimization, the substrate temperature was fixed at 400 °C and the total pressure in the reactor was kept at 30 mbar during the deposition. The thickness of the obtained films was estimated gravimetrically using a microbalance, with a resolution of 1 μg.

Characterization

A Philips X'Pert Pro MDR diffractometer with a PW3830 X-ray generator was used to record the XRD patterns. The crystalline phases were identified by referring to the powder XRD database (JCPDS-ICDD), and the crystallite sizes were calculated using the Scherrer equation. Raman spectra were obtained with a home-made Raman spectrometer.[37] The surface microstructure was examined with a Carl Zeiss Orion Plus® helium ion microscope (HIM). The helium ion beam was operated at 35 kV acceleration voltage at a current of 0.5 pA. A 5 μm aperture at a setting of "spot control 4" was used. The working distance was 9 mm, and the sample tilt was 0°. The samples were plasma-cleaned in the HIM load lock for 8 min before measurement. The chemical composition was determined by UHV-XPS (Multiprobe, Omicron Nanotechnology, base pressure about 10^{-10} mbar) using a monochromated Al Kα X-ray source (1486.7 eV, 280 W) under an angle of 13° from the surface normal to the electron detector. CasaXPS was used to analyse the spectra with Shirley backgrounds and Scofield cross sections. The evaluation of the Co and Fe spectra is not straightforward since an Auger peak from one metal overlays the 2p peak of the other metal. To overcome this effect, reference samples of cobalt and iron oxide were measured to calculate the 2p to Auger area ratio. With this, the areas used for the elemental composition were corrected (see details in the ESI†).

The redox properties of the Co–Fe–O composites coated on stainless steel substrates were evaluated by temperature-programmed reduction (TPR); this was followed by re-oxidation (TPO). Both analyses were performed from 100 to 500 °C with a ramp of 3 °C min^{-1}, under an argon flow of 0.05 L min^{-1} containing 5 vol.% of H_2 (TPR) or O_2 (TPO), respectively. Emission FTIR spectra were recorded continuously during the TPR/TPO analyses and characteristic bands were integrated *versus* temperature. This technique allowed for substantial improvement of the sensitivity towards dynamic changes in the gas composition. UV-vis spectra were recorded (UV-2501PC, SHIMADZU) to determine the optical properties.

Catalytic tests

The catalytic performance of the Co–Fe–O composites was evaluated using a 30 cm long quartz plug-flow reactor with a diameter of 0.9 cm. A 20 mg catalyst (supported on a grid mesh of stainless steel) was used. The reaction gas mixture consisted of 1% CO and 10% O_2 diluted in argon with a total flow rate of 15 mL min^{-1}, corresponding to a weight hourly space velocity (WHSV) of 45 000 mL g^{-1} cat h^{-1}. The flow rates of gases were controlled by MKS mass flow controllers, and the temperature of the reactor was raised with a ramp of 3 °C min^{-1} using a HT60 controller (Horst). The temperature of the mesh inside of the reactor was recorded using K-type thermocouples and a digital thermometer (GMH3250, Greisinger). The composition of the effluent gas was detected in the wavelength range of 400–4000 cm^{-1} with an online FTIR spectrometer equipped with a KBr transmission cell. Details of data treatment can be found in ref. 38. It should be noted that the aim here was not to maximize the surface area but to investigate the effect of Co addition on the properties of Fe_2O_3 under well-defined conditions. The CVD synthesis approach offers, in principle, to coat structures with larger surface area by, *e.g.*, using washcoats or porous structures as templates.

Results and discussion

Structure

The structural investigation of the deposited thin films with a thickness of ~250 nm was performed using XRD and Raman spectroscopy, as shown in Fig. 1. The XRD patterns of the cubic *Fd*3*m* spinel Co_3O_4 (ref. 35) and hexagonal *Ia*3 hematite (α-Fe_2O_3)[20] from our recent work are presented as references. The deposited Co–Fe–O films exhibit a cubic *Fd*3*m* inverse spinel structure like the reference $CoFe_2O_4$ inverse spinel (JCPDS no. 03-0864) and no extra diffraction peaks associated with the formation of other phases were detected. Starting from hematite (α-Fe_2O_3), a non-spinel with a hexagonal structure, Fe substitution by Co induces a structure transformation to an inverse spinel structure even at very low Co content. A decrease in the lattice constant from 8.39 to 8.21 Å (Table 1) was noted with the increase in cobalt content, which is visualised by the peak shift of diffraction peaks towards higher angles. The calculated values of the lattice constants vary from those of the reference materials $CoFe_2O_4$ (8.4 Å) and Co_3O_4 (8.1 Å). Hematite has a hexagonal close-packed structure with all Fe^{3+} ions in O-sites, whereas Co_3O_4

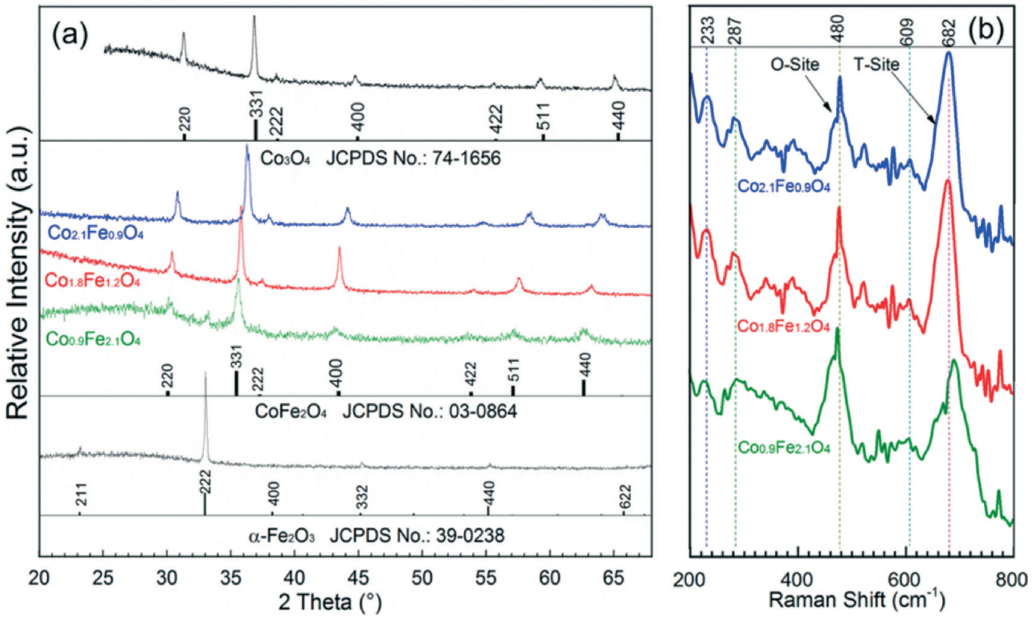

Fig. 1 (a) XRD patterns of Co–Fe–O oxides, pure Co_3O_4 (ref. 35) and α-Fe_2O_3 (ref. 20); (b) Raman spectra of the deposited Co–Fe–O films. The sample $Co_{2.1}Fe_{0.9}O_4$ is reproduced from ref. 31.

Table 1 Characteristics of Co–Fe–O thin films[a]

Composition	D (nm)	a (Å)	E_g (eV)	T_{TPR} (°C)	T_{TPO} (°C)	T_{10} (°C)	T_{50} (°C)	T_{90} (°C)
$Co_{0.9}Fe_{2.1}O_4$	20	8.39	1.60	295	309	170	205	230
$Co_{1.8}Fe_{1.2}O_4$	33	8.36	1.90	300	338	210	232	250
$Co_{2.1}Fe_{0.9}O_4$	35	8.21	2.09	317	350	215	260	300
α-Fe_2O_3 (ref. 20)	—	—	2.16	—	—	262	325	384

[a] D is the particle size; T_{TPR} and T_{TPO} refer to the temperature of complete reduction and re-oxidation, respectively; T_{10}, T_{50} and T_{90} stand for the temperatures corresponding to 10%, 50% and 90% CO conversion, respectively.

has a normal spinel structure in which tetrahedral sites (T-sites) are occupied by Co^{2+} ions and octahedral sites (O-site) by Co^{3+} ions: $[Co^{2+}]_{T\text{-site}}[Co^{3+}Co^{3+}]_{O\text{-site}}O_4$. In contrast, $CoFe_2O_4$ has an inverse spinel structure in which Fe^{3+}, Co^{3+} and Co^{2+} ions are distributed in both T- and O-sites. A systematic analysis of a series of Co–Fe–O with similar compositions has been reported by Le Trong *et al.* using Mössbauer spectroscopy.[39] Following their analysis, we assigned the following distribution to our oxides upon increasing the Co content, *i.e.* $[Co^{2+}Fe^{3+}Co^{3+}]_{T\text{-site}}[Co^{2+}Fe^{3+}Co^{3+}]_{O\text{-site}}O_4$, $[Co^{2+}Fe^{3+}]_{T\text{-site}}[Co^{2+}Fe^{3+}Co^{3+}]_{O\text{-site}}O_4$, and $[Co^{2+}Fe^{3+}]_{T\text{-site}}[Fe^{3+}Co^{2+}]_{O\text{-site}}O_4$ for $Co_{2.01}Fe_{0.9}O_4$, $Co_{1.8}Fe_{1.2}O_4$ and $Co_{0.9}Fe_{2.1}O_4$, respectively. The observed decrease in the lattice constant with increasing Co content can be associated to this changing distribution. In fact, according to Le Trong *et al.*,[39] when the amount of cobalt increases, the cell parameter decreases and there is gradual evolution toward a normal spinel structure as observed in our XRD patterns. This is due to the fact that the diamagnetic Co^{3+} cations replace the Fe^{3+} cations in the octahedral position and the octahedral preference of the Co^{2+} cations becomes less dominant.

The particle size was evaluated by XRD analysis with the Scherrer equation. Increasing cobalt content tends to sharpen the peaks progressively. The Scherrer line-broadening analysis on the (331) plane reveals that the volume-averaged crystallite size increases from 20 to 35 nm upon cobalt insertion. The agglomeration of small grain sizes to form larger particles may be one reason for the increase of the particle size.

Further structure information was obtained from Raman spectra of the deposited thin films, recorded at room temperature, and presented in Fig. 1b. Five Raman-active modes are observed: the modes at ~609 and ~682 cm^{-1} are related to the T-site mode; other peaks at ~233, ~287 and ~480 cm^{-1} correspond to the O-site mode.[40] These assignments are in excellent agreement with the previously reported results for the Co–Fe–O system.[24,41,42] Thus, pure-phase Co–Fe–O spinel can be easily synthesized with PSE-CVD through the accurate adjustment of the feedstock composition.

Chemical composition

Ex situ XPS was used to investigate the surface composition and chemical species of the cobalt ferrite thin films. Despite the presence of both metals and oxygen, carbon was found on all samples. Carbon and oxygen can be contamination products arising from precursor decomposition and from ambient air. Therefore, the Fe/Co ratio was used to calculate the chemical compositions and the results are listed in Table 1. Details regarding XPS measurement and evaluation are collected in the ESI:† Table S1, Fig. S1 and S2.

High-resolution XPS spectra of Fe2p, Co2p, and O1s are shown in Fig. 2. To compare the metal spectra to that in the literature, the overlaying Auger peaks were directly subtracted from the data. It is worth mentioning that even for clear spectra, the identification and fitting of chemical species are not unique. This Auger correction gives an additional source of error, although it is the best route in this study (see the original data in Fig. S2†). The Fe2p spectra are visible in Fig. 2a. The signals at 710.6 and 723.3 eV with the separation of 12.7 eV and a small satellite structure at ~734 eV have been reported to indicate the presence of Fe^{3+}.[43] Inspection of the measured Co2p peak (Fig. 2b) shows that it is composed of the main doublet with peaks at around 780 and 795 eV, indicating the presence of oxidized species. Only the $2p_{1/2}$ parts of the spectra were fitted as it is less affected by the Auger correction. Here, the species interpretation according to Gautier *et al.*[44] was used. The main peak consists of two species: one at ~795.2 eV for Co^{3+} and one at ~796.4 eV for Co^{2+}. A broad satellite peak at 802.8 eV is assigned to originate from Co^{2+}.

As shown in Fig. 2c, the O1s spectra for all samples were deconvoluted in three peaks in the BE range of 530–533 eV. The lower peak (~530 eV) could be assigned to the lattice oxygen species O^{2-}. The two species at higher BE are generally assigned to "adsorbed oxygen".[45] The peak at ~531.4 eV is explained to be the hydroxyl species (OH^-) or defective oxygen,[46] whereas the peak at 533.2 eV probably comes from carbonate species, CO_3^{2-} or defects in the structure. From the XPS spectra of all samples, lattice and adsorbed oxygen are observed. Both O_2^{2-} and O^- species are strongly electrophilic reactants, which can attack an organic molecule in the region of its highest electron density and therefore result in the oxidation of the carbon skeleton.[19] For CO conversion over oxides, electrophilic oxygen species such as lattice and adsorbed oxygen are generally responsible for the total oxidation.[10,47] Thus, these electrophilic oxygen species (O_2^{2-} or O^-) present at the surface of Co–Fe–O oxides are expected to benefit the total oxidation of CO.

Morphology

The surface morphology of the thin films was studied with HIM and a few representative micrographs of the obtained

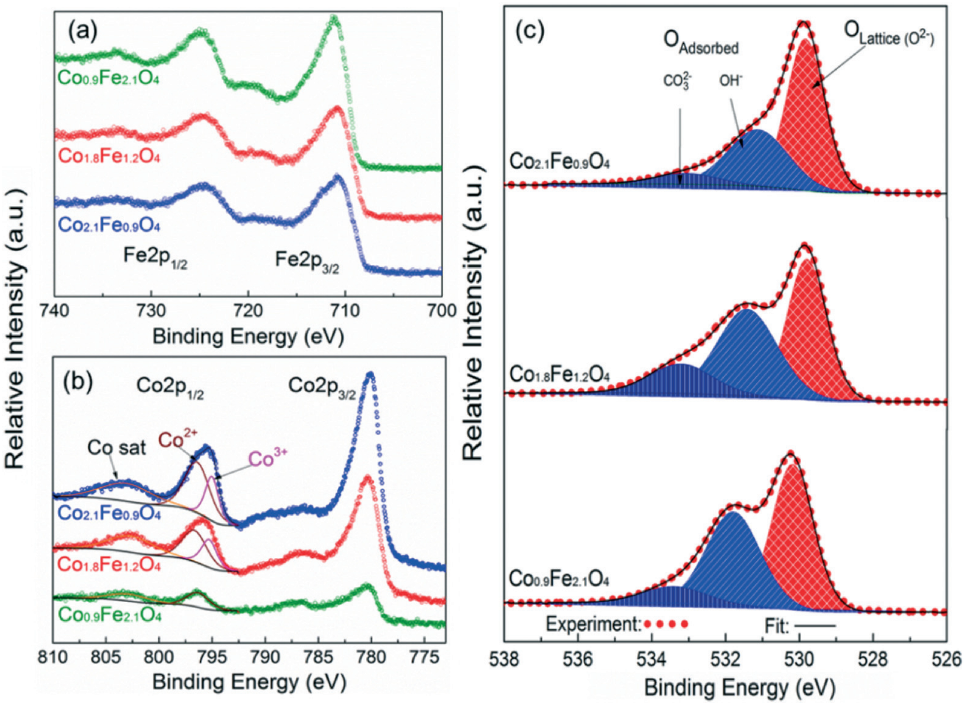

Fig. 2 XPS spectra of the Co–Fe–O samples: (a) Fe2p; (b) Co2p; (c) O1s. In the case of the metals an overlaying Auger signal has been subtracted (see ESI†). An offset is added for better visibility. The sample $Co_{2.1}Fe_{0.9}O_4$ is reproduced from ref. 31.

films are shown in Fig. 3 (additional images can be found in Fig. S3†). The images revealed significant differences between the samples of different composition, whereas the $Co_{1.8}Fe_{1.2}O_4$ sample (Fig. 3b, e and h) shows better defined crystals with a pyramidal shape embedded in a matrix consisting of small cubic grains. The $Co_{2.1}Fe_{0.9}O_4$ sample (Fig. 3c, f and i) shows films composed of large grains which exhibit a cauliflower structure; these films show apparent open porosity; thus no particular defined geometry is observed due to the complete loss of the crystallinity. By increasing the Co content, the grain size apparently becomes larger due to the agglomeration of small grains with average values of about 20–35 nm. HIM images confirm visually that the increase in grain size upon Co addition is in accord with the estimation by XRD analysis. The grain size of $Co_{0.9}Fe_{2.1}O_4$ films is the smallest, followed by $Co_{1.8}Fe_{1.2}O_4$ and $Co_{2.1}Fe_{0.9}O_4$. Usually, the smaller the grain size, the larger the specific surface area.[47,48] Therefore, the difference in grain size may influence the physicochemical properties as well as the catalytic performance.

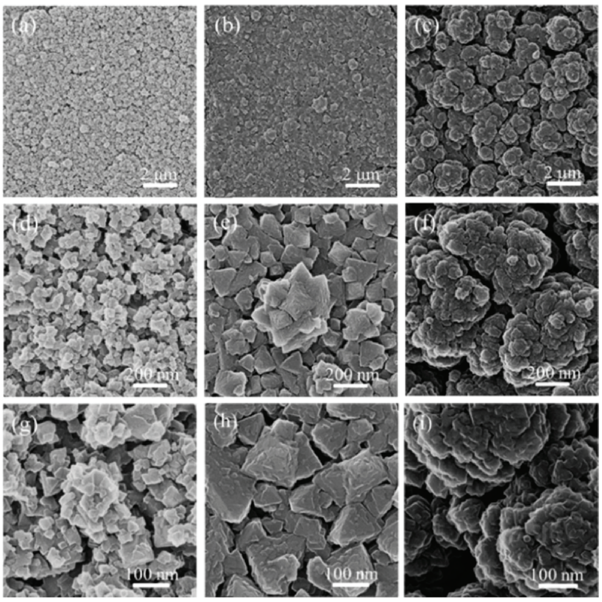

Fig. 3 High magnification HIM images of Co–Fe–O thin films coated on stainless steel at 400 °C, (a, d, g) $Co_{0.9}Fe_{2.1}O_4$, (b, e, h) $Co_{1.8}Fe_{1.2}O_4$ and (c, f, i) $Co_{2.1}Fe_{0.9}O_4$.

Optical properties

The controlled variation of the band gap energy (E_g) in a material could be used as a tool to reflect its performance. As an example it has been demonstrated that metal oxides with low E_g can exhibit good catalytic performance.[49,50] To investigate the influence of the Co content on the optical properties, the UV-vis spectra for the samples were measured in order to estimate the optical band gap.

Typical UV-vis spectra of the thin films are displayed in Fig. 4a. The collected absorption spectra were then used to evaluate the direct E_g from the Tauc equation: $\alpha h\nu = A(h\nu - E_g)^n$, where α represents the absorption coefficient, $h\nu$ is the photon energy, A is the refractive index constant and n is a

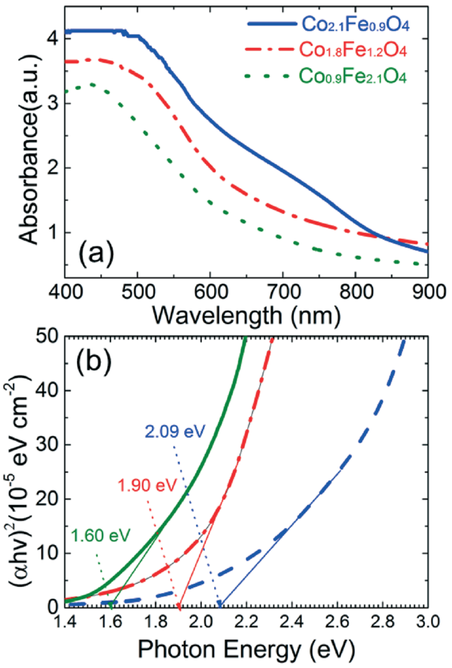

Fig. 4 (a) Optical absorption spectrum and (b) Tauc's plot resulting in an optical E_g for the different Co–Fe–O composites.

constant associated with the nature of the transition (1/2 for direct allowed transitions). E_g is estimated from the intercept of the extrapolated linear fit to the experimental data of $(\alpha h\nu)^2$ *vs.* $h\nu$, see Fig. 4b. Results for $Co_{0.9}Fe_{2.1}O_4$, $Co_{1.8}Fe_{1.2}O_4$ and $Co_{2.1}Fe_{0.9}O_4$ thin films calculated from the linear fit are 1.60, 1.90 and 2.09 eV, respectively. These values are larger than that of 1.44 eV reported by Rai *et al.*[51] and smaller than 2.61 eV by Ravindra *et al.*[52] for similar cobalt ferrites. It is important to note that E_g increases upon Fe substitution with Co. Several factors could influence the E_g of semiconductors: defects, charged impurities, disorder at the grain boundaries, cationic distribution as well as three-dimensional quantum size effects. These influences have not been discussed in detail for our materials in the literature. The only pertinent studies reported the effect of grain size evolution and distribution on the optical properties of pure V_2O_5 thin films prepared by pulsed-laser deposition.[53] The decreases in E_g and changes in the spectral characteristics were attributed to the increase in the grain size, the random grain distribution and the structural modification of the material.[53] This last assumption seems to be more applicable to our deposited films because the insertion of the cobalt in the matrix of the iron oxide is expected to create some structural disorder in the material and a perturbation of the band structure which can influence the band gap. The UV-vis spectra of PSE-CVD-deposited Fe_2O_3 thin films exhibit one absorption band corresponding to an optical band gap energy of 2.16 eV[20] which is assigned to the ligand–metal charge transfer $O^{2-} \rightarrow Fe^{3+}$. The combination of two transition metals with variable oxidation states has caused a structural modification and perturbation of the band structure which is responsible for the shift of the optical band gap of the Co–Fe–O materials to lower values, which would also enable their application to photo-catalysis. The increase of the optical band gap of the deposited films with the increase in the cobalt content can be logically associated to the structural modification arising with the cationic re-distribution in both the O- and T-sites which is in line with the XRD and XPS results. This approach is consolidated by Auvergne *et al.*[54] who reported that the band shift in oxides is due to Coulomb interaction between species which occurs as a result of doping. These observations and concepts also seem useful with respect to the present composite oxides and their electronic and optical applications. It is well known that materials with narrow energy band gaps offer higher electron mobility, and the correlation of the electron availability and mobility with the redox activity of a respective catalyst has been reported.[55] According to Zaki *et al.*,[55] the electron availability and mobility of lattice and surface oxygen species determine the redox activity of their catalysts. It is therefore crucial to investigate the redox properties of the prepared sample.

Redox properties

To investigate the redox properties of the mixed oxides, TPR and TPO were carried out with emission FTIR as an *in situ* monitoring technique, using 5% of H_2 or O_2 in Ar (0.05 L min^{-1}). Fig. 5 displays the redox behaviour of the samples. The typical feature of the integrated IR band intensity of Fe–Co–O as a function of the temperature in the TPR is presented in Fig. 5a. As the temperature increases, a progressive red shift of the two bands at around 530 cm^{-1}

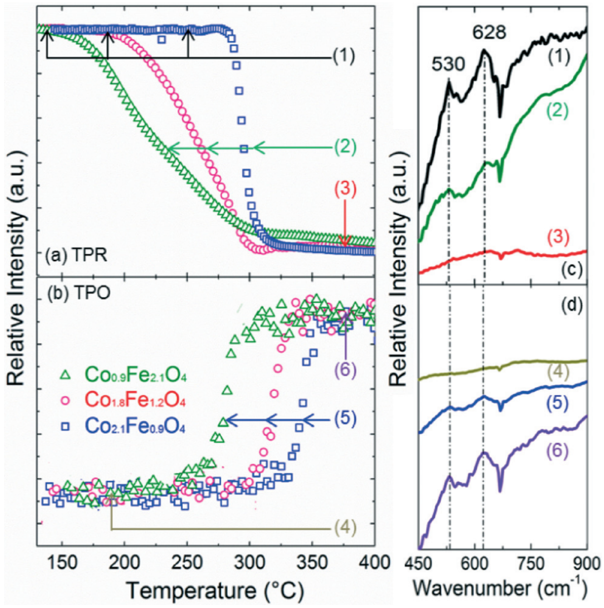

Fig. 5 Redox behaviour of the selected Co–Fe–O oxides: (a) TPR; (b) TPO; (c) progressive loss of the spinel structure and (d) recovery of Co–Fe–O IR vibration. The sample $Co_{2.1}Fe_{0.9}O_4$ is reproduced from ref. 31.

and 628 cm^{-1} (Fig. 5c) is observed. The complete reduction is characterized by a plateau at 300 °C. Fig. 5b and d display the TPO profiles and the total recovery of the inverse spinel structure in the oxidation step, respectively. The reducibility and the re-oxidation order for the three samples is $Co_{2.1}Fe_{0.9}O_4$ < $Co_{1.8}Fe_{1.2}O_4$ < $Co_{0.9}Fe_{2.1}O_4$. The reduction and oxidation temperatures are notably shifted to higher values, indicating that the increase in the Co content can give rise to unexpected changes of the Co–Fe–O structure and thereby make it more difficult to be reduced. The presence of anionic vacancies in the lattice of Mn-doped[38] and Ce-doped Co_3O_4 (ref. 56) has been reported to also increase the reducibility temperature. In this study, this kind of vacancies can also be generated upon cobalt insertion and make the corresponding material less reducible. The $Co_{2.1}Fe_{0.9}O_4$ sample shows a high reduction and oxidation temperature (low lattice oxygen mobility), followed by $Co_{1.8}Fe_{1.2}O_4$, whereas the $Co_{0.9}Fe_{2.1}O_4$ sample, with low cobalt content, is reduced and re-oxidized at low temperature (high lattice oxygen mobility).

Taking also the optical properties into consideration, $Co_{0.9}Fe_{2.1}O_4$ and $Co_{1.8}Fe_{1.2}O_4$ samples might allow high electron mobility due to their narrow E_g, with the knowledge that the reduction/oxidation of oxide material can proceed with electron transfer.[57,58] Consistently, the redox behaviour of samples with low Co content (low E_g) can be explained in terms of easy migration of the O^{2-} to the surface due to the high electron mobility during the electron transfer process. It could thus be suggested that the redox properties (lattice oxygen mobility) of the Co–Fe–O in this study might also be influenced by the band gap energy (electron mobility) variation.

Catalytic performance

To evaluate the catalytic performance of the prepared cobalt ferrite mixed oxides, the oxidation of CO was investigated at atmospheric pressure over all samples. The results were thus compared with that obtained with pure α-Fe_2O_3 from previous work[20] and a blank sample of non-coated mesh, as shown in Fig. 6. Single α-Fe_2O_3 becomes active in CO oxidation at around 230 °C and achieves complete CO conversion to CO_2 above 450 °C. Co–Fe–O composites exhibit lower temperatures for the initiation of CO oxidation than single α-Fe_2O_3. The complete CO oxidation over $Co_{0.9}Fe_{2.1}O_4$, $Co_{1.8}Fe_{1.2}O_4$ and $Co_{2.1}Fe_{0.9}O_4$ occurs at 255, 275 and 325 °C, respectively. The catalytic performance of various catalysts can be more easily compared by T_{50} (the reaction temperature corresponding to a 50% CO conversion), as presented in Table 1. The T_{50} for single α-Fe_2O_3 is 350 °C. T_{50} sharply decreases to ~232 °C for $Co_{1.8}Fe_{1.2}O_4$ and further decreases to 205 °C for $Co_{0.9}Fe_{2.1}O_4$. T_{50} thus increases with further substitution of Fe by Co in the Co–Fe composites. Only a small amount of Co is sufficient to shift the oxidation temperature of CO toward lower values. These results indicate that cobalt ferrite oxides are more catalytically active than the pure α-Fe_2O_3 single oxide. The performance order is as follows: α-Fe_2O_3 < $Co_{2.1}Fe_{0.9}O_4$ < $Co_{1.8}Fe_{1.2}O_4$ < $Co_{0.9}Fe_{2.1}O_4$.

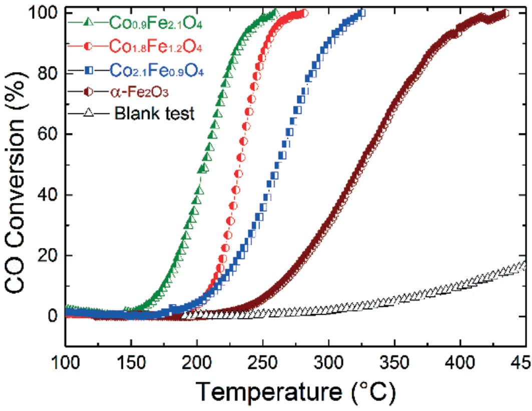

Fig. 6 Light-off curves of CO conversion with the Co–Fe–O samples and α-Fe_2O_3 as well as the non-coated mesh. The results obtained over α-Fe_2O_3.[20]

To understand the difference observed in the catalytic performance upon Co addition, a study of the phenomena that govern the catalytic oxidation on the surface is needed. From a viewpoint of oxygen species participating in the catalysis, adsorbed (and/or surface) oxygen and lattice oxygen are supposed to contribute to the suprafacial and intrafacial processes, respectively. XPS results revealed the presence of cations (Co^{3+}, Co^{2+} and Fe^{3+}) and anions (O^{2-}, OH^- as well as $CO_3^{\ 2-}$) in the Co–Fe–O structure. The activity of Co–Fe–O composites should be dominated by the exposed fraction of the active species of the Co–Fe–O composite. We will therefore discuss how either the redox properties or the adsorbed oxygen at the surface of Co–Fe–O may be involved in the CO catalytic oxidation process in this work.

It is generally accepted that CO oxidation over oxides follows a Mars van Krevelen-type mechanism,[59,60] where the reactions involve alternate reduction and oxidation of the oxide surface with formation of surface oxygen vacancies (as the key step) and their replenishment by gas-phase oxygen. Thus, the density of surface oxygen vacancies in the solid oxide plays an important role in their catalytic activity in CO oxidation. Nevertheless, according to Tascón *et al.*,[61] the CO oxidation reaction over mixed oxides may also follow a suprafacial mechanism in which lattice oxygen is not involved as presented in the following mechanism:[62]

$$O_2\ (g) + e^- \rightarrow O_2^-\ (ads);\ O_2^-\ (ads) + e^- \rightarrow 2O^-\ (ads) \qquad (E1)$$

$$CO\ (g) \rightarrow CO\ (ads) \qquad (E2)$$

$$CO\ (ads) + 2O^-\ (ads) \rightarrow CO_3^{\ 2-}\ (ads) \qquad (E3)$$

$$CO_3^{\ 2-}\ (ads) \rightarrow CO_2\ (ads) + O^-\ (ads) + e^- \qquad (E4)$$

$$CO_2\ (ads) \rightarrow CO_2\ (g) \qquad (E5)$$

In the present study, XPS analyses indicate the presence of both $O_{Lattice}$ and $O_{Adsorbed}$ species (Fig. 2c). As mentioned above, a shoulder of $O_{Adsorbed}$ at high BE is identified to be hydroxyl groups, mainly Fe–OH and Co–OH and CO_3^{2-}.[63] The catalyst with low Co content tended to have a larger amount of surface-adsorbed oxygen in comparison with the sample with high Co content. It is therefore suggested that the adsorbed oxygenated species, mainly Co_3^{2-} and OH^-, could effectively participate in the oxidation of CO.

The TPR/TPO experiment reveals that the Co–Fe–O redox reaction is shifted to higher temperatures, increasing the Co content. In an ideal state the reduction of Fe_2O_3 requires a higher temperature than that of Co_3O_4. The Co^{2+}–Co^{3+} ion pairs are known to be very active in low-temperature CO oxidation[33] over cobalt oxide; this higher activity is strongly dependent on the reduction of Co^{3+} to Co^{2+} after CO adsorption.[32,64] Therefore, the presence in Co–Fe–O composites of both Co^{2+} and Co^{3+} together with Fe^{3+} in the O- and T-sites should enable a decrease of the reduction temperature, accompanied by an improvement of the catalytic performance of CO over samples with higher Co content ($Co_{2.1}Fe_{0.9}O_4$ and $Co_{1.8}Fe_{1.2}O_4$), which have the following cationic distribution in the O-site: $[Co^{2+}Fe^{3+}Co^{3+}]_{O\text{-site}}$. Surprisingly, the opposite behaviour is observed with $Co_{0.9}Fe_{2.1}O_4$ (the most active sample) in which only Fe^{3+} and Co^{2+} are present in the O-site: $[Fe^{3+}Co^{2+}]_{O\text{-site}}$. A similar behaviour has been observed by Yu Yao[33] with $CoAl_2O_4$ spinel in which Co was stabilized as Co^{2+}, causing its inactivity in the CO oxidation through a redox mechanism. It can therefore be suggested here that the CO oxidation over a Co–Fe–O catalyst does not proceed through a redox mechanism even if $Co_{0.9}Fe_{2.1}O_4$ presents the lowest reduction temperature. This hypothesis is strongly supported by the fact that CO oxidation of $Co_{2.1}Fe_{0.9}O_4$ is initiated at ~200 °C while the reduction (Fig. 5a) started at ~280 °C. The earlier initiation of the reaction at low temperature can be assigned to the surface-adsorbed oxygen revealed by XPS analysis. Summarizing these observations, it is thus proposed that CO oxidation over Co–Fe–O follows a suprafacial mechanism where CO molecules react with adsorbed oxygen, mainly as CO_3^{2-} and OH^-, to form CO_2. This is in excellent agreement with the results reported in the literature for the same material.[30,65]

In this investigation, the results demonstrate that the combination of Fe and Co in the same phase intrinsically influences the redox properties and the catalytic performance of Co–Fe–O *vs.* Fe_2O_3 in CO oxidation and causes the shift of the optical band gap toward lower values. It is therefore likely that the controlled variation of the Co : Fe ratio in the cobalt ferrite oxides could be used as a tool to reflect their properties.

Conclusions

Cobalt–iron mixed oxide thin films were prepared by pulsed spray evaporation chemical vapour deposition and their properties were systematically characterised. The results show that the Co : Fe ratio in Co–Fe–O thin films strongly influences their physicochemical properties. In particular, the variation of the cobalt amount in the Co–Fe–O structure plays a decisive role in controlling both the band gap energies and the redox properties of Co–Fe–O films. Co–Fe mixed oxides exhibit better performance than pure α-Fe_2O_3. The performance of Fe–Co mixed oxide catalysts for the CO oxidation reaction was significantly affected by the adsorbed oxygen species and the cobalt content. The XPS and TPR analyses suggest that the suprafacial mechanism is dominant in the CO oxidation over Co–Fe–O catalysts.

Acknowledgements

P. Mountapmbeme Kouotou and A. El Kasmi kindly acknowledge the Deutscher Akademischer Austauschdienst (DAAD) for the financial support during their research stays at Bielefeld University. Z.Y. Tian is grateful for a fellowship of the Alexander von Humboldt Foundation, and P.H. Tchoua Ngamou acknowledges partial support by the DFG.

Notes and references

1 W. Gac, *Appl. Catal., B*, 2007, **75**, 107.
2 M. S. Chen and D. W. Goodman, *Science*, 2004, **306**, 252.
3 T. Cheng, Z. Fang, Q. Hu, K. Han, X. Yang and Y. Zhang, *Catal. Commun.*, 2007, **8**, 1167.
4 C. Jones, K. J. Cole, S. H. Taylor, M. J. Crudace and G. J. Hutchings, *J. Mol. Catal. A: Chem.*, 2009, **305**, 121.
5 M. Haruta, *Nature*, 2005, **437**, 1098.
6 S. Wicker, K. Großmann, N. Bârsan and U. Weimar, *Sens. Actuators, B*, 2013, **185**, 644.
7 R. K. Kunkalekar and A. V. Salker, *Catal. Commun.*, 2010, **12**, 193.
8 J. Shao, P. Zhang, X. Tang, B. Zhang, W. Song, Y. Xu and W. Shen, *Chin. J. Catal.*, 2007, **28**, 163.
9 I. X. Green, W. Tang, M. Neurock and J. T. Yates Jr., *Science*, 2011, **333**, 736.
10 L. F. Liotta, H. Wu, G. Pantaleo and A. M. Venezia, *Catal. Sci. Technol.*, 2013, **3**, 3085.
11 W. Song and E. J. M. Hensen, *Catal. Sci. Technol.*, 2013, **3**, 3020.
12 M. F. M. Zwinkels, S. G. Järås, P. G. Menon and T. A. Griffin, *Catal. Rev.: Sci. Eng.*, 1993, **35**, 319.
13 D. Barreca, D. Bekermann, E. Comini, A. Devi, R. A. Fischer, A. Gasparotto, M. Gavagnin, C. Maccato, C. Sada, G. Sberveglieri and E. Tondello, *Sens. Actuators, B*, 2011, **160**, 79.
14 M. J. Aaron and C. A. Heather, *ACS Appl. Mater. Interfaces*, 2010, **2**, 2804.
15 X. C. Jiang and A. B. Yu, *J. Mater. Process. Technol.*, 2009, **209**, 4558.
16 X. Liu, J. Liu, Z. Chang, X. Sun and Y. Li, *Catal. Commun.*, 2011, **12**, 530.
17 W. K. Jozwiak, E. Kaczmarek, T. P. Maniecki, W. Ignaczak and W. Maniukiewicz, *Appl. Catal., A*, 2007, **326**, 17.
18 S. C. Kwon, M. Fan, T. D. Wheelock and B. Saha, *Sep. Purif. Technol.*, 2007, **58**, 40.

19 P. Li, D. E. Miser, S. Rabiei, R. T. Yadav and M. R. Hajaligol, *Appl. Catal., B*, 2003, **43**, 151.
20 P. Mountapmbeme Kouotou, Z. Y. Tian, H. Vieker and K. Kohse-Höinghaus, *Surf. Coat. Technol.*, 2013, **230**, 59.
21 Y. Lou, L. Wang, Y. Zhang, Z. Zhao, Z. Zhang, G. Lu and Y. Guo, *Catal. Today*, 2011, **175**, 610.
22 S. Sun, L. Yang, G. Pang and S. Feng, *Appl. Catal., A*, 2011, **401**, 199.
23 Z. Zhao, R. Jin, T. Bao, X. Lin and G. Wang, *Appl. Catal., B*, 2011, **110**, 154.
24 N. Ballarini, F. Cavani, S. Passeri, L. Pesaresi, A.F. Lee and K. Wilson, *Appl. Catal., A*, 2009, **366**, 184.
25 T. A. S. Ferreira, J. C. Waerenborgh, M. H. R. M. Mendonca, M. R. Nunes and F. M. Costa, *Solid State Sci.*, 2003, **5**, 383.
26 S. Kawano, N. Achiwa, N. Yamamoto and S. N. Higashi, *Mater. Res. Bull.*, 1976, **11**, 911.
27 G. D. Rieck and J. J. M. Thijssen, *Acta Crystallogr., Sect. B: Struct. Crystallogr. Cryst. Chem.*, 1968, **24**, 982.
28 J. G. Na, T. D. Lee, E. C. Kim and S. J. Park, *J. Mater. Sci. Lett.*, 1993, **12**, 361.
29 V. Crocellà, F. Cavani, G. Cerrato, S. Cocchi, M. Comito, G. Magnacca and C. Morterra, *J. Phys. Chem. C*, 2012, **116**, 14998.
30 A. Biabani-Ravandi, M. Rezaei and Z. Fattah, *Chem. Eng. Sci.*, 2013, **94**, 237.
31 Z. Y. Tian, P. Mountapmbeme Kouotou, A. El Kasmi, P. H. Tchoua Ngamou, H. Vieker, A. Beyer, A. Gölzhäuser and K. Kohse-Höinghaus, *Proc. Combust. Inst.*, in press, DOI: 10.1016/j.proci.2014.06.111.
32 M. Haruta, S. Tsubota, T. Kobayashi, H. Kageyama, M. J. Genet and B. Delmon, *J. Catal.*, 1993, **144**, 175.
33 Y.-F. Y. Yao, *J. Catal.*, 1974, **33**, 108.
34 J.-P. Sénateur, C. Dubourdieu, F. Weiss, M. Rosina and A. Abrutis, *Adv. Mater.*, 2000, **10**, 155.
35 P. Mountapmbeme Kouotou, Z. Y. Tian, U. Mundloch, N. Bahlawane and K. Kohse-Höinghaus, *RSC Adv.*, 2012, **2**, 10809.
36 P. H. Tchoua Ngamou and N. Bahlawane, *Chem. Mater.*, 2010, **22**, 4158.
37 V. Vannier, M. Schenk, K. Kohse-Höinghaus and N. Bahlawane, *J. Mater. Sci.*, 2012, **47**, 1348.
38 Z. Y. Tian, P. H. Tchoua Ngamou, V. Vannier, K. Kohse-Höinghaus and N. Bahlawane, *Appl. Catal., B*, 2012, **117–118**, 125.
39 H. Le Trong, L. Presmanes, E. De Grave, A. Barnabé, C. Bonningue and P. Tailhades, *J. Magn. Magn. Mater.*, 2013, **334**, 66.
40 T. Yu, Z. X. Shen, Y. Shi and J. Ding, *J. Phys.: Condens. Matter*, 2002, **14**, 613.
41 Y. Qu, H. Yang, N. Yang, Y. Fan, H. Zhu and G. Zou, *Mater. Lett.*, 2006, **60**, 3548.
42 N. Viart, G. Rebmann, G. Pourroy, J. L. Loison, G. Versini, F. Huber, C. Ulhaq-Bouillet, C. Meny, P. Panissod and L. Saviot, *Thin Solid Films*, 2005, **471**, 40.
43 C. Altavilla, E. Ciliberto and A. Aiello, *Chem. Mater.*, 2007, **19**, 5980.
44 J. L. Gautier, E. Rios, M. Gracia, J. F. Marco and J. R. Gancedo, *Thin Solid Films*, 1997, **311**, 51.
45 Z. Zhou, Y. Zhang, Z. Wang, W. Wei, W. Tang, J. Shi and R. Xiong, *Appl. Surf. Sci.*, 2008, **254**, 6972.
46 M. C. Biesinger, B. P. Payne, A. P. Grosvenor, L. W. M. Lau, A. R. Gerson and R. St. C. Smart, *Appl. Surf. Sci.*, 2011, **257**, 2717.
47 M. Arenz, K. J. J. Mayrhofer, V. Stamenkovic, B. B. Blizanac, T. Tomoyuki, P. N. Ross and N. M. Markovic, *J. Am. Chem. Soc.*, 2005, **127**, 6819.
48 E. Frackowiak and F. Béguin, *Carbon*, 2001, **39**, 937.
49 B. Y. Jibril, *React. Kinet. Catal. Lett.*, 2005, **86**, 171.
50 Z. Y. Tian, N. Bahlawane, V. Vannier and K. Kohse-Höinghaus, *Proc. Combust. Inst.*, 2013, **34**, 2261.
51 R. C. Rai, S. Wilser, M. Guminiak, B. Cai and M. L. Nakarmi, *Appl. Phys. A: Mater. Sci. Process.*, 2012, **106**, 207.
52 A. V. Ravindra, P. Padhan and W. Prellier, *Appl. Phys. Lett.*, 2012, **101**, 161902.
53 A. Bielański and J. Haber, *Catal. Rev.: Sci. Eng.*, 1979, **19**, 1.
54 D. Auvergne, J. Camassel and H. Mathieu, *Phys. Rev. B: Solid State*, 1975, **11**, 2251.
55 M. I. Zaki, M. A. Hasan and L. Pasupulety, *Appl. Catal., A*, 2000, **198**, 247.
56 F. Wyrwalski, J.-M. Giraudon and J.-F. Lamonier, *Catal. Lett.*, 2010, **137**, 141.
57 P. J. Gellings and H. J. M. Bouwmeester, *Catal. Today*, 1992, **12**, 1.
58 J. Y. Lee, S. P. Cho, S. H. Hong, S. H. Choi and S. C. Hong, *Proc. of 2nd Joint Int. Conf. on "Sustainable Energy and Environment"*, Nov. 21–13, 2006, Bangkok, Thailand, D-014 (P).
59 H. Bao, X. Chen, J. Fang, Z. Jiang and W. Huang, *Catal. Lett.*, 2008, **125**, 160.
60 E. Aneggi, J. Llorca, M. Boaro and A. Trovarelli, *J. Catal.*, 2005, **234**, 88.
61 J. M. D. Tascón, J. L. G. Fierro and L. G. Tejuca, *Z. Phys. Chem.*, 1981, **124**, 249.
62 W. Yang, R. Zhang, B. Chen, N. Bion, D. Duprez and S. Royer, *J. Catal.*, 2012, **295**, 45.
63 Q. Yang, H. Choi, S. R. Al-Abed and D. D. Dionysiou, *Appl. Catal., B*, 2007, **74**, 170.
64 X. Xie, Y. Li, Z.-Q. Liu, M. Haruta and W. Shen, *Nature*, 2009, **458**, 746.
65 G. Evans, I. V. Kozhevnikov, E. F. Kozhevnikova, J. B. Claridge, R. Vaidhyanathan, C. Dickinson, C. D. Wood, A. I. Cooper and M. J. Rosseinsky, *J. Mater. Chem.*, 2008, **18**, 5518.

3.3.4.1 Electronic Supporting Information (ESI)

*Table 1: (**ESI 1**): Estimated composition at the surface of the Co-Fe thin films.*

	C1s	O1s	Co2p	Fe2p	Co/Fe	Co	Fe	O
$Co_{0.9}$ $Fe_{2.1}O_4$	43%	49%	3%	6%	0.43	0.9	2.1	4
$Co_{1.8}$ $Fe_{1.2}O_4$	37%	51%	7%	5%	1.47	1.8	1.2	4
$Co_{2.1}$ $Fe_{0.9}O_4$	35%	49%	11%	5%	2.23	2.1	0.9	4

3.3.4.2 Details about the XPS analysis

The surface composition was determined by the means of X-ray photoelectron spectroscopy (XPS). XPS was done in a multi technique ultra-high vacuum instrument (Multiprobe, Omicron Nanotechnology) using a monochromatic Al Kα X-ray source (1486.7 eV, 280 W) and a hemi-spherical electron energy analyzer (Sphera) in constant analyzer energy mode (25 eV) and a step size of 0.05 eV. The sample was located under an angle of 13° from the surface normal to the electron detector. The base pressure of the chamber is 2×10^{-10} mbar. CasaXPS was used to analyze the spectra, and a Shirley background subtraction procedure was employed. The elemental composition was calculated using the area of the Fe2p, Co2p, C1s and O1s peaks with the according Scofield cross-sections. The peak areas of the Fe2p and Co2p signals were corrected for Auger LMM peaks that each metal has in the 2p-area of the other metal. In both cases, mainly the $2p_{3/2}$ parts of the spectra are affected. To do the correction, 2 sputter-cleaned metal oxide samples made by PSE-CVD were measured as references. The intensity correction of the peak area was done according to the following formula:

$$A(\mathrm{Fe}-2\mathrm{p}) = \frac{M(Fe) - K(Co)M(Co)}{1-(K(C0)K(Fe))} \qquad A(\mathrm{Co}-2\mathrm{p}) = \frac{M(Co) - K(Fe)M(Fe)}{1-(K(C0)K(Fe))}$$

Definitions:
A = Area
K = [A(LMM) / A(2p)] (Correction factor)
Measured Areas:
M(Fe) = A(Fe-2p+Co-LMM)
M(Co) = A(Co-2p+Fe-LMM)

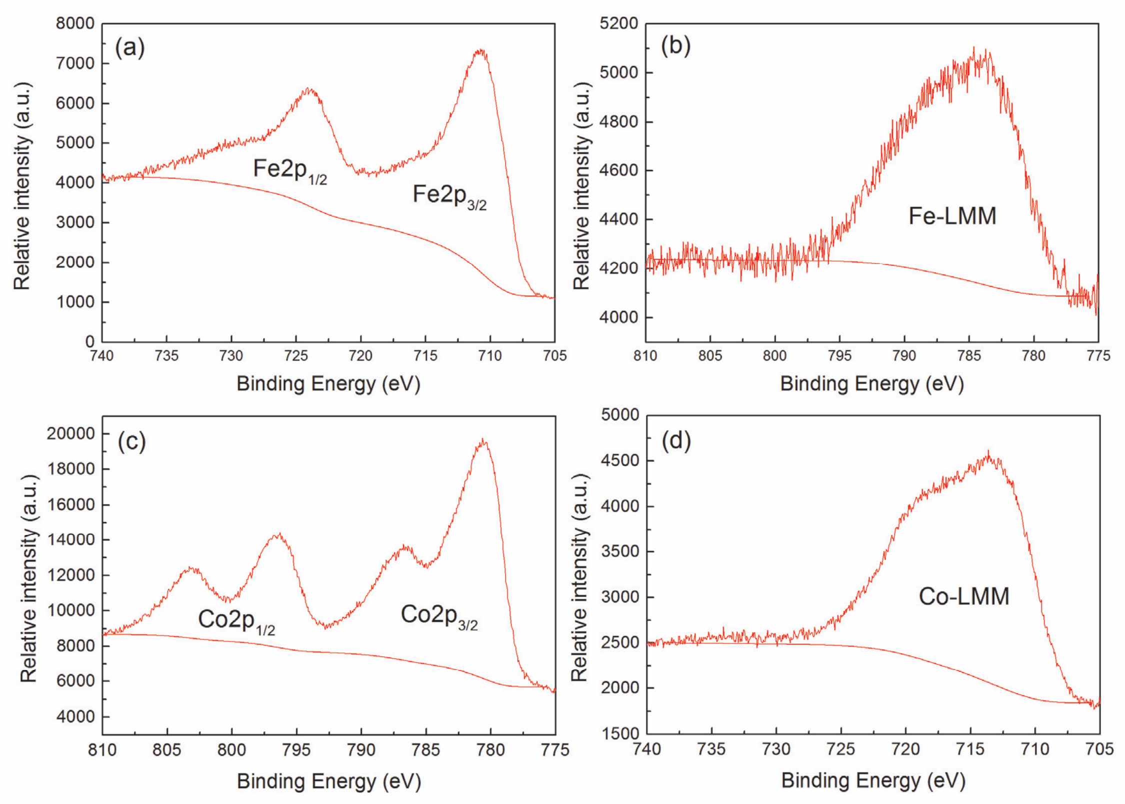

Figure 39: (ESI 1): Pure iron oxide (a, b) and cobalt oxide (c, d) reference sample.

Area ratio K (Fe) = A(Fe-LMM) / A(Fe-2p) = 14.3 / 84.8 = 0.148

Area ratio K (Co) = A(Co-LMM) / A(Co-2p) = 41.1 / 206.8 = 0.210

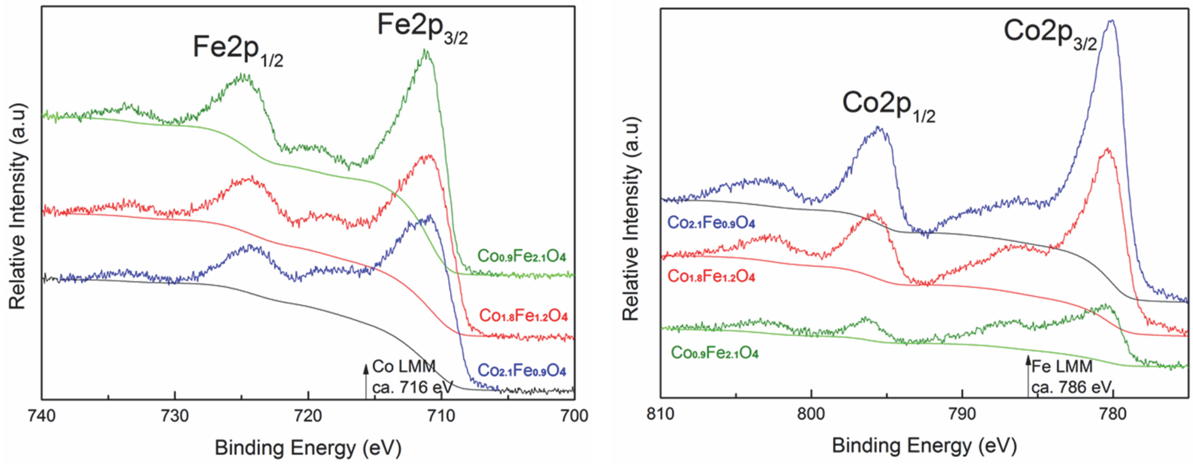

Figure 40: (ESI 2) The original XPS spectra of Fe2p and Co2p with the corresponding Shirley backgrounds.

In addition, the subtraction of the Auger signals was done to obtain less-disturbed iron and cobalt spectra. This was done with CasaXPS by subtracting the LMM references from the 2p data (see Fig 2a and 2b in the main text).

3.4 Rutherford backscattered ion (RBI) imaging

Imaging with backscattered ions gives additional information about the elemental composition of samples compared to the standard secondary electron (SE) imaging mode in the helium ion microscope. Unfortunately there is no real spectroscopic information with the standard multichannel plate (MCP) detector, but it is well possible to distinguish known elements from each other. The examples shown in this chapter consist of gold with the highest known backscatter yield, and on the other hand of carbon and silicon with rates more than 50 times lower.[29,30]

3.4.1 Defect analysis on phase plates for use in a TEM

This study is a cooperative work with PD Dr. Daniel Rhinow from the Max-Planck-Institute of Biophysics, Frankfurt.[97]

To maximize in-focus phase contrast in TEM of weak-phase objects like biological specimen, a Boersch phase plate (BPP) can be used. The BPP is an electrostatic einzel lens that shifts the phase of the unscattered beam by up to 90°. It poses several technological challenges to actually produce such lenses and to operate them continuously. The goal of this work was the investigation of possible sources of BPP contamination and failure by helium ion microscopy (HIM).

The principle of phase contrast TEM with a BPP is shown in Figure 41a. Figure 41b,c show BPP devices imaged in a helium ion microscope, indicating alternating layers of conductive (Au) and isolating materials (Si_3N_4) of the electrode ring. The locally confined electrostatic field of the electrode ring shifts the phase of the unscattered electrons by an angle that depends on the applied voltage.

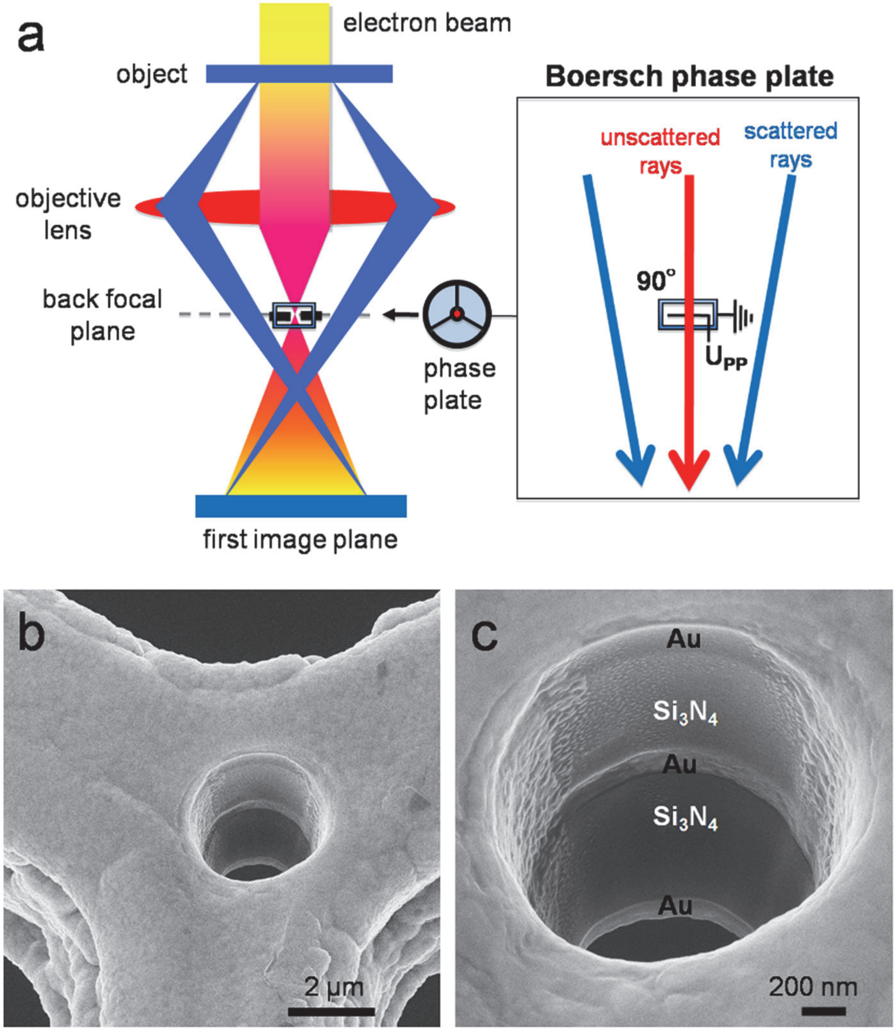

Figure 41 (a): Schematic of a Phase contrast TEM with a BPP (b,c): HIM images of the central BPP electrode show alternating layers of conductive and insulating materials in the BPP. Reprinted with permission.[97]

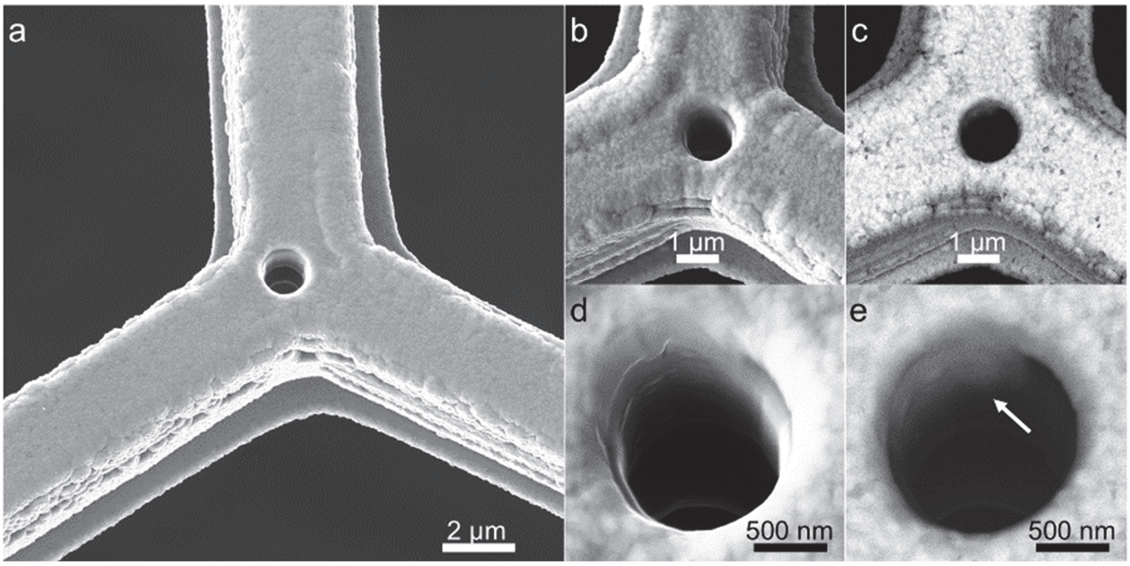

Figure 42: HIM micrographs of a BPP. (a) HIM image of a BPP in secondary electron (SE) mode. (b) HIM image of the central electrode in SE mode and (c) the same area in RBI mode. (d) HIM image of the central hole and (e) the corresponding RBI image. In RBI mode gold appears particularly bright. An area of gold re-deposited during the FIB process is highlighted (arrow). Reprinted with permission.[97]

Figure 42 shows a HIM image of a BPP, which produced strong disturbances due to charging. HIM images of the central electrode were acquired simultaneously in secondary electron (SE) and RBI mode. Some black dots in the RBI image (see Figure 42c) originate from ion channeling effects of gold grains. The bright area on the upper left of the central hole in Figure 42e (arrow) is interpreted as a thin film of gold re-deposited during the final production step (FIB milling of the BPP).

There were no indications for gross contaminations like large silicon nitride particles in the vicinity of the central hole. Therefore, the deposition of gold in the central hole is most likely responsible for leak currents or even short-circuits, which are observed with many BPPs. Furthermore, thin films consisting of gold islands might be susceptible to electrostatic charge build-up. In short, HIM analysis revealed that FIB milling of BPPs is accompanied by undesired re-deposition of gold in the central hole.

3.4.2 **Analyzing gold nanowires**

This chapter reports about the analysis of electrospun gold nanowires. It concentrates on the aspects of HIM imaging, whereas chapter 3.4.4 presents a full paper with synthesis and characterization of such nanowires. This work is done in collaboration with the group of Prof. Greiner in Marburg, and now in Bayreuth.

The wires are produced by electrospinning a polymer solution with gold nanoparticles (AuNPs). Subsequent annealing evaporates the polymer and melts the AuNPs to a continuous smooth wire.

In Figure 43 the different contrast effects of secondary electron (SE) and Rutherford backscattered ion (RBI) images are visible. The SE image in (a) shows the surface topography in detail. The lower part of the wire is only slightly visible, indicating a charge buildup due to the ion beam. The corresponding RBI image in (b) shows a different appearance. Due to the high energy of the backscattered ions, RBI images are not affected by charging. The high brightness of the complete wire leads to the conclusion that the wire actually consists of a high amount of material with high atomic number. As only gold and carbon are possible, it is identified as gold. At the positions where charging gets visible in the SE image, the wires seem not to be continuing in RBI mode, whereas the outline is still visible in the SE image (see arrows). It is very reasonable to conclude that in these positions leftover carbon acts as an insulator.

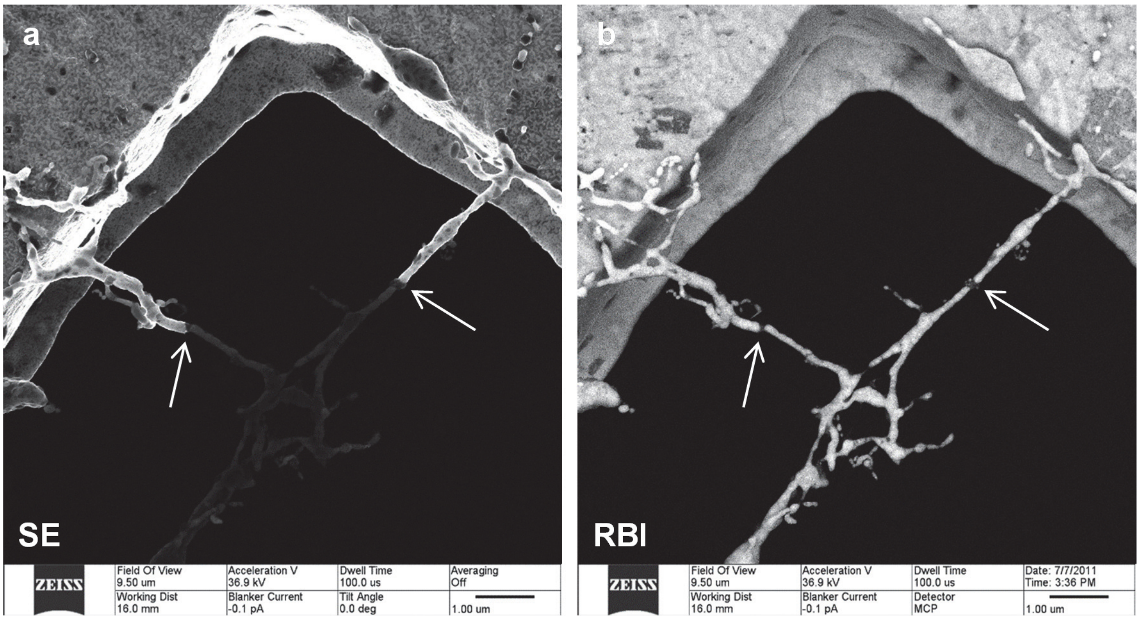

Figure 43: HIM images of gold nanowires, where both images were taken at the same time with the SE detector (a) and RBI detector (b). They are mechanically supported by a gold TEM grid on the upper part of the image.

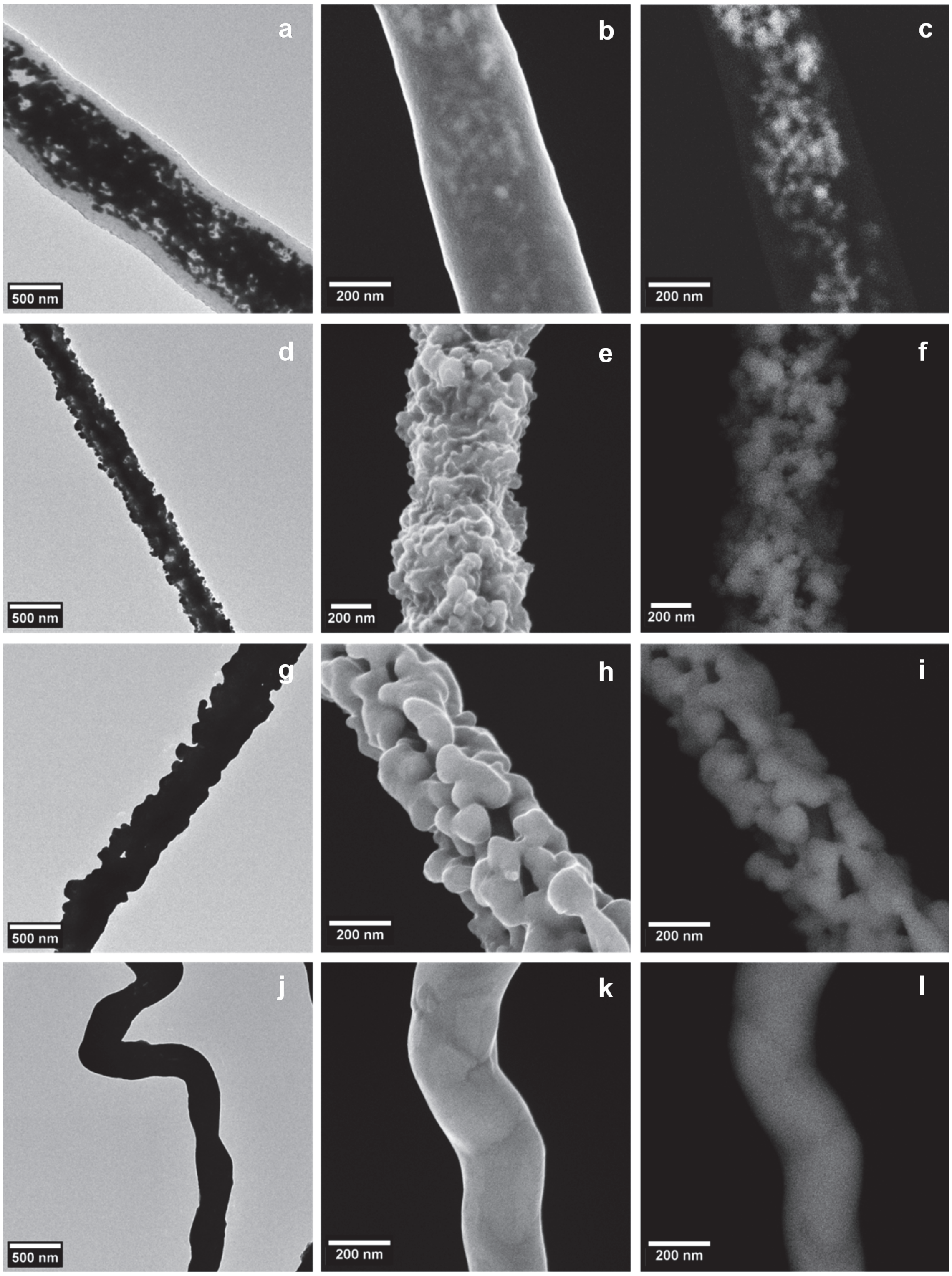

Figure 44: Micrographs depicting the temperature-induced transition to gold-nanowires (top to bottom). Left: TEM pictures; middle: HIM micrographs based on secondary electrons (SE) showing the surface and induced charging in the first row causing a low SE-yield; right: HIM images based on Rutherford backscattered ions highlighting areas of high gold content. Accepted by Macromolecular Rapid Communications, 2014.[98]

In a following experiment, such nanowires were modified before the annealing step. The fibers were coated with a highly thermally stable polymer to obtain more regular wires in the end. Due to this polymer, thermal treatment up to 1050 °C led to the degradation of the polymer material while fusing the gold aggregates in the confinement of the polymer tubes together.[98]

Figure 44 shows the effect of rising annealing temperature from top to bottom. Comparable TEM images (left column) are added to the HIM SE (middle column) and RBI images (right column). The polymer coating of the tubes degraded as the temperature increased, resulting in a very rough and inhomogeneous surface. At higher temperatures reaching up to 1050 °C, the remaining gold aggregates fused together and eventually led to continuous nanowires featuring a smooth surface. Throughout the transition, the average fiber diameter decreased significantly, whereas no insulating wires were found as in Figure 43.

3.4.3 **Summary: using RBI imaging in HIM**

RBI imaging adds the possibility to simultaneously acquire a second image which is sensitive to the elemental composition of the sample under investigation. In defect analysis on Boersch phase plates this information in combination with the other high resolution images were proven to be useful.

In the analysis of gold nanowires this combination was especially informative, as it is possible to distinguish between the two ingredients of the wires (carbon and gold). The combination with voltage contrast is advantageous in the assessment of defects in the wires as they get instantly visible.

3.4.4 Publication: Preparation of Continuous Gold Nanowires by Electrospinning of High-Concentration Aqueous Dispersions of Gold Nanoparticles (Small 2012)

This Chapter is reprinted with permission from Wiley. The original article appeared as:

> Gries K, Vieker H, Gölzhäuser A, Agarwal S and Greiner A 2012 Preparation of Continuous Gold Nanowires by Electrospinning of High-Concentration Aqueous Dispersions of Gold Nanoparticles *Small* **8** 1436–41

Contribution:

Helium Ion Microscopy was performed by the author.

Preparation of Continuous Gold Nanowires by Electrospinning of High-Concentration Aqueous Dispersions of Gold Nanoparticles

*Katharina Gries, Henning Vieker, Armin Gölzhäuser, Seema Agarwal, and Andreas Greiner**

Gold nanowires are prepared by the electrospinning of highly concentrated aqueous dispersions of gold nanoparticles (AuNPs) in the presence of poly(vinyl alcohol) and subsequent annealing at higher temperatures. Continuous wires of sintered AuNPs are obtained as a result of this process. The Au wires are characterized by transmission electron microscopy, helium ion microscopy, optical microscopy, and X-ray diffractometry.

1. Introduction

Metal nanofibers are of interest to the investigation of electrical and magnetic properties. Numerous examples of metal nanowires have been published in the literature.[1–15] These include nanowires made from Fe_3O_4 nanoparticles that were prepared via magnetic-field-induced self-assembly,[5] semiconductor nanowires of CoTe and NiTe alloy,[6] and palladium nanowires synthesized in hexagonal mesophases.[7] Recently, the preparation of copper,[8] cobalt,[9] and iron wires[9] out of electrospun fibers has been reported. Following this concept, composite nanofibers of metal salts and polymers were prepared by electrospinning of the corresponding solutions and subsequent thermal treatment under reductive conditions. Metal nanofibers with diameters less than 100 nm were obtained, which showed good electrical conductivity (Cu) and ferromagnetic properties (Co, Fe). Other examples of metal nanowires obtained from electrospun fibers include magnetic nickel nanowires,[10] platinum nanowires for methanol oxidation,[11] and Co_3O_4 nanofibers for selective glucose detection.[12] Pol et al. prepared gold nanowires using platinum electrodes in the electrospinning of metal salt solutions.[13] Furthermore, in some of the reported examples the conversion of metal salt/polymer composite fibers to metal wires by reduction in a hydrogen atmosphere at high temperatures is described, which is quite dangerous.[8,9,14,15] Gold nanowires prepared by other techniques have been reported in the literature as well.[16–25] Additional examples of the successful preparation of gold nanowires are those prepared by electrodeposition into nanoporous aluminum oxide templates, which had an average diameter of 47 nm.[22] In a different approach, Huo et al. prepared ultrathin gold nanowires with a diameter of only 1.6 nm by wet-chemical preparation.[24] Similar works were simultaneously published by Lu et al. and Wang et al.[25,26] The disadvantage of the above-mentioned approaches is the use of metal salts, which are highly corrosive, particularly in the case of precious metals, such as gold or platinum. The avoidance of corrosive metal salts is an advantage, which is not only important for the preparation of nanowires of precious metals by electrospinning, but also for other preparation techniques, such as hydrothermal preparation processes using a stainless steel autoclave.[27,28]

Several examples have been published of electrospun composite fibers with metal nanoparticles and polymers.[29–39] Examples are electrospun polyethylene oxide (PEO) fibers containing dodecanethiol-capped gold nanoparticles (AuNPs),[33] fibers of poly(ε-caprolactone) loaded with FePt particles,[34] nickel nanoparticles in polystyrene fibers,[35] and Ag nanoparticle dimers or larger aggregates in poly(vinyl alcohol) (PVA) fibers.[40] Further examples include the preparation of ferromagnetic iron oxide nanoparticles in electrospun poly(vinyl pyrrolidone) fibers[36] as well

---

K. Gries, Prof. S. Agarwal, Prof. A. Greiner
Department of Chemistry
Philipps-Universität Marburg
Hans-Meerwein-Strasse, 35032 Marburg, Germany
E-mail: greiner@staff.uni-marburg.de
H. Vieker, Prof. A. Gölzhäuser
Physik Supramolekularer Systeme und Oberflächen
Universität Bielefeld
Universitätsstrasse 25, 33615 Bielefeld, Germany

DOI: 10.1002/smll.201102308

as silver nanoparticles in polyacrylonitrile nanofibers.[38] Following the concept of electrospinning, Long et al. prepared Au/polyaniline microfibers with a core/shell structure with a diameter of the gold-containing inner core of 140–180 nm.[37] In a similar approach by Pol et al., a solution of gold acid in aqueous poly(acrylic acid) was electrospun to yield gold-containing polymer fibers.[13] In another study, Park et al. presented gold nanowires prepared from electrospun polystyrene-*block*-poly(4-vinylpyridine) fibers, which were immersed in a gold salt solution and consecutively treated in oxygen plasma.[41] These examples clearly prove that, in general, the preparation of gold wires by electrospinning should be possible.

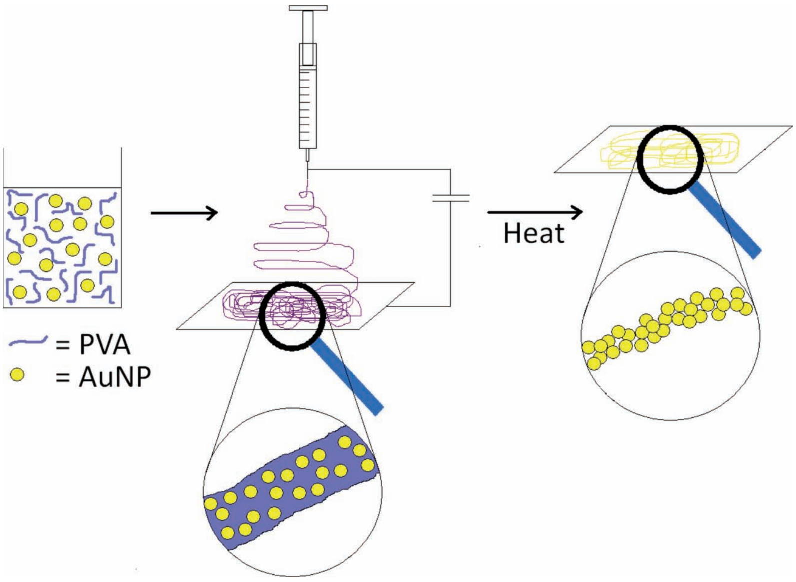

Figure 1. Schematic illustration of the preparation steps of gold nanowires via electrospinning.

Our hypothesis was that access to gold wires should be possible through polymer nanofibers with a high content of AuNPs. This is in itself a challenge but could be useful for other applications as well, for example catalysis, which is not the topic of this contribution. Gold nanowires should be obtainable by annealing of such composite nanofibers. The annealing process should result in decomposition of the polymer and fusion of AuNPs, thereby forming the corresponding gold nanowires. According to the literature, the melting point of small particles is below that of bulk material[42,43] and the interaction between particles affects the melting point.[44] We assumed that these effects would allow the fusion of the AuNPs at lower temperatures than the bulk melting temperature, and thereby prevent the nanowires from disintegrating in shape at fusion temperature. We assumed that the success of gold nanowire formation from AuNPs, and thus its transition from nanoparticles to bulk state, should be accompanied by significant changes in the solid-state structure, which can be analyzed by wide-angle X-ray scattering (WAXS). PVA was used as the matrix polymer due to its excellent electrospinning properties, but accepting a relatively high carbon residue which is expected to remain after pyrolysis of the fibers.[45] To analyze gold wires and carbon residues, we employed a new technique called helium ion microscopy, which is superior to energy-dispersive X-ray (EDX) analysis in the detection of carbon, which we used here for comparison.

2. Results and Discussion

The preparation of the gold nanowires was carried out in two steps, as schematically shown in **Figure 1**. First, PVA/AuNP composite fibers were prepared by electrospinning, followed by pyrolysis of PVA and simultaneous formation of the gold wires by sintering of the AuNPs.

PVA was used as the matrix polymer due to its excellent electrospinning properties. A general problem with all organic compounds that are used as templates and removed by pyrolysis is some percentage of carbon residue, which is expected to remain after pyrolysis of the fibers. It is about 2 wt% in the case of PVA.[45] AuNPs with an average size of approximately 13 nm (**Figure 2**a) were used for electrospinning with PVA. Aqueous dispersions with a high content of AuNPs were prepared by reducing gold acid with trisodium citrate. The concentration of the resulting AuNP dispersion

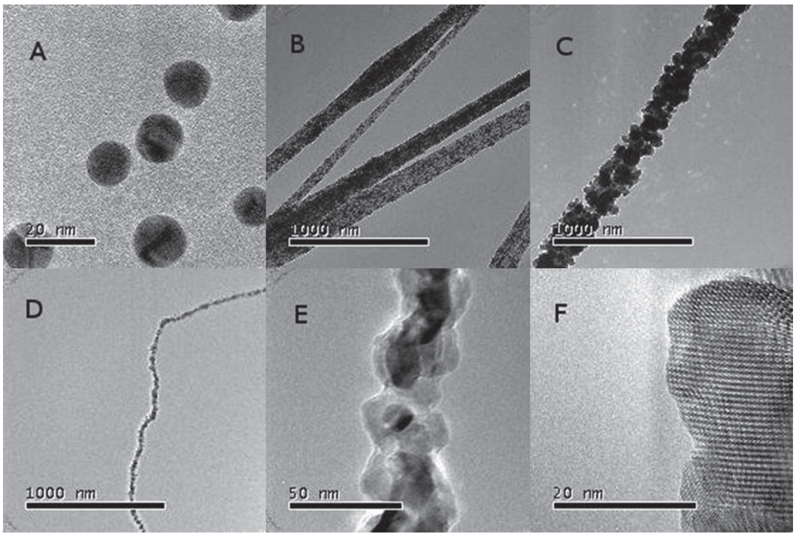

Figure 2. Transmission electron microscopy (TEM) images of citrate-capped AuNPs from aqueous dispersion (A), electrospun PVA/AuNP composite fibers (B), after annealing in air (C–E), and a high-resolution TEM image of a gold wire (F).

was increased to 0.125 wt% by water evaporation in the presence of PVA. Excess trisodium citrate was removed by dialysis against deionized water, sodium dodecyl sulfate (SDS) was added, and then evaporation of water was continued to increase the concentration to 7.1 wt% Au and 7.1 wt% PVA. As a result, a viscous dark purple aqueous dispersion composed of 50% PVA and 50% AuNPs was obtained. The dispersion showed a maximum UV/Vis absorption at 520 nm, which did not change during the individual processing steps (Supporting Information). However, the zeta potential changed during the individual processing steps. While a citrate-stabilized AuNP dispersion lacking the addition of PVA showed a negative zeta potential of –48.66 mV, it changed to 1.52 mV after the addition of PVA. After purification by dialysis, the zeta potential became negative (–17.60 mV). The size distribution measured by dynamic light scattering (DLS) gave mainly constant values. Before the addition of PVA, the number distribution value was 11.2 ± 2.6 nm, but after adding PVA, the value slightly increased to 13.9 ± 3.8 nm and was 13.2 ± 1.2 nm after dialysis. As DLS gave the hydrodynamic radius of the particles, it was not surprising that the values slightly increased after addition of PVA.

The readily prepared dispersion was directly used for the preparation of PVA/AuNP nanofibers by electrospinning under standard conditions. Clearly, a dense population of AuNPs of 49% by weight (according to elemental analysis) relative to PVA could be observed in electrospun PVA nanofibers by TEM imaging (Figure 2B). Annealing of these AuNP/PVA composite nanofibers in air at 300 °C for 7 h then at 500 °C for 1 h resulted in almost quantitative pyrolysis of PVA and, hence, the formation of gold nanowires (Figure 2C–E). In the high-resolution image (Figure 2F) the crystalline nature of the nanowire could be verified. A well-developed crystalline gold lattice as well as a rather uneven structure of the gold wires could be seen in the TEM images (Figure 2C–F).

WAXS analyses of AuNPs obtained from the dispersion and gold nanowires showed significant differences (**Figure 3**). Amorphous halos were observed for PVA/AuNP composite fibers but strong reflexes were observed for gold nanowires. These reflexes correspond well with the reflexes for bulk gold.[46]

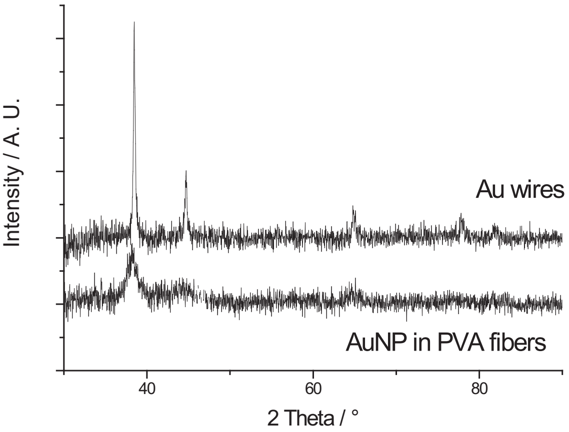

Figure 3. X-ray diffraction diagram ($Cu_{K\alpha}$ radiation) of submicrometer gold wires on a glass slide. The background signal of the glass slide was subtracted. Upper curve: gold wires after 7 h of annealing; lower curve: AuNPs in electrospun PVA fibers.

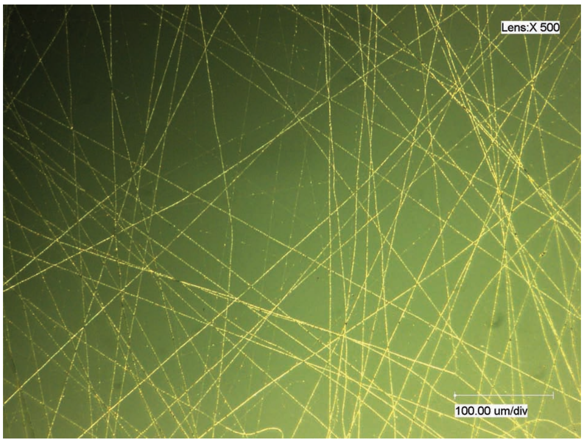

Figure 4. Optical microscopy image of gold nanowires on a mica slide; scale bar: 100 µm.

Inspection of the gold nanowires by optical microscopy showed long wires at least several millimeters in length, which was not unexpected as electrospun fibers tend to be long (**Figure 4**).

The nanowires were also characterized by helium ion microscopy (HIM). HIM is a recently developed imaging technique that shares similarities with scanning electron microscopy (SEM). In HIM, a finely focused beam of helium ions with a diameter down to 0.25 nm is scanned over the sample, and the secondary particles generated by the He^+ impact are detected. Two images are obtained simultaneously: the intensity of secondary electrons (SEs) and of Rutherford backscattered ions (RBIs).[47]

In SE imaging, the topology of the sample produces contrast as more electrons are ejected when the He^+ beam hits the sample at glancing incidence. The energy of the SE is very low, which results in a high surface sensitivity. Electrical fields can further hinder the low-energy SEs from leaving the sample, thus leading to an additional voltage contrast that allows the visualization of insulated sample regions.

In RBI imaging, backscattered He^+ ions are measured. As these originate from the bulk of the sample and possess a high energy, the RBI signal is not sensitive to topology or charging. The rate of backscattering rises with the atomic number of the sample material; however, oscillations have been reported.[48] In our case, gold has one of the highest backscatter yields, producing a clear contrast to carbon, which has a very low yield.

For HIM measurements, nanowires were prepared on a gold grid. **Figure 5**A shows an overview of a grid with suspended nanowires. They were found all over the grid, on the gold mesh as well as freely standing in the gaps. The SE image shows topological contrast, whereas the RBI image shows the elemental contrast. In the latter, both grid and wires appear in the same gray value as both consist of gold. In Figure 5B–D**,** SE and RBI images of freestanding nanowires are shown together with a part of the supporting grid at the bottom

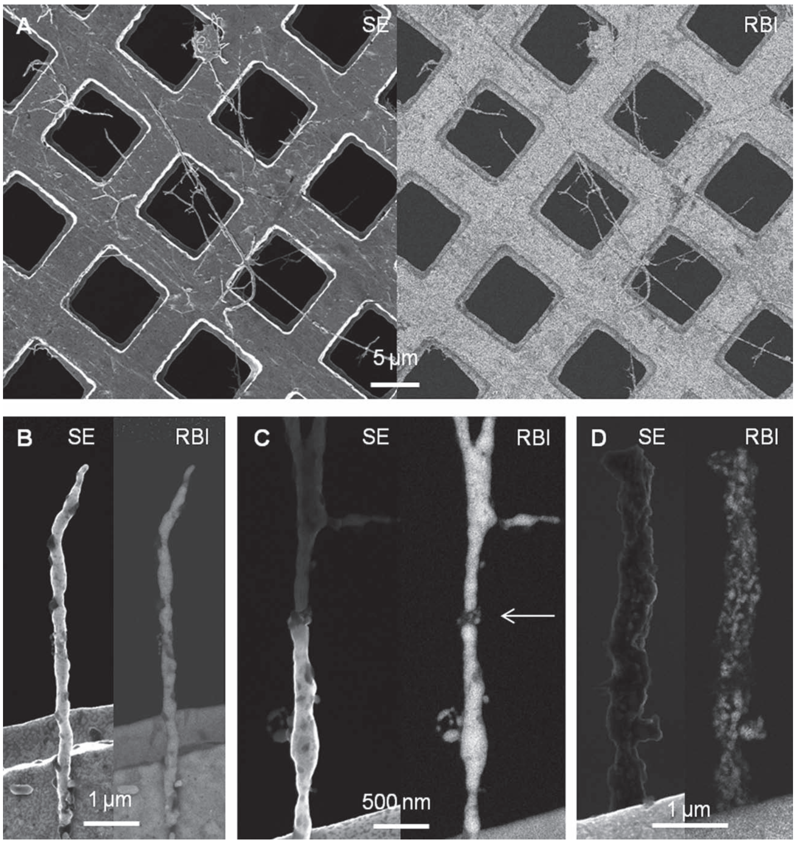

Figure 5. HIM measurement of gold nanowires showing secondary electron (SE) and Rutherford backscattered ion (RBI) images that were recorded simultaneously. A) The wires were spun and annealed on a supporting gold grid. B,C) Only a little contamination is visible on the wires. In (C) the conductivity of a wire is interrupted at the white arrow, thus causing a darker appearance in the upper part of the SE image, whereas in the RBI image, the small interrupting gap is visible. There, presumably leftover carbon acts as isolator. D) A fiber before the final annealing step at 500 °C. The SE image is very dark, which indicates nonconductive behavior. This is supported by the RBI image, where the AuNPs appear as single bright spots with a lot of remaining polymer between them.

of the image. Figure 5B shows a typical wire consisting of merged AuNPs. Some darker spots on the wire surface result from the remaining polymer. The appearance of some wires in SE mode changes from bright to dark from one position to another, whereas the RBI mode indicates that there is still gold in place. In Figure 5C, it is shown that such a wire is interrupted by a region of low RBI yield, presumably carbon (see arrow). Above this carbonaceous region, the SE image appears darker, which indicates localized electric charging.

Gold nanowires that were not annealed at 500 °C were found to still contain residual polymer between the AuNPs. They appear dark in SE mode, where mostly the outline is visible (see Figure 5D). In RBI mode, a complex structure of particles and gaps was visible, which was interpreted as the individual AuNPs still within the polymer matrix. The AuNPs were not electrically connected, and the wire was showing insulating behavior in the SE image.

The results of HIM contrast with those of the EDX spectra of the annealed wires, which did not show any signal for leftover carbon (Supporting Information). As EDX analysis has a relatively low sensitivity towards carbon, the method is less suitable for checking quantitative pyrolysis of the matrix polymer.

3. Conclusion

Highly concentrated aqueous dispersions of AuNPs were obtained in the presence of PVA. Clearly, PVA stabilized highly concentrated dispersions of AuNPs against aggregation. These dispersions were used for the preparation of PVA nanofibers with a high content of nonaggregated AuNPs. Annealing PVA/AuNP composite nanofibers at 300–500 °C in air resulted in gold nanowires, which represent solid structures like bulk gold. The nonaggregated AuNPs were welded to bulk Au at a temperature several hundred degrees lower than the melting point of bulk Au. Defect analysis of gold nanowires with an extremely high resolution was performed by HIM. EDX resolution was not sufficient for monitoring such defects. The HIM technique, in future, could be of great help in understanding the properties of nanowires, such as electrical conductivity. The electrical conductivity of gold nanowires prepared by electrospinning originating from AuNPs of different sizes and shapes, as well as a more detailed study about the effects of polymer concentration, particle distribution in the fibers, and annealing conditions, will be the topic of forthcoming articles.

4. Experimental Section

Materials: Hydrogen tetrachloroaurate(III) trihydrate ($HAuCl_4 \cdot 3H_2O$) was purchased from ChemPur. Trisodium citrate and SDS were purchased from Aldrich. PVA (56–98; M_w = 195 000 g mol^{-1}) was purchased from Kuraray. All chemicals were used without further purification. Dialysis was performed in Visking cellulose membranes with a molecular weight cutoff at 14 000, purchased from Carl Roth.

Measurements: Thermogravimetric analysis (TGA) was carried out on a Mettler 851 TG module under a nitrogen atmosphere at a flow rate of 50 mL min^{-1} and a heating rate of 10 K min^{-1}. DLS and zeta potential measurements were carried out in a flow cell using a Delsa Nano instrument by Beckman Coulter. CHN analyses were carried out on a Elementar Vario EL III analyzer. The amount of gold was determined with an atomic absorption spectrophotometer 5000 (Perkin–Elmer) after dissolving the sample in perchloric acid and aqua regia.

Samples of fibers for TEM were prepared by electrospinning directly onto either a copper grid (300 mesh, Quantifoil) or a gold grid (1500 mesh, Agar Scientific). To measure annealed samples, grids with fibers were heated in an oven and were consequently submitted to TEM analysis. Samples of free AuNPs were prepared by dipping a carbon-covered copper grid (carbon support films, 300 mesh, Quantifoil) into the nanoparticle-containing aqueous solution. TEM images were obtained using a JEOL JEM 3010 microscope with an acceleration voltage of 300 kV and an integrated four-megapixel CCD camera.

EDX spectra were recorded using a CamScan-4DV instrument (by CamScan) equipped with a Pioneer detector and an ultrathin window (Vogager, Thermo Noran). X-ray diffraction measurements were performed using an X'Pert-PRO diffractometer (by PANalytical) applying $Cu_{K\alpha}$ radiation and with a PIXcel detector. Samples were measured on glass slides in the range from 30 to 90° for 10 min. Optical microscopy was carried out using a Keyence VHX-100 digital microscope.

Helium ion microscopy (HIM) was performed with a Carl Zeiss Orion Plus microscope. The helium ion beam was operated with an acceleration voltage of about 36 kV, and secondary electrons (SEs) were collected by an Everhart–Thornley detector. Rutherford backscattered ions (RBIs) were detected by a microchannel plate (MCP) detector. Samples were prepared on gold grids (1500 mesh, Agar Scientific).

Detailed descriptions of the electrospinning setup were published in previous works.[49] Annealing of the samples was carried out in an electrical tube furnace.

Synthesis Procedures: Citrate-capped AuNPs were prepared using a slightly modified approach according to Turkevich et al.[50] In a typical procedure, a solution of $HAuCl_4 \cdot 3H_2O$ (125 mg) in deionized H_2O (500 mL) and a solution of trisodium citrate (500 mg) in deionized H_2O (500 mL) were heated separately to 60 °C, then poured together into an open beaker. After approximately 10 min, a color change occurred from pale yellow to black-blue to wine red. When the color change started, the mixture was heated to boiling. After 30 min of boiling, a 10 wt% PVA solution (625 mg) was added and boiling was continued until the total volume was reduced to approximately 50 mL. The remaining mixture was transferred to a dialysis tube and dialyzed against deionized water for 24 h; the dialysis bath was changed three times to remove excess trisodium citrate. SDS (3.1 mg, 5 wt% relative to PVA) was added to the remaining solution and boiling was continued to reach a total weight of 0.94 g.

Electrospinning: Electrospinning of the AuNP–PVA dispersion was carried out by applying a voltage of 10 kV on both electrodes at a distance of 15 cm. The flow rate of the solution was adjusted to 300 µL h^{-1}. Glass, aluminum foil, or baking paper were used as substrates. The temperature was 21 °C and the air humidity was 42%. Elemental analysis calcd for PVA–AuNP fibers: C 24.02, H 4.03, Au 50.00; found: C 28.89, H 4.72, Au 49.44.

To anneal the fibers, samples on glass slides were placed into an electric oven and heated in air at 300 °C for 7 h and then at 500 °C for 1 h.

Supporting Information

Supporting Information is available from the Wiley Online Library or from the author.

Acknowledgements

We thank Dr. Klaus Harms for help with the X-ray diffraction measurements and Michael Hellwig for the EDX measurements.

[1] J. B. Yang, H. Xu, S. X. You, X. D. Zhou, C. S. Wang, W. B. Yelon, W. J. James, *J. Appl. Phys.* **2006**, *99*, 08Q507.

[2] Y. Sun, Y. Yin, B. T. Mayers, T. Herricks, Y. Xia, *Chem. Mater.* **2002**, *14*, 4736.

[3] S. Vaddiraju, H. Chandrasekaran, M. K. Sunkara, *J. Am. Chem. Soc.* **2003**, *125*, 10792.

[4] A. W. Hassel, B. B. Rodriguez, S. Milenkovic, A. Schneider, *Electrochim. Acta* **2005**, *51*, 795.

[5] R. Sheparovych, Y. Sahoo, M. Motornov, S. Wang, H. Luo, P. N. Prasad, I. Sokolov, S. Minko, *Chem. Mater.* **2006**, *18*, 591.

[6] Q. Peng, Y. Dong, Y. Li, *Inorg. Chem.* **2003**, *42*, 2174.

[7] F. Ksar, G. Surendran, L. Ramos, B. Keita, L. Nadjo, E. Prouzet, P. Beaunier, A. Hagge, F. Audonnet, H. Remita, *Chem. Mater.* **2009**, *21*, 1612.

[8] M. Bognitzki, M. Becker, M. Graeser, W. Massa, J. H. Wendorff, A. Schaper, D. Weber, A. Beyer, A. Gölzhäuser, A. Greiner, *Adv. Mater.* **2006**, *18*, 2384.

[9] M. Graeser, M. Bognitzki, W. Massa, C. Pietzonka, A. Greiner, J. H. Wendorff, *Adv. Mater.* **2007**, *19*, 4244.

[10] N. A. M. Barakat, B. Kim, H. Y. Kim, *J. Phys. Chem. C* **2009**, *113*, 531.

[11] J. M. Kim, H. I. Joh, S. M. Jo, D. J. Ahn, H. Y. Ha, S. A. Hong, S. K. Kim, *Electrochim. Acta* **2010**, *55*, 4827.

[12] Y. Ding, Y. Wang, L. A. Su, M. Bellagamba, H. Zhang, Y. Lei, *Biosens. Bioelectron.* **2010**, *26*, 542.

[13] V. G. Pol, E. Koren, A. Zaban, *Chem. Mater.* **2007**, *20*, 3055.

[14] H. Wu, R. Zhang, X. Liu, D. Lin, W. Pan, *Chem. Mater.* **2007**, *19*, 3506.

[15] Y. S. Kim, S. H. Nam, H.-S. Shim, H.-J. Ahn, M. Anand, W. B. Kim, *Electrochem. Commun.* **2008**, *10*, 1016.

[16] Y. Kang, X. Ye, C. B. Murray, *Angew. Chem. Int. Ed.* **2010**, *122*, 1.

[17] K. Vasilev, T. Zhu, M. Wilms, G. Gillies, I. Lieberwirth, S. Mittler, W. Knoll, M. Kreiter, *Langmuir* **2005**, *21*, 12399.

[18] J. Burdick, E. Alonas, H.-C. Huang, K. Rege, J. Wang, *Nanotechnology* **2009**, *20*, 065306.

[19] M. Wilms, J. Conrad, K. Vasilev, M. Kreiter, G. Wegner, *Appl. Surf. Sci.* **2004**, *238*, 490.

[20] S. Karim, K. Maaz, G. Ali, W. Ensinger, *J. Phys. D: Appl. Phys.* **2009**, *42*, 185403.

[21] J. C. Zhou, Y. Gao, A. A. Martinez-Molares, X. Jing, D. Yan, J. Lau, T. Hamasaki, C. S. Ozkan, M. Ozkan, E. Hu, B. Dunn, *Small* **2008**, *4*, 1507.

[22] K. Biswas, Y. Qin, M. DaSilva, R. Reifenberger, T. Sands, *Phys. Status Solidi A* **2007**, *204*, 3152.

[23] Y. Peng, T. Cullis, B. Inkson, *Appl. Phys. Lett.* **2008**, *93*, 183112.

[24] Z. Huo, C.-K. Tsung, W. Huang, X. Zhang, P. Yang, *Nano Lett.* **2008**, *8*, 2041.

[25] X. Lu, M. S. Yavuz, H.-Y. Tuan, B. A. Korgel, Y. Xia, *J. Am. Chem. Soc.* **2008**, *130*, 8900.

[26] C. Wang, Y. Hu, C. M. Lieber, S. Sun, *J. Am. Chem. Soc.* **2008**, *130*, 8902.

[27] W. Xu, S.-H. Yu, *Small* **2009**, *5*, 460.

[28] M.-R. Gao, W.-H. Xu, L.-B. Luo, Y.-J. Zhan, S.-H. Yu, *Adv. Mater.* **2010**, *22*, 1977.

[29] Y. Wang, Y. Li, G. Sun, G. Zhang, H. Liu, J. Du, S. Yang, J. Bai, Q. Yang, *J. Appl. Polym. Sci.* **2007**, *105*, 3618.

[30] K. M. Sawicka, P. Gouma, *J. Nanopart. Res.* **2006**, *8*, 769.

[31] X. Lu, C. Wang, Y. Wei, *Small* **2009**, *5*, 2349.

[32] Z. Li, H. Huang, C. Wang, *Macromol. Rapid Commun.* **2006**, *27*, 152.

[33] G.-M. Kim, A. Wutzler, H.-J. Radusch, G. H. Michler, P. Simon, R. A. Sperling, W. Parak, *Chem. Mater.* **2005**, *17*, 4949.
[34] T. Song, Y. Z. Zhang, T. J. Zhou, *J. Magn. Magn. Mater.* **2006**, *303*, e286.
[35] X. Chen, S. Wei, C. Gunesoglu, J. Zhu, C. S. Southworth, L. Sun, A. B. Kark, D. P. Young, Z. Guo, *Macromol. Chem. Phys.* **2010**, *211*, 1775.
[36] C. R. Lin, T. C. Tsai, M. Chung, S. Z. Lu, *J. Appl. Phys.* **2009**, 105.
[37] Y. Long, K. Huang, J. Yuan, D. Han, L. Niu, Z. Chen, C. Gu, A. Jin, J. L. Duvail, *Appl. Phys. Lett.* **2006**, *88*, 162113.
[38] Y. Wang, Q. Yang, G. Shan, C. Wang, J. Du, S. Wang, Y. Li, X. Chen, X. Jing, Y. Wei, *Mater. Lett.* **2005**, *59*, 3046.
[39] X. Lu, Y. Zhao, C. Wang, *Adv. Mater.* **2005**, *17*, 2485
[40] D. He, B. Hu, Q.-F. Yao, K. Wang, S.-H. Yu, *ACS Nano* **2009**, *3*, 3993.
[41] S. Park, S. C. Moon, D. Chen, R. J. Farris, T. P. Russell, *J. Mater. Chem.* **2010**, *10*, 1198.
[42] S. L. Lai, J. Y. Guo, V. Petrova, G. Ramanath, L. H. Allen, *Phys. Rev. Lett.* **1996**, *77*, 99.
[43] J. Lee, J. Lee, T. Tanaka, H. Mori, *Nanotechnology* **2009**, *20*, 475706.
[44] O. A. Yeshchenko, I. M. Dmitruk, K. P. Grytsenko, V. M. Prokopets, A. V. Kotko, *J. Appl. Phys.* **2009**, *105*, 094326.
[45] J. A. Lewis, *Annu. Rev. Mater. Sci.* **1997**, *27*, 147.
[46] I.-K. Suh, H. Ohta, Y. Waseda, *J. Mater. Sci.* **1988**, *23*, 757.
[47] L. Scipioni, C. A. Sanford, J. Notte, B. Thompson, S. McVey, *J. Vac. Sci. Technol. B* **2009**, *27*, 3250.
[48] S. Sijbrandij, B. Thompson, J. Notte, B. W. Ward, N. P. Economou, *J. Vac. Sci. Technol. B* **2008**, *26*, 2103.
[49] A. Greiner, J. H. Wendorff, *Angew. Chem. Int. Ed.* **2007**, *46*, 5670.
[50] B. V. Enüstün, J. Turkevich, *J. Am. Chem. Soc.* **1963**, *85*, 3317.

Received: November 1, 2011
Revised: December 19, 2011

4 Lithography and nanomachining with helium ions

In earlier years of HIM, lithographic applications and especially direct modification of materials was a major focus of the user community. This has good reasons, as the helium beam allows directly visible improvements to the established Gallium Focused Ion Beam (Ga-FIB) technique. The length scales available in direct materials modification are well below compared to what was previously possible due to the small beam diameter and sputter rate. Also, sample contamination by helium-ion implantation is usually less problematic than with gallium ions.[99] On the other hand - a severe disadvantage in HIM is the so-called swelling of substrates, rendering the lithography of extended structures difficult. Swelling is the accumulation of helium in deeper regions of a solid, which are actually forming gas filled bubbles in depths of some 100 nm in the substrate that cause a deformation of the surface.[100] Recently, strategies were published to reduce this effect.[101]

In resist-based lithography, the ability to write 6 nm sized dots in hydrogen silsesquioxane (HSQ, a typical high resolution resist) was demonstrated. This is comparable to electron-beam systems, where the limiting factor in both cases seems to be the photoresist itself.[102] An advantage of HIM was the drastic reduction of any proximity effect, allowing a 14 nm pitch of the dots (repeat distance). Potentially, there could be advantages in the exposure of very thick resist systems as the He+ beam is less scattered within solid material.

Direct writing or sputtering of features in samples has been demonstrated by a number of researchers. Drilling of defined holes in silicon nitride membranes has also been performed in Bielefeld,[103,104] but was first reported by Adam Hall who investigated this application in depth.[105–107] Precise cutting of graphene structures with nanometer precision is performed by various groups.[60–63,108–110] Unfortunately, graphene itself tends to be very sensitive to the He ion beam, loosing its unique properties already at low ion doses.[111,112] Another focus of the community are gold nanostructures, which are produced in manifold variations.[113–118]

4.1 Lithography with the Orion Plus HIM

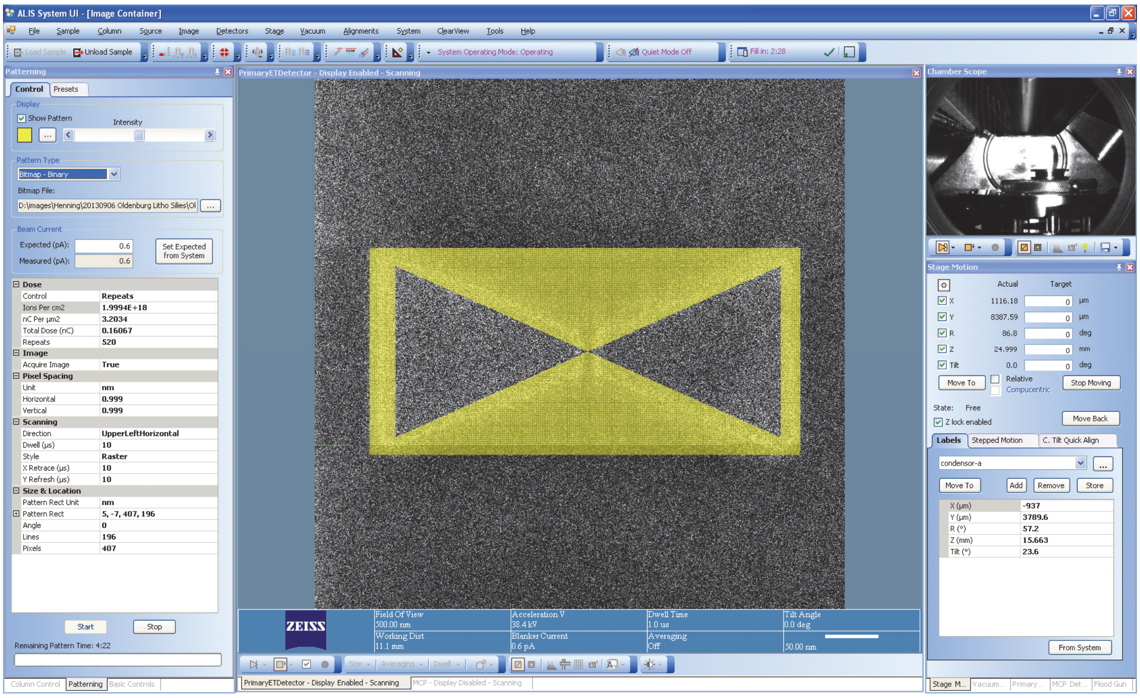

☑ Show Pattern

Pattern Type: Bitmap - Binary

Bitmap File: D:\images\Henning\20130906 Oldenburg Litho Silies\Ol

Beam Current

Expected (pA): 0.6

Measured (pA): 0.6

Set Expected from System

Dose	
Control	Repeats
Ions Per cm2	1.9994E+18
nC Per µm2	3.2034
Total Dose (nC)	0.16067
Repeats	520
Image	
Acquire Image	True
Pixel Spacing	
Unit	nm
Horizontal	0.999
Vertical	0.999
Scanning	
Direction	UpperLeftHorizontal
Dwell (µs)	10
Style	Raster
X Retrace (µs)	10
Y Refresh (µs)	10
Size & Location	
Pattern Rect Unit	nm
Pattern Rect	5, -7, 407, 196
Angle	0
Lines	196
Pixels	407

Remaining Pattern Time: 4:22

Field Of View	Acceleration V	Dwell Time	Tilt Angle
500.00 nm	38.4 kV	1.0 us	0.0 deg
Working Dist	Blanker Current	Averaging	
11.1 mm	0.6 pA	Off	50.00 nm

	Actual	Target	
☑ X	1116.18	0	µm
☑ Y	8387.59	0	µm
☑ R	86.8	0	deg
☑ Z	24.999	0	mm
☑ Tilt	0.0	0	deg

☐ Relative

☐ Compucentric

State: Free

☑ Z lock enabled

condensor-a

X (µm)	-937
Y (µm)	3789.6
R (°)	57.2
Z (mm)	15.663
Tilt (°)	23.6

Figure 45: Screenshot of a typical lithography task with the Orion Plus User Interface (UI). The patterning settings are in the left column. In the middle, the writing pattern is overlaid on the last image taken. The right column shows an IR-camera live view in the main chamber and the stage position menu.

The tasks in this work were performed with the in-build patterning tool of the microscope user interface. It allows to pattern lines and boxes, as well as bitmap files with a limited number of pixels (~600x600 pixel). It is possible to use the pixel brightness value of such bitmaps as multiplication factor to the dwell time of the written point. Unfortunately, the ion dose calculation then has to be done manually.

Recently, a dedicated patterning system has been installed to the Orion in Bielefeld. This allows more sophisticated writing strategies and the automation of processes.

4.2 Helium-ion milled gold nanoantennas for plasmonic applications

Plasmonic nanoantennas are versatile tools for coherently controlling and directing light on the nanoscale. For these antennas, current fabrication techniques such as electron beam lithography (EBL) or focused ion beam (FIB) milling with Ga^+-ions routinely achieve feature sizes above the 10 nm range (see Figure 46a,b).

This study is a cooperation with Martin Silies and Heiko Kollmann from Oldenburg University. It employed a combined approach of gallium-FIB and helium-ion lithography (HIL). A direct fabrication of such structures only by HIM is impossible due to the low sputter yield (time), and substrate swelling by helium accumulation in bubbles.[100] The goal of this study is the fabrication of better defined nanoantennas for improved optical activity. At the end, Gold bowtie antennas with less than 6 nm gap size were fabricated with single-nanometer accuracy and high reproducibility (Figure 46d-f).

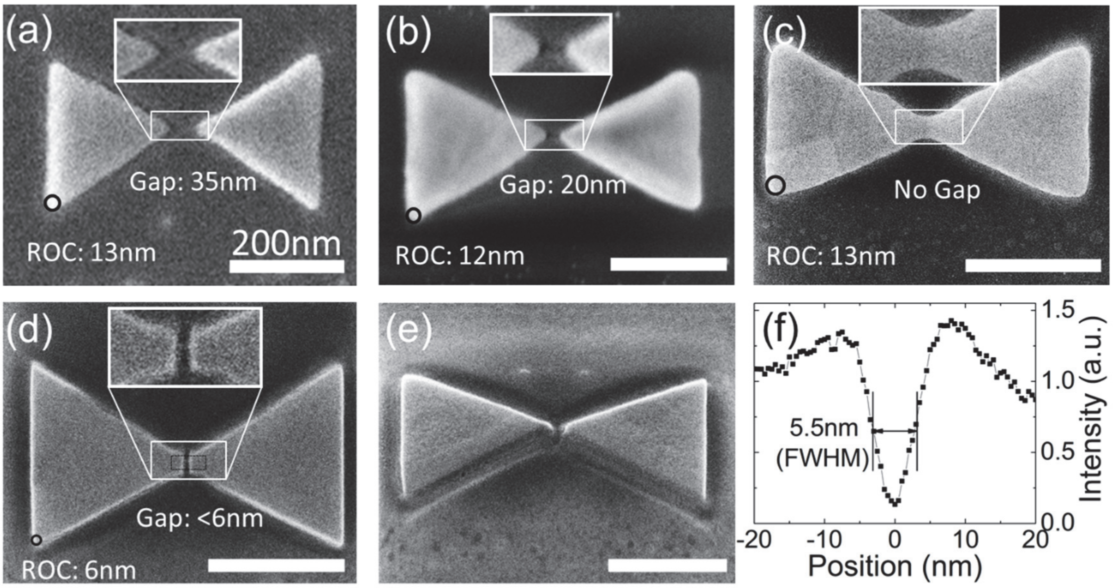

Figure 46: SEM (a−c) and HIM (d,e) images of bowtie nanoantennas fabricated by Ga - ion (a−c) and He - ion (d−f) beam milling. (a,b):Antenna before- and after opminization of the FIB milling procedure. In all cases, there are rounded corners with a radius of curvature (ROC) of about 13 nm. (d): With HIL, the corners are considerably smaller, and a much smaller gap size of less than 6 nm can be routinely obtained. (e) Tilted view of the same antenna (angle 35°). (f) Plot of the SE intensity of image (d), indicating a gap width of 5.5 nm. All scale bars are 200 nm long. Reprinted with permission.[119]

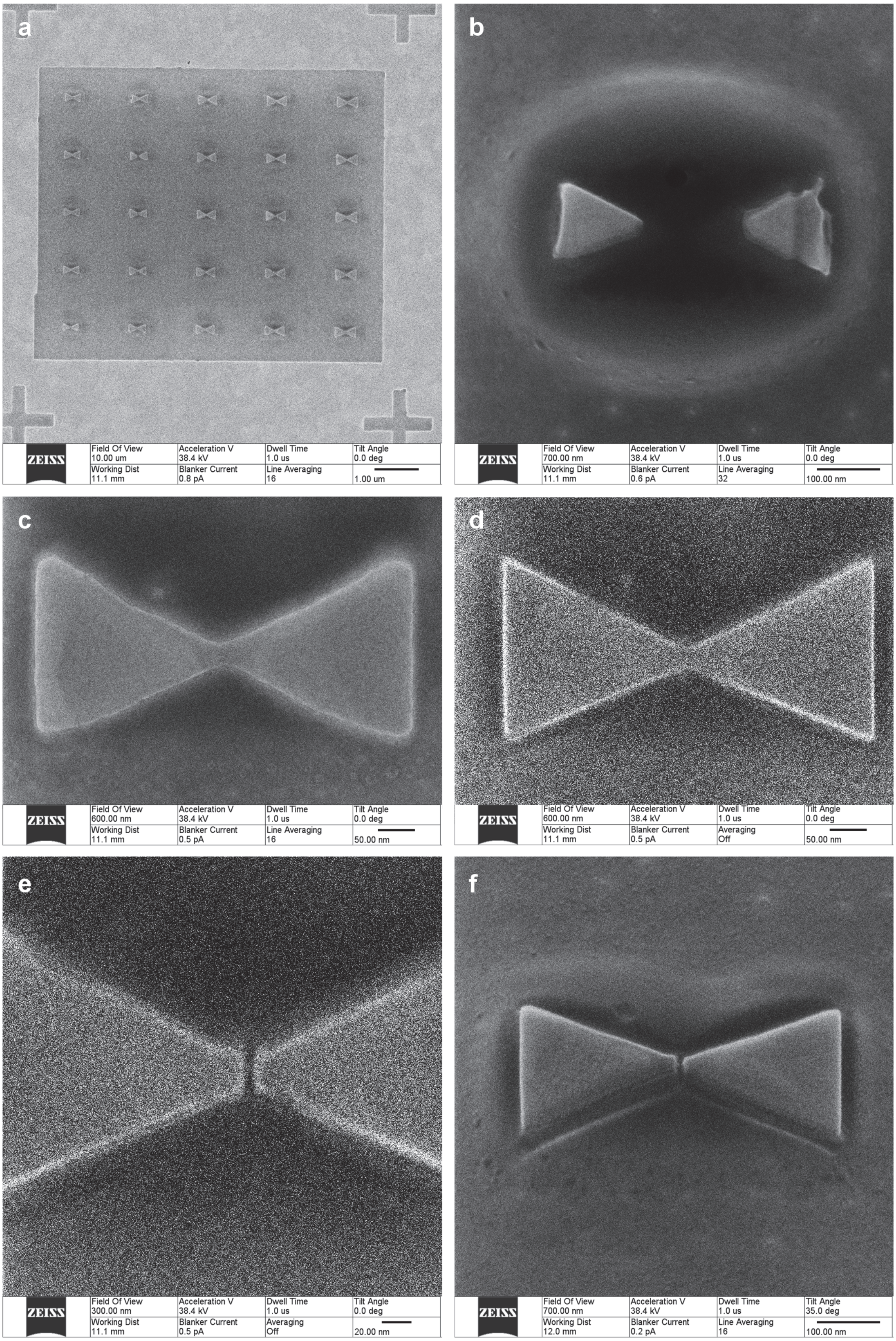

Figure 47: Milling of Bow-Ties by Helium-Ion lithography (HIL). (a): Typical structure prepared ex-situ by Ga-FIB. (b): structure after milling a pre-structured bow-tie with the mask of Figure 45. Helium implantation in the substrate causes swelling and severe destruction of the intended structure. (c-f): fabrication path of a final bow-tie using HIL starting with the structure prepared by conventional Ga-FIB: first the edges are sharpened (d), followed by the final cut in the middle. (f): tilted image of the final structure with well defined, steep edges. The fabrication process and several imaging scans induced a slight swelling of the substrate.

Other HIM groups investigated similar approaches with pre-structured gold substrates made by either resist based e-beam lithography or direct FIB milling. They achieved sub-10 nm feature sizes by HIM milling and produced plasmonic structures with gaps of similar size as presented here. They studied simple dipole structures (rectangles) and investigated the gap width[116] or the effect of cutting of only a lateral or vertical part of the gap.[113]

New in this study is the use of bow-ties as structures, and the enhancement of all edges around the structure. In addition, it is the first time where nonlinear optical properties of HIL-fabricated nanostructures are analyzed.

All antennas produced in this study were fabricated in a 30 nm thick polycrystalline gold film evaporated onto a glass substrate. Bow-tie structures without gap are milled by Ga-FIB in 5x5 fields as visible in Figure 47a. The samples with bow-ties as in Figure 47c are then introduced into the HIM. As next step, the outer boundary is carefully sharpened to obtain well-defined borders and edges. This material removal is done by applying about 1.8E18 Ions / cm², using 1 nm pixel spacing and repeated scanning. A corner radius of 6 nm and smaller is easily obtained. Subsequently, the two triangles are separated by writing a single line scan with 100 ms dwell time and 1 nm pixel spacing at 0.5 pA. These values are a compromise between the size of the gap and the assurance of a thorough cut through the gold layer.

Figure 47f is a tilted view showing the excellent aspect ratios of the final structure. Also, a slight bending caused by substrate swelling is visible. This was caused by the milling process and a high number of slow imaging scans done on this structure to obtain images in high quality. All bow-tie structures investigated for optical measurements were only imaged at the minimal possible level needed to properly align the lithography process. In any case, swelling did not cause disturbing effects here.

The samples were then irradiated with ultrashort (~8 fs) laser pulses in the near-infrared spectral range. Such irradiation induces surface plasmons in metallic structures. In case of high intensities, non-linear effects cause the emission of higher harmonic photons, light with a multiple frequency compared to the incident light. In this case, the third harmonic (TH) is measured which is proportional to the sixth power of the local electric field at the milled structure. This local electric field depends especially on the geometric parameters of the antenna. Steep edges and the small gap “compress” the electric field in a very small volume of nanometer dimensions. For the HIM-milled samples, nonlinear TH emission is severely enhanced compared to all prior fabricated samples. For details of the TH measurements together with some emission simulations, the reader is directed to the corresponding publication in Nano Letters.[119]

This performance is an excellent testimonial to the application of He^+-ion beam milling for ultrahigh precision nanofabrication on solid materials, which can be applied for a number of different scientific applications. With the now available successor of the HIM, the Orion Nanofab, such a combined approach with different milling beams is possible in just one tool.

4.3 Cutting of nanogaps into carbon nanotubes (CNTs)

The use of individual metallic carbon nanotubes (CNTs) as electrodes is attractive for single molecules conductivity measurements. Due to the small size (almost one-dimensional) and favorable electronic properties they offer advantages compared to metals of the same dimensions.[120] With such a direct measurement, a better understanding of electronic transport for (future) organic semiconductor materials is possible.

In this study, single metallic CNTs were embedded in functional devices. Nanogaps of only (2.8 ± 0.6) nm size in the CNTs were subsequently produced by the helium ion beam sputtering. CNT device preparation and electrical measurements on oligo(phenylene ethynylene) molecular rods (OPE, length: 3.9 nm) were performed by Cornelius Thiele in the group of Prof. Ralph Krupe, both from the Karlsruhe Institute of Technology. Details thereof are in the following publication. Prior to these experiments, electron beam induced oxidation in an SEM was used for cutting the nanogaps, where the electron beam induces oxidation at the focal point. The average gap size obtained with this method was (19 ± 5) nm.[121]

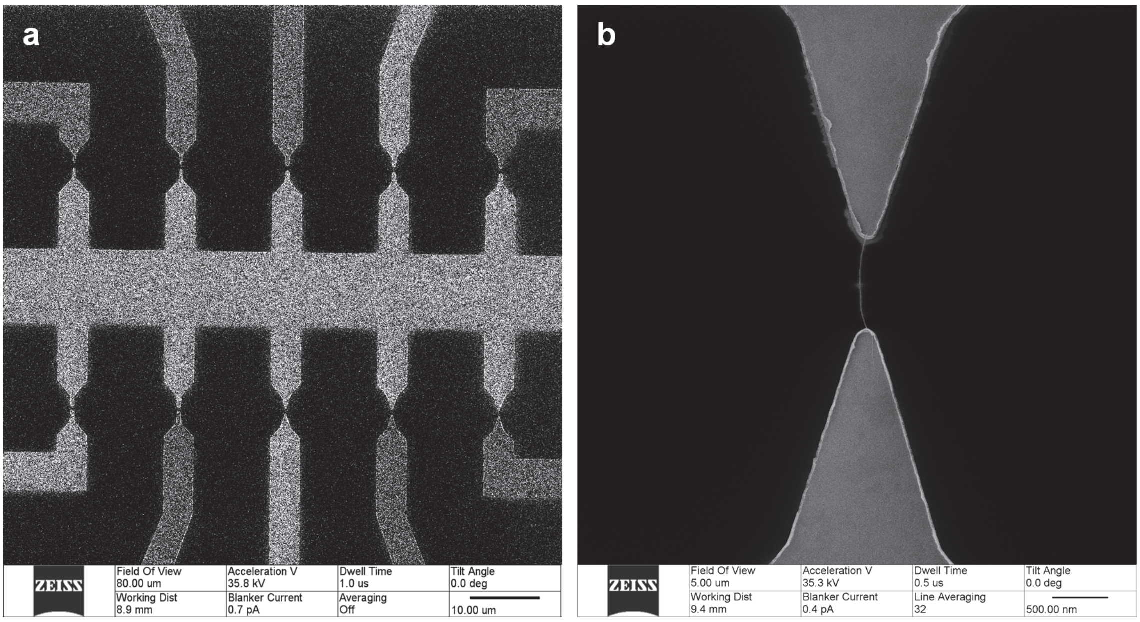

Figure 48: Overview of the devices used. (a): The middle bar is connected to ground. If no electric connection is present between the metallic contacts to the top and bottom, the material charges up during imaging and appears darker than other contacts.

In Figure 48, an overview of the used devices is visible. The nanotubes are deposited on tungsten electrodes and supported by SiO_2/Si substrates. Single CNTs were deposited between the electrodes by a process called “dielectrophoresis” developed in the group of Prof. Krupke.[122] A drop of CNT dispersion is brought on the device while an AC and

DC voltage is applied on the contacts leading to an alignment of single tubes. Before HIM measurements, all devices were annealed at 600°C to eliminate contaminations. Nonetheless, it was necessary to leave the samples in the HIM vacuum chamber for some hours before the lithography steps in order to ensure a good vacuum.

To cut the CNTs, a single line was written with the HIM. A pixel distance of 0.25 nm at a dwell time of 1 ms was sufficient to fully disrupt the electric conductivity through the nanotube. These values were obtained on test structures as in Figure 48a, where only the middle electrode was grounded. After a successful cut, the other electrode was left floating, so charge from the helium beam accumulates and causes a darkening in the image (see also Figure 49d). Prior to the cutting process, a fast alignment scan was performed to locate the CNT and to align the cut perpendicular.

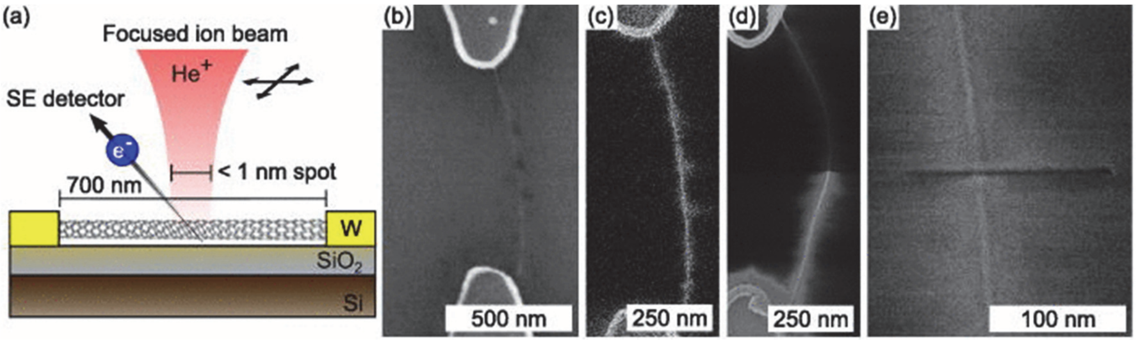

Figure 49: (a) Scheme of the CNT-device and the HIM-cutting. (b) SEM image of a CNT device after dielectrophoretic deposition. (c) Fast alignment scan of the same device with the helium ion microscope. (d) Slow scan of a device after gap formation. One of the electrodes is now electrically floating and accumulates positive charges during scanning. (e) Slow scan of a device with higher resolution showing only the CNT with the gap produced by helium ion beam milling. Reprinted with permission.[123]

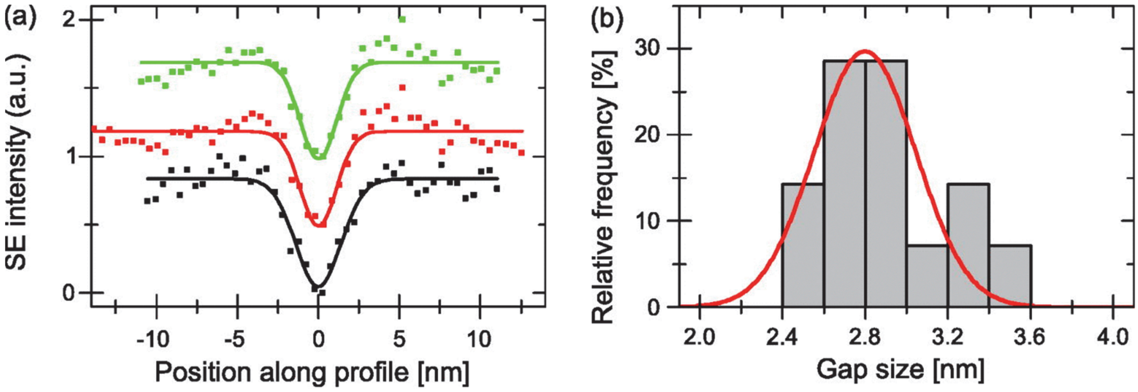

Figure 50: (a) Secondary-electron intensity profiles from three different nanogaps. (b) Histogram of 14 nanogap sizes. Reprinted with permission.[123]

The cutting was later performed on devices with both contacts grounded. One example for these structures is shown in Figure 49e, a high resolution image of the vertical CNT and the horizontal gap. A clear trench is visible, also in the silicon oxide substrate. A number of such images were analyzed to determine the gap size. The SE intensity along 3 CNTs was plotted in Figure 50 to measure the gap width. For 14 analyzed devices, the gap size histogram in Figure 50b shows a mean size of 2.8 nm and a very narrow size distribution.

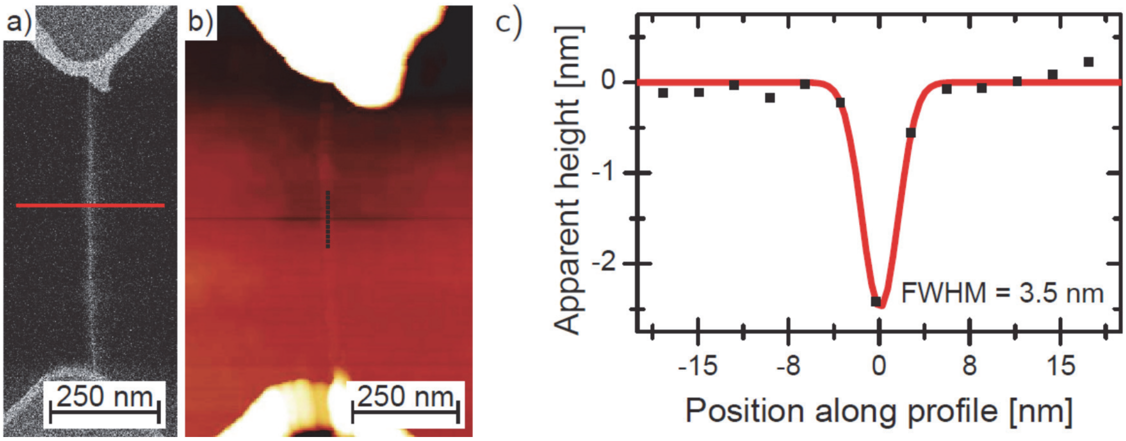

Figure 51: Atomic force microscopy (AFM) applied on a HIM-cutted CNT device. (a): HIM image of the device with the gap position indicated. (b): AFM topography image with the vertical line profile analyzed in (c). Figure reprinted.[124]

To confirm the gap size with another method, AFM was applied in Karlsruhe. Figure 51 depicts the results of such a measurement, showing similar gap sizes as the SE analysis shown before. A line profile along the CNT was fitted with an inverted Gaussian profile resulting in a gap size of 3.5 nm and a depth of the trench of about 2 nm, which is also visible along the sputtered line.

Finally, about 50 working CNT nanogap devices were tested with OPE nanorods, a 3.9 nm long molecule. Due to the similar length, one single molecule should fit in the gap to be measured. Details thereof are in the following publication (chapter 4.3.1).

In this study, the reproducible production of nanogaps of less than 3 nm in carbon nanotubes is shown. This reliable fabrication method for nanoscale electrodes will in future allow the electrical measurement of many other small organic or inorganic systems.

4.3.1 Publication: Fabrication of carbon nanotube nanogap electrodes by helium ion sputtering for molecular contacts (APL 2014)

This Chapter is reprinted with permission from AIP Publishing LLC. The original article appeared as:

> Thiele, C.; Vieker, H.; Beyer, A.; Flavel, B. S.; Hennrich, F.; Torres, D. M.; Eaton, T. R.; Mayor, M.; Kappes, M. M.; Gölzhäuser, A.; *et al.* Fabrication of Carbon Nanotube Nanogap Electrodes by Helium Ion Sputtering for Molecular Contacts. *Applied Physics Letters* **2014**, *104*, 103102.

Contribution:

Helium Ion Microscopy and Lithography was performed by the author.

APPLIED PHYSICS LETTERS **104**, 103102 (2014)

Fabrication of carbon nanotube nanogap electrodes by helium ion sputtering for molecular contacts

Cornelius Thiele,[1,2,a)] Henning Vieker,[3] André Beyer,[3] Benjamin S. Flavel,[1]
Frank Hennrich,[1] David Muñoz Torres,[4] Thomas R. Eaton,[4] Marcel Mayor,[1,2,4]
Manfred M. Kappes,[1,2,5] Armin Gölzhäuser,[3] Hilbert v. Löhneysen,[1,2,6,7]
and Ralph Krupke[1,2,8,b)]
[1]*Institute of Nanotechnology, Karlsruhe Institute of Technology, 76021 Karlsruhe, Germany*
[2]*DFG Center for Functional Nanostructures (CFN), 76028 Karlsruhe, Germany*
[3]*Faculty of Physics, Bielefeld University, 33615 Bielefeld, Germany*
[4]*Department of Chemistry, University of Basel, 4056 Basel, Switzerland*
[5]*Institut für Physikalische Chemie, Karlsruhe Institute of Technology, 76131 Karlsruhe, Germany*
[6]*Physikalisches Institut, Karlsruhe Institute of Technology, 76128 Karlsruhe, Germany*
[7]*Institut für Festkörperphysik, Karlsruhe Institute of Technology, 76021 Karlsruhe, Germany*
[8]*Institut für Materialwissenschaft, Technische Universität Darmstadt, 64287 Darmstadt, Germany*

(Received 6 February 2014; accepted 24 February 2014; published online 10 March 2014)

Carbon nanotube nanogaps have been used to contact individual organic molecules. However, the reliable fabrication of a truly nanometer-sized gap remains a challenge. We use helium ion beam lithography to sputter nanogaps of only (2.8 ± 0.6) nm size into single metallic carbon nanotubes embedded in a device geometry. The high reproducibility of the gap size formation provides a reliable nanogap electrode testbed for contacting small organic molecules. To demonstrate the functionality of these nanogap electrodes, we integrate oligo(phenylene ethynylene) molecular rods, and measure resistance before and after gap formation and with and without contacted molecules. © *2014 AIP Publishing LLC*. [http://dx.doi.org/10.1063/1.4868097]

The use of individual metallic carbon nanotubes (CNTs) as electrodes is attractive for contacting nanocrystals,[1] single molecules,[2] and functional materials, such as phase-change materials,[3] due to the CNT's intrinsic one-dimensionality and electrical conductivity. The formation of CNT electrodes starts, typically, with a pristine CNT on a surface, where the nanotube is contacted by lithographically defined metallic electrodes. Subsequently, two opposing CNT electrodes are generated by forming a gap in the CNT near its center. The molecule or material of interest is assembled between or deposited onto the CNT electrodes.

Different methods for fabricating such nanogaps have been reported. For example, current-induced breakdown in high vacuum,[1] which has been shown to produce gaps down to 7 nm, however, the typical gap size is often much larger. Alternatively, plasma oxidation through a lithographic mask, a complicated technique, limited by reliability problems and highly variable gap sizes.[3] The use of electron-beam-induced oxidation has been shown to overcome variability in gap size,[4] but resulted in a typical gap of ≈20 nm, which is an order of magnitude too large for most organic molecules.

In this work, we report on the use of a helium ion microscope (HIM) to reliably fabricate nanogaps of (2.8 ± 0.6) nm in metallic single-walled carbon nanotubes (mSWNTs), see Fig. 1(a) for a scheme. The optimum helium ion sputtering condition for gap formation was determined by *in-situ* voltage-contrast microscopy analysis. The functionality of the nanogaps was demonstrated by contacting of oligo(phenylene ethynylene) (OPE) molecular rods and electrical characterization throughout the fabrication process.

Tungsten electrodes with a separation of 700 nm were fabricated on a silicon substrate with 800 nm of thermal oxide, using a two-layer photoresist system comprising 180 nm poly(methyl methacrylate) (PMMA) 600 K EL11 and 200 nm of PMMA 950 K A4.5. Standard electron-beam lithography was used to pattern the photoresist. To obtain a nearly flat sample surface, metallic electrodes were "buried" into the oxide by etching their pattern into the surface with a CHF_3 plasma. Sputter deposition was then used to fill these electrode trenches with tungsten. Finally, the photoresist and the undesired metal were lifted off in an acetone bath.

The mSWNTs were prepared by S-200 gel filtration and density-gradient ultracentrifugation (DGU). For an initial suspension, typically, 10 mg of raw CNT material from pulsed laser vaporization[5] was suspended in 15 ml H_2O with 1 wt. % of sodium dodecyl sulfate (SDS) using a tip sonicator (Bandelin, 200 W maximum power, 20 kHz, 100 ms pulses) for 2 h at ≈20% power. During sonication, the suspension was cooled by a 500 ml water bath. The resulting dispersion was then centrifuged with ≈100.000 *g* for 1.5 h and carefully decanted from the pellet, which was formed during centrifugation. The centrifuged CNT suspension was used as the starting suspension for gel filtration fractionation. Gel filtration was performed in a glass column of 20 cm length and 2 cm inner diameter. After filling the glass column with the filtration medium, the gel was slightly compressed to yield a final height of ≈14 cm. For the separation, ≈10 ml of initial suspension was applied to the top of the column and subsequently a solution of 1 wt. % SDS in H_2O as eluant was pushed through the column with compressed air by applying sufficient pressure to ensure a flow of ≈1 ml/min. After ≈10 ml of this eluant had been added most of the mSWNTs had moved through the column, whereas the semiconducting

---

[a)] Cornelius.Thiele@kit.edu
[b)] krupke@kit.edu

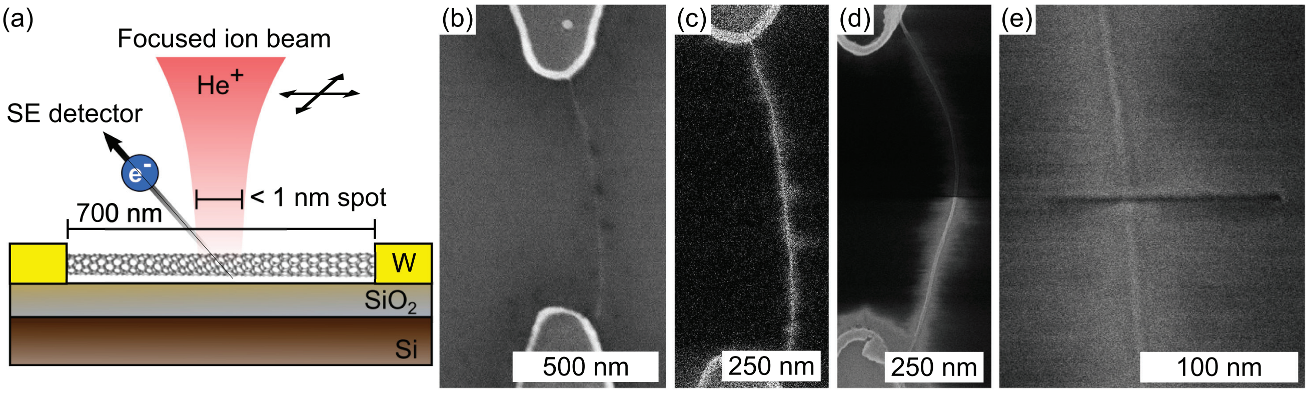

FIG. 1. (a) Scheme of helium ion sputtering of mSWNTs embedded in a device geometry. The nanotubes are deposited on tungsten electrodes and supported by SiO_2/Si substrates. (b) SEM image of a mSWNT device after dielectrophoretic deposition. (c) Fast alignment scan of the same device with the helium ion microscope. (d) Slow scan of a device after gap formation. One of the electrodes is now electrically floating and accumulates positive charges during scanning. (e) Slow scan of a device with both electrodes grounded after gap formation. A clear trench is visible, also in the silicon oxide substrate.

CNTs remained trapped in the upper part of the gel.[6] The mSWNTs were collected and used for DGU, to remove defected mSWNTs and any additional carbonaceous species present. Ultracentrifugation was performed in 20 wt. % iodixanol and 1 wt. % SDS in H_2O. mSWNTs with a diameter distribution of (1.2 ± 0.2) nm were used in this work.

mSWNTs were deposited between the tungsten electrodes using dielectrophoresis.[7] An alternating voltage with a frequency of 300 kHz and a peak-to-peak voltage between 1.0 and 1.3 V was applied between source and drain contacts, while a $\approx$50-μl drop of CNT dispersion with a concentration of $\approx$5 CNTs per μm^3 was placed on the device. After 5 min, the drop was first diluted with doubly distilled water, followed by methanol and finally allowed to dry.

Before the samples were transferred to the HIM, CNT deposition was assessed with a conventional scanning electron microscope (SEM), see Fig. 1(b). To eliminate any effects from electron-beam exposure, samples were annealed in a vacuum oven ($p = 10^{-6}$ millibars) at 600 °C for 30 min after imaging. Electrical characterization of pristine devices showed an Ohmic current-voltage behavior with a resistance of, typically, 500 kΩ.

The Zeiss Orion Plus HIM used in this work allows imaging similar to an SEM, except for a helium ion beam being scanned over the sample. The image is generated by the detection of secondary electrons from the sample. Due to the very small effective source size, favorable beam-sample interaction and a much smaller de Broglie wavelength of helium ions compared to electrons, the HIM offers an improved resolution compared to traditional SEMs.[8,9] The acceleration voltage of the HIM was always set to 35 kV. The 5-μm aperture was used, resulting in a spot size of below 1 nm and a beam current of $\approx$0.4 pA. The signal-to-noise ratio of an image and the implanted ion dose is depend on the beam current, the dwell time per pixel and the averaging settings. To minimize the ion dose, fast alignment images were recorded using the following settings: Pixel spacing 1 nm, dwell time 0.5 μs, no averaging. This led to a line dose of 0.2 nC/m per scan line. Later, slow scans for characterization were performed with fixed parameters: A pixel spacing of 5 Å, a dwell time of 0.5 μs, and 32× line averaging. This led to a line dose of 13 nC/m per scan line.

The focused helium ion beam can also be used to pattern samples by physical sputtering, similar to gallium ions in a focused ion beam instrument. This has been demonstrated, e.g., for graphene,[10–12] silicon nitride,[13] and recently gold nanorods.[14] Here, we employed helium ion beam lithography to pattern nanogaps into metallic carbon nanotubes, in a device geometry. These nanogaps were then used as contacts for a molecular wire, to demonstrate their practical usage. To reduce hydrocarbon deposition on the surface, all samples were stored in the helium ion microscope chamber under high vacuum for at least several hours. The chamber pressure, typically, reached 2.5×10^{-7} millibars before experiments were started.

In order to cut CNTs, a single pixel line with a pixel spacing of 2.5 Å and a dwell time in the millisecond range was scanned across a nanotube. To align this line perpendicularly to the nanotube, a fast scan was performed before the lithography was started, see Fig. 1(c).

To ascertain the critical dose for gap formation, we employed voltage-contrast microscopy (VCSEM), which is capable of locating defects and gaps within a nanotube and to reveal the nanotube's electronic type.[15] In our devices, this was realized by grounding one of the two metal electrodes. The other electrode remained floating, albeit connected to the grounded electrode by the mSWNT. After a single pixel line was scanned across the nanotube, a slow scan image of the device was acquired. Once an electrically insulating nanogap was formed in the metallic CNT, the floating electrode accumulated positive charges, thereby inhibiting secondary electrons from reaching the detector. Thus, the floating electrode appeared darker in the image, while the grounded electrode and the CNT segment connected to it appeared brighter, see Fig. 1(d) for an example. Using this experimental procedure, the critical dose for gap formation was determined to be $\approx$24 μC/m. Before proceeding to cut further nanogaps, the beam current was measured and the pixel dwell time adjusted accordingly to accommodate this value. We note that the line doses implanted by our fast- and slow-scan images are at least three orders of magnitude lower, and thus, have a negligible sputtering effect.

In order to precisely measure the size of the gap formed, the electrostatic charging of floating electrodes had to be avoided as charging always caused drifts. Also, the different secondary electron intensities on opposite sides of the gap would make an analysis difficult. To avoid charging, the samples were mounted in commercial 16-pin dual in-line package chip carriers, where the common drain electrode and source electrodes of devices were bonded to the chip carrier with Al wires. A customized sample holder in the HIM connected all pins to the stage/ground potential. In this way, detailed slow scans of the nanogaps after lithography were made possible, see Fig. 1(e).

Secondary electron intensity profiles were then recorded across 14 nanogaps in different carbon nanotube devices. The resulting curves were fitted with inverted Gaussians, see Fig. 2(a). A histogram of FWHM of the nanogaps is plotted in Fig. 2(b). With an average nanogap size of (2.8 ± 0.6) nm, direct helium ion sputtering is more precise by almost an order of magnitude than electron-beam-induced etching and a factor of 2–3 better than the smallest gaps achievable by current-induced breakdown. Most striking is the comparably narrow gap size distribution, which is an indication of the highly reproducible nature of this method. As we were targeting the smallest gap size possible for the subsequent insertion of molecules, we did not explore the formation of larger gaps.

Electrical measurements were performed on pristine mSWNTs and on mSWNTs after gap formation. The resistance of pristine mSWNTs yielded (479 ± 193) kΩ and is comparable to 1.2 nm diameter mSWNTs on Pd electrodes.[16] mSWNTs with nanogaps had a resistance of (643 ± 311) TΩ, which is nine orders of magnitude higher than in pristine devices. We attempted to measure tunneling or field-emission currents through the air gap and to correlate the current with the HIM derived gap size. However, despite the large electric fields of up to 5 V/nm in these nanogaps, we were not able to detect any sign of field emission.

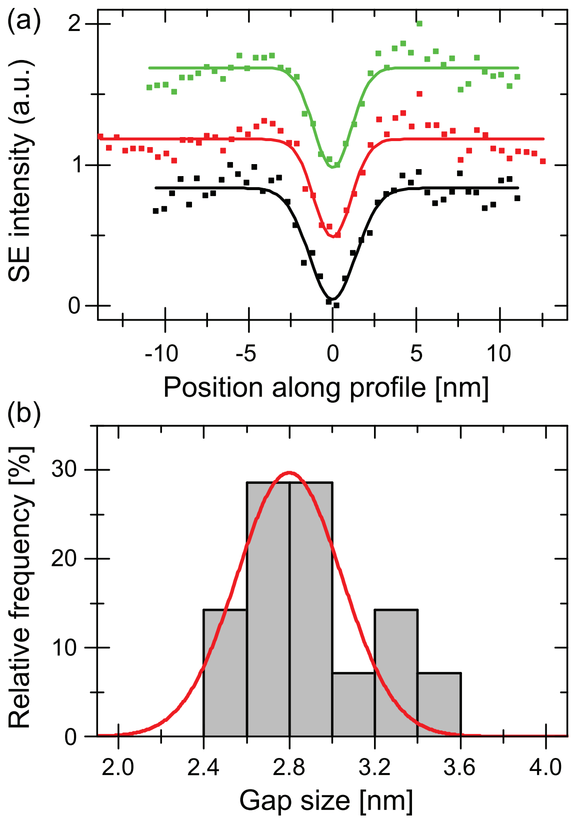

FIG. 2. (a) Secondary-electron intensity profiles from three different nanogaps. (b) Histogram of 14 nanogap sizes.

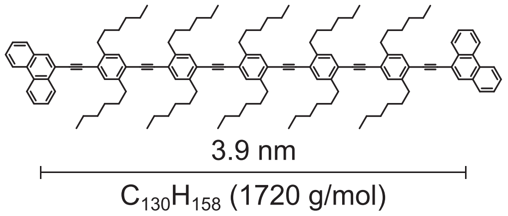

FIG. 3. Structure of **OPE Rod 1** which was contacted by the nanogaps. Phenanthrene anchor groups on each side couple to the sidewalls of a carbon nanotube.[17]

To demonstrate the utility of these nanogaps for contacting organic molecules, **OPE Rod 1**, a symmetric molecular wire of 3.9 nm length, with five subunits and phenanthrene anchor groups at each end was synthesized by performing a series of acetylene protection and deprotection steps,[18] similar to the molecule used by Grunder *et al.*,[19] see Fig. 3. A voltage of 1 V was applied across the nanogap device and the current monitored, and a drop of very dilute **OPE Rod 1** solution (less than 1 μg/ml in methylene chloride) was placed on the device and allowed to dry under ambient conditions. This process took, typically, no longer than 2 min, after which the devices exhibited a low-bias resistance of (90 ± 85) GΩ. See Fig. 4 for a resistance histogram over the lifetime of nanogap devices, including 50 devices with OPE molecules. For reference, experiments with clean solvent without the OPE molecule, the conductance of a nanogap was not changed. Interestingly, it was possible to wash off contacted molecules using clean solvent, thereby, restoring the conductance of a device to the level of an empty nanogap.

Scanning tunneling microscope break-junction measurements on an OPE of similar length revealed a resistance of ≈200 MΩ for a single molecule, albeit with the molecule covalently bonded to gold on both sides.[20] We observe an

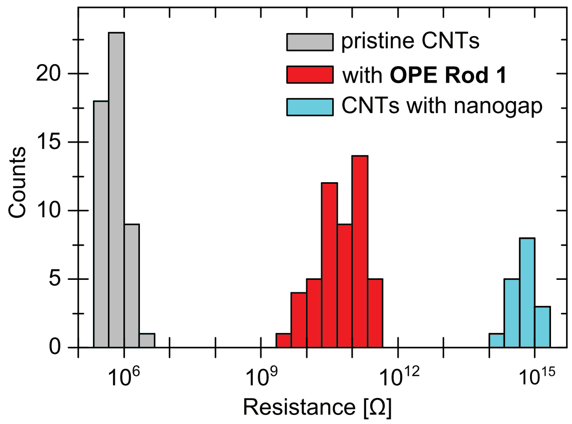

FIG. 4. Resistance histogram over the lifetime of nanogap electrode devices, including 50 CNT-OPE-CNT contacts. Pristine mSWNT devices: (479 ± 193) kΩ; CNTs with nanogap: (643 ± 311) TΩ; with OPE molecules: (90 ± 85) GΩ.

average resistance almost three orders of magnitude higher, with values spread over roughly two orders of magnitude. We ascribe this to a varying imperfect attachment of the molecules' anchor groups to the CNT electrodes and conformational freedom of molecules in the junction; both profoundly deteriorating the conductance.[21] Currently, STM investigations of the molecule and its electronic properties are underway to resolve these issues.

The reproducible engineering of nanogaps in carbon nanotubes that we have achieved will allow the study of many other organic or inorganic systems of nanoscale dimensions at the single-molecule or few-atom level, by providing a reliable way to fabricate nanoscale electrodes. Future work will have to address the issue of establishing reliable contacts between CNT electrodes and molecules.

[1] P. Qi, A. Javey, M. Rolandi, Q. Wang, E. Yenilmez, and H. Dai, J. Am. Chem. Soc. **126**, 11774 (2004).

[2] C. W. Marquardt, S. Grunder, A. Błaszczyk, S. Dehm, F. Hennrich, H. v. Löhneysen, M. Mayor, and R. Krupke, Nat. Nanotechnol. **5**, 863–867 (2010).

[3] F. Xiong, A. D. Liao, D. Estrada, and E. Pop, Science **332**, 568–570 (2011).

[4] C. Thiele, M. Engel, F. Hennrich, M. M. Kappes, K.-P. Johnsen, C. G. Frase, H. v. Löhneysen, and R. Krupke, Appl. Phys. Lett. **99**, 173105 (2011).

[5] S. Lebedkin, P. Schweiss, B. Renker, S. Malik, F. Hennrich, M. Neumaier, C. Stoermer, and M. M. Kappes, Carbon **40**, 417–423 (2002).

[6] K. Moshammer, F. Hennrich, and M. M. Kappes, Nano Res. **2**, 599–606 (2009).

[7] A. Vijayaraghavan, S. Blatt, D. Weissenberger, M. Oron-Carl, F. Hennrich, D. Gerthsen, H. Hahn, and R. Krupke, Nano Lett. **7**, 1556 (2007).

[8] D. C. Bell, Microsc. Microanal. **15**, 147 (2009).

[9] R. Hill, J. A. Notte, and L. Scipioni, in *Advances in Imaging and Electron Physics*, edited by P. W. Hawkes (Elsevier, 2012), Vol. 170, pp. 65–148.

[10] D. Bell, M. Lemme, L. Stern, J. Williams, and C. Marcus, Nanotechnology **20**, 455301 (2009).

[11] M. Lemme, D. Bell, J. Williams, L. Stern, B. Baugher, P. Jarillo-Herrero, and C. Marcus, ACS Nano **3**, 2674 (2009).

[12] D. Fox, Y. B. Zhou, A. O'Neill, S. Kumar, J. J. Wang, J. N. Coleman, G. S. Duesberg, J. F. Donegan, and H. Z. Zhang, Nanotechnology **24**, 335702 (2013).

[13] M. M. Marshall, J. Yang, and A. R. Hall, Scanning **34**, 101 (2012).

[14] O. Scholder, K. Jefimovs, I. Shorubalko, C. Hafner, U. Sennhauser, and G.-L. Bona, Nanotechnology **24**, 395301 (2013).

[15] A. Vijayaraghavan, S. Blatt, C. Marquardt, S. Dehm, R. Wahi, F. Hennrich, and R. Krupke, Nano Res. **1**, 321 (2008).

[16] W. Kim, A. Javey, R. Tu, J. Cao, Q. Wang, and H. Dai, Appl. Phys. Lett. **87**, 173101 (2005).

[17] S. Gotovac, Y. Hattori, D. Noguchi, J.-I. Miyamoto, M. Kanamaru, S. Utsumi, H. Kanoh, and K. Kaneko, J. Phys. Chem. B **110**, 16219 (2006).

[18] See supplementary material at http://dx.doi.org/10.1063/1.4868097 for full synthetic details.

[19] S. Grunder, D. Muñoz Torres, C. Marquardt, A. Blaszczyk, R. Krupke, and M. Mayor, Eur. J. Org. Chem. **2011**, 478 (2011).

[20] Q. Lu, K. Liu, H. Zhang, Z. Du, X. Wang, and F. Wang, ACS Nano **3**, 3861 (2009).

[21] L. Venkataraman, J. E. Klare, C. Nuckolls, M. S. Hybertsen, and M. L. Steigerwald, Nature **442**, 904 (2006).

4.4 Carbon nanomembrane (CNM) lithography

In chapter 3.1, imaging of carbon nanomembranes (CNMs) was extensively studied. This thematic was expanded to the question whether it is possible to modify CNMs with the helium ion beam. The fabrication of CNMs by structured crosslinking is so far demonstrated by EUV[49,54] or E-Beam lithography.[125] Another approach is the subsequent destruction of parts of the membrane by UV/ozone.[126] In this work, two possible routes are presented: milling of freestanding CNMs, and the production of structured CNMs by using helium ions to crosslink SAMs to CNMs.

4.4.1 Direct milling of structures in CNMs

For the first time, it was tried to directly mill freestanding CNMs. A mask of circular features was created by using a bitmap file with circle diameter decreasing from left to right, and dose increasing in 10% steps (10%, 20%, … 100%) from bottom to top (see Figure 52a).

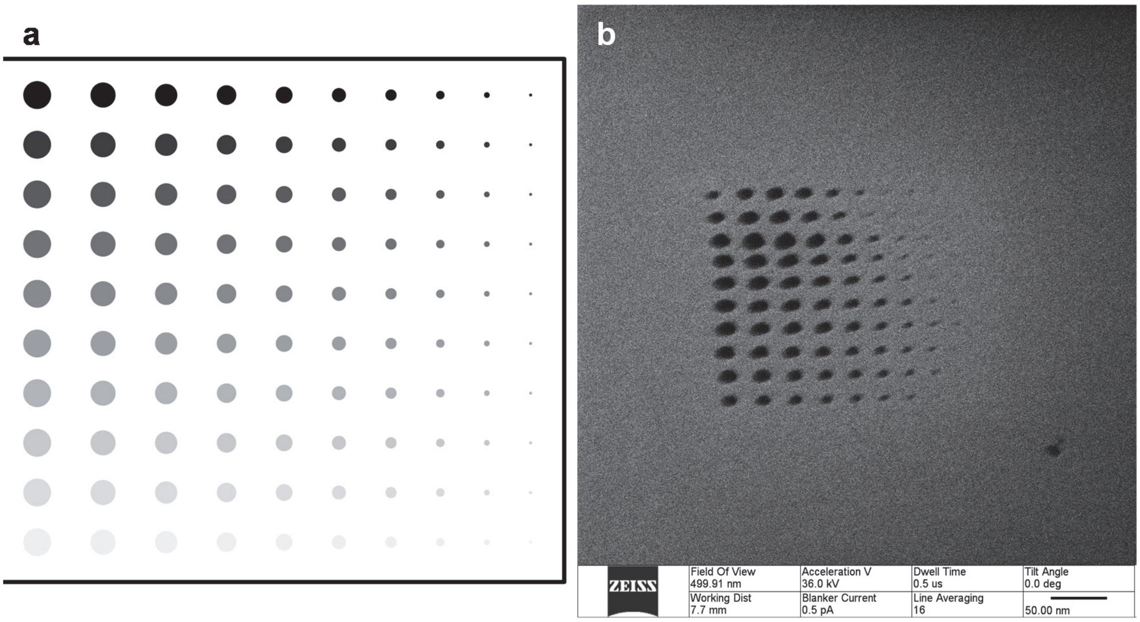

Figure 52: Helium ion milling of carbon nanomembranes. (a): milling mask used in this experiment. (b): Image of milled pores in a freestanding CNM. The structured area is about 250 by 250 nm.

The structure was milled in a freestanding BPT CNM on carbon-covered copper grid with 1 µm holes (Quantifoil 1/4). Milling was performed at a pixel spacing of 0.5 nm, 0.5 pA current and a dwell time between 2 to 25 ms per pixel. The structure in Figure 52b shows the pores milled in this process. Some distortions due to drift, moving of the sample and the deposition of contaminants is visible, but it is proven that it is possible to pattern small structures in freestanding CNMs. This work is currently continued by Daniel Emmrich, and expanded to explore the limits of this technique.

4.4.2 **Fabrication of CNMs by helium ion irradiation**

Here the use of helium ions to crosslink SAMs to form a CNM is presented. The results were ex-situ transferred onto oxidized Si-surfaces and then imaged in the HIM. The ion beam used for cross-linking is again programmed to irradiate an array of circular features as seen in Figure 52a. Due to the discreteness of bitmap files, the helium ion beam is intentionally slightly defocused in order to obtain overlapping irradiation. Figure 53a shows the irradiated structures on gold. In Figure 53b, these CNMs were transferred to SiO_2. The non-crosslinked molecules are lost during this process, so that only the crosslinked CNMs remain.

The He^+ dose density for a complete crosslinking is determined to be 850 µC/cm² (Figure 53c). Overdosing starts at about 5 times this dose and leads to a destruction of the membrane (Figure 53d). Compared to the crosslinking with electrons, the necessary ion intensity is about 60 times smaller.

Finally, a lithographic crosslinking of SAMs to CNMs by helium ions was shown for the first time. The crosslinking process was also thoroughly analyzed. The irradiation dose density applied to the sample was varied, and 3-stage model for the growth are presented: the initial nucleation, 1D growth and 2D growth are related to differences in activation energy. This is in detail presented in the following publication.

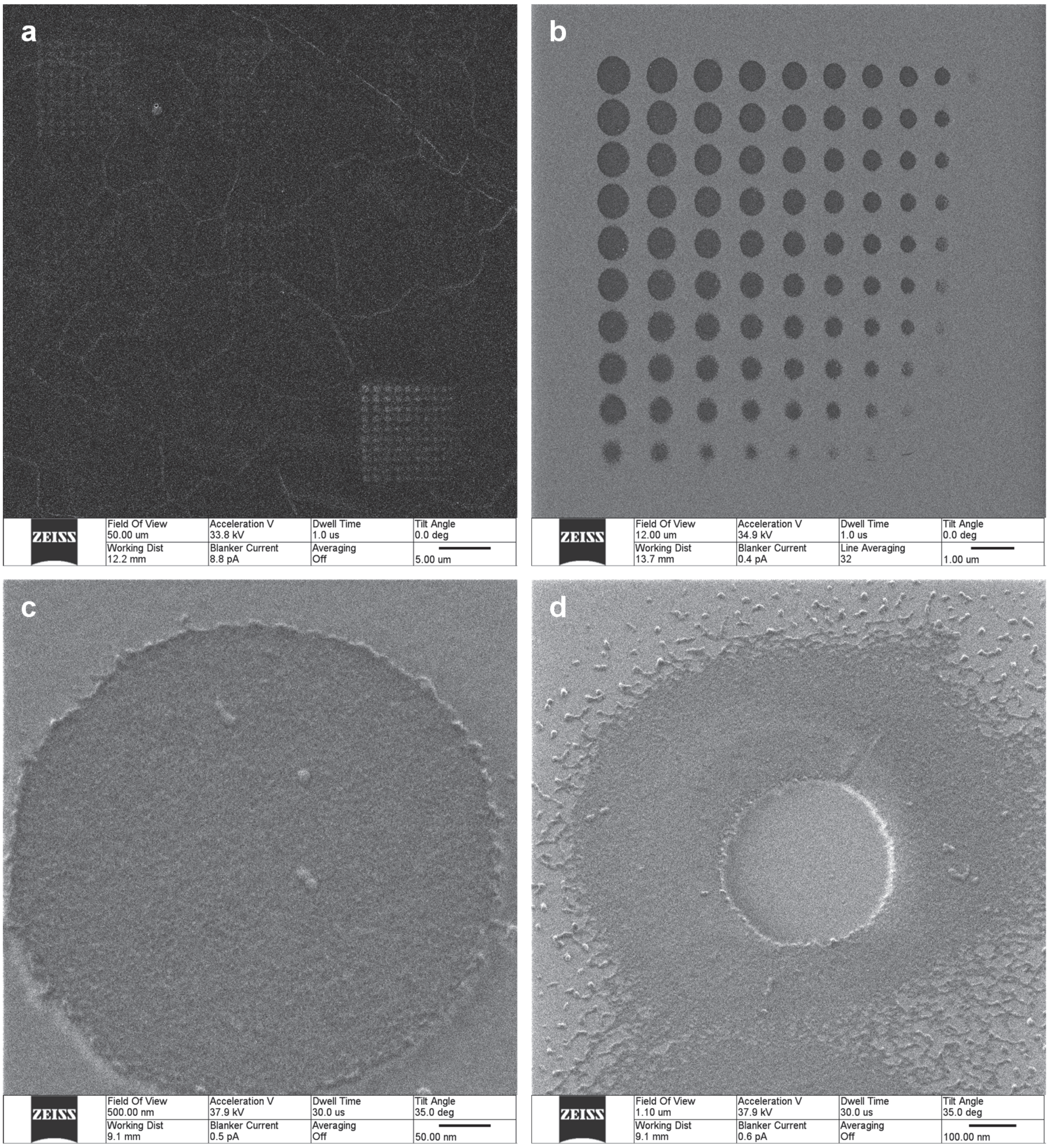

Figure 53: Helium ion fabrication of carbon nanomembranes.(a): Image of SAM on gold after structured He-ion irradiation. The structure of gold grain boundaries is visible. (b): Irradiated structure after transfer on SiO_2 wafer. (c): Magnification of one CNM, crosslinked with optimal ion dose density. (d): over-exposure leads to destruction of the CNM (please note the increased FOV compared to image c).

4.4.3 Publication: Fabrication of carbon nanomembranes by helium ion beam lithography (BJNano 2014)

This Chapter is reprinted with permission from the Beilstein foundation. The original article appeared as:

> Zhang, X.; Vieker, H.; Beyer, A.; Gölzhäuser, A. Fabrication of Carbon Nanomembranes by Helium Ion Beam Lithography. *Beilstein Journal of Nanotechnology* **2014**, *5*, 188–194.

Contribution:

Helium Ion Microscopy and Lithography was performed by the author.

Beilstein Journal of Nanotechnology

Fabrication of carbon nanomembranes by helium ion beam lithography

Xianghui Zhang*, Henning Vieker, André Beyer and Armin Gölzhäuser

Full Research Paper

Open Access

Address:
Department of Physics, Physics of Supramolecular Systems and Surfaces, Bielefeld University, 33615 Bielefeld, Germany

Email:
Xianghui Zhang* - zhang@physik.uni-bielefeld.de

* Corresponding author

Keywords:
carbon nanomembranes; dissociative electron attachment; helium ion microscopy; ion beam-organic molecules interactions; self-assembled monolayers

Beilstein J. Nanotechnol. **2014,** *5,* 188–194.
doi:10.3762/bjnano.5.20

Received: 24 September 2013
Accepted: 22 January 2014
Published: 21 February 2014

This article is part of the Thematic Series "Helium ion microscopy".

Associate Editor: J. Sagiv

Abstract

The irradiation-induced cross-linking of aromatic self-assembled monolayers (SAMs) is a universal method for the fabrication of ultrathin carbon nanomembranes (CNMs). Here we demonstrate the cross-linking of aromatic SAMs due to exposure to helium ions. The distinction of cross-linked from non-cross-linked regions in the SAM was facilitated by transferring the irradiated SAM to a new substrate, which allowed for an ex situ observation of the cross-linking process by helium ion microscopy (HIM). In this way, three growth regimes of cross-linked areas were identified: formation of nuclei, one-dimensional (1D) and two-dimensional (2D) growth. The evaluation of the corresponding HIM images revealed the dose-dependent coverage, i.e., the relative monolayer area, whose density of cross-links surpassed a certain threshold value, as a function of the exposure dose. A complete cross-linking of aromatic SAMs by He^+ ion irradiation requires an exposure dose of about 850 $\mu C/cm^2$, which is roughly 60 times smaller than the corresponding electron irradiation dose. Most likely, this is due to the energy distribution of secondary electrons shifted to lower energies, which results in a more efficient dissociative electron attachment (DEA) process.

Introduction

Carbon nanomembranes (CNMs) with monomolecular thickness and macroscopic lateral size represent a new type of functional two-dimensional (2D) materials [1]. A universal scheme to fabricate CNMs is the irradiation-induced cross-linking of aromatic self-assembled monolayers (SAMs), which allows for creating a variety of functional nanomembranes by using different molecular precursors as building blocks [2]. The properties of CNMs, such as stiffness, chemical functionality and porosity, can be tailored through a prudent choice of the molecular precursors and the fabrication conditions. CNMs are capable of being released from the substrate and transferred onto arbitrary substrates, e.g., solid supports and holey substrates [3]. Mechanical properties of freestanding CNMs were characterized by bulge test in an atomic force microscope (AFM): biphenyl-based CNMs possess a Young's modulus of ca. 10 GPa and a remarkable tensile strength of ca. 600 MPa

[4]. The possibility of transferring CNMs and their high mechanical strength make them suitable candidates for nanoelectromechanical systems (NEMS). Postsynthetic modifications, e.g., multilayer stacking [5], thermal annealing [6], chemical functionalization [7], and perforation [8,9], lead to a further tailoring of the performance of the CNMs and enable various investigations and applications.

The cross-linking of SAMs is so far conducted by exposure to electrons [10] and photons [11]. Electron irradiation induces the dissociation of C–H bonds at the phenyl rings. The consequent cross-linking between adjacent aromatic moieties is a critical step in the formation of CNMs. Both electron beam lithography and extreme ultraviolet (EUV) lithography have been utilized to fabricate CNMs from SAMs [11,12]. The EUV photon induced cross-linking is, for that matter, related to secondary electrons generated by the photoemission process [11]. Turchanin et al. investigated the electron induced cross-linking of biphenylthiol (BPT) SAMs on gold with complementary spectroscopic techniques and they suggested a dissociative electron attachment (DEA) as the dominating process to which both primary electrons and secondary electrons contribute [13]. However, a detailed picture of how the spatial distribution of cross-links evolves until a complete CNM has been formed is still missing.

Further modification and patterning of SAMs have been achieved by using ion irradiation (e.g. Ar^+, Ga^+, Si^+, etc.), which leads to the desorption and the fragmentation of molecules [14,15]. High energy helium ions passing through polymer films modify the macroscopic properties of these films, too. This is related to changes in the chemical structures of the polymers [16,17]. Recently, the helium ion microscope (HIM) has been employed as an imaging and measurement tool for nanotechnology, for which the sub-nanometer sized ion probe and its resulting high brightness lead to a higher resolution and the small convergence angle of the ion beam leads to a larger depth of field. As an imaging tool, this instrument has a high surface sensitivity and is particularly advantageous to distinguish monolayers from the supporting substrate [18,19]. As a tool for nanofabrication, the low proximity effect that arises from the finite excited volume, in which the ion–material interaction takes place, extending deeply into the material, and the confinement of ion scattering to the secondary electron escape depth promise an outstanding performance of HIM [20]. So far, various approaches have been used to exploit the capabilities of HIM, such as ion milling [21], scanning helium ion beam lithography (SHIBL) [22], and helium ion beam induced deposition (HIBID) [20].

Here we used 4'-nitro-1,1'-biphenyl-4-thiol (NBPT) as a molecular precursor to form SAMs on a Au substrate and employed HIM both as a nanofabrication tool to cross-link SAMs and as an imaging tool for the ex situ observation of the crosslinking process. As regards the nanofabrication, both supported and freestanding CNMs were fabricated by transferring them onto a silicon substrate and a transmission electron microscopy (TEM) grid, respectively. As regards the investigation of the cross-linking process, the helium ion beam was programmed to irradiate NBPT SAMs with a series of different doses. The separation of cross-linked and non-cross-linked SAMs was conducted by transferring them onto a Si substrate with an oxide layer. The observation was done by using HIM in doing so taking advantage of the high surface sensitivity of the instrument.

Results and Discussion

Figure 1 shows a schematic representation of the cross-linking and transfer process. Firstly, the SAM that consists of closely packed NBPT molecules is formed on a gold substrate; secondly, the SAM is irradiated locally with He^+ ions; thirdly, the transfer is assisted by a layer of poly(methyl methacrylate) (PMMA) for mechanical stabilization, which allows the dissolu-

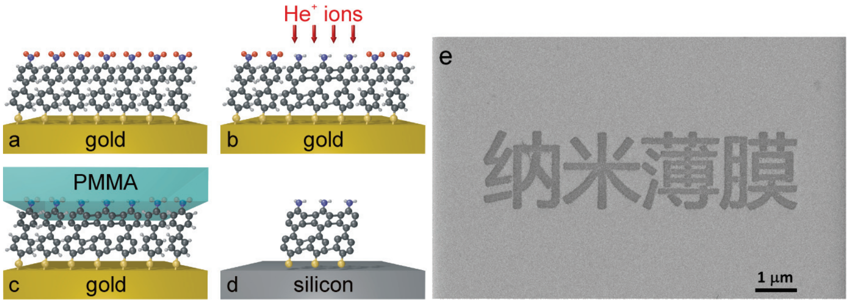

Figure 1: (a–d) A schematic representation of the NBPT SAM cross-linked with He^+ ions and the transfer onto a Si substrate: (a) Formation of SAM on Au; (b) Local exposure to He^+ ions; (c) Transfer of CNM with a polymeric film; (d) Separation of cross-linked from non-cross-linked regions. (e) A demonstration of lithographic CNMs in Chinese characters *nanomembranes* transferred on a silicon substrate.

tion of underlying Au layer; lastly, the PMMA layer is dissolved and only the cross-linked SAM is transferred onto another substrate, e.g., SiO_2/Si. Figure 1e demonstrates a successful transfer of structured CNMs in Chinese characters which means *nanomembranes*: the grey background is SiO_2/Si substrate and the darker features are transferred CNMs.

For the fabrication of freestanding CNMs, NBPT SAMs were irradiated in square patterns by helium ions at 35 keV and holey carbon-coated TEM grids were used as supporting substrates. Figure 2a shows the HIM image of a CNM with a size of 50 × 50 μm^2 on a TEM grid and the corresponding irradiation dose is approximately 500 $\mu C/cm^2$. The CNM is supported by a holey carbon film on a grid. The holey carbon film appears brighter and the CNM slightly darker due to the charging effect. To identify the CNM, its three corners are marked with arrows. Figure 2b shows the higher magnification HIM micrograph of the CNM in Figure 2a. It is noticeable that the CNM has many tiny holes, indicating that the crosslinking is not complete at this dose. Figure 2c and Figure 2d show the HIM micrographs of a CNM with an irradiation dose of ca. 1000 $\mu C/cm^2$. The CNM shows homogeneous features and no pores are visible here, which indicates a complete crosslinking. The CNM in the upper–left corner is damaged and the dark features arise from the sample stage beneath the TEM grid (see Figure 2d). Notice that imaging doses are at least one order of magnitude smaller than the irradiation dose, no further modification of CNMs is expected during imaging.

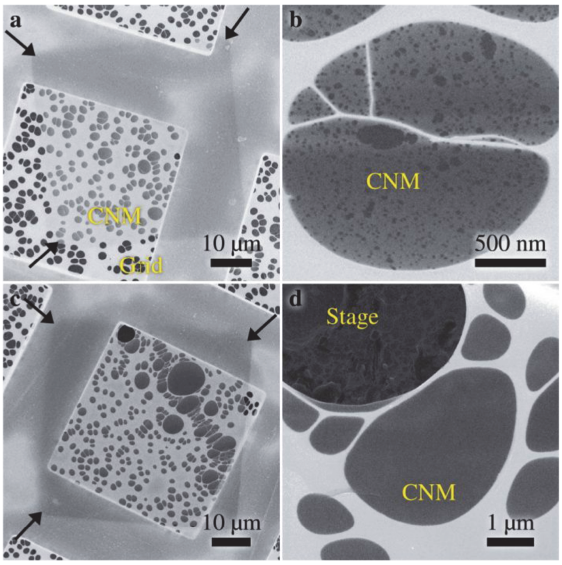

Figure 2: Freestanding CNMs with a dimension of 50 × 50 μm^2 supported by a TEM grid with a holey carbon film: (a) the HIM micrograph of a CNM with an irradiation dose of 500 $\mu C/cm^2$, where three arrows mark its corners; (b) the high magnification HIM micrograph shows that the CNM contains tiny holes; (c) the HIM image of a CNM with an irradiation dose of 1000 $\mu C/cm^2$; (d) the high magnification HIM image shows that the CNM contains no microscopic defects. (Imaging doses: a) 0.27 $\mu C/cm^2$, b) 55.9 $\mu C/cm^2$, c) 3.36 $\mu C/cm^2$ and d) 33.6 $\mu C/cm^2$).

In order to observe the development of the crosslinking of the SAM, the NBPT SAM was irradiated in circular regions by helium ion beam with a series of different doses. The variations of the irradiation dose are achieved by controlling the dwell time of the beam. Provided that the fabrication conditions are the same for the whole series, the irradiation dose is proportional to the total irradiation time. Therefore, the dynamics of cross-linking and growth regimes can be studied by making ex situ observations of the development of cross-linked SAMs. To this end, the distinction of cross-linked from non-cross-linked regions in the SAM was facilitated by transferring the irradiated SAM to a new substrate. Strictly speaking, there exists a threshold value, which is given by the density of cross-links that is required for a successful transfer of a monolayer. Below this threshold, the formed supramolecular network is not dense enough to sustain a lift-off from its initial substrate. Therefore, the transfer distinguishes the irradiated SAMs whose density of cross-links surpasses the threshold value from those below the threshold. Figure 3 shows a series of HIM images of a cross-linked SAM that have been transferred onto a SiO_2/Si substrate. Interestingly, the first step is the formation of circular shaped nuclei, which is analogous to the nucleation for thin films or polymer crystallization [23]. After a dose of 176 $\mu C/cm^2$ (Figure 3a), the average diameter of the nuclei is 9.0 ± 1.7 nm, which means that each nucleus consists of ca. 300 molecules, and the nucleus density is approximately 450 μm^{-2}. When the dose is 225 $\mu C/cm^2$, the nucleus density increases to approximately 930 μm^{-2} (see Figure 3b). The above mentioned threshold is related to the density of the cross-links of these smallest patches (nuclei) that are able to be transferred. After the early stage, the nuclei start to grow in one dimension and chainlike structures with a typical length of about 100 nm become the dominant features, as shown in Figure 3c. Figure 3d shows a marked change of structures, i.e., chain thickening, which indicates that a two dimensional (2D) growth (or lateral growth) begins to take place. Figure 3g and Figure 3h show an incomplete CNM with tiny holes and a complete CNM without holes, respectively. In order to make sure that all these structures are indeed CNMs and to exclude the possibility that some features (especially the small nuclei) might be due to contaminations from the transfer process, the sample (irradiated SAM on SiO_2) was annealed up to 300 °C in ultra-high vacuum (UHV). The subsequent imaging with HIM confirms that no change of the structures occurs. It is also worth mentioning that an excessive exposure to He^+ ions (>4000 $\mu C/cm^2$) leads to a damage of the CNMs, which is attributed to the swelling of the Au substrate from ion implantation [24].

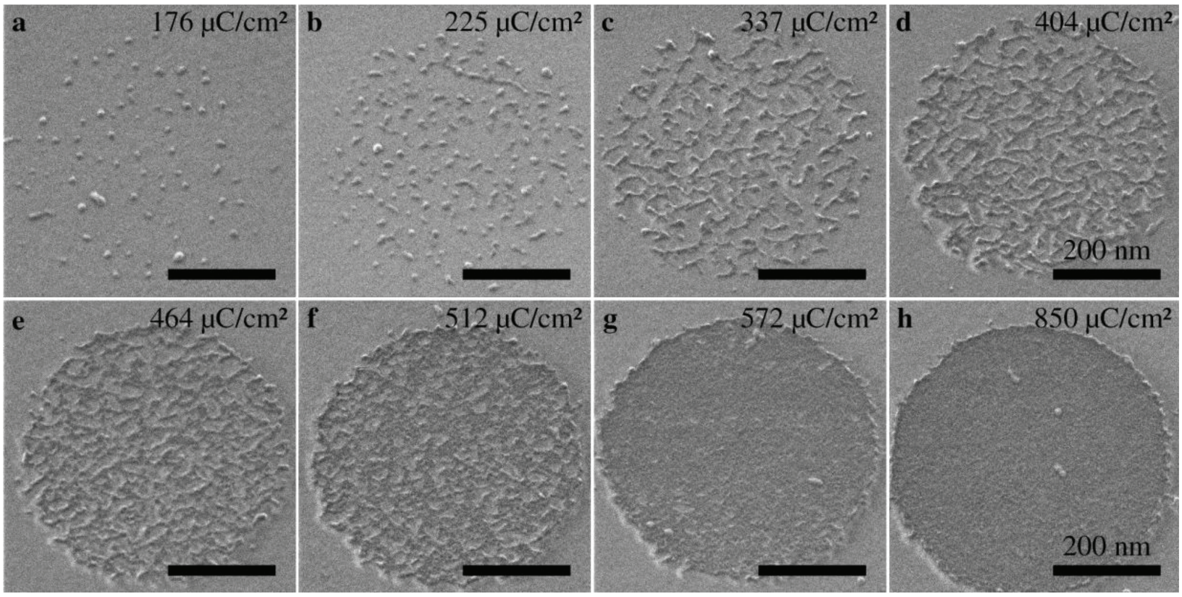

Figure 3: A series of HIM images showing the cross-linking of a NBPT SAM induced by helium ion irradiation, where the cross-linked SAM was transferred onto a SiO_2/Si substrate after being cross-linked within a circular region with the dose given in the upper right corner of each image: (a) formation of circular shaped nuclei which are widely separated and randomly distributed. (b) more nuclei come into being and some of them start to grow one dimensionally; (c) chainlike structures with a typical length of ca. 100 nm become the majority; (d) chain thickening indicates a two-dimensional (2D) growth beginning to take place; (e–f) 2D growth plays a dominating role; (g) the CNM contains tiny holes; (h) the CNM forms completely and no defects are observed, indicating the status of a complete cross-linking. The scale bars are 200 nm.

A complete cross-linking of NBPT SAMs by He^+ ion irradiation requires an exposure dose of approximately 850 µC/cm^2, which is roughly 60 times smaller than the corresponding electron irradiation dose (ca. 50,000 µC/cm^2, 100 eV) [13]. The energy loss of helium ions in alkanethiol SAMs on Au were investigated by neutral impact collision ion scattering spectroscopy (NICISS) and the stopping power was determined to be about 3.7 eV/Å for the ion energy of 4 keV [25]. Though the total scattering cross–section of He^+ ions by the SAM is very small, the energy transfer could induce molecular excitation and bond scissions, which may contribute to the cross-link formation to a certain extent. However, the tremendous dose difference can be associated with distinctive characteristics of secondary electrons that are excited by the helium ions. Firstly, the secondary electron yield for 35 keV He^+ ions impinging perpendicularly on a Au substrate is calculated by the software package IONiSE to be about 2.7 [26]. And this is approximately three times higher than the experimentally determined secondary electron yield (approximately 0.85) for 100 eV electrons [27]. Secondly, the energy spectrum of secondary electrons excited by 35 keV He^+ ions on Au showed a peak around 2 eV, with a small shoulder in the range of 5–6 eV [28]. For the excitation by electrons at 100 eV, the energy distribution of secondary electrons shows a peak at about 5 eV [27]. It is known that secondary electrons at energies well below the ionization threshold could produce single strand and double strand breaks in DNA and thus induce genotoxic effects in living cells [29]. These breaks are attributed to the DEA process, in which the attachment of incident electrons leads to the formation of a transient molecular anion (TMA) state and this TMA decays by electron autodetachment or by dissociation of a specific bond. The probability of forming a TMA, i.e., the electron capture cross section, varies inversely with the energy of the TMA state with respect to the ground state. In addition, the life time of TMAs increases with decreasing their energies [30]. This indicates that in the case of electron irradiation in NBPT SAMs, by analogy with strand-breaks in DNA, the DEA process is more efficient for secondary electrons with lower energies around 2 eV.

The DEA process is endothermic, as the electron affinity of a biphenyl molecule (3–7 kJ/mol) is much smaller than the bond energy of C–H (ca. 430 kJ/mol) [31,32]. The characteristic energy barriers for cross-linking arise from the activation energy for the DEA process and the entropic barrier to form a covalent bond among adjacent molecules. The activation energy and the above mentioned energy-dependent DEA cross section determine the rate coefficient of the DEA process [33]. The entropic barrier can be associated with a conformational entropy reduction of a molecule after being cross-linked, as a single molecule is more flexible and thus possesses higher degrees of freedom compared to a molecule being cross-linked and constrained by covalent bonds. The sequence of cross-linking depends on the characteristic energy barriers, as the entire region is irradiated homogeneously. A formation of nuclei would be associated with minimum activation energies in the SAMs. Further crosslinking prefers to occur around those already cross-linked nuclei, instead of regions that are not cross-linked. This implies that activation energies in cross-linked regions are relatively smaller, as π-electrons are laterally delocalized due to the cross-links and the electron mobility in cross-linked regions increases as well. The formation of interfaces between cross-linked and non-cross-linked region could result in entropic barriers due to steric hindrance. Note that the orientation of the 1D structures appears to be closer to the horizontal (scan) direction than to the vertical direction, which implies that the activation energy could be slightly brought down by the helium ion beam scanning due to the local electronic field around the growth front. Therefore, the growth direction of the nuclei is determined by the growth front that exhibits the lowest activation energies as well as the lowest entropic barriers. Lastly, the fact that a 2D growth follows the 1D growth could be attributed to a higher entropic barrier encountered at the sides of 1D structures. As regards the entropic barrier, an extreme example would be that for the insurmountable entropic barriers the crosslinking does not occur and vacancies that contain isolated molecules are formed. XPS spectra showed that the maximum degree of crosslinking of the BPT SAM was approximately 90% and further crosslinking was sterically hindered [13].

As mentioned above, three stages of the crosslinking process were designated: the formation of nuclei, 1D growth, and 2D growth of cross-linked regions. Figure 4 shows the percentage of the cross-linked area as a function of the irradiation doses: (1) the initial formation of nuclei occurs up to a surface coverage of 6–10%; (2) the 1D growth dominates for a coverage up to about 35%; (3) the 2D growth dominates for a coverage above about 35%. We employed Gaussian distributions to describe the probability of surpassing the threshold cross-linking density at a given dose. As shown in Figure 4, the cross-linked area coverage in dependence on the exposure dose can be described by two superimposed sigmoid functions represented by the following cumulative Gaussian distribution functions

$$\theta(D) = \frac{I_1}{I_1+I_2}\frac{1}{2}\left[1+\operatorname{erf}\left(\frac{D-D_1}{\sigma_1\sqrt{2}}\right)\right] + \frac{I_2}{I_1+I_2}\frac{1}{2}\left[1+\operatorname{erf}\left(\frac{D-D_2}{\sigma_2\sqrt{2}}\right)\right] \qquad (1)$$

where θ is the cross-linked area coverage, D is the irradiation dose, D_1 = (204 ± 18) μC/cm^2 is the mean dose of the first Gaussian distribution, σ_1 = (42 ± 24) μC/cm^2 is the corresponding standard deviation, and I_1 = 0.22 ± 0.04 is the magnitude of the first cumulative Gaussian distribution. The corresponding quantities of the second Gaussian distribution are D_2 = (476 ± 8) μC/cm^2, σ_2 = (56 ± 7) μC/cm^2 and I_2 = 0.78 ± 0.04. The existence of two distinct Gaussian distributions indicates that two types of monolayer regions for 1D and 2D growth regimes are involved, which require different doses for cross-linking with mean values of approximately 200 μC/cm^2 and approximately 480 μC/cm^2, respectively.

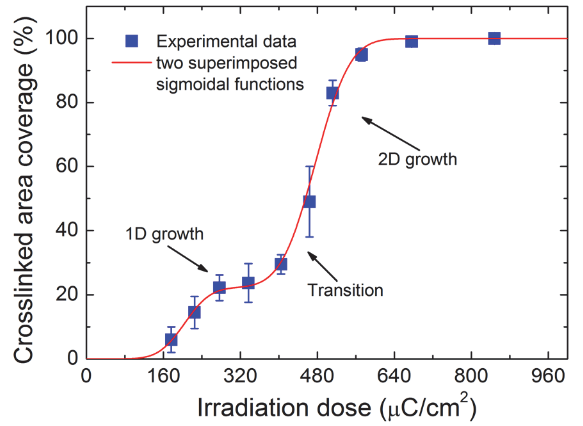

Figure 4: Percentage of the cross-linked area plotted as a function of the irradiation dose: (1) no CNM forms below the threshold dose of approximately 160 μC/cm^2; (2) the formation of nuclei occurs up to a surface coverage of 6–10%; (3) the 1D growth dominates for a coverage of up to about 35% and the required mean dose is approximately 200 μC/cm^2; (4) the 2D growth dominates for a coverage above about 35% and the required mean dose is approximately 480 μC/cm^2.

A possible explanation for this behaviour can be found by considering the in-plane tension of cross-linked SAMs. It is known that free-standing CNMs from fully cross-linked NBPT SAMs exhibit an in-plane tensile residual strain of about 1% [4]. This strain is expected to be introduced during the cross-linking process, as new bonds are created between neighbouring molecules. Figure 3a shows the formation of small nuclei in the initial phase of the cross-linking process. Such island-like structures are known to partially relax compressive as well as tensile strain by slight expansion or shrinkage, respectively [34]. A 10 nm sized nucleus may shrink up to 1 Å by relaxing a tensile strain of 1%. Consequently, the distance between neighbouring molecules adjacent to such cross-linked nuclei should increase, which will reduce the probability of a new cross-link formation. This increases the mean dose for the non-cross-linked monolayer areas near cross-linked patches to reach the threshold cross-linking density. The two distinct Gaussian distributions in Figure 4 can be understood to reflect the cross-linking of unstrained and strained regions with mean doses of approximately 200 μC/cm^2 and approximately 480 μC/cm^2, respectively. A consequence of this interpretation is that the formation of nuclei as well as the formation of 1D structures is assigned to the cross-linking process with the lower mean dose, i.e., to the unstrained monolayer regions. This is obvious by Figure 3c and Figure 4. The HIM image of Figure 3c shows the occurrence of 1D structures while the second sigmoidal function in Figure 4 possesses a negligible value at this dose. Therefore, cross-linked patches are not isotropically surrounded by strained regions but in certain directions the adjacent monolayer is unstrained, which results in the observed formation of 1D cross-linked structures with the lower mean dose. The 2D growth of cross-linked areas is then assigned to the higher mean dose due to the strain in these monolayer regions.

Conclusion

Freestanding carbon nanomembranes were successfully fabricated from aromatic self-assembled monolayers by using helium ion beam lithography. Three distinct stages of the cross-linking process, i.e., the initial nucleation, 1D growth and 2D growth, were observed ex situ by helium ion microscopy. Such a sequence could be related to different activation energies of dissociative electron attachment process as well as different entropic barriers encountered by the growth fronts. The irradiation dose for a complete cross-linking with helium ions is roughly 60 times smaller than that with electrons. Most likely, this is due to the energy distribution of helium ion excited secondary electrons being shifted to lower energies.

Experimental

Preparation of self-assembled monolayers

For the preparation of 4'-nitro-1,1'-biphenyl-4-thiol (NBPT) SAMs we used a 300 nm polycrystalline Au layer with (111) crystal planes epitaxially grown on a mica substrate (Georg Albert Physical Vapor Deposition, Germany). The substrate was cleaned with a UV/ozone cleaner (UVOH 150 LAB FHR) for 5 min, rinsed with ethanol, and then blown dry under a nitrogen stream. Afterwards the substrates were immersed into 10 mL of a solution of dry and degassed dimethylformamide (DMF) with ca. 10 mmol NBPT molecules for 72 h in a sealed flask under nitrogen atmosphere.

Helium ion lithography and helium ion microscopy

The experiments were conducted with a Carl Zeiss Orion Plus® helium ion microscope at room temperature. The irradiation of NBPT SAMs was performed by using the built-in software. The ion beam is programmed to irradiate an array of circular features by using a bitmap file and the dose variations are achieved by controlling the dwell time per pixel. The helium ion beam was operated at an acceleration voltage of 34.8 kV and a current of 3.5 pA. Due to the discreteness of bitmap files, the helium ion beam is intentionally slightly defocused in order to minimize any inhomogeneities in crosslinking. One circular feature consists of 2160 write points at a pixel distance of 10 nm. The fabrication of freestanding square CNMs was carried out by irradiating NBPT SAMs by HIM in a repeated scanning mode. The sizes of CNMs are the same to the field of view (FOV) and dose variations are achieved by controlling the total scanning time. For imaging, the helium ion beam was operated at acceleration voltages of 36.5–37.9 kV and currents of 0.3–0.6 pA. Images on SiO_2 were acquired at a working distance of 9 mm and a tilt angle of 35° with 30 μs dwell time per pixel. Images on grid were acquired at a working distance of 30 mm with 0.5 μs dwell time and 128 frames averaged.

Transfer of carbon nanomembranes

After helium ion irradiation, the whole NBPT CNMs were transferred onto another substrate for further investigations again with the HIM. For the transfer of NBPT CNMs onto a SiO_2/Si substrate the samples were spin-coated with a layer of poly(methyl methacrylate) (PMMA) for stabilization and baked on a hotplate at 90 °C for 5 min. The separation of the PMMA/CNM/Au layer from the mica substrate was achieved by carefully dipping the sample into water. Subsequently, the Au layer was completely etched by a gold etchant (5 wt % I_2 and 10 wt % KI in water). Afterwards, the PMMA/CNM layer was transferred to a Si substrate with an oxide layer with the thickness of 300 nm and the sample was immersed into acetone for 40 min for the dissolution of the PMMA layer. For the fabrication of freestanding NBPT CNMs on a TEM grid the same process was carried out, except for the drying process being conducted in a critical-point dryer (CPD, Autosamdri-815B, Tousimis, USA) to yield intact and suspended CNMs.

Acknowledgements

We thank David C. Joy for providing the software package IONiSE, Udo Werner, Albert Schnieders and Xiankun Lin for valuable discussions, Nils-Eike Weber and Berthold Völkel for technical support. Financial support from the Volkswagenstiftung, BMBF and the Deutsche Forschungsgemeinschaft (SFB 613) is gratefully acknowledged.

References

1. Turchanin, A.; Gölzhäuser, A. *Prog. Surf. Sci.* **2012,** *87,* 108–162. doi:10.1016/j.progsurf.2012.05.001
2. Angelova, P.; Vieker, H.; Weber, N.-E.; Matei, D.; Reimer, O.; Meier, I.; Kurasch, S.; Biskupek, J.; Lorbach, D.; Wunderlich, K.; Chen, L.; Terfort, A.; Klapper, M.; Müllen, K.; Kaiser, U.; Gölzhäuser, A.; Turchanin, A. *ACS Nano* **2013,** *7,* 6489–6497. doi:10.1021/nn402652f

3. Nottbohm, C. T.; Beyer, A.; Sologubenko, A. S.; Ennen, I.; Hütten, A.; Rösner, H.; Eck, W.; Mayer, J.; Gölzhäuser, A. *Ultramicroscopy* **2009,** *108,* 885–892. doi:10.1016/j.ultramic.2008.02.008
4. Zhang, X.; Beyer, A.; Gölzhäuser, A. *Beilstein J. Nanotechnol.* **2011,** *2,* 826–833. doi:10.3762/bjnano.2.92
5. Nottbohm, C. T.; Turchanin, A.; Beyer, A.; Stosch, R.; Gölzhäuser, A. *Small* **2011,** *7,* 874–883. doi:10.1002/smll.201001993
6. Turchanin, A.; Beyer, A.; Nottbohm, C. T.; Zhang, X.; Stosch, R.; Sologubenko, A.; Mayer, J.; Hinze, P.; Weimann, T.; Gölzhäuser, A. *Adv. Mater.* **2009,** *21,* 1233–1237. doi:10.1002/adma.200803078
7. Zheng, Z.; Nottbohm, C. T.; Turchanin, A.; Muzik, H.; Muzik, A.; Heilemann, M.; Sauer, M.; Gölzhäuser, A. *Angew. Chem.* **2010,** *122,* 8671–8675. doi:10.1002/ange.201004053 *Angew. Chem., Int. Edit.* **2010,** *49,* 8493–8497. doi:10.1002/anie.201004053
8. Ritter, R.; Wilhelm, R. A.; Stöger-Pollach, M.; Heller, R.; Mücklich, A.; Werner, U.; Vieker, H.; Beyer, A.; Facsko, S.; Gölzhäuser, A.; Aumayr, F. *Appl. Phys. Lett.* **2013,** *102,* 063112. doi:10.1063/1.4792511
9. Schnietz, M.; Turchanin, A.; Nottbohm, C. T.; Beyer, A.; Solak, H. H.; Hinze, P.; Weimann, T.; Gölzhäuser, A. *Small* **2009,** *5,* 2651–2655. doi:10.1002/smll.200901283
10. Gölzhäuser, A.; Eck, W.; Geyer, W.; Stadler, V.; Weimann, T.; Hinze, P.; Grunze, M. *Adv. Mater.* **2001,** *13,* 806–809. doi:10.1002/1521-4095(200106)13:11%3C803::AID-ADMA806%3E3.0.CO;2-W
11. Turchanin, A.; Schnietz, M.; El-Desawy, M.; Solak, H. H.; David, C.; Gölzhäuser, A. *Small* **2007,** *3,* 2114–2119. doi:10.1002/smll.200700516
12. Nottbohm, C. T.; Turchanin, A.; Beyer, A.; Gölzhäuser, A. *J. Vac. Sci. Technol., B* **2009,** *27,* 3059–3062. doi:10.1116/1.3253536
13. Turchanin, A.; Käfer, D.; El-Desawy, M.; Wöll, C.; Witte, G.; Gölzhäuser, A. *Langmuir* **2009,** *25,* 7342–7352. doi:10.1021/la803538z
14. Ada, E. T.; Hanley, L.; Etchin, S.; Melngailis, J.; Dressick, W. J.; Chen, M.-S.; Calvert, J. M. *J. Vac. Sci. Technol., B* **1995,** *13,* 2189–2196. doi:10.1116/1.588102
15. Cyganik, P.; Vandeweert, E.; Postawa, Z.; Bastiaansen, J.; Vervaecke, F.; Lievens, P.; Silverans, R. E.; Winograd, N. *J. Phys. Chem. B* **2005,** *109,* 5085–5094. doi:10.1021/jp0478209
16. Evelyn, A. L.; Ila, D.; Zimmerman, R. L.; Bhat, K.; Poker, D. B.; Hensley, D. K.; Klatt, C.; Kalbitzer, S.; Just, N.; Drevet, C. *Nucl. Instrum. Methods Phys. Res., Sect. B* **1999,** *148,* 1141–1145. doi:10.1016/S0168-583X(98)00858-1
17. Rangel, E. C.; Cruz, N. C.; Lepienski, C. M. *Nucl. Instrum. Methods Phys. Res., Sect. B* **2002,** *191,* 704–707. doi:10.1016/S0168-583X(02)00637-7
18. Postek, M. T.; Vladár, A.; Archie, C.; Ming, B. *Meas. Sci. Technol.* **2011,** *22,* 024004. doi:10.1088/0957-0233/22/2/024004
19. Bell, D. C. *Microsc. Microanal.* **2009,** *15,* 147–153. doi:10.1017/S1431927609090138
20. Maas, D.; van Veldhoven, E.; Chen, P.; Sidorkin, V.; Salemink, H.; van der Drift, E.; Alkemade, P. *Proc. SPIE* **2010,** *7638,* 763814. doi:10.1117/12.862438
21. Bell, D. C.; Lemme, M. C.; Stern, L. A.; Williams, J. R.; Marcus, C. M. *Nanotechnology* **2009,** *20,* 455301. doi:10.1088/0957-4484/20/45/455301
22. Sidorkin, V.; van Veldhoven, E.; van der Drift, E.; Alkemade, P.; Salemink, H.; Maas, D. *J. Vac. Sci. Technol., B* **2009,** *27,* L18–L20. doi:10.1116/1.3182742
23. Muthukumar, M. *Adv. Chem. Phys.* **2004,** *128,* 1–63. doi:10.1002/0471484237.ch1
24. Veligura, V.; Hlawacek, G.; Berkelaar, R. P.; van Gastel, R.; Zandvliet, H. J. W.; Poelsema, B. *Beilstein J. Nanotechnol.* **2013,** *4,* 453–460. doi:10.3762/bjnano.4.53
25. Andersson, G.; Morgner, H. *Nucl. Instrum. Methods Phys. Res., Sect. B* **1999,** *155,* 357–368. doi:10.1016/S0168-583X(99)00475-9
26. Ramachandra, R.; Griffin, B.; Joy, D. *Ultramicroscopy* **2009,** *109,* 748–757. doi:10.1016/j.ultramic.2009.01.013
27. Völkel, B.; Gölzhäuser, A.; Müller, H. U.; David, C.; Grunze, M. *J. Vac. Sci. Technol., B* **1997,** *15,* 2877–2881. doi:10.1116/1.589748
28. Petrov, Yu. V.; Vyvenko, O. F.; Bondarenko, A. S. *J. Surf. Invest.: X-Ray, Synchrotron Neutron Tech.* **2010,** *4,* 792–795. doi:10.1134/S1027451010050186
29. Boudaiffa, B.; Cloutier, P.; Hunting, D.; Huels, M. A.; Sanche, L. *Science* **2000,** *287,* 1658–1660. doi:10.1126/science.287.5458.1658
30. Martin, F.; Burrow, P. D.; Cai, Z.; Cloutier, P.; Hunting, D.; Sanche, L. *Phys. Rev. Lett.* **2004,** *93,* 068101. doi:10.1103/PhysRevLett.93.068101
31. Fielding, W.; Pritchard, H. O. *J. Phys. Chem.* **1962,** *66,* 821–823. doi:10.1021/j100811a011
32. Arulmozhiraja, S.; Fujii, T. *J. Chem. Phys.* **2001,** *115,* 10589–10594. doi:10.1063/1.1418438
33. Fabrikant, I. I.; Hotop, H. *J. Chem. Phys.* **2008,** *128,* 124308. doi:10.1063/1.2841079
34. Voigtländer, B. *Surf. Sci. Rep.* **2001,** *43,* 127–254. doi:10.1016/S0167-5729(01)00012-7

License and Terms

5 Summary and conclusions

In this work, several examples of the use of helium ion microscopy (HIM) on actual scientific challenges have been presented. These examples demonstrate major advantages of HIM compared to the established technique of scanning electron microscopy (SEM). In most cases, the extraordinary small spot size and thus the achieved high lateral resolution are of importance.

For ultrathin carbon nanomembranes (CNMs), the combination of high surface sensitivity, resolution and tolerance to insulating samples in HIM provides images that in a quality that is impossible from other methods. A good contrast of such membranes on all tested substrates is shown. Characteristic features like folds, cracks and the general morphology are well visible from the macro- to the nanoscale. On freestanding CNMs, the possibility to investigate porosity down to the nanometer-size is demonstrated. Thus, a time-efficient production control for the manufacturing of CNMs is possible with HIM.

A further challenging carbonaceous material investigated are nascent soot nanoparticles from combustion processes. The high contrast on samples composed of light elements, again in combination with the high lateral resolution, is a key advantage of using HIM. HIM allowed the time efficient probing of a high number of particles for size and shape down to 2 nm. Thus a statistical analysis was possible. Especially, the assumption that nascent soot is not a sphere could be supported. The growth of such nanoparticles was then systematically studied for different flame conditions and fuels. The composition was also tested by X-ray photoelectron spectroscopy (XPS), indicating that soot at early stages is highly reactive in air.

A variety of transition metal oxide (TMO) films were imaged, where the high depth of field provided well resolved images on these highly corrugated films. The understanding of the growth and the catalytic activity of such films was enhanced with this work. These films are intended to be used as better and cheaper catalysts in combustion processes. Here, again XPS was additionally used to investigate the elemental species involved in catalytic processes at the surface. The results were combined with a variety of other characterization techniques performed by the collaborating group to thoroughly investigate and test all films.

All examples so far use the detection of secondary electrons. Another imaging mode of the HIM is the detection of Rutherford backscattered ions (RBI). This mode is especially sensitive to the atomic number of a solid material. Its usability is demonstrated by an example of defect analysis on Boersch phase plates for use in TEM. The second example is the analysis of the effect of annealing on electrospun gold nanowires. Voltage contrast provides information about insulating parts in freestanding wires, where the RBI mode shows positions of high gold concentration in the wires.

Due to the high momentum of helium ions compared to electrons, sputtering is a relevant factor in the HIM. Compared to the commonly used gallium focused ion beam (FIB), the sputter rate is small and the interaction is collimated to a smaller spot. This provides scientists with new possibilities to directly manipulate solids with prior impossible feature detail, which is demonstrated on gold bow-tie structures where edges were sharpened and reproducible cuts of less than 6 nm size were added. Carbon nanotubes within functional devices were cut with dimensions of less than 3 nm. This is small enough for single organic molecules to be directly measured between these electrodes.

Finally, some lithographic possibilities were explored. The irradiation (crosslinking) of self-assembled monolayers, which leads to crosslinking an eventually to the formation of CNMs by helium ions was demonstrated for the first time. The dose dependency of the crosslinking process was investigated and described. Also, the necessary irradiation dose was observed to be extraordinary low compared to electrons.

6 References

(1) Abbe, E. Beiträge zur Theorie des Mikroskops und der mikroskopischen Wahrnehmung. *Arch. Für Mikrosk. Anat.* **1873**, *9*, 413–418.

(2) Goldstein, J. *Scanning Electron Microscopy and X-Ray Microanalysis: Third Edition*; Auflage: 3rd Corrected ed. 2003. Corr. 2nd printing 2007.; Springer: New York, 2007.

(3) Hill, R.; Notte, J. A.; Scipioni, L.; Hawkes, P. W. Chapter 2 - Scanning Helium Ion Microscopy. In *Advances in Imaging and Electron Physics*; Elsevier, 2012; Vol. Volume 170, pp. 65–148.

(4) Cohen-Tanugi, D.; Yao, N. Superior Imaging Resolution in Scanning Helium-Ion Microscopy: A Look at Beam-Sample Interactions. *J. Appl. Phys.* **2008**, *104*, 063504.

(5) Morgan, John; Notte, John; Hill, Rymond; Ward, Bill. An Introduction to the Helium Ion Microscope. *Microsc. Today* **2006**, *22*.

(6) Zeiss. Carl Zeiss Press Release: New Benchmark http://www.smt.zeiss.com/C1256A770030BCE0/WebViewAllE/F4BF4E46C9379912C1257508002B9F7C (accessed Aug 22, 2014).

(7) Hill, R.; Notte, J.; Ward, B. The ALIS He Ion Source and Its Application to High Resolution Microscopy. *Phys. Procedia* **2008**, *1*, 135–141.

(8) Ward, B. W.; Notte, J. A.; Economou, N. P. Helium Ion Microscope: A New Tool for Nanoscale Microscopy and Metrology. *J. Vac. Sci. Technol. B* **2006**, *24*, 2871–2874.

(9) Joy, D. C. *Helium Ion Microscopy : Principles and Applications*; Springer, 2013.

(10) Maas, D. J.; Gastel, R. van. Helium Ion Microscopy. In *Surface Science Techniques*; Bracco, G.; Holst, B., Eds.; Springer Series in Surface Sciences; Springer Berlin Heidelberg, 2013; pp. 461–497.

(11) Hlawacek, G.; Veligura, V.; Gastel, R. van; Poelsema, B. Helium Ion Microscopy. *J. Vac. Sci. Technol. B* **2014**, *32*, 020801.

(12) Bell, D. C. Contrast Mechanisms and Image Formation in Helium Ion Microscopy. *Microsc. Microanal.* **2009**, *15*, 147–153.

(13) Guo, H. X.; Fujita, D. Scanning Helium Ion Microscopy. In *Characterization of Materials*; John Wiley & Sons, Inc., 2012.

(14) Scipioni, L.; Sanford, C. A.; Notte, J.; Thompson, B.; McVey, S. Understanding Imaging Modes in the Helium Ion Microscope. *J. Vac. Sci. Technol. B* **2009**, *27*, 3250–3255.

(15) Economou, N. P.; Notte, J. A.; Thompson, W. B. The History and Development of the Helium Ion Microscope. *Scanning* **2011**.

(16) Müller, E. W. Das Feldionenmikroskop. *Z. Für Phys.* **1951**, *131*, 136–142.

(17) Müller, E. W. Field Ion Microscopy. *Science* **1965**, *149*, 591–601.

(18) Gölzhäuser, A.; Ehrlich, G. Atom Movement and Binding on Surface Clusters: Pt on Pt(111) Clusters. *Phys. Rev. Lett.* **1996**, *77*, 1334–1337.

(19) Notte, J.; Ward, B.; Economou, N.; Hill, R.; Percival, R.; Farkas, L.; McVey, S. An Introduction to the Helium Ion Microscope. In *AIP Conference Proceedings*; AIP Publishing, 2007; Vol. 931, pp. 489–496.

(20) Petrov, Y. V.; Vyvenko, O. F.; Bondarenko, A. S. Scanning Helium Ion Microscope: Distribution of Secondary Electrons and Ion Channeling. *J. Surf. Investig. X-Ray Synchrotron Neutron Tech.* **2010**, *4*, 792–795.

(21) Hlawacek, G.; Ahmad, I.; Smithers, M. A.; Kooij, E. S. To See or Not to See: Imaging Surfactant Coated Nano-Particles Using HIM and SEM. *Ultramicroscopy* **2013**, *135*, 89–94.

(22) Ramachandra, R.; Griffin, B.; Joy, D. A Model of Secondary Electron Imaging in the Helium Ion Scanning Microscope. *Ultramicroscopy* **2009**, *109*, 748–757.

(23) Castaldo, V.; Hagen, C. W.; Kruit, P.; van Veldhoven, E.; Maas, D. On the Influence of the Sputtering in Determining the Resolution of a Scanning Ion Microscope. *J. Vac. Sci. Technol. B* **2009**, *27*, 3196.

(24) Ohya, K.; Yamanaka, T. Modeling Secondary Electron Emission from Nanostructured Materials in Helium Ion Microscope. *Nucl. Instrum. Methods Phys. Res. Sect. B Beam Interact. Mater. At.* **2013**, *315*, 295–299.

(25) Ohya, K. Simulation of Insulating-Layer Charging on a Conductive Substrate Irradiated by Ion and Electron Beams. *J. Vac. Sci. Technol. B* **2014**, *32*, 06FC01.

(26) Boden, S. A.; Asadollahbaik, A.; Rutt, H. N.; Bagnall, D. M. Helium Ion Microscopy of Lepidoptera Scales. *Scanning* **2012**, *34*, 107–120.

(27) Joens, M. S.; Huynh, C.; Kasuboski, J. M.; Ferranti, D.; Sigal, Y. J.; Zeitvogel, F.; Obst, M.; Burkhardt, C. J.; Curran, K. P.; Chalasani, S. H.; *et al.* Helium Ion Microscopy (HIM) for the Imaging of Biological Samples at Sub-Nanometer Resolution. *Sci. Rep.* **2013**, *3*.

(28) Carl Zeiss SMT. *Instruction Manual: Orion Plus^{TM} Helium Ion Microscope*; 2009.

(29) Sijbrandij, S.; Thompson, B.; Notte, J.; Ward, B. W.; Economou, N. P. Elemental Analysis with the Helium Ion Microscope. *J. Vac. Sci. Technol. B* **2008**, *26*, 2103.

(30) Kostinski, S.; Yao, N. Rutherford Backscattering Oscillation in Scanning Helium-Ion Microscopy. *J. Appl. Phys.* **2011**, *109*, 064311.

(31) Hill, R.; Faridur Rahman, F. H. M. Advances in Helium Ion Microscopy. *Nucl. Instrum. Methods Phys. Res. Sect. Accel. Spectrometers Detect. Assoc. Equip.* **2011**, *645*, 96–101.

(32) Sijbrandij, S.; Notte, J.; Scipioni, L.; Huynh, C.; Sanford, C. Analysis and Metrology with a Focused Helium Ion Beam. *J. Vac. Sci. Technol. B* **2010**, *28*, 73.

(33) Takei, H.; Bessho, N.; Ishii, A.; Okamoto, T.; Beyer, A.; Vieker, H.; Gölzhäuser, A. Enhanced Infrared LSPR Sensitivity of Cap-Shaped Gold Nanoparticles Coupled to a Metallic Film. *Langmuir* **2014**, *30*, 2297–2305.

(34) Smentkowski, V. S.; Moore, C. A. In-Situ Plasma Cleaning of Samples to Remove Hydrocarbon And/or Polydimethylsiloxane prior to ToF-SIMS Analysis. *J. Vac. Sci. Technol. A* **2013**, *31*, 06F105.

(35) Vickerman, J. C.; Gilmore, I. *Surface Analysis: The Principal Techniques*; Auflage: 2. Auflage.; John Wiley & Sons: Chichester, U.K, 2009.

(36) Briggs, D.; Seah, M. P. *Practical Surface Analysis, Auger and X-Ray Photoelectron Spectroscopy*; Wiley, 1990.

(37) Biesinger, M. C.; Payne, B. P.; Grosvenor, A. P.; Lau, L. W. M.; Gerson, A. R.; Smart, R. S. C. Resolving Surface Chemical States in XPS Analysis of First Row Transition Metals, Oxides and Hydroxides: Cr, Mn, Fe, Co and Ni. *Appl. Surf. Sci.* **2011**, *257*, 2717–2730.

(38) Biesinger, M. C.; Lau, L. W. M.; Gerson, A. R.; Smart, R. S. C. Resolving Surface Chemical States in XPS Analysis of First Row Transition Metals, Oxides and Hydroxides: Sc, Ti, V, Cu and Zn. *Appl. Surf. Sci.* **2010**, *257*, 887–898.

(39) Biesinger, M. C.; Payne, B. P.; Lau, L. W. M.; Gerson, A.; Smart, R. S. C. X-Ray Photoelectron Spectroscopic Chemical State Quantification of Mixed Nickel Metal, Oxide and Hydroxide Systems. *Surf. Interface Anal.* **2009**, *41*, 324–332.

(40) Powell, C. J.; Jablonski, A. Surface Sensitivity of X-Ray Photoelectron Spectroscopy. *Nucl. Instrum. Methods Phys. Res. Sect. Accel. Spectrometers Detect. Assoc. Equip.* **2009**, *601*, 54–65.

(41) Powell, C. J.; Jablonski, A. Progress in Quantitative Surface Analysis by X-Ray Photoelectron Spectroscopy: Current Status and Perspectives. *J. Electron Spectrosc. Relat. Phenom.* **2010**, *178-179*, 331–346.

(42) Powell, C. J.; Jablonski, A. *NIST Electron Effective-Attenuation-Length Database - Version 1.3,*; National Institute of Standards and Technology, Gaithersburg, MD, 2011.

(43) Crist, B. V. *Handbook of Monochromatic XPS Spectra. 3 Volume Set: Handbook of Monochromatic XPS Spectra: Volume 3: Polymers and Polymers Damaged by X-Rays*; 1. Auflage.; John Wiley & Sons, 2000.

(44) Scofield, J. H. Hartree-Slater Subshell Photoionization Cross-Sections at 1254 and 1487 eV. *J. Electron Spectrosc. Relat. Phenom.* **1976**, *8*, 129–137.

(45) Nottbohm, C. T.; Turchanin, A.; Beyer, A.; Stosch, R.; Gölzhäuser, A. Mechanically Stacked 1-Nm-Thick Carbon Nanosheets: Ultrathin Layered Materials with Tunable Optical, Chemical, and Electrical Properties. *Small* **2011**, *7*, 874–883.

(46) Turchanin, A.; Beyer, A.; Nottbohm, C. T.; Zhang, X.; Stosch, R.; Sologubenko, A.; Mayer, J.; Hinze, P.; Weimann, T.; Gölzhäuser, A. One Nanometer Thin Carbon Nanosheets with Tunable Conductivity and Stiffness. *Adv. Mater.* **2009**, *21*, 1233–1237.

(47) Ritter, R.; Wilhelm, R. A.; Stöger-Pollach, M.; Heller, R.; Mücklich, A.; Werner, U.; Vieker, H.; Beyer, A.; Facsko, S.; Gölzhäuser, A.; *et al.* Fabrication of Nanopores in 1 Nm Thick Carbon Nanomembranes with Slow Highly Charged Ions. *Appl. Phys. Lett.* **2013**, *102*, 063112–063112 – 5.

(48) Geyer, W.; Stadler, V.; Eck, W.; Zharnikov, M.; Gölzhäuser, A.; Grunze, M. Electron-Induced Crosslinking of Aromatic Self-Assembled Monolayers: Negative Resists for Nanolithography. *Appl. Phys. Lett.* **1999**, *75*, 2401–2403.

(49) Turchanin, A.; Schnietz, M.; El-Desawy, M.; Solak, H. H.; David, C.; Gölzhäuser, A. Fabrication of Molecular Nanotemplates in Self-Assembled Monolayers by Extreme-Ultraviolet-Induced Chemical Lithography. *Small* **2007**, *3*, 2114–2119.

(50) Eck, W.; Küller, A.; Grunze, M.; Völkel, B.; Gölzhäuser, A. Freestanding Nanosheets from Crosslinked Biphenyl Self-Assembled Monolayers. *Adv. Mater.* **2005**, *17*, 2583–2587.

(51) Turchanin, A.; Weber, D.; Büenfeld, M.; Kisielowski, C.; Fistul, M. V.; Efetov, K. B.; Weimann, T.; Stosch, R.; Mayer, J.; Gölzhäuser, A. Conversion of Self-

Assembled Monolayers into Nanocrystalline Graphene: Structure and Electric Transport. *Acs Nano* **2011**, *5*, 3896–3904.

(52) Rhinow, D.; Weber, N.-E.; Turchanin, A. Atmospheric Pressure, Temperature-Induced Conversion of Organic Monolayers into Nanocrystalline Graphene. *J Phys Chem C* **2012**.

(53) Ai, M.; Shishatskiy, S.; Wind, J.; Zhang, X.; Nottbohm, C. T.; Mellech, N.; Winter, A.; Vieker, H.; Qiu, J.; Dietz, K.-J.; *et al.* Carbon Nanomembranes (CNMs) Supported by Polymer: Mechanics and Gas Permeation. *Adv. Mater.* **2014**, *26*, 3421–3426.

(54) Schnietz, M.; Turchanin, A.; Nottbohm, C. T.; Beyer, A.; Solak, H. H.; Hinze, P.; Weimann, T.; Gölzhäuser, A. Chemically Functionalized Carbon Nanosieves with 1-Nm Thickness. *Small* **2009**.

(55) Turchanin, A.; Tinazli, A.; El-Desawy, M.; Großmann, H.; Schnietz, M.; Solak, H. H.; Tampé, R.; Gölzhäuser, A. Molecular Self-Assembly, Chemical Lithography, and Biochemical Tweezers: A Path for the Fabrication of Functional Nanometer-Scale Protein Arrays. *Adv. Mater.* **2008**, *20*, 471–477.

(56) Turchanin, A.; Gölzhäuser, A. Carbon Nanomembranes from Self-Assembled Monolayers: Functional Surfaces without Bulk. *Prog. Surf. Sci.* **2012**, *87*, 108–162.

(57) Nottbohm, C. T. Carbon Nanosheets and Their Applications, Universität Bielefeld, Fakultät für Physik, Physik Supramolekularer Systeme, 2009.

(58) Meyerbröker, N.; Zharnikov, M. Modification of Nitrile-Terminated Biphenylthiol Self-Assembled Monolayers by Electron Irradiation and Related Applications. *Langmuir* **2012**, *28*, 9583–9592.

(59) Meyerbröker, N.; Li, Z.-A.; Eck, W.; Zharnikov, M. Biocompatible Nanomembranes Based on PEGylation of Cross-Linked Self-Assembled Monolayers. *Chem. Mater.* **2012**, *24*, 2965–2972.

(60) Abbas, A. N.; Liu, G.; Liu, B.; Zhang, L.; Liu, H.; Ohlberg, D.; Wu, W.; Zhou, C. Patterning, Characterization, and Chemical Sensing Applications of Graphene Nanoribbon Arrays Down to 5 Nm Using Helium Ion Beam Lithography. *ACS Nano* **2014**, *8*, 1538–1546.

(61) Bell, D. C.; Lemme, M. C.; Stern, L. A.; Williams, J. R.; Marcus, C. M. Precision Cutting and Patterning of Graphene with Helium Ions. *Nanotechnology* **2009**, *20*, 455301.

(62) Lemme, M. C.; Bell, D. C.; Williams, J. R.; Stern, L. A.; Baugher, B. W. H.; Jarillo-Herrero, P.; Marcus, C. M. Etching of Graphene Devices with a Helium Ion Beam. *ACS Nano* **2009**, *3*, 2674–2676.

(63) Archanjo, B. S.; Fragneaud, B.; Cançado, L. G.; Winston, D.; Miao, F.; Achete, C. A.; Medeiros-Ribeiro, G. Graphene Nanoribbon Superlattices Fabricated via He Ion Lithography. *Appl. Phys. Lett.* **2014**, *104*, 193114.

(64) Weber, N.-E. Präparation Und Charakterisierung von Graphen Basierend Auf Selbst-Organisierten Monolagen. Dissertation, Universität Bielefeld, 2014.

(65) Guo, H.; Gao, J.; Ishida, N.; Xu, M.; Fujita, D. Characterization of Two-Dimensional Hexagonal Boron Nitride Using Scanning Electron and Scanning Helium Ion Microscopy. *Appl. Phys. Lett.* **2014**, *104*, 031607.

(66) Hlawacek, G.; Veligura, V.; Lorbek, S.; Mocking, T. F.; George, A.; van Gastel, R.; Zandvliet, H. J. W.; Poelsema, B. Imaging Ultra Thin Layers with Helium Ion Microscopy: Utilizing the Channeling Contrast Mechanism. *Beilstein J. Nanotechnol.* **2012**, *3*, 507–512.

(67) Ritter, Robert. Nanostructures Formed on Surfaces due to the Impact of Slow Highly Charged Ions, TU Wien: Wien, 2013.

(68) Angelova, P.; Vieker, H.; Weber, N.-E.; Matei, D.; Reimer, O.; Meier, I.; Kurasch, S.; Biskupek, J.; Lorbach, D.; Wunderlich, K.; *et al.* A Universal Scheme to Convert Aromatic Molecular Monolayers into Functional Carbon Nanomembranes. *ACS Nano* **2013**, *7*, 6489–6497.

(69) Schenk, M.; Lieb, S.; Vieker, H.; Beyer, A.; Gölzhäuser, A.; Wang, H.; Kohse-Höinghaus, K. Imaging Nanocarbon Materials: Soot Particles in Flames Are Not Structurally Homogeneous. *ChemPhysChem* **2013**, *14*, 3248–3254.

(70) Schenk, M.; Lieb, S.; Vieker, H.; Beyer, A.; Gölzhäuser, A.; Wang, H.; Kohse-Höinghaus, K. Morphology of Nascent Soot in Ethylene Flames. *Proc. Combust. Inst.* **2014**, DOI: 10.1016/j.proci.2014.05.009.

(71) Schenk, M.; Hansen, N.; Vieker, H.; Beyer, A.; Gölzhäuser, A.; Kohse-Höinghaus, K. PAH Formation and Soot Morphology in Flames of C4 Fuels. *Proc. Combust. Inst.* **2014**, DOI: 10.1016/j.proci.2014.06.139.

(72) Wang, H. Formation of Nascent Soot and Other Condensed-Phase Materials in Flames. *Proc. Combust. Inst.* **2011**, *33*, 41–67.

(73) Kumfer, B.; Kennedy, I. The Role of Soot in the Health Effects of Inhaled Airborne Particles. In *Combustion Generated Fine Carbonaceous Particles*; KIT Scientific Publishing, 2009.

(74) Bond, T. C.; Doherty, S. J.; Fahey, D. W.; Forster, P. M.; Berntsen, T.; DeAngelo, B. J.; Flanner, M. G.; Ghan, S.; Kärcher, B.; Koch, D.; *et al.* Bounding the Role of Black Carbon in the Climate System: A Scientific Assessment. *J. Geophys. Res. Atmospheres* **2013**, *118*, 5380–5552.

(75) Donnet, J. B. Structure and Reactivity of Carbons: From Carbon Black to Carbon Composites. *Carbon* **1982**, *20*, 267–282.

(76) Zhao, B.; Uchikawa, K.; Wang, H. A Comparative Study of Nanoparticles in Premixed Flames by Scanning Mobility Particle Sizer, Small Angle Neutron Scattering, and Transmission Electron Microscopy. *Proc. Combust. Inst.* **2007**, *31*, 851–860.

(77) Wang, H.; Zhao, B.; Wyslouzil, B.; Streletzky, K. Small-Angle Neutron Scattering of Soot Formed in Laminar Premixed Ethylene Flames. *Proc. Combust. Inst.* **2002**, *29*, 2749–2757.

(78) King, W. E.; Campbell, G. H.; Frank, A.; Reed, B.; Schmerge, J. F.; Siwick, B. J.; Stuart, B. C.; Weber, P. M. Ultrafast Electron Microscopy in Materials Science, Biology, and Chemistry. *J. Appl. Phys.* **2005**, *97*, 111101–111101 – 27.

(79) Abid, A. D.; Heinz, N.; Tolmachoff, E. D.; Phares, D. J.; Campbell, C. S.; Wang, H. On Evolution of Particle Size Distribution Functions of Incipient Soot in Premixed Ethylene–oxygen–argon Flames. *Combust. Flame* **2008**, *154*, 775–788.

(80) Gaddam, C. K.; Vander Wal, R. L. Physical and Chemical Characterization of SIDI Engine Particulates. *Combust. Flame* **2013**, *160*, 2517–2528.

(81) Kaciulis, S. Spectroscopy of Carbon: From Diamond to Nitride Films. *Surf. Interface Anal.* **2012**, *44*, 1155–1161.

(82) Cain, J. P.; Gassman, P. L.; Wang, H.; Laskin, A. Micro-FTIR Study of Soot Chemical Composition—evidence of Aliphatic Hydrocarbons on Nascent Soot Surfaces. *Phys. Chem. Chem. Phys.* **2010**, *12*, 5206–5218.

(83) Kouotou, P. M.; Tian, Z.-Y.; Vieker, H.; Beyer, A.; Gölzhäuser, A.; Kohse-Höinghaus, K. Selective Synthesis of A-Fe2O3 Thin Films and Effect of the Deposition Temperature and Lattice Oxygen on the Catalytic Combustion of Propene. *J. Mater. Chem. A* **2013**, *1*, 10495–10504.

(84) Kouotou, P. M.; Tian, Z.-Y.; Vieker, H.; Kohse-Höinghaus, K. Pulsed-Spray Evaporation CVD Synthesis of Hematite Thin Films for Catalytic Conversion of CO. *Surf. Coat. Technol.* **2013**, *230*, 59–65.

(85) Ngamou, P. H. T.; El Kasmi, A.; Kohse-Höinghaus, K.; Vieker, H.; Beyer, A.; Weiss, T.; Zielasek, V.; Bäumer, M. Growth Behavior of Chemical-Vapor-Deposited Cobalt Thin Films Using Ethanol Solutions of Co (II) and Co (III) Acetylacetonate. **2015**, *Manuscript in preparation*.

(86) Tian, Z.-Y.; Herrenbrück, H. J.; Kouotou, P. M.; Vieker, H.; Beyer, A.; Gölzhäuser, A.; Kohse-Höinghaus, K. Facile Synthesis of Catalytically Active Copper Oxide from Pulsed-Spray Evaporation CVD. *Surf. Coat. Technol.* **2013**, *230*, 33–38.

(87) Kouotou, P. M.; Vieker, H.; Tian, Z.-Y.; Ngamou, P. T.; Kasmi, A. E.; Beyer, A.; Gölzhäuser, A.; Kohse-Höinghaus, K. Structure-Activity Relation of Spinel-Type Co-Fe Oxides for Low-Temperature CO Oxidation. *Catal. Sci. Technol.* **2014**, *4*, 3359–3367.

(88) Tian, Z.-Y.; Kouotou, P. M.; El Kasmi, A.; Tchoua Ngamou, P. H.; Kohse-Höinghaus, K.; Vieker, H.; Beyer, A.; Gölzhäuser, A. Low-Temperature Deep Oxidation of Olefins and DME over Cobalt Ferrite. *Proc. Combust. Inst.* **2014**, DOI: 10.1016/j.proci.2014.06.111.

(89) Tian, Z.-Y.; Vieker, H.; Kouotou, P. M.; Beyer, A. In-Situ Characterization of Cu-Co Oxides for Catalytic Application. *Faraday Discuss.* **2014**, *Manuscript accepted*.

(90) McMichael, A. J.; Woodruff, R. E.; Hales, S. Climate Change and Human Health: Present and Future Risks. *The Lancet* **2006**, *367*, 859–869.

(91) Kung, H. H. *Transition Metal Oxides: Surface Chemistry and Catalysis*; Elsevier, 1989.

(92) Sénateur, J.-P.; Dubourdieu, C.; Weiss, F.; Rosina, M.; Abrutis, A. Pulsed Injection MOCVD of Functional Electronic Oxides. *Adv. Mater. Opt. Electron.* **2000**, *10*, 155–161.

(93) Kouotou, P. M. Synthesis and Catalytic Application of Functional Transition Metal Oxides. Dissertation, Universität Bielefeld, 2014.

(94) Grosvenor, A. P.; Kobe, B. A.; Biesinger, M. C.; McIntyre, N. S. Investigation of Multiplet Splitting of Fe 2p XPS Spectra and Bonding in Iron Compounds. *Surf. Interface Anal.* **2004**, *36*, 1564–1574.

(95) Yamashita, T.; Hayes, P. Analysis of XPS Spectra of Fe2+ and Fe3+ Ions in Oxide Materials. *Appl. Surf. Sci.* **2008**, *254*, 2441–2449.

(96) Ma, J.; Teo, J.; Mei, L.; Zhong, Z.; Li, Q.; Wang, T.; Duan, X.; Lian, J.; Zheng, W. Porous Platelike Hematite Mesocrystals: Synthesis, Catalytic and Gas-Sensing Applications. *J. Mater. Chem.* **2012**, *22*, 11694–11700.

(97) Walter, A.; Muzik, H.; Vieker, H.; Turchanin, A.; Beyer, A.; Gölzhäuser, A.; Lacher, M.; Steltenkamp, S.; Schmitz, S.; Holik, P.; *et al.* Practical Aspects of Boersch Phase Contrast Electron Microscopy of Biological Specimens. *Ultramicroscopy* **2012**, *116*, 62–72.

(98) Mitschang, F.; Langner, M.; Vieker, H.; Beyer, A.; Greiner, A. Preparation of Conductive Gold Nanowires in Confined Environment of Gold-Filled Polymer Nanotubes. *Macromol. Rapid Commun.* **2014**, *Manuscript accepted*.

(99) Fox, D.; Chen, Y.; Faulkner, C. C.; Zhang, H. Nano-Structuring, Surface and Bulk Modification with a Focused Helium Ion Beam. *Beilstein J. Nanotechnol.* **2012**, *3*, 579–585.

(100) Livengood, R.; Tan, S.; Greenzweig, Y.; Notte, J.; McVey, S. Subsurface Damage from Helium Ions as a Function of Dose, Beam Energy, and Dose Rate. *J. Vac. Sci. Technol. B Microelectron. Nanometer Struct.* **2009**.

(101) Rudneva, M.; van Veldhoven, E.; Malladi, S. K.; Maas, D.; Zandbergen, H. W. Novel Nanosample Preparation with a Helium Ion Microscope. *J. Mater. Res.* **2013**, *28*, 1013–1020.

(102) Sidorkin, V.; van Veldhoven, E.; van der Drift, E.; Alkemade, P.; Salemink, H.; Maas, D. Sub-10-Nm Nanolithography with a Scanning Helium Beam. *J. Vac. Sci. Technol. B Microelectron. Nanometer Struct.* **2009**, *27*, L18.

(103) Knust, S.; Spiering, A.; Vieker, H.; Beyer, A.; Gölzhäuser, A.; Tönsing, K.; Sischka, A.; Anselmetti, D. Video-Based and Interference-Free Axial Force Detection and Analysis for Optical Tweezers. *Rev. Sci. Instrum.* **2012**, *83*, 103704–103704 – 6.

(104) Spiering, A.; Knust, S.; Getfert, S.; Beyer, A.; Rott, K.; Redondo, L.; Tönsing, K.; Reimann, P.; Sischka, A.; Anselmetti, D. Single-Molecule DNA Translocation Through Si 3 N 4 - and Graphene Solid-State Nanopores. In *Nanopores for Bioanalytical Applications: Proceedings of the International Conference*; 2012.

(105) Yang, J.; Ferranti, D. C.; Stern, L. A.; Sanford, C. A.; Huang, J.; Ren, Z.; Qin, L.-C.; Hall, A. R. Rapid and Precise Scanning Helium Ion Microscope Milling of Solid-State Nanopores for Biomolecule Detection. *Nanotechnology* **2011**, *22*, 285310.

(106) Marshall, M. M.; Yang, J.; Hall, A. R. Direct and Transmission Milling of Suspended Silicon Nitride Membranes With a Focused Helium Ion Beam. *Scanning* **2012**.

(107) Hall, A. R. In Situ Thickness Assessment During Ion Milling of a Free-Standing Membrane Using Transmission Helium Ion Microscopy. *Microsc. Microanal.* **2013**, *19*, 740–744.

(108) Annamalai, M.; Mathew, S.; Viswanathan, V.; Fang, C.; Pickard, D. S.; Palaniapan, M. Design, Fabrication and Helium Ion Microscope Patterning of Suspended Nanomechanical Graphene Structures for NEMS Applications. In *Solid-State Sensors, Actuators and Microsystems Conference (TRANSDUCERS), 2011 16th International*; IEEE, 2011; pp. 2578–2581.

(109) Lehtinen, O.; Kotakoski, J.; Krasheninnikov, A. V.; Keinonen, J. Cutting and Controlled Modification of Graphene with Ion Beams. *Nanotechnology* **2011**, *22*, 175306.

(110) Mizuta, H.; Moktadir, Z.; Boden, S. A.; Kalhor, N.; Hang, S.; Schmidt, M. E.; Cuong, N. T.; Chi, D. H.; Otsuka, N.; Muruganathan, M.; *et al.* Fabrication and *ab Initio* Study of Downscaled Graphene Nanoelectronic Devices. **2012**, 846206–846206.

(111) Hang, S.; Moktadir, Z.; Mizuta, H. Raman Study of Damage Extent in Graphene Nanostructures Carved by High Energy Helium Ion Beam. *Carbon* **2014**.

(112) Fox, D.; Zhou, Y. B.; O'Neill, A.; Kumar, S.; Wang, J. J.; Coleman, J. N.; Duesberg, G. S.; Donegan, J. F.; Zhang, H. Z. Helium Ion Microscopy of

Graphene: Beam Damage, Image Quality and Edge Contrast. *Nanotechnology* **2013**, *24*, 335702.

(113) Wang, Y.; Abb, M.; Boden, S. A.; Aizpurua, J.; de Groot, C. H.; Muskens, O. L. Ultrafast Nonlinear Control of Progressively Loaded, Single Plasmonic Nanoantennas Fabricated Using Helium Ion Milling. *Nano Lett.* **2013**, *13*, 5647–5653.

(114) Sarriugarte, P.; Schnell, M.; Chuvilin, A.; Hillenbrand, R. Polarization-Resolved Near-Field Characterization of Nanoscale Infrared Modes in Transmission Lines Fabricated by Gallium and Helium Ion Beam Milling. *ACS Photonics* **2014**.

(115) Kuznetsov, A. I.; Miroshnichenko, A. E.; Hsing Fu, Y.; Viswanathan, V.; Rahmani, M.; Valuckas, V.; Ying Pan, Z.; Kivshar, Y.; Pickard, D. S.; Luk'yanchuk, B. Split-Ball Resonator as a Three-Dimensional Analogue of Planar Split-Rings. *Nat. Commun.* **2014**, *5*.

(116) Scholder, O.; Jefimovs, K.; Shorubalko, I.; Hafner, C.; Sennhauser, U.; Bona, G.-L. Helium Focused Ion Beam Fabricated Plasmonic Antennas with Sub-5 Nm Gaps. *Nanotechnology* **2013**, *24*, 395301.

(117) Melli, M.; Polyakov, A.; Gargas, D.; Huynh, C.; Scipioni, L.; Bao, W.; Ogletree, D. F.; Schuck, P. J.; Cabrini, S.; Weber-Bargioni, A. Reaching the Theoretical Resonance Quality Factor Limit in Coaxial Plasmonic Nanoresonators Fabricated by Helium Ion Lithography. *Nano Lett.* **2013**, *13*, 2687–2691.

(118) Scipioni, L.; Ferranti, D. C.; Smentkowski, V. S.; Potyrailo, R. A. Fabrication and Initial Characterization of Ultrahigh Aspect Ratio Vias in Gold Using the Helium Ion Microscope. *J. Vac. Sci. Technol. B* **2010**, *28*, C6P18–C6P23.

(119) Kollmann, H.; Piao, X.; Esmann, M.; Becker, S. F.; Hou, D.; Huynh, C.; Kautschor, L.-O.; Bösker, G.; Vieker, H.; Beyer, A.; *et al.* Toward Plasmonics with Nanometer Precision: Nonlinear Optics of Helium-Ion Milled Gold Nanoantennas. *Nano Lett.* **2014**, *14*, 4778–4784.

(120) Marquardt, C. W.; Grunder, S.; Błaszczyk, A.; Dehm, S.; Hennrich, F.; Löhneysen, H. v.; Mayor, M.; Krupke, R. Electroluminescence from a Single Nanotube–molecule–nanotube Junction. *Nat. Nanotechnol.* **2010**, *5*, 863–867.

(121) Thiele, C.; Engel, M.; Hennrich, F.; Kappes, M. M.; Johnsen, K.-P.; Frase, C. G.; Löhneysen, H. v.; Krupke, R. Controlled Fabrication of Single-Walled Carbon Nanotube Electrodes by Electron-Beam-Induced Oxidation. *Appl. Phys. Lett.* **2011**, *99*, 173105.

(122) Vijayaraghavan, A.; Blatt, S.; Weissenberger, D.; Oron-Carl, M.; Hennrich, F.; Gerthsen, D.; Hahn, H.; Krupke, R. Ultra-Large-Scale Directed Assembly of Single-Walled Carbon Nanotube Devices. *Nano Lett.* **2007**, *7*, 1556–1560.

(123) Thiele, C.; Vieker, H.; Beyer, A.; Flavel, B. S.; Hennrich, F.; Torres, D. M.; Eaton, T. R.; Mayor, M.; Kappes, M. M.; Gölzhäuser, A.; *et al.* Fabrication of Carbon Nanotube Nanogap Electrodes by Helium Ion Sputtering for Molecular Contacts. *Appl. Phys. Lett.* **2014**, *104*, 103102.

(124) Thiele, Cornelius. STM Characterization of Phenylene-Ethynylene Oligomers on Au(111) and Their Integration into Carbon Nanotube Nanogaps. Dissertation, Universität Karlsruhe, 2014.

(125) Nottbohm, C. T.; Turchanin, A.; Beyer, A.; Goelzhaeuser, A. Direct E-Beam Writing of 1 Nm Thin Carbon Nanoribbons. *J. Vac. Sci. Technol. B* **2009**, *27*, 3059–3062.

(126) Nottbohm, C. T.; Wiegmann, S.; Beyer, A.; Gölzhäuser, A. Holey Nanosheets by Patterning with UV/ozone. *Phys. Chem. Chem. Phys.* **2010**, *12*, 4324–4328.

7 List of Abbreviations

acac	acetylacetonate ($CH_3COCHCOCH_3$)
AuNP	Gold NanoParticle
AFM	Atomic Force Microscope/Microscopy
BPP	Boersch Phase Plate
BPT	BiPhenyl-Thiol
CNM(s)	Carbon NanoMembrane(s)
CNT(s)	Carbon NanoTube(s)
CVD	Chemical Vapor Deposition
EBL	Electron Beam Lithography
EDX/EDS	Energy Dispersive X-ray Spectroscopy
ESCA	Electron Spectroscopy for Chemical Analysis
FE-SEM	Field Emission SEM
(Ga-)FIB	(Gallium) Focused Ion Beam
FTIR	Fourier Transform InfraRed
GFIS	Gas Field Ion Source
HBC	Hexa-Peri-Benzocoronene
HCI	Highly Charged Ion(s)
HIL	Helium Ion Lithography
HIM	Helium Ion Microscope/Microscopy
HOPG	Highly Ordered Pyrolytic Graphite
LEED	Low Energy Electron Diffraction
MCP	MultiChannel Plate
HSQ	Hydrogen SilsesQuioxane
OPE	Oligo(Phenylene Ethynylene)

PAH	Polycyclic Aromatic Hydrocarbons
PDMS	PolyDiMethylSiloxane
PSE-CVD	Pulsed Spray Evaporation Chemical Vapor Deposition
RBI	Rutherford Backscattered Ion
RBS	Rutherford Backscattered Spectroscopy
SAM	Self-Assembled Monolayer
SE	Secondary Electron
SEM	Scanning Electron Microscope/Microscopy
SERS	Surface Enhanced Raman Spectroscopy
SFIM	Scanning Field Ion Microscopy/Microscopy
SHIM	Scanning Helium Ion Microscope/Microscopy
SMPS	Scanning Mobility Particle Sizer
STM	Scanning Tunneling Microscope/Microscopy
TEM	Transmission Electron Microscope/Microscopy
TMO	Transition Metal Oxide
UHV	Ultra-High Vacuum
UV-Vis	Ultraviolet–Visible spectroscopy
VOC	Volatile Organic Compound
XPS	X-Ray Photoelectron Spectroscopy
XRD	X-Ray Diffraction

8 List of figures

9 Danksagung

Die vorliegende Arbeit entstand von 2010 bis 2014 an der Fakultät für Physik der Universität Bielefeld in der Arbeitsgruppe Physik Supramolekularer Systeme und Oberflächen unter der Leitung von Prof. Dr. Armin Gölzhäuser.

Bei so einer experimentellen wissenschaftlichen Arbeit ist man selten alleine – aktuelle wissenschaftliche Fragestellungen werden in der Regel durch Zusammenarbeit vieler Experten unterschiedlicher Bereiche gelöst. In den Jahren der Forschung an dieser Arbeit hatte ich die Gelegenheit eine Vielzahl toller Menschen kennenzulernen, von denen ich hier nur einen Teil erwähnen kann.

Mein besonderer Dank gilt:

- Meinem Betreuer **Armin Gölzhäuser** für das regelmäßige Weisen in die „große Richtung“ dieser Arbeit, für die Möglichkeit meine Ergebnisse auch international vorzutragen und die spannenden Projekte auch außerhalb des eigentlichen Themas. Weiterhin meinem „Co-Betreuer“ **André Beyer**, der immer ein offenes Ohr für alle Ideen, Anregungen und die ganz alltäglichen Fragen hatte.
- **Ursula Lorentzen**, **Udo Werner** und **Karin Lacey**, die bei Ärger mit „dem Papierkram“ immer helfen konnten.
- **Polina Angelova** und **Xianghui Zhang** für spannende gemeinsame Projekte, die Möglichkeit mein Englisch zu verbessern und vieles mehr.
- **Andrey Turchanin**, der nicht nur als Wissenschaftler sondern auch als Reiseplaner eine gute Figur macht.
- Meinen langjährigen Bürokollegen **Nils-Eike Weber**, **Andreas Winter**, **Matthias Büenfeld**, **Heiko Kampmann** und **Marc Schnietz** für das gute Miteinander, die Gespräche über Wissenschaft und Anderes, und die insgesamt tolle Zeit. Weiterhin den SAMs: **Isabella Meier**, **Marta Trelka**, **Natalie Frese**, **Nils Mellech**, **Dan Matei**, **Daniel Emmrich**, **Emanuel Marschewski**, **Paul Penner**, **Oliver Reimer**, **Annika Willunat** und **Min Ai**. **Berthold Völkel** für Unterstützung bei allen möglichen und unmöglichen technischen Problemen.
- **Albert Schnieders** für das ausführliche Korrekturlesen dieser Arbeit.

- Der gesamten PC I der Uni Bielefeld, zuerst **Katharina Kohse-Höinghaus**, die eine Reihe spannende Projekte ermöglicht hat und für die Bereitschaft diese Arbeit zu begutachten. Besonders **Marina Schenk** für die tolle Zusammenarbeit bei fast unendlichen Messreihen, aber auch der gesamten CVD-Mannschaft um **Zhen-Yu Tian**: **Patrick Mountapmbeme-Kouotou**, **Achraf El Kasmi** und **Patrick Tchoua**.
- Der Zeiss-Mannschaft für die Entwicklung dieser Technik, die vielen Diskussionen und gerade am Anfang für das Lösen von technischen Problemen. Stellvertretend möchte ich hier **John Notte**, **Frank Wenners** und **Lorenz Lechner** nennen.
- Meiner Familie und meiner Frau Antje für die Unterstützung während der gesamten Zeit.

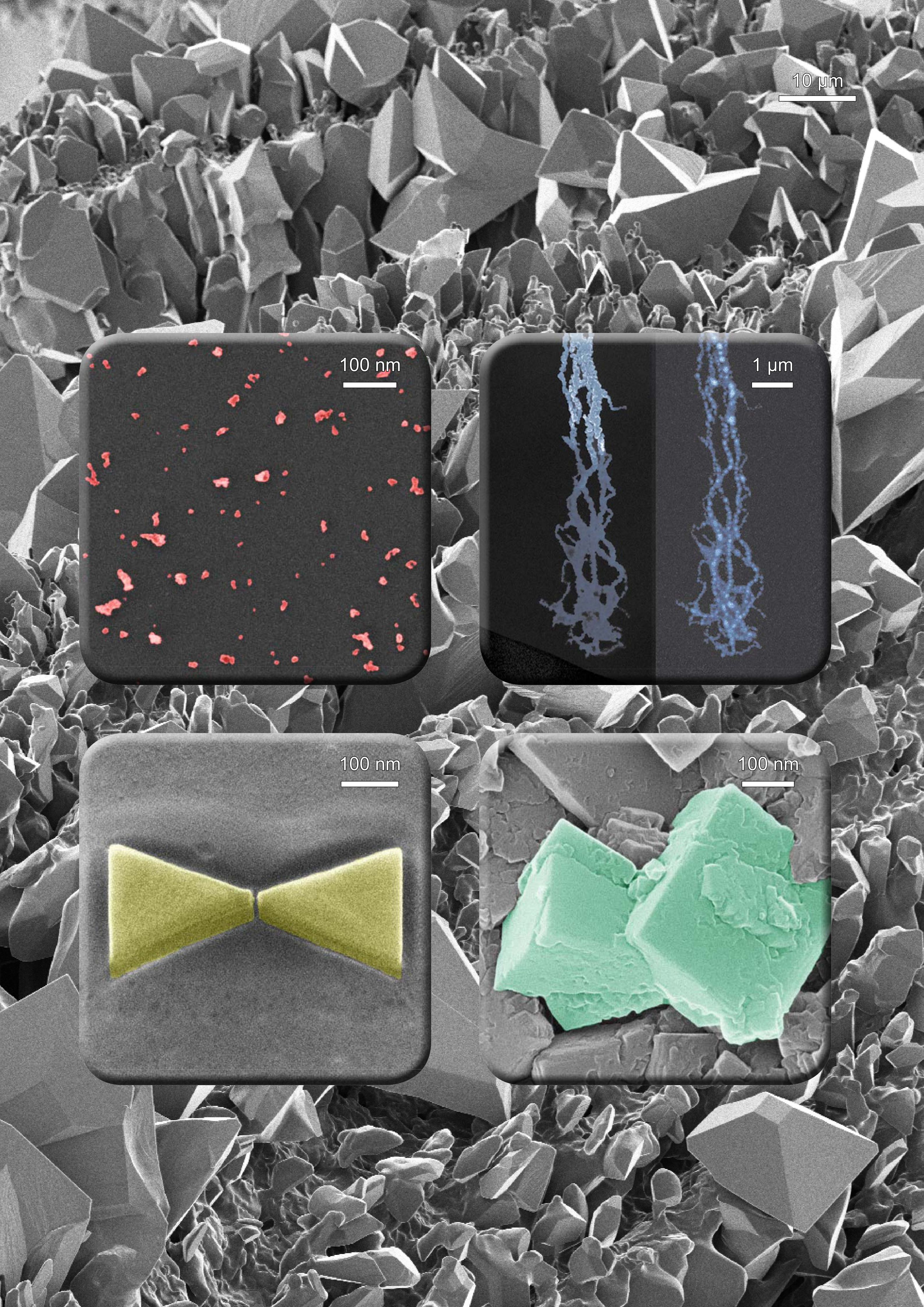
10 μm
100 nm
1 μm
100 nm
100 nm